

# The production and properties of lightweight bulk metallic glasses

**Author:**

Laws, Kevin J.

**Publication Date:**

2007

**DOI:**

<https://doi.org/10.26190/unsworks/6587>

**License:**

<https://creativecommons.org/licenses/by-nc-nd/3.0/au/>

Link to license to see what you are allowed to do with this resource.

Downloaded from <http://hdl.handle.net/1959.4/40462> in <https://unsworks.unsw.edu.au> on 2024-04-20



UNSW



>014168006



**THE UNIVERSITY OF NEW SOUTH WALES**  
**Thesis/Dissertation Sheet**

Surname or Family name: LAWS

First name: Kevin

Other name/s: James

Abbreviation for degree as given in the University calendar:

School: Materials Science and Engineering

Faculty: Science

Title: The Production and Properties of Lightweight Bulk Metallic Glasses

An inverted die casting technique was developed for the rapid and reproducible production of lightweight bulk metallic glass (BMG) castings. Processing maps for producing  $\text{Mg}_{65}\text{Cu}_{25}\text{Y}_{10}$  and  $\text{Ca}_{65}\text{Mg}_{15}\text{Zn}_{20}$  BMG samples of cross section 3.15 mm  $\times$  7 mm and a length of 125 mm were developed to identify the optimum conditions for producing castings of high structural integrity, maximum length and enhanced surface quality. As part of the experimental program, critical cooling rate and critical casting thickness experiments were also carried out for these alloys.

Isochronal and isothermal differential scanning calorimetry experiments were carried out on as-cast samples to determine their thermal properties. It was found that the  $\text{Mg}_{65}\text{Cu}_{25}\text{Y}_{10}$  BMG had a glass transition temperature of 148 °C and a crystallisation temperature of 213 °C for a heating rate of 20 °C/min, indicates a supercooled liquid (SCL) interval of 65 °C. The  $\text{Ca}_{65}\text{Mg}_{15}\text{Zn}_{20}$  BMG was found to have glass transition temperature of 105 °C and a crystallisation temperature of 137 °C for a heating rate of 20 °C/min indicating a SCL interval of 32 °C.

The elevated temperature tensile properties of these BMGs were studied. It was found that; an increase in test temperature resulted in a decrease in flow stress and an increase in strain rate resulted in an increase in flow stress. It was established that Newtonian flow occurred at high temperatures and lower strain rates in the SCL region.

The  $\text{Ca}_{65}\text{Mg}_{15}\text{Zn}_{20}$  BMG was found to be more strain rate sensitive with respect to brittle fracture, exhibiting a maximum achievable strain rate for homogeneous flow of  $10^{-3}$ /s compared to  $10^{-1}$ /s for the  $\text{Mg}_{65}\text{Cu}_{25}\text{Y}_{10}$  BMG. Elongations achieved for the  $\text{Mg}_{65}\text{Cu}_{25}\text{Y}_{10}$  BMG exceeded 1300% compared to 598% for the  $\text{Ca}_{65}\text{Mg}_{15}\text{Zn}_{20}$  BMG under constant temperature/strain rate conditions.

Both BMGs were found to crystallise under certain deformation conditions. The  $\text{Mg}_{65}\text{Cu}_{25}\text{Y}_{10}$  BMG displayed a stress increase due to crystallisation prior to times determined by static crystallisation whereas the  $\text{Ca}_{65}\text{Mg}_{15}\text{Zn}_{20}$  BMG displayed a delayed stress increase due to crystallisation. The dynamic stabilisation of the amorphous phase in the  $\text{Ca}_{65}\text{Mg}_{15}\text{Zn}_{20}$  alloy was found to decrease with increasing test temperature and decreasing strain rate.

**Declaration relating to disposition of project thesis/dissertation**

I hereby grant to the University of New South Wales or its agents the right to archive and to make available my thesis or dissertation in whole or in part in the University libraries in all forms of media, now or here after known, subject to the provisions of the Copyright Act 1968. I retain all property rights, such as patent rights. I also retain the right to use in future works (such as articles or books) all or part of this thesis or dissertation.

I also authorise University Microfilms to use the 350 word abstract of my thesis in Dissertation Abstracts International (this is applicable to doctoral theses only).

Signature

Witness

Date

The University recognises that there may be exceptional circumstances requiring restrictions on copying or conditions on use. Requests for restriction for a period of up to 2 years must be made in writing. Requests for a longer period of restriction may be considered in exceptional circumstances and require the approval of the Dean of Graduate Research.

**FOR OFFICE USE ONLY**

Date of completion of requirements for Award:

20 108

# **THE PRODUCTION AND PROPERTIES OF LIGHTWEIGHT BULK METALLIC GLASSES**

A Thesis

by

**Kevin J. Laws**

Submitted in complete fulfilment of the requirements for the award of  
the degree of

**Doctor of Philosophy**

School of Materials Science and Engineering

University of New South Wales



## ORIGINALITY STATEMENT

'I hereby declare that this submission is my own work and to the best of my knowledge it contains no materials previously published or written by another person, or substantial proportions of material which have been accepted for the award of any other degree or diploma at UNSW or any other educational institution, except where due acknowledgement is made in the thesis. Any contribution made to the research by others with whom I have worked at UNSW or elsewhere, is explicitly acknowledged in the thesis. I also declare that the intellectual content of this thesis is the product of my own work, except to the extent that assistance from others in the project's design and conception or in style, presentation and linguistic expression is acknowledged.'

Signed.

Date.....22/01/08.....

## COPYRIGHT STATEMENT

'I hereby grant the University of New South Wales or its agents the right to archive and make available my thesis or dissertation in whole or part in the University libraries in all forms of media, now or here after known, subject to the provisions of the Copyright Act 1968. I retain all proprietary rights, such as patent rights. I also retain the right to use in future works (such as articles or books) all or part of this thesis or dissertation. I also authorise University Microfilms to use the 350 word abstract of my thesis in Dissertation Abstract International (this is applicable to doctoral thesis only). I have either used no substantial portions of copyright material in my thesis or I have obtained permission to use copyright material; where permission has not been granted I have applied/will apply for a partial restriction of the digital copy of my thesis or dissertation.'

Signed.....

Date.....22/01/08.....

## AUTHENTICITY STATEMENT

'I certify that the library deposit digital copy is a direct equivalent of the final officially approved version of my thesis. No emendation of content has occurred and if there are any minor variations in formatting, they are the result of conversion to digital format.'

Signed.

Date.....22/01/08.....

## ACKNOWLEDGEMENTS

The research work presented in this thesis was carried out in the laboratories of the School of Materials Science and Engineering at the University of New South Wales, with minor works being carried out in the respective electron microscopy units at the University of New South Wales and the University of Sydney. The fabrication and construction of laboratory equipment required for the project was carried out personally at the business location of P & C Laws Automotive Engineers, Richmond, NSW.

I would personally like to thank:

- My advisor, **Professor Michael Ferry** firstly for the opportunity he gave a student who's academic marks weren't exceptional and, most importantly his supervision, assistance, input and unconditional trust and faith in my ideas and ability. In addition, co-supervisors **Professor Paul Munroe** and **Professor Alan Crosky** for their input and assistance in the project and reference material.
- **Bulent Gun**, my esteemed colleague whose work has run hand in hand with my own for the last five years for his help in all project areas, especially late night casting and tensile testing.
- **Colin Laws**, **Peter Laws** and **Peter Laws (Snr)** for; their endless input, ideas, interest and assistance throughout the entire duration of the project; the unimpeded access to workshop and machine shop facilities used to construct the tensile specimen grinder and every copper mould and crucible seen in this document and those not seen. In addition, the workshop space I'd utilised for the two or so months it took to construct the Induction-heated inverted die-casting unit (informally yet affectionately known as 'Britney'). Further gratitude needs to be given to Colin Laws for his time and efforts in the aid in construction of the die-caster melting chamber and every prototype leading up to its conception.
- **Mark Tarnawski** and **Michael Tarnawski** for their assistance and advice in the electronics associated with the base RF induction unit of the induction furnace, and **Ronald McKenzie** for his help in the connection of the electronic control circuits.
- **Warren McKenzie** for his expertise, assistance and persistence in FIB milling of TEM foils and atom probe posts, **David Saxey** for running the posts in the LEAP and his aid in results analysis and **Barry Searle** and **Irene Wainwright** for their expertise in composition analysis.
- **Professor Chris Sorrell**, **Professor Oleg Ostrovski**, **Dr Owen Standard**, **Dr Yu Wang**, **Phillip Chatfield**, **Lana Strizhevsky**, **Anil Singh-Prakash**, **Flora Lau**, **Jane Gao**, **Cathryn Lee** and **Lori Bassman** for their assistance in a variety of matters, means and measures pertaining to the completion of this thesis.



# LIST OF PUBLICATIONS

## REFEREED PAPERS

- [1] Laws, K.J., McKenzie, W.R., Gun. B. and Ferry, M. (2007). Dynamic segregation prior to crystallisation in the  $\text{Mg}_{65}\text{Cu}_{25}\text{Y}_{10}$  bulk metallic glass using atom probe tomography characterization. **Scripta Materialia** (submitted).
- [2] Laws, K.J., Gun. B. and Ferry, M. (2007). Factors effecting glass forming ability in bulk metallic glasses. **Journal of Non-Crystalline Solids** (submitted).
- [3] Laws, K.J., Gun. B. and Ferry, M. (2007). Mechanical stability of  $\text{Ca}_{65}\text{Mg}_{15}\text{Zn}_{20}$  bulk metallic glass during deformation in the supercooled liquid region. **Materials Science & Engineering A** (*In Press, Accepted Manuscript, Available online 21 July 2007*).
- [4] Laws, K.J., Gun. B. and Ferry, M. (2007). Large-scale production of Ca-base bulk metallic glass samples by low pressure die casting. **Materials Science & Engineering A** (*In Press, Corrected Proof, Available online 20 April 2007*).
- [5] Laws, K.J., Gun. B. and Ferry, M. (2007). The production of  $\text{Ca}_{65}\text{Mg}_{15}\text{Zn}_{20}$  bulk metallic glass samples by low-pressure die-casting, PRICM-6 conference, 10-15 November, 2007, Deju Island, Korea. **Materials Science Forum** (*In Press*).
- [6] Laws, K.J., Gun. B. and Ferry, M. (2007). Mechanical Behavior of  $\text{Ca}_{65}\text{Mg}_{15}\text{Zn}_{20}$  Bulk Metallic Glass in the Supercooled Liquid Region, PRICM-6 conference, 10-15 November, 2007, Deju Island, Korea. **Materials Science Forum** (*In Press*).
- [7] Gun. B., Laws, K.J. and Ferry, M. (2007). Elevated temperature flow behaviour in an Mg-base bulk metallic glass. **Materials Science & Engineering A** (*In Press, Corrected Proof, Available online 7 March 2007*).
- [8] Laws, K.J., Gun, B and Ferry, M. (2006). Effect of die-casting parameters on the production of high quality Mg-base bulk metallic glass samples. **Materials Science & Engineering A**. 425, pp.114-120.
- [9] Gun. B., Laws, K.J. and Ferry, M. (2006). Superplastic flow of a Mg-based bulk metallic glass in the supercooled liquid region. **Journal of Non-Crystalline Solids**. 352, pp.3896-3902.
- [10] Gun. B., Laws, K.J. and Ferry, M. (2006). Static and dynamic crystallization in  $\text{Mg}_{65}\text{Cu}_{25}\text{Y}_{10}$  bulk metallic glass. **Journal of Non-Crystalline Solids**. 352, pp.3887-3895.

## REFEREED CONFERENCE PAPERS

- [11] Laws, K.J., Gun. B. and Ferry, M. (2007). The production and elevated temperature deformation characteristics of  $\text{Ca}_{65}\text{Mg}_{15}\text{Zn}_{20}$  bulk metallic glass, Materials and AustCeram – International Conference and Exhibition, 4-6 July, 2007, Sydney, Australia. IMEA (submitted).
- [12] Laws, K.J., Gun, B. and Ferry, M. (2006). Production of high quality bulk metallic glass components by low pressure die casting. 4<sup>th</sup> International Symposium on Bulk Metallic Glasses. Eds P.K. Liaw and R.A. Buchanan, TMS, March 12-16, San Antonio, Texas, USA, pp. 119-126.

- [13] Gun, B., Laws, K.J. and Ferry, M. (2006). Elevated temperature mechanical behaviour of Mg-based amorphous alloys produced by low-pressure die-casting. 4<sup>th</sup> International Symposium on Bulk Metallic Glasses. Eds P.K. Liaw and R.A. Buchanan, TMS, March 12-16, San Antonio, Texas, USA, pp. 51-58.

## **CONFERENCE PRESENTATIONS**

- [14] "The production and elevated temperature properties of  $\text{Ca}_{65}\text{Mg}_{15}\text{Zn}_{20}$  bulk metallic glass", PRICM-6 conference, 10-15 November, 2007, Deju Island, Korea.
- [15] "The production and elevated temperature deformation characteristics of  $\text{Ca}_{65}\text{Mg}_{15}\text{Zn}_{20}$  bulk metallic glass", Materials and AustCeram – International Conference and Exhibition, 4-6 July, 2007, Sydney, Australia.
- [16] Laws, K.J., Gun, B. and Ferry, M. (POSTER) "The Production and elevated temperature mechanical behaviour Mg-based bulk metallic glasses". ARC Centre of Excellence for design in light metals workshop 21-22 November, 2006, Melbourne, Australia.
- [17] "The production and properties of  $\text{Mg}_{65}\text{Cu}_{25}\text{Y}_{10}$  bulk metallic glass by low pressure die-casting", ARNAM workshop 28-30 June, 2006, Brisbane, Australia
- [18] "Production of high quality bulk metallic glass components by low pressure die casting". TMS 2006 135<sup>th</sup> Annual Meeting and Exhibition, 12-16 March, 2006, San Antonio, Texas, USA.



## ABSTRACT

An inverted die casting technique has been developed for the rapid and reproducible production of high quality lightweight bulk metallic glass (BMG) castings. Comprehensive processing maps for producing lightweight BMG samples of cross section 3.15 mm × 7 mm and a length of 125 mm were developed as a means of identifying the optimum casting conditions for producing casting of high structural integrity, maximum length and enhanced surface quality. Utilising these maps,  $\text{Mg}_{65}\text{Cu}_{25}\text{Y}_{10}$  and  $\text{Ca}_{65}\text{Mg}_{15}\text{Zn}_{20}$  BMGs were consistently produced using the inverted injection die casting method and a naturally cooled copper mould, by choosing injection parameters that stabilise the molten metal flow front within the mould cavity. Highest quality  $\text{Mg}_{65}\text{Cu}_{25}\text{Y}_{10}$  BMG bars were produced in the casting temperature range of 560 °C to 580 °C and gate velocities in the range of 12.5 to 15 m/s. Highest quality  $\text{Ca}_{65}\text{Mg}_{15}\text{Zn}_{20}$  BMG bars were produced in the casting temperature range of 480 °C to 520 °C and gate velocities in the range of 13.8 to 14.7 m/s. The casting parameter range for achieving the highest quality castings for the lightweight BMGs examined was found to be practically identical and related to the casting system geometry. The use of higher holding pressures when casting was also found to increase the sample surface quality due to a post-casting consolidation process during sample cooling.

As part of the experimental program, critical cooling rate experiments were carried out, whereby the change in casting temperature over time was measured between  $T_l$  and  $T_g$ . The resulting castings were analysed using x-ray diffraction (XRD). The  $\text{Mg}_{65}\text{Cu}_{25}\text{Y}_{10}$  BMG was found to have a critical cooling rate between 49 and 61 °C/sec, and may be gravity cast in a copper mould to achieve a completely amorphous structure between 3 and 3.75 mm, or readily cast using the inverted injection method successfully to obtain a thickness of 3.15 mm. The  $\text{Ca}_{65}\text{Mg}_{15}\text{Zn}_{20}$  BMG was found to have a critical cooling rate between 150 and 170 °C/sec, and may be cast using the inverted injection method to achieve a completely amorphous structure of a diameter 8 to 9 mm.

From the as-cast samples, differential scanning calorimetry (DSC) experiments were carried out as to determine the thermal properties of both materials where it was found that the  $\text{Mg}_{65}\text{Cu}_{25}\text{Y}_{10}$  BMG had glass transition and crystallisation temperatures that varied with heating rate.  $T_g$  varied from 138 °C for a heating rate of 2 °C/min to 148 °C for a heating rate of 20 °C/min.  $T_X$  varied from 195 °C for a heating rate of 2 °C/min to 213 °C for a heating rate of 20 °C/min. This indicates a supercooled liquid (SCL) interval of 57 to 65 °C. The  $\text{Ca}_{65}\text{Mg}_{15}\text{Zn}_{20}$

BMG was found to have glass transition and crystallisation temperatures that were almost independent of heating rate.  $T_g$  varied from 102 °C for a heating rate of 5 °C/min to 105 °C for a heating rate of 20 °C/min.  $T_x$  remained relatively unchanged with heating rate at 137 °C, indicating a SCL interval of 32°C. Isothermal DSC results show that the onset of crystallisation occurs much more quickly in the  $\text{Ca}_{65}\text{Mg}_{15}\text{Zn}_{20}$  BMG and follows a non-Arrhenius type relationship as opposed to the slower, Arrhenius crystallisation kinetics displayed by the  $\text{Mg}_{65}\text{Cu}_{25}\text{Y}_{10}$  BMG.

In conjunction with this work, the elevated temperature mechanical properties of these BMGs was studied. When deformed in tension at an elevated temperature under constant strain rate conditions, it was found that an increase in test temperature resulted in a decrease in both peak stress and flow stress. It was also found that an increase in strain rate resulted in an increase in both peak stress and flow stress. It was established that Newtonian flow occurred at high temperatures in the SCL region and at lower strain rates. The  $\text{Ca}_{65}\text{Mg}_{15}\text{Zn}_{20}$  BMG was found to be far more strain rate sensitive with respect to brittle fracture, exhibiting a maximum achievable strain rate for homogeneous flow of  $10^{-3}$ /s compared to  $10^{-1}$ /s for the  $\text{Mg}_{65}\text{Cu}_{25}\text{Y}_{10}$  BMG. Elongations achieved for the  $\text{Mg}_{65}\text{Cu}_{25}\text{Y}_{10}$  BMG exceeded 1300% compared to a maximum elongation of 598% for the  $\text{Ca}_{65}\text{Mg}_{15}\text{Zn}_{20}$  BMG under constant temperature/ constant strain rate conditions, with elongation usually limited due to the onset of crystallisation.

Both BMGs were found to crystallise under certain deformation conditions. For these conditions, the Mg-based BMG was found to display a stress increase due to crystallisation prior to the times determined by static crystallisation experiments due to dynamic segregation of the amorphous phase into Cu rich and Y rich regions, as determined by atom probe tomography (APT). Where crystallisation occurred in the Ca-based BMG under dynamic conditions a delayed stress increase due to crystallisation was observed in comparison to static crystallisation experiments. The dynamic stabilisation (time delay to crystallisation) of the amorphous phase in the  $\text{Ca}_{65}\text{Mg}_{15}\text{Zn}_{20}$  alloy was found to decrease with increasing test temperature and decreasing strain rate. Constant load deformation experiments were carried out at a constant heating rate of 5 °C/sec for the  $\text{Ca}_{65}\text{Mg}_{15}\text{Zn}_{20}$  BMG. It was found that stress overshoot behaviour was avoided and a strain of 850% was achieved prior to crystallisation hardening and subsequent failure which is larger than that observed in constant strain rate testing.



# TABLE OF CONTENTS

ORIGINALITY STATEMENT .....	ii
COPYRIGHT STATEMENT .....	ii
AUTHENTICITY STATEMENT .....	ii
ACKNOWLEDGEMENTS .....	iii
LIST OF PUBLICATIONS .....	iv
ABSTRACT .....	vi
TABLE OF CONTENTS .....	viii
 SECTION 1 - INTRODUCTION .....	 1
SECTION 2 - LITERATURE REVIEW .....	4
2.1. BACKGROUND .....	4
2.1.1 Discovery of Bulk Metallic Glasses .....	4
2.1.2 Bulk Metallic Glass-Forming Systems .....	5
2.2. CONDITIONS FOR GLASS FORMATION IN METALLIC SYSTEMS.....	7
2.2.1 Multi-Component Alloy Systems .....	7
2.2.2 Atomic Size Difference .....	7
2.2.3 Large Negative Heats of Mixing .....	12
2.3. GLASS-FORMING ABILITY .....	13
2.3.1 Thermodynamic Aspects of Crystallisation .....	14
2.3.2 Kinetics of Crystallisation .....	17
2.3.3 Structure of Bulk Metallic Glasses .....	21
2.3.4 Crystallisation .....	23
2.4. PARAMETERS USED TO DETERMINE GLASS-FORMING ABILITY .....	27
2.4.1 Reduced Glass Transition Temperature .....	27
2.4.2 Supercooled Liquid Region .....	27
2.4.3 Fractional Departure .....	28
2.4.4 Order Parameter .....	30
2.4.5 Time-Temperature-Transformation and C-Curve Estimation .....	31
2.5. PREPARATION OF BULK METALLIC GLASSES FROM A MELT.....	32
2.5.1 Arc-Melting .....	33
2.5.2 Unidirectional Zone Melting .....	33
2.5.3 Conventional Copper Mould Casting .....	33
2.5.4 Water Quenching .....	33
2.5.5 Vacuum Casting into a Copper Mould .....	36
2.5.6 Injection Casting into a Copper Mould .....	37
2.5.7 Strip Casting .....	38
2.6. PROPERTIES OF BULK METALLIC GLASSES .....	39
2.6.1 Modulus, Strength and Hardness .....	39
2.6.2 Fracture Toughness and Impact Energy of BMGs .....	43
2.6.3 Fatigue, Resilience and Damping Capacity .....	46
2.6.4 Superplastic Properties of Bulk Metallic Glasses .....	47
2.6.5 Corrosion Resistance .....	53
2.7. SUMMARY AND SCOPE OF THESIS .....	54

<b>SECTION 3 - PRODUCTION AND PROPERTIES OF A MAGNESIUM-BASED BMG</b> .....	<b>55</b>
<b>3.1. BACKGROUND</b> .....	<b>55</b>
<b>3.2. ALLOY PREPARATION</b> .....	<b>57</b>
<b>3.3. DETERMINATION OF CRITICAL THICKNESS, COOLING RATE AND THERMAL PROPERTIES OF THE <math>Mg_{65}Cu_{25}Y_{10}</math> BMG</b> .....	<b>59</b>
3.3.1 Experimental Procedure .....	60
3.3.2 Evaluation of the $Mg_{65}Cu_{25}Y_{10}$ Wedge Casting .....	60
<b>3.4. GRAVITY CASTING INTO A COPPER PLATE MOULD</b> .....	<b>67</b>
3.4.1 Experimental Procedure .....	67
3.4.2 Evaluation of the $Mg_{65}Cu_{25}Y_{10}$ Plate Casting .....	68
<b>3.5. DEVELOPMENT OF THE INVERTED INJECTION DIE CASTING TECHNIQUE FOR THE PRODUCTION OF BMG SAMPLES</b> .....	<b>69</b>
3.5.1 Background Work.....	69
3.5.2 Casting Methodology .....	71
<b>3.6. PRELIMINARY DIE CASTING INVESTIGATIONS</b> .....	<b>72</b>
3.6.1 Experimental Procedure .....	73
3.6.2 Preliminary Die-Casting Results and Analysis .....	73
<b>3.7. IMPROVEMENT OF THE INVERTED INJECTION DIE CASTING TECHNIQUE FOR THE <math>Mg_{65}Cu_{25}Y_{10}</math> BMG</b> .....	<b>76</b>
3.7.1 Experimental Procedure .....	77
3.7.2 Injection Die Casting Results and Analysis.....	79
3.7.3 Cavity Filling .....	82
3.7.4 Voids, Porosity and Surface Defects in As-Cast Samples .....	86
<b>3.8. DEVELOPMENT OF A TECHNIQUE FOR PRODUCING TENSILE TEST SAMPLES FROM DIE-CAST BMGS</b> .....	<b>89</b>
<b>3.9. ELEVATED TEMPERATURE MECHANICAL BEHAVIOUR OF THE <math>Mg_{65}Cu_{25}Y_{10}</math> BMG</b> .....	<b>90</b>
3.9.1 Experimental Procedure .....	91
3.9.2 Constant Strain Rate Tensile Testing.....	92
3.9.3 The Effect of Deformation Temperature on Flow Behaviour .....	94
3.9.4 The Effect of Strain Rate on Flow Behaviour .....	96
3.9.5 Flow Characterisation of the $Mg_{65}Cu_{25}Y_{10}$ BMG using the Free Volume Model.....	98
3.9.6 Fragility Determination of the $Mg_{65}Cu_{25}Y_{10}$ BMG Using the VFT Equation .....	99
3.9.7 The Effect of Temperature, Strain and Time on Plastic Flow .....	102
<b>3.10. CRYSTALLISATION BEHAVIOUR OF THE <math>Mg_{65}Cu_{25}Y_{10}</math> BMG</b> .....	<b>105</b>
3.10.1 Time-Temperature-Transformation Diagram Development.....	105
3.10.2 Preliminary Static Crystallisation Investigation .....	106
3.10.3 Transmission Electron Microscopy (TEM) and Atom Probe Tomography (APT) .....	106
3.10.4 Sample Preparation for Atom Probe Tomography .....	107
3.10.5 APT Sample Investigation by TEM.....	109
3.10.6 APT Analysis .....	110



<b>SECTION 4 - PRODUCTION AND PROPERTIES OF A CALCIUM-BASED BMG</b>	<b>114</b>
4.1. BACKGROUND	114
4.2. FURTHER DEVELOPMENT OF THE INVERTED INJECTION DIE CASTING TECHNIQUE - INDUCTION HEATING	116
4.3. ALLOY PREPARATION	120
4.4. DETERMINATION OF CRITICAL THICKNESS, COOLING RATE AND THERMAL PROPERTIES OF THE $\text{Ca}_{65}\text{Mg}_{15}\text{Zn}_{20}$ BMG	123
4.4.1 Experimental Procedure	124
4.4.2 Evaluation of the $\text{Ca}_{65}\text{Mg}_{15}\text{Zn}_{20}$ Graduated Cylinder Casting	124
4.5. INJECTION DIE CASTING OF $\text{Ca}_{65}\text{Mg}_{15}\text{Zn}_{20}$ BMG	133
4.5.1 Experimental Procedure	133
4.5.2 Effect of Injection Temperature on As-Cast $\text{Ca}_{65}\text{Mg}_{15}\text{Zn}_{20}$ Samples	135
4.5.3 Effect of Injection Pressure/Velocity on As-Cast $\text{Ca}_{65}\text{Mg}_{15}\text{Zn}_{20}$ Samples	139
4.5.4 Effect of Relief Pressure on As-Cast $\text{Ca}_{65}\text{Mg}_{15}\text{Zn}_{20}$ Samples	141
4.6. ELEVATED TEMPERATURE MECHANICAL BEHAVIOUR OF THE $\text{Ca}_{65}\text{Mg}_{15}\text{Zn}_{20}$ BMG	145
4.6.1 Experimental Procedure	145
4.6.2 Constant Strain Rate Tensile Testing	147
4.6.3 Effect of Deformation Temperature on Flow Behaviour	149
4.6.4 Effect of Strain Rate on Flow Behaviour	150
4.6.5 Flow Characterisation using the Free Volume Model	153
4.6.6 Determination of Fragility using the VFT Equation	154
4.6.7 Strain Rate Sensitivity and Superplastic Flow Behaviour	156
4.6.8 Effect of Temperature, Strain Rate and Time on Plastic Flow	157
4.6.9 Constant Load Tensile Testing	159
4.7. CRYSTALLISATION BEHAVIOUR OF THE $\text{Ca}_{65}\text{Mg}_{15}\text{Zn}_{20}$ BMG	162
4.7.1 TTT Diagram Development	162
4.7.2 Electron Microscopy	163
<b>SECTION 5 - GENERAL DISCUSSION</b>	<b>166</b>
5.1. GLASS STABILITY	166
5.1.1 Glass Structure	166
5.1.2 Thermal Properties of BMGs	168
5.1.3 Critical Thickness and Cooling Rate Determination for Copper Mould Casting	169
5.1.4 Glass Transition and Crystallisation Behaviour	172
5.1.5 Chemical Reactivity	177
5.2. CASTABILITY OF BMGs	178
5.2.1 Composition Characteristics	178
5.2.2 Sample Density and Injection Velocity Range	181
5.3. ELEVATED TEMPERATURE MECHANICAL PROPERTIES	182
5.3.1 Effects of Temperature and Strain Rate on BMG Flow Stress and Viscosity	182
5.3.2 Fragility	185
5.3.3 Workability of Bulk Metallic Glasses	186
5.3.4 Influence of Dynamic Crystallisation on Flow Behaviour	187
5.3.5 Dynamic Stabilisation and Deterioration of the Amorphous Structure	188

<b>CONCLUSIONS.....</b>	<b>190</b>
<b>REFERENCES .....</b>	<b>194</b>
<b>APPENDIX A - CALCULATION OF COOLING RATE .....</b>	<b>203</b>
<b>APPENDIX B - CALCULATION OF INJECTION VELOCITY (I) .....</b>	<b>204</b>
<b>APPENDIX C - DETERMINATION OF FLOW STRESS .....</b>	<b>206</b>
<b>APPENDIX D - CALCULATION OF NORMALISED VISCOSITY .....</b>	<b>207</b>
<b>APPENDIX E - CALCULATION OF STRAIN RATE SENSITIVITY.....</b>	<b>209</b>
<b>APPENDIX F - CALCULATION OF INJECTION VELOCITY (II).....</b>	<b>210</b>
<b>APPENDIX G - CALCULATION OF SAMPLE COOLING RATE.....</b>	<b>215</b>
<b>APPENDIX H - CALCULATION OF CHAMBER PRESSURE INCREASE.....</b>	<b>218</b>
<b>APPENDIX I - DETERMINATION OF LOCAL; ACTIVATION ENERGY, AND AVRAMI EXPONENT .....</b>	<b>222</b>
<b>APPENDIX J - ANGEL PLOT CONSTRUCTION .....</b>	<b>225</b>

## SECTION 1 - INTRODUCTION

It has been long known that the process of nucleation and growth of a crystalline phase in some metallic alloy melts could be kinetically bypassed upon rapid cooling to produce a metastable amorphous phase (of frozen liquid configuration) which exhibits indefinite structural relaxation times - that is, a metallic glass. Metallic glasses have received renewed attention due to the more recent discovery of multi-component alloy systems with high glass-forming ability (GFA) that form glasses from the melt at relatively low cooling rates (from 100 °C/sec to 0.1 °C/sec or less). Particular compositions of these glassy alloys can be produced in bulk sample sizes in excess of 100 mm by conventional copper mould casting. Alloy systems that form these bulk metallic glasses (BMGs) are somewhat impervious to crystallisation and constitute a significant advance in materials science and engineering. The term 'bulk metallic glass' is generally given to alloy systems that retain a completely amorphous structure for a section greater than 1 mm in thickness when cast into a copper mould.

The absence of crystalline characteristics such as ordered atomic structures, grain boundaries and dislocations accounts for the vastly different thermal, chemical and physical attributes exhibited by BMGs when compared to their crystalline counterparts. Some of these outstanding properties include; extraordinarily high specific strengths; high hardness (hence wear resistance), extremely low damping characteristics (high resilience); the ability to be superplastically formed at slightly elevated temperatures; exceptional corrosion resistance, and unique soft magnetic properties. BMGs may also be partially crystallised to achieve strength values higher than that of the completely amorphous structure (due to a composite effect).

Rapid advancement in the BMG field over the last decade has seen a significant effort in the exploitation of the unique physical, mechanical and chemical properties of these materials. The absence of a grain structure in these materials means that their strength and stiffness is defined by atomic bond strengths rather than grain related mechanisms. Hence these materials display strength and hardness values typically three to four times higher than corresponding crystalline alloys. On the other hand the stiffness of BMGs is generally less than that of corresponding crystalline materials. Also attributed to their structure is the extremely low damping capacity and high elastic limit which deems BMGs an optimal material for mechanical energy storage and transfer devices such as springs.

However, the lack of a crystalline structure and dislocations exposes the poor ability of BMGs to accommodate strain, deeming them intrinsically brittle in the bulk glassy state. Contrary to this, is the fact that the brittle nature of BMGs is eliminated below a critical geometrical size. These constraints are related to the size of the plastic zone at a progressing crack tip. Below this critical geometry (say thin sheets or fibres), BMGs are quite tough.

Similar to regular ceramic or oxide glasses, BMGs exhibit a distinct glass transition temperature, which signifies the transition of the material from a somewhat brittle glassy solid at room temperature to a supercooled liquid at elevated temperature whereby the viscosity of the material decreases dramatically. It is this decrease in viscosity that allows BMGs to be superplastically deformed in the supercooled liquid region to strains in excess of 20,000% and at strain rates well in excess of  $10^{-2}\text{s}^{-1}$ . The low viscosity of BMGs in the supercooled liquid region and the absence of microstructural features to hinder fine feature replication also allows for the micro and nano forming/indentation of such materials. The high corrosion resistance of BMGs is also attributed to the lack of microstructural features such as different intermetallic phases and grain boundaries which, in crystalline materials, act as instigators for anodic/cathodic reactions within the material, thereby accelerating corrosion.

Of interest in this study are the lightest of BMG forming systems based on magnesium and calcium. Both base elements of these systems display low densities and, of interest to large-scale commercial production, are relatively inexpensive and already available in current industry processes.

Discovered in the early 1990's, magnesium-based BMGs display several advantageous properties over commercial magnesium-based alloys. The Mg-based BMGs display a much higher specific strength and hardness than commercial crystalline Mg-based alloys and exhibit superior corrosion resistance. The formability/ductility of crystalline magnesium alloys is quite poor due to the limited number of slip systems available in their hexagonal close packed structure, whereas the Mg-based BMGs may be superplastically formed at slightly elevated temperatures.

Discovered in 2002, calcium-based BMGs have extremely low densities, very low glass transition temperatures (hence low superplastic forming temperatures) and could be considered as engineering materials, unlike the highly reactive calcium metal. Another attractive aspect of the Ca-based BMGs is their biocompatible compositions, appointing them as prospective dissolvable implant materials.

Promising lightweight BMG systems that exhibit high glass-forming ability include the Mg-Cu-Y system, ( $\text{Mg}_{65}\text{Cu}_{25}\text{Y}_{10}$ ) and the Ca-Mg-Zn system ( $\text{Ca}_{65}\text{Mg}_{15}\text{Zn}_{20}$ ). Both systems have a relatively low liquidus temperature, are very close to eutectic compositions and have experimentally accessible supercooled liquid regions. These alloys will be used as the base materials in this thesis.

Throughout this study, various casting techniques have been researched, examined and developed as a means of producing large quantities of magnesium- and calcium-based BMG castings of reproducible high quality and practical geometry to be used for further material testing. In conjunction with this work, both the mechanical and visco-elastic properties of these alloys over varying temperatures and strain rates will be examined as to determine practical processing routes for the manufacture of BMG components.

The motivation for this work is the development of an in depth understanding of the nature of these materials in terms of their production and properties, such that the knowledge and experience generated within this project may be applied beyond the laboratory scale, which may eventually see these materials gain acceptance in industrial applications and the market place.



## SECTION 2 - LITERATURE REVIEW

### 2.1. BACKGROUND

For over fifty years, it has been known from the work of Buckel and Hilsch<sup>[1]</sup> that a non-crystalline metallic solid can be made by the condensation of metals onto a cooled substrate. The formation of the first metallic glass from a melt, of composition  $\text{Au}_{75}\text{Si}_{25}$  was reported by Duwez et al, at Caltech, USA, in 1960.<sup>[2]</sup> Their work showed that the process of nucleation and growth of a crystalline phase could be kinetically bypassed in some alloy melts to yield a frozen liquid configuration, that is, a metallic glass.<sup>[3]</sup> Research in the field of metallic glasses gained momentum in the early 1970s and 1980s when continuous casting processes for the manufacture of metallic glass ribbons, wire, and sheets were developed<sup>[4]</sup> leading to the discovery of a multitude of glass-forming binary systems consisting of one or more transition metals<sup>[5-8]</sup> or simple metals.<sup>[9,10]</sup>

Turnbull and coworkers identified the similarities between metallic glasses and non-metallic glass systems such as silicates, ceramic glasses, and polymers. It was shown in their work that a glass transition in conventional glass-forming melts could also be observed in rapid quenched metallic glasses.<sup>[11,12]</sup> The glass transition was found to occur at a well-defined temperature that varied only slightly as the heating rate was changed.<sup>[13]</sup> Turnbull also predicted that a ratio of the glass transition temperature  $T_g$  to the melting point, or liquidus temperature  $T_m$  of an amorphous alloy, referred to as the reduced glass transition temperature  $T_{rg} = T_g / T_m$ , can be used as a criterion for determining the glass-forming ability (GFA) of the alloy.<sup>[14,15]</sup>

#### 2.1.1 Discovery of Bulk Metallic Glasses

The universal definition for a bulk metallic glass (BMG) is an alloy that can be cast conventionally with a critical casting thickness of one millimetre or greater. According to this definition the first BMG was the ternary Pd–Cu–Si alloy prepared by Chen in 1974.<sup>[16]</sup> They used simple suction-casting methods to form millimetre-diameter rods of Pd–Cu–Si metallic glass at a low cooling rate of  $10^3$  K/s.<sup>[16]</sup> In 1982, Turnbull and co-workers<sup>[17,18]</sup> successfully prepared the well-known Pd–Ni–P BMG by using a boron oxide fluxing method to purify the melt and to eliminate heterogeneous nucleation.

By the late 1980s, Inoue and co-workers of Tohoku University, Japan succeeded in finding new multi-component alloy systems consisting mainly of common metallic elements with

considerably lower critical cooling rates.<sup>[19,20]</sup> By systematically investigating the GFA of ternary alloys, they observed exceptional GFA in the rare-earth-based alloys, for example, La–Al–Ni and La–Al–Cu.<sup>[19]</sup> By casting the molten alloy into water-cooled Cu moulds, they obtained fully amorphous rods and bars with thicknesses of several millimetres. Based on this work, the research group developed similar quaternary and quinary BMGs (e.g. La–Al–Cu–Ni and La–Al–Cu–Ni–Co) with cooling rates under 100 °C/s and the critical casting thicknesses reaching several centimetres.<sup>[21]</sup> Similar alloys with rare-earth metals being replaced by Mg, such as Mg–Cu–Y, Mg–Ni–Y, were also developed,<sup>[22]</sup> along with multi-component Zr-based BMGs<sup>[23]</sup> (e.g. Zr–Cu–Ni and Zr–Cu–Ni–Al).

The work of Inoue and co-workers opened the door to the design of new BMG systems and demonstrated that high GFA was not limited to Pd-based alloys and could be achieved in an incredible array of alloys. At present, the Pd<sub>40</sub>Cu<sub>30</sub>Ni<sub>10</sub>P<sub>20</sub> alloy has the lowest critical cooling rate for a BMG of around 0.1 °C/s which equates to a maximum sample thickness in excess of 137 mm.<sup>[24]</sup> Currently, the BMG with the largest supercooled liquid region of 135 °C is the (Zr<sub>82.5</sub>Ti<sub>17.5</sub>)<sub>55</sub>(Ni<sub>54</sub>Cu<sub>46</sub>)<sub>18.75</sub>Be<sub>26.25</sub> alloy.<sup>[25]</sup>

The design of the Zr–Ti–Cu–Ni–Be glass-forming alloy family by Peker and Johnson<sup>[26]</sup> was a significant step forward. The now commercial Vitreloy 1 (vit1) of composition Zr<sub>41</sub>Ti<sub>14</sub>Cu<sub>12.5</sub>Ni<sub>10</sub>Be<sub>22.5</sub>, is one of the most extensively studied BMGs in the family. The formation of BMGs in this family requires no fluxing or special processing treatments and can form bulk glass by conventional metallurgical casting methods. Its GFA and processing ability are comparable to those of many silicate glasses. This finding illustrates the possibility of processing metallic glasses by common foundry methods.<sup>[25]</sup> BMGs that exhibit high thermal stability and superb properties have considerable potential as advanced engineering materials. Some of the Zr-based BMGs have found applications in sporting goods<sup>[20]</sup> and other components.<sup>[27,28]</sup>

### 2.1.2 Bulk Metallic Glass-Forming Systems

New BMG forming systems are constantly being discovered and developed in a bid to improve their glass-forming ability and application properties so that they may be utilised as useful, bulk, construction materials. A range of the major glass-forming alloy systems is given in **Table 2.1**, along with their year of publication.

**Table 2.1:** Bulk metallic glass-forming systems and their publication years.

<b>BMG System</b>	<b>YEAR</b>	<b>REF</b>
Pd–Cu–Si	1974	[16]
Pt–Ni–P	1975	[29]
Au–Si–Ge	1975	[29]
Pd–Ni–P	1982	[17]
Mg–Ln–(Cu, Ni, Zn)	1988	[19]
Ln–Al–TM	1989	[21]
Zr–Ti–Al–TM	1990	[22]
Ti–Zr–TM	1993	[20]
Zr–Ti–Cu–Ni–Be	1993	[26]
Nd(Pr)–Al–Fe–Co	1994	[30]
Zr–(Nb, Pd)–Al–TM	1995	[25]
Cu–Ti–Zr–Ni	1995	[31]
Fe–(Al, Ga)–(P, C, B, Si, Ge)	1995	[20]
Fe–(Nb, Mo)–(Al, Ga)–(P, B, Si)	1995	[20]
Pd–Cu(Fe)–Ni–P	1996	[24]
Co–(Al, Ga)–(P, B, Si)	1996	[20]
Fe–(Zr, Hf, Nb)–B	1996	[20]
Co–Fe–(Zr, Hf, Nb)–B	1996	[20]
Ni–(Zr, Hf, Nb)–(Cr, Mo)–B	1996	[20]
Pd–Cu–B–Si	1997	[20]
Ti–Ni–Cu–Sn	1998	[20]
La–Al–Ni–Cu–Co	1998	[32]
Fe–Co–Ln–B	1998	[20]
Ni–Nb	1999	[33]
Fe–(Nb, Cr, Mo)–(P, C, B)	1999	[20]
Ni–(Nb, Cr, Mo)–(P, B)	1999	[20]
Zr–Nb–Cu–Fe–Be	2000	[34]
Fe–Mn–Mo–Cr–C–B	2002	[35]
Ca–Mg–(Cu, Ag)	2002	[36,37]
Ni–Nb–(Sn, Ti)	2003	[38]
Pr(Nd)–(Cu, Ni)–Al	2003	[39]
Ca–(Mg, Al)–(Cu, Ag, Zn)	2004	[40]
Co–Fe–Ta–B	2004	[41]
Mg–Zn–Ca	2005	[42]
(Ce, La, Pr, Nd)–Al–Ni–Co	2005	[43]
(Gd, Tb, Dy, Ho, Er, Sc)–Y–Al–Co	2005	[43]

**Key:**

Ln = Lanthanide Metal, TM = VI – VIII Group Transition Metal

## 2.2. CONDITIONS FOR GLASS FORMATION IN METALLIC SYSTEMS

To date, the mechanisms that establish a stable amorphous structure in metals are not fully understood. Various methods and models have been developed to produce metallic glasses in bulk. Based on various works, the prediction of high glass-forming alloy compositions was simplified by Inoue who proposed three empirical rules, relating to: multi-component alloy systems; atomic sizes of alloy constituents, and heats of mixing between constituents.<sup>[20]</sup> It is claimed that alloys satisfying the three empirical rules have unique atomic configurations in the liquid state which are significantly different from those of the corresponding crystalline phases. These atomic configurations tend to favour glass formation in terms of thermodynamics and kinetics as well as hinder the development of a crystalline microstructure.

### 2.2.1 Multi-Component Alloy Systems

Inoue had proposed that to form a bulk metallic glass, a multi-component alloy system containing three or more atomic species is necessary. (First Empirical Rule).<sup>[20]</sup> In general, the GFA in BMGs tends to increase as more atomic species are added to the alloy. This is commonly accepted as the “confusion principle”,<sup>[44]</sup> which suggests that a greater number of atomic species present in an alloy tends to destabilise long range atomic configurations during cooling, hence suppressing the tendency of an alloy to crystallise.

### 2.2.2 Atomic Size Difference

One of the general guiding principles to designing alloys that form BMGs is to choose elements with large differences in atomic size or specific atomic size ratios that leads to a complex structure that may promote an efficient local atomic packing density and hence suppress crystallisation.<sup>[10,45]</sup> An atomic size ratio above 12% among the three main constituent elements was proposed by Inoue for BMG forming systems.<sup>[20]</sup> Recently, topological,<sup>[45-47]</sup> and thermodynamic<sup>[48]</sup> models have been developed in an attempt to understand this phenomenon. The latter model also predicts an increase in glass-forming ability with the increase in the atomic size of the solvent element. This prediction agrees with the experimental observations whereby amorphisation of alloys based on elements with relatively large atomic radii occurs more easily than in those based on elements with smaller atomic radii. It also agrees with an earlier prediction of Davies<sup>[49]</sup> that the rate of crystallisation decreases with an increase in the atomic size of the solvent atom.

In 1984, Egami and Waseda<sup>[50]</sup> applied the fundamentals of the Hume-Rothery rules (the role of atomic size and the critical concentration of an alloying element in a phase transformation) to metallic glass formation to develop a topological criterion. According to this criterion, amorphisation takes place when local atomic strains caused by the relative size proportion of the solute and solvent atom reach a critical point, where instability in the crystalline lattice is induced by changing the local coordination number. The following relationship was developed for the minimum solute concentration required for glass formation as a function of the size of the solute and solvent atoms:

$$C_{\min} = \frac{0.1}{[(R_B/R_A)-1]} \quad (2.1)$$

where  $R_A$  and  $R_B$  is the radius of the solvent (matrix) atom  $A$  and solute atom  $B$ , respectively.

Using this relation, it can be seen that the critical solute concentration for glass formation decreases as the difference in size of the solute and solvent atom increases. This model, albeit designed for binary systems, is supported by experimental data for binary, ternary and quaternary ordinary amorphous alloys, which generally exhibit a characteristic concave downward atomic size distribution plot (ASDP) as seen in **Figures 2.1 - 2.3**. Considering that alloying atoms occupy only substitutional sites, the Egami-Waseda model is not applicable for the majority of the bulk metallic glasses, which generally have a characteristic concave upward ASDP.<sup>[51]</sup>

In order to find more specific criteria for discovering alloy systems with high glass-forming ability, Senkov and Miracle<sup>[45,46]</sup> considered topological differences between ordinary and bulk amorphous alloys. By using powder metallurgy analogy (i.e. random packing density can be increased if the different-sized particles present in the material are in certain proportions), they considered ways to increase the density of the amorphous phase. The atomic size distribution plots (ASDPs) of more than 100 alloys containing at least three elements were analysed. In this study, binary amorphous alloy systems were excluded due to the fact that BMGs were not produced in binaries. Atomic concentrations were plotted against atomic radii of the constituent elements to get the atomic size distribution for each amorphous alloy. A remarkable difference in the shapes of the composition-atomic radius curves for ordinary and bulk amorphous alloy systems was observed.



It was found that majority of the BMGs have a characteristic dependence of the alloying elements on their atomic radius ratio ( $R$ ) value as follows:

$$R = \frac{R_B}{R_A} \quad (2.2)$$

where  $R$  is defined as the radius of the solute atom divided by the radius of the solvent atom.

It was found that ordinary amorphous alloys had ASDPs with a concave downward shape as seen in **Figure 2.1**. It was also observed that BMGs had ASDPs both in concave downward and upward shapes. As can be seen in **Figure 2.2a**), ASDPs for Mg-based and Cu-based BMGs displayed curves similar to ordinary amorphous alloy systems apart from the fact that they were not symmetrical about their maximum.

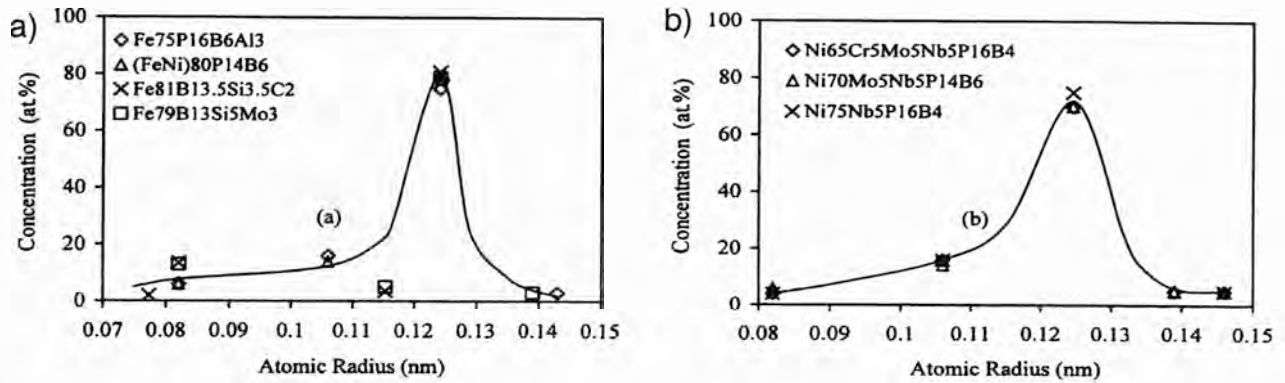


**Figure 2.1:** Atomic size distribution plots for several a) Fe-based and b) Ni-based amorphous alloys.<sup>[46]</sup>

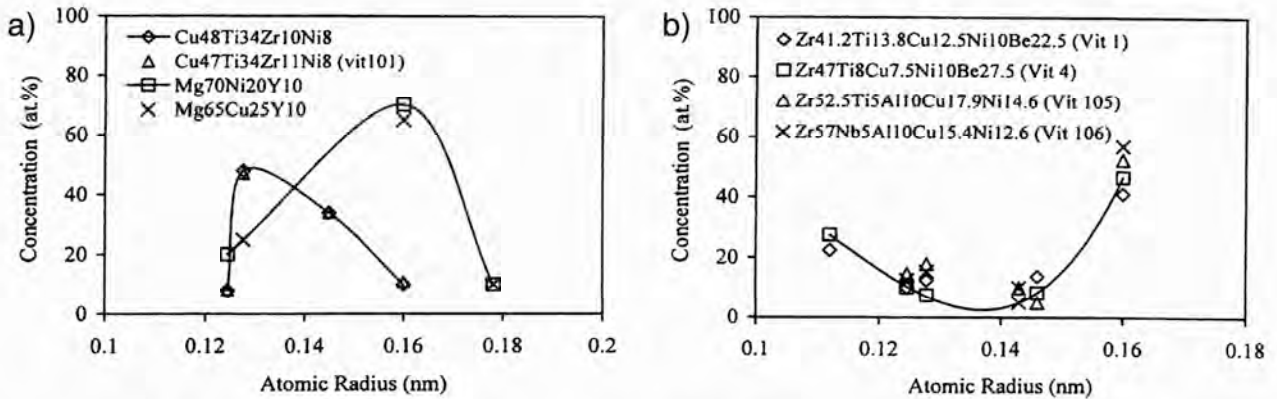


**Figure 2.2:** Atomic size distribution plots for a) Mg- and Cu-based BMGs and b) Zr-based BMGs.<sup>[46]</sup>

Conversely, ASDPs of Zr-, Pd- and Ln-based alloys produced different shapes, concave upward with a minimum at an intermediate atomic size. In these systems, the base element typically has the largest atomic size and the smallest atom often had the next highest concentration.

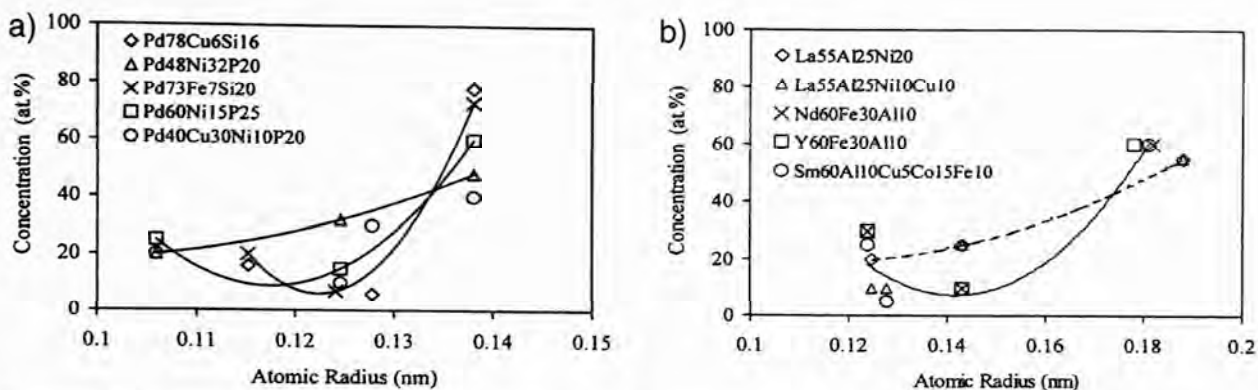


**Figure 2.3:** Atomic size distribution plots for a) Pd-based and b) Ln-based BMGs.<sup>[46]</sup>

Senkov and Miracle proposed a model for BMGs with concave-upward ASDP. According to this model, all alloying elements are smaller than the solvent (matrix) element, and some of them are positioned in interstitial sites while others substitute matrix atoms. It was suggested that the interstitial and substitutional atoms attract each other and form short-range ordered atomic configurations that may stabilise the amorphous state. This model suggests that when the size ratio between the alloying and the matrix atoms decreases, the critical concentration of an alloying element required to stabilise the amorphous state first decreases, approaches a minimum and then increases.

Interstitial sites can be produced for the solvent atoms as the atomic size difference between solvent and a solute atom increases. Senkov and Miracle<sup>[51]</sup> proposed a topological criterion for metallic glass formation through destabilisation of the matrix crystalline lattice by substitutional and/or interstitial solute atoms. This model suggests that an alloying element can be in either a substitutional or interstitial site or both depending on the relative size to the matrix (solvent) atom.

Recent works by Senkov, Miracle and Scott<sup>[51,52]</sup> have established a more specific topological criterion for easy glass-forming systems, which can narrow the selection of alloying elements and their concentrations based on relative atomic sizes. Local atomic packing configurations based on polyhedra that are common in crystalline solids, with  $N = 8$  or  $12$ . (Values of  $R^*$  are rarely smaller than  $\approx 0.6$  in metallic glasses, hence  $N \geq 8$ ). A capped trigonal prism with  $N = 9$  has been established,<sup>[53]</sup> and atomic clusters with  $N = 10$  or  $11$  may exist in metallic glasses with appropriate values of  $R$ , but are not yet established. Little work has been reported for clusters in systems with  $R > 1$ . In Frank–Kasper phases, atomic clusters with  $N = 14$ ,  $15$  or  $16$  have been described in detail,<sup>[54,55]</sup> however; these clusters were constructed with constraints

that may not represent the most efficiently packed configurations. It is also imperative to note that solutes with  $R$  as large as 1.4 are observed in metallic glasses, suggesting that clusters with  $N$  as large as 19 may be relevant.

**Figure 2.4** shows histograms displaying the correlation between predicted radius ratios ( $R^*$ ), shown as vertical lines in the figures, and solute-to-solvent radius ratios observed in: a) binary metallic glasses; b) metallic glasses with marginal glass-forming ability, and c) bulk metallic glasses. A summation of these three plots is shown in d).<sup>[52]</sup>

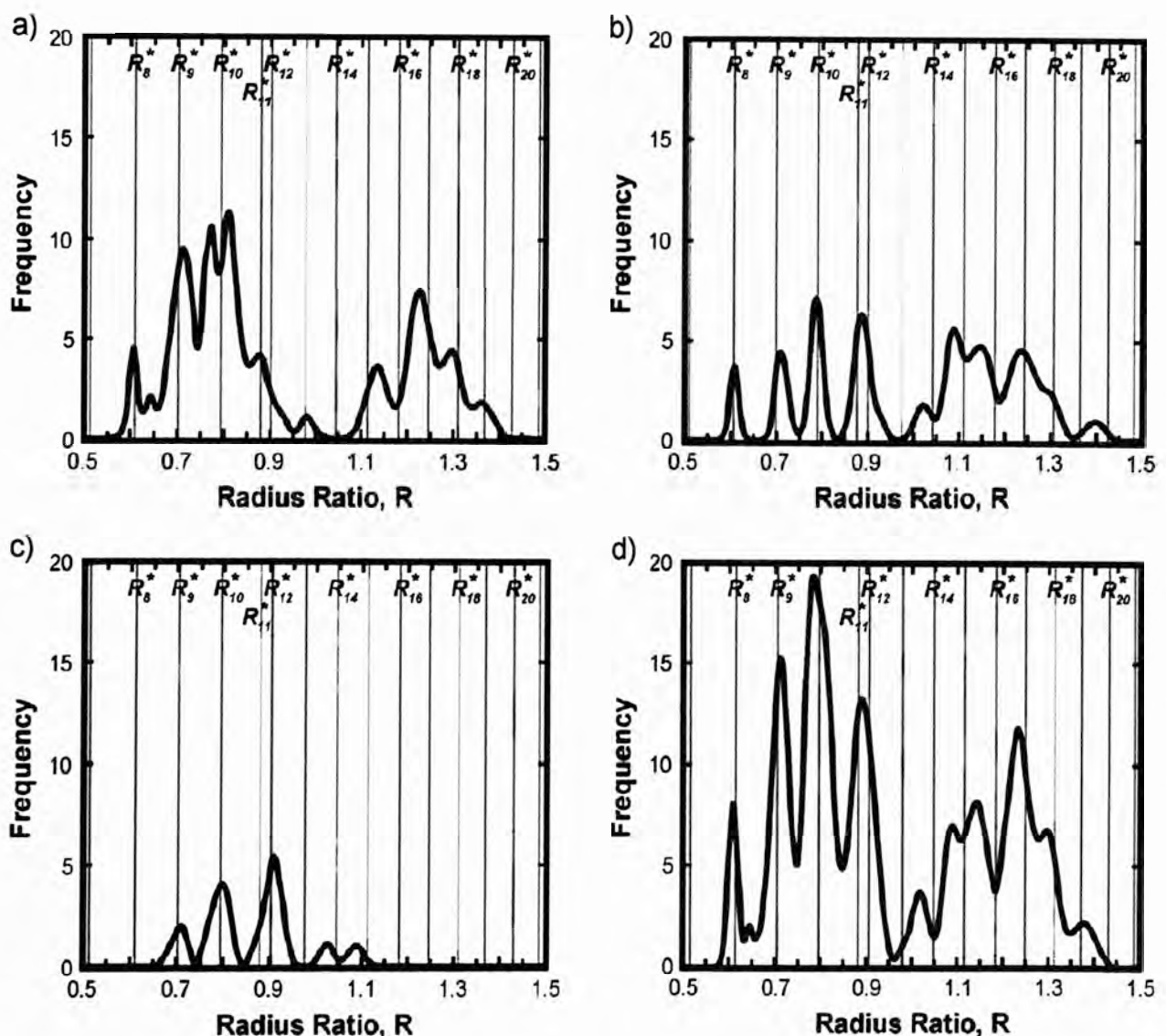


**Figure 2.4:** Histograms displaying the correlation between predicted radius ratios  $R^*$  in: a) binary metallic glasses; b) metallic glasses with marginal glass-forming ability; c) bulk metallic glasses and d) a summation of these three plots.<sup>[52]</sup>

Based on the analysis of the influence of the efficient atomic packing on the constitution of metallic glasses by Miracle, Sanders and Senkov,<sup>[49]</sup> it can be seen that values of  $R$ , or  $R^*$ , such as 0.62, 0.71, 0.80, 0.88, 0.90 etc., are preferred for the formation of metallic glasses.

Based on this criterion, a new method for selection of BMG compositions was formulated.

These criteria are:

- A solvent (main) element is selected with an atomic radius of 150 pm or larger. The larger the radius of the solvent element, the better the expected glass-forming ability of the corresponding alloy.
- Two or more solute elements are selected with atomic radii that correspond to critical values of  $R^*$ , relative to the selected solvent element. Due to some uncertainties in the determination of the atomic radii,  $R$  can deviate from the critical  $R^*$  values by up to 3%.
- The concentrations of the selected elements for a certain alloy are chosen in such a way that a concave upward ASDP is produced. Namely, the atomic concentration of the solvent element is selected in the range of 40-70%, the concentration of the solute elements with  $R$  of ~0.62 and /or ~0.71 are in the range of 15-35% and are higher than the concentrations of the elements with  $R$  of ~0.80, 0.88 and /or 0.90.
- The number of solute elements with  $R$  of ~0.62, 0.71 and 0.80 is further narrowed by leaving only elements that form binary eutectics with the solvent and each other (as discussed in the next section).

Senkov and Scott have successfully used these new criteria to develop a number of calcium-based BMGs.<sup>[40]</sup>

### **2.2.3 Large Negative Heats of Mixing**

Turnbull (1969) recognised the close correlation between the thermal stability of binary metallic glasses and the eutectic melting temperatures of the corresponding alloys.<sup>[14,15]</sup> In 1978, St. Amand and Giessen<sup>[10]</sup> also noted this relationship within simple metal binary metallic glass systems. This relationship was observed in BMGs, such that the glass-forming composition range generally coincides within alloy compositions that display deep eutectic reactions (which form liquids that are stable at relatively low temperatures) and negative heats of mixing.<sup>[20,25]</sup> In a more practical sense, a lower liquidus temperature enables a lower casting temperature, which allows a mould to cool a melt more rapidly.

### 2.3. GLASS-FORMING ABILITY

In order to understand the high thermal stability and excellent glass-forming ability (GFA) of BMGs, it is important to understand the crystallisation behaviour of the supercooled liquid. BMGs have a very stable supercooled liquid state and high thermal stability against crystallisation. The ability to form a glass by cooling from an equilibrium liquid is equivalent to suppressing crystallisation within the supercooled liquid. If steady-state nucleation is assumed, the nucleation rate,  $I$ , is determined by the product of a thermodynamic and a kinetic factor<sup>[57,58]</sup> as shown:

$$I = A \frac{D_L}{D_{LM}} \exp \left[ -\frac{\Delta G^*}{k_B T} \right] \quad (2.3)$$

where  $A$  depends on critical nucleus size and surface energy, and may be taken as a constant of about  $10^{33}$ ,<sup>[59]</sup>  $D_L$  and  $D_{LM}$  are the diffusivity of the supercooled liquid at  $T$  and  $T_m$ , respectively,  $\Delta G^*$  is the thermodynamic free-energy barrier for nucleation of a critical nucleus and  $k_B$  is Boltzmann's constant. According to the standard theory of the first-order phase transition, the size of a critical nucleus is estimated as  $r_c = 2\gamma/\delta G$ , where  $\delta G$  is the free energy difference per unit volume between a supercooled liquid and a crystal and  $\gamma$  is the interfacial energy between them. Hence, the free-energy barrier for nucleation is given by:<sup>[58]</sup>

$$\Delta G^* = \frac{16\pi\gamma^3}{3\delta G^2} \quad (2.4)$$

Provided that there is no difference in the heat capacity between the liquid and the crystal, namely,  $\delta C_p = 0$ , Turnbull deduced that:

$$\delta G = \Delta H_f \left( \frac{1-T}{T_m} \right) \quad (2.5)$$

where  $\Delta H_f$  is the enthalpy of fusion. Hence, vitrification can be achieved by generating: (i) a large free-energy barrier for nucleation, namely, large  $\gamma^3/\Delta H_f^2$ , (ii) large  $T_{rg} = T_g/T_m$ , and (iii) slow translational diffusion constant in the supercooled liquid region. These three conditions are known as 'Turnbull's Criteria'.<sup>[15]</sup> Conditions (i) and (ii) are of the thermodynamic origin, while condition (iii) is kinetic in origin.



### 2.3.1 Thermodynamic Aspects of Crystallisation

BMGs exhibit a low driving force for crystallisation in the supercooled liquid state. This low driving force results in low nucleation rates which tends to improve GFA. Thermal analysis allows the determination of the Gibbs free-energy difference,  $\Delta G_{L-S}$ , between the supercooled liquid and crystalline solid. Generally, a high GFA is favoured by small values of  $\Delta G_{L-S}$ , which can be calculated by integrating the specific heat capacity difference  $\Delta C_P^{L-S}(T)$  according to the equation;<sup>[27]</sup>

$$\Delta G_{L-S}(T) = \Delta H_f - \Delta S_f T_0 - \int_T^{T_0} \Delta C_P^{L-S}(T) \delta T + \int_T^{T_0} \frac{\Delta C_P^{L-S}(T)}{T} \delta T \quad (2.6)$$

where  $\Delta H_f$  and  $\Delta S_f$  are the enthalpy and entropy of fusion, respectively, at a temperature  $T$ , where the crystal solid and the liquid are in equilibrium. A low  $\Delta G_{L-S}$  means a small enthalpy of fusion  $\Delta H_f$  and large entropy of fusion  $\Delta S_f$ . The large  $\Delta S_f$  is expected to be associated with multi-component alloys because  $\Delta S_f$  is proportional to the number of microscopic states.<sup>[22]</sup> The free energy at a constant temperature also decreases in the case of low chemical potential caused by the low enthalpy and high value of  $T_{rg}$  as well as the large liquid/solid interfacial energy.<sup>[22]</sup> Therefore, the increase in the number of alloy components leads to the increase in  $\Delta S_f$  and causes the increase in the degree of dense random packing in the liquid state. This is favourable for the decrease in  $\Delta H_f$  and the solid/liquid interfacial energy. This concept is also consistent with the aptly named 'confusion principle'<sup>[44]</sup> and Inoue's first empirical rule.<sup>[20]</sup>

**Figure 2.5a)** shows the specific heat capacities based on the thermodynamic data in the supercooled liquid for several alloys.<sup>[60,61]</sup> **Figure 2.5b)** illustrates the calculated entropy of the undercooled Vitreloy1 melt with respect to the crystalline state.<sup>[61]</sup> The entropy of the undercooled liquid decreases with increasing undercooling until it reaches the entropy of the crystal at the Kauzmann temperature,  $T_K$ . The calculated Gibbs free-energy function with respect to the crystalline state is shown in **Figure 2.6a)**,<sup>[61]</sup> from which it can be seen that for larger undercoolings, the real Gibbs free-energy difference becomes smaller due to the relative stabilisation of the undercooled melt. This stabilisation is attributed to the increasing specific heat capacity which arises from a decreasing free volume, and possibly a gradual gain of short-range order in the alloy melt.

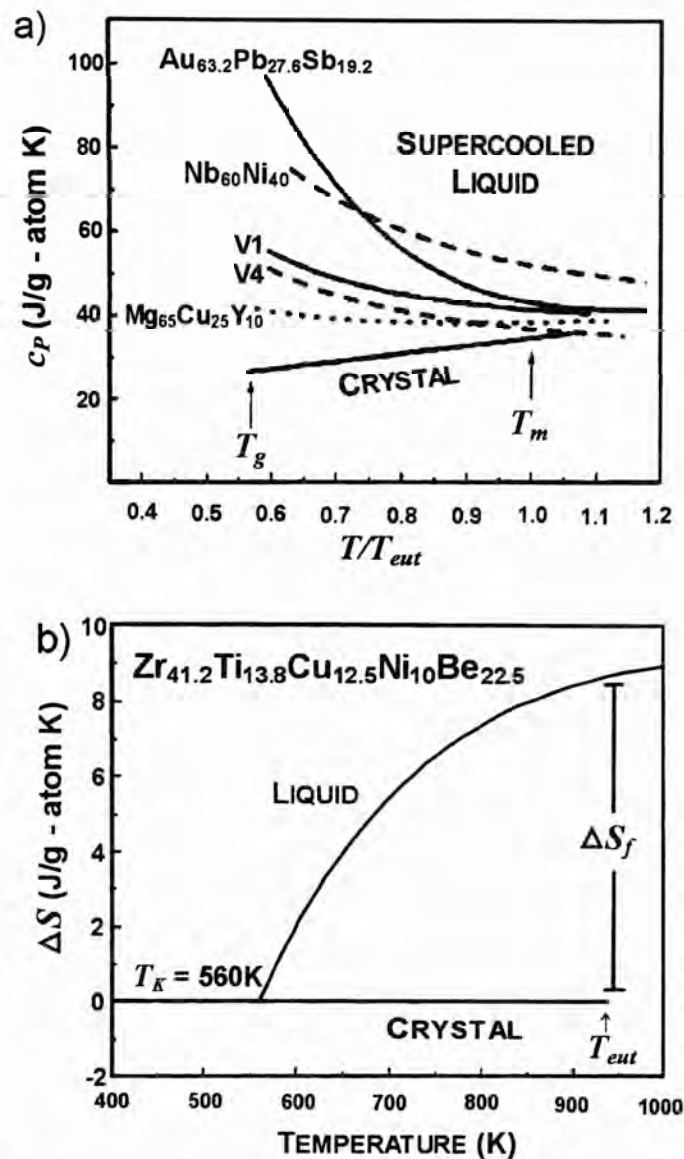


**Figure 2.5:** a) Specific heat capacities in the supercooled liquid for several BMGs normalised to the eutectic temperature,  $T_{eut}$ .<sup>[60]</sup> b) The calculated entropy of the supercooled  $Zr_{41}Ti_{14}Cu_{12.5}Ni_{10}Be_{22.5}$  melt with respect to the crystalline state.<sup>[61]</sup>

The calculated Gibbs free-energy difference between the liquid and solid state stays small even for large undercoolings. This relatively small Gibbs free-energy difference is considered to be a contributing factor to the high GFA of the alloy.<sup>[61]</sup> Figure 2.6b) shows the Gibbs free-energy difference between the supercooled liquid and the crystalline mixture for different glass-forming alloys.<sup>[60]</sup> The Gibbs free-energy difference is compared with those of other typical eutectic, or close to eutectic, glass-forming systems. The alloys show different critical cooling rates between 1 °C/s for vit1 and about 10<sup>4</sup> °C/s for the binary  $Zr_{62}Ni_{38}$  alloy. The glass formers with lower critical cooling rates have smaller Gibbs free-energy differences with respect to the crystalline state than the glass formers with high critical cooling rates.

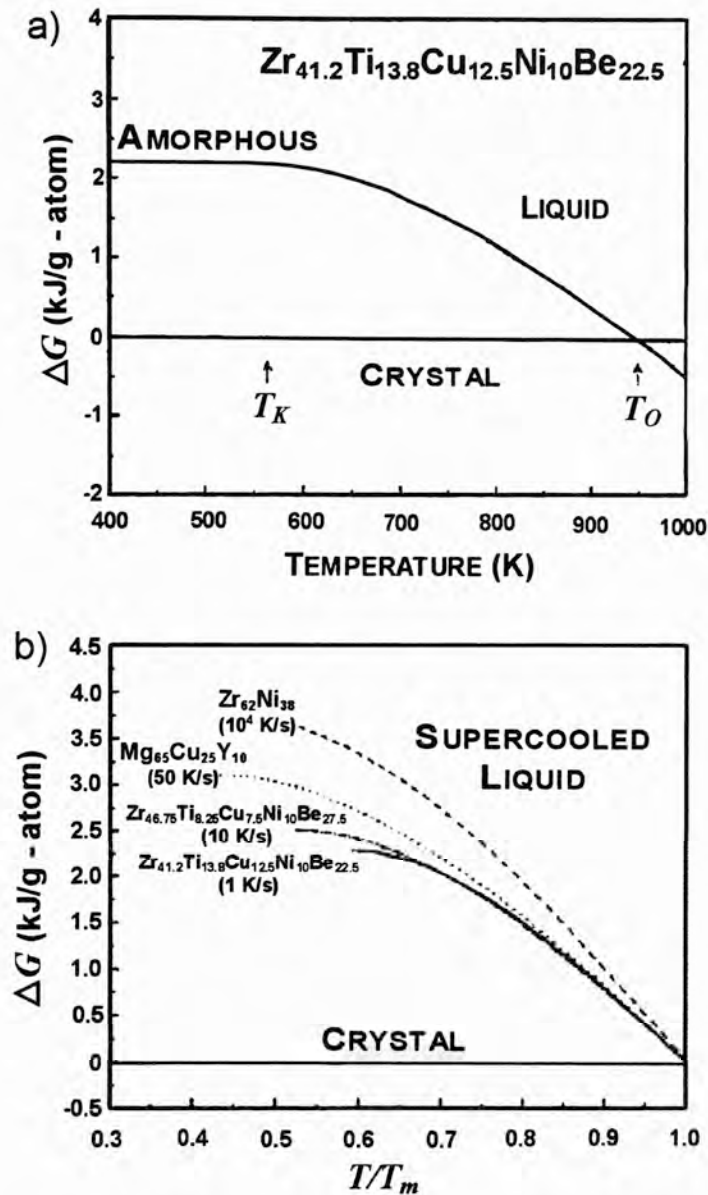


**Figure 2.6:** a) The calculated Gibbs free-energy with respect to the crystalline state.<sup>[61]</sup> b) Gibbs free-energy difference between the supercooled liquid and the crystalline mixture for different BMGs.<sup>[60]</sup>

The small free-energy difference of these deep eutectic bulk metallic glass-forming systems in the melt suggests that they already have a small free volume and a tendency to develop chemical short range order at or close to their melting point. These findings are consistent with the assumption that, in multi-component systems, the crystalline phases exhibit relatively large configurational entropies of mixing and with the fact that BMG formers are quite viscous and relatively dense liquids at both their melting point and upon undercooling.<sup>[60]</sup>

### 2.3.2 Kinetics of Crystallisation

Despite the change in specific heat observed at the glass transition of amorphous alloys, the transition from the molten to glassy state is not considered a thermodynamic phase transformation. The glass transition temperature,  $T_g$  is dependant on the heating or cooling rate. To better understand the GFA of BMG systems, one needs to be familiar with the crystallisation kinetics of these alloys. The viscosity  $\eta$  has conventionally been regarded as a kinetic factor controlling the jumping and rotation rates of atoms or molecules across the nucleus-liquid interface.<sup>[15,22,60-63]</sup> Viscosity can be measured in bulk glass-forming systems in wide temperature/time scales. **Figure 2.7a)** shows the viscosities of the BMG vit4 measured by parallel plate rheometry.<sup>[64,65]</sup> It can be seen that the viscosity data can be described well with the Vogel–Fulcher-Tammann (VFT) relation.<sup>[66,67]</sup> The VFT equation for the viscosity of a liquid in the Newtonian flow regime (low strain rates) can be generally expressed in the form:

$$\eta(v_e) = \eta_o \exp \left[ \frac{v_{crit}}{(v_e - v_o)} \right] \quad (2.7)$$

where  $v_e = v_e(T, P)$  is the temperature dependent (and more generally pressure dependent) molar volume of an equilibrium liquid,  $v_{crit}$  is a critical volume, and  $\eta_o = h/v_e$  is viscosity of the liquid at the high temperature “gas” limit ( $h$ =Planck’s constant), and  $v_o$  is the VFT volume. The viscosity of an equilibrium liquid diverges at  $v_o$ . Equivalently, Eq. (2.7) is often written in the form:

$$\eta(v_e) = \eta_o \exp \left[ \frac{D^* T_o}{(T - T_o)} \right] \quad (2.8)$$

where  $T_o$  is the VFT-temperature at which the barriers with respect to flow would go to infinity and  $D^*$  is called the ‘Fragility’ parameter of the liquid. In real liquids  $D^*$  ranges from ~3 to 5 for a fragile liquid, such as a pure metal, and from 40–100 for a strong liquid, such as  $\text{SiO}_2$  glass. Bulk metallic glass-forming liquids tend to exhibit “strong” liquid behaviour with  $D^*$ -values typically in the range 15 - 25.<sup>[60,63-65]</sup> For Vitreloy 4,  $T_o$  is found to be far below the calorimetric glass transition. This indicates that the BMG-forming liquids behave kinetically much closer to silicate melts which have excellent GFA. The change of viscosity of a liquid as a function of undercooling can be used to distinguish different liquids as it reflects the change of mobility of atoms during supercooling.<sup>[66-71]</sup>

It has also been confirmed that the material transport for crystallisation is not controlled by rotational diffusion,  $D_r$  ( $\propto 1/\eta$ ), but by translational diffusion,  $D_t$ , reflecting the translational/rotational decoupling below  $T_m$  that leads to the breakdown of the Einstein-Stokes relation  $D_t \propto D_r \propto 1/\eta$ .<sup>[63]</sup> Thus,  $I$  in Eq. (2.3) is not directly proportional to  $1/\eta$ , but should be proportional to  $D_t$ .

**Figure 2.7b)** compares the change in viscosity (normalised to  $10^{12}$  Pa.s using  $T_g^*$ )<sup>[67]</sup> of three BMGs with a selection of non-metallic liquids, of which  $\text{SiO}_2$  is the strongest glass former. It exhibits a very small VFT temperature and high melt viscosity. On the other hand, O-terphenyl is a typical fragile glass with a low melt viscosity. It shows a more abrupt change in the kinetics close to the glass transition temperature.<sup>[60]</sup>

The concept of fragility was introduced by Angell<sup>[66-68]</sup> to characterise how steeply viscosity increases upon cooling. It can be regarded as a measure of the degree of co-operativity of motion. Fragility of liquids is defined as the apparent activation energy of shear viscosity,  $\eta$ , or structural relaxation time at the glass transition temperature,  $T_g$ , normalised to  $T_g^*$ <sup>[66-68]</sup> as follows:

$$m = \left. \frac{\partial \log \eta(T)}{\partial (T_g/T)} \right|_{T=T_g} \quad (2.9)$$

It characterises the steepness of the slope of  $\log \eta$  dependence on  $T_g/T$  near  $T_g$  (**Figure 2.7b)**). A stronger deviation from Arrhenius behaviour corresponds to a more fragile system. For strong liquids,  $m < 30$  with a lower limit of  $\approx 16$ . For example,  $\text{SiO}_2$  and  $\text{GeO}_2$  have  $m \approx 20$  at  $T_g$ . On the other hand, fragile liquids are associated with  $m \gg 100$ . BMG forming liquids show behaviour closer to strong glasses than that of fragile glasses and have fragility terms ( $m$ ) from 30-60.<sup>[66]</sup> The melt viscosities of BMGs are in the order of 2 - 5 Pa.s compared to  $10^{-3}$  Pa.s of pure metals.<sup>[25]</sup> The positive correlation between GFA and the strong nature of liquids was recently suggested by Busch et al.,<sup>[60]</sup> Perera,<sup>[70]</sup> and Lu et al.<sup>[71]</sup> on the basis of the experimental results of various metallic glass-forming systems.



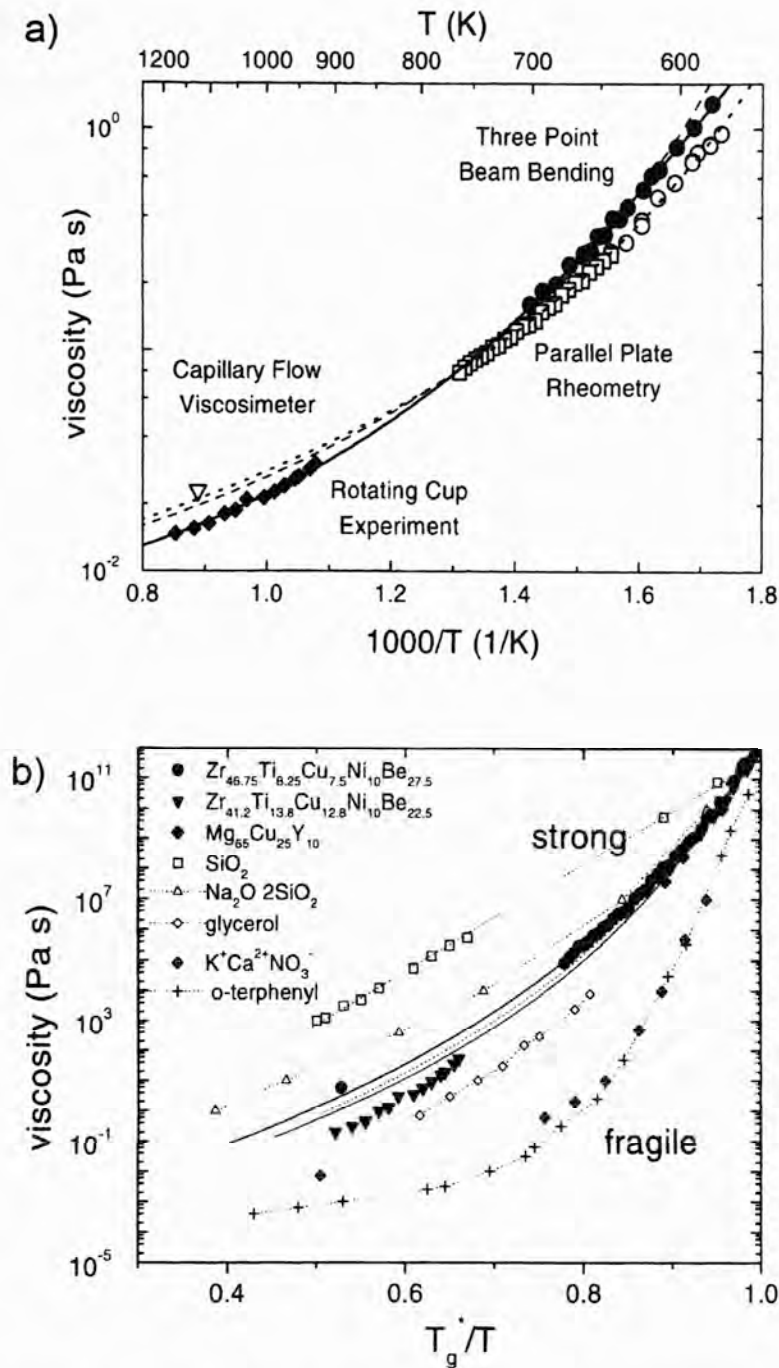


**Figure 2.7:** a) Viscosity as a function of temperature for the supercooled liquid of vit4. Also shown is the Vogel-Fulcher fit to the data.<sup>[60]</sup> b) An 'Angel plot' which provides a comparison of viscosity of various glass-forming liquids normalised to  $T_g^*$ .<sup>[60]</sup>

Another form of VFT equation was introduced using the dependence of  $T_g$  on the inverse of heating rate,  $\beta$ :<sup>[60]</sup>

$$\beta^{-1} = \tau_o \exp\left(\frac{D^* T_o}{T_g - T_o}\right) \quad (2.10)$$

where  $\tau_o$  is a pre-exponential factor,  $T_g$  is the onset glass transition temperature. Eq. (2.10) combines the kinetics of glass transition to the equilibrium viscosity. In addition to this, Busch et

al. stated that the heating rate dependence of the glass transition is also a measure of the fragility of the glass. Here, a lower heating rate dependence indicates a more fragile glass, while a higher heating rate dependence indicates a stronger glass.<sup>[60]</sup>

The relaxation behaviour of BMG forming liquids studied by neutron scattering is also similar to the nature of strong liquids.<sup>[72,73]</sup> The strong liquid behaviour implies high viscosity and sluggish kinetics in the supercooled liquid state. This greatly retards the formation of stable nuclei in the melt. The growth of the thermodynamically favoured phases is inhibited by the poor mobility of the constituents. The nucleation and growth of the crystalline phase in the supercooled state is hindered, thus leading to large GFA and high thermal stability of the SCL state.

**Figure 2.8** gives a schematic diagram showing the high stability of the BMG forming supercooled liquid for up to several thousands of a second.<sup>[74]</sup> The conventional metallic glasses have nucleation kinetics in the undercooled region such that the onset time for crystallisation was in the regime of  $10^{-4}$  to  $10^{-3}$  s at the “nose” of the C-curve. For BMG forming systems, there can be C-curves with noses at time scale of the order of 100 - 1000 s. Takeuchi et al.<sup>[75]</sup> have developed a model specific to BMGs in which atomic composition, thermal stability and viscosity are used in the prediction of the nose of C-curves, which will be discussed further in SECTION 2.4.

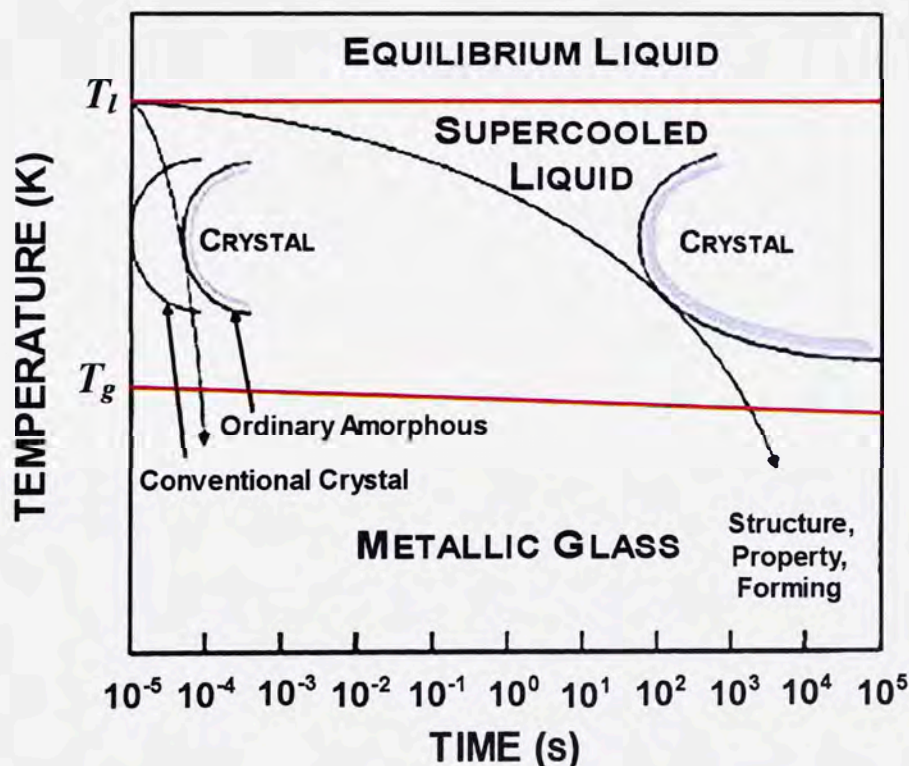


**Figure 2.8:** A schematic C-curve representation of the high stability of a BMG-forming supercooled liquid.<sup>[74]</sup>



### 2.3.3 Structure of Bulk Metallic Glasses

BMGs are dense liquids with small free volumes and high viscosities which are several orders of magnitude higher than those of pure metals or previously known alloys. They are found to have a unique type of glassy structure with a high degree of dense randomly packed atomic clusters similar to that of the liquid alloy and exhibit long-range homogeneity. Density measurements show that the density difference between BMGs and the fully crystallised state (BMGs are less dense than their crystalline counterparts) is in the range 0.3–1.0%,<sup>[47,76,77,78]</sup> which is much smaller than the reported range of about 2% for ordinary amorphous alloys.<sup>[78]</sup> They have unique local atomic cluster configurations, which introduces multi-component interactions on a short-range scale, which promotes an increase of solid-liquid interfacial energy, favourable for the suppression of nucleation of a crystalline phase. These atomic cluster configurations, which are quite different from those of the corresponding crystalline phases, hinder atomic rearrangement within a liquid. This leads to a decrease in atomic diffusivity and an increase in viscosity. The requirement of atomic rearrangements of these clusters on a long-range scale for crystallisation to occur leads to the suppression of crystalline phases and high glass-forming ability.<sup>[78-81]</sup>

Inoue classified BMGs into three types; metal–metal, metal–metaloid and the Pd–metaloid-type alloys.<sup>[20,79]</sup> The configurations of each are shown in **Figure 2.9**.

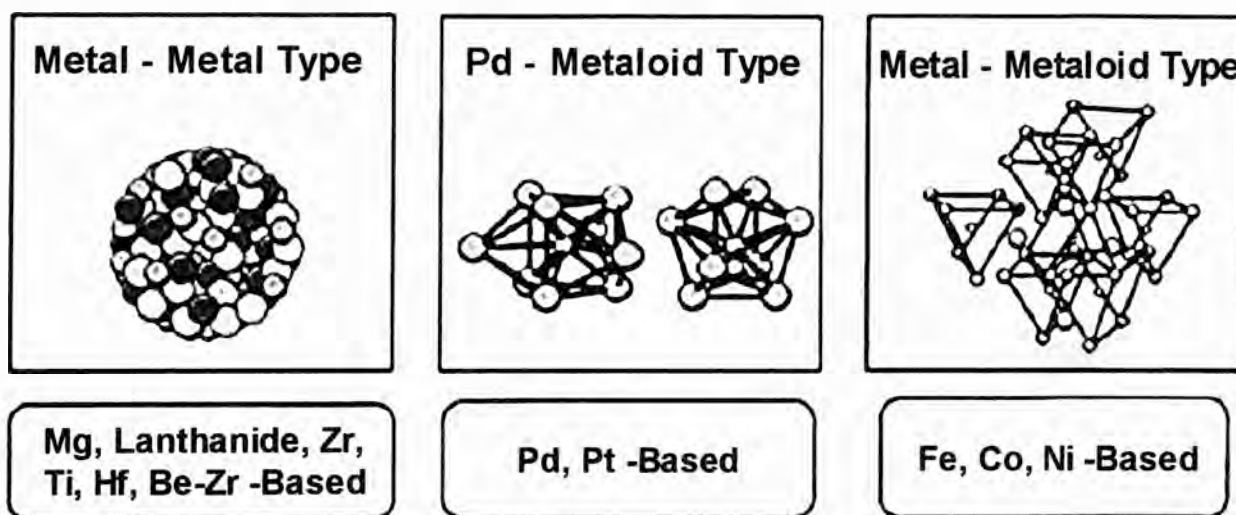


**Figure 2.9:** The proposed atomic configurations of the three different BMG types.<sup>[20]</sup>

In the metal-metal alloy, numerous studies have revealed that the glass consists of icosahedral clusters.<sup>[81-83]</sup> When the BMG is annealed in the supercooled liquid region, the icosahedral quasi-crystalline phase (I-phase) precipitates in the primary crystallisation step, and the I-phase transforms to stable crystalline phases at higher temperatures.<sup>[81-84]</sup> The structural features of

BMGs provides a reasonable explanation for their excellent GFA,<sup>[85]</sup> as icosahedral clusters (icosahedral short-range order) in the amorphous state would provide an additional barrier to the nucleation of crystalline phases as they must be dissociated before the formation of the crystalline phases. This results in extremely low atomic mobility,<sup>[86]</sup> thereby making the redistribution of atoms on a large scale very difficult. This fundamental structural discontinuity between the crystalline and the amorphous state suppresses the nucleation and growth of the crystalline phase from the supercooled liquid and results in an excellent GFA.

Metal-metal BMGs were further categorised by Poon et al. into two sub-classes based on atomic size and composition.<sup>[87]</sup> The first BMG class includes BMGs with midsize atoms as the majority component, small atoms as the next-majority component, and large-size atoms as the minority component producing an ASDP with a concave downward shape, referred to as MSL BMGs (medium – small – large). In MSL alloy systems, it is noted that the heats of mixing are negative and large in magnitude for the large–small atomic pairs, in many cases even larger than those between elements in these pairs and their corresponding medium (solute) atom components.<sup>[45,87]</sup> The large and small atoms are seen as forming a strong L–S network or reinforced ‘backbone’ in the amorphous structure. Presumably, this backbone structure enhances the stability of the undercooled melt that further suppresses crystallisation in these glasses.<sup>[45,87]</sup>

The other BMG class includes alloys composed primarily of large-size atoms and small-size atoms producing an ASDP with a concave upward shape. This group of BMGs is referred to as the large atom-small atom or small atom-large atom (LS/SL) class, to which the majority of glass-forming systems belong, which, as mentioned previously rely upon the binding strength of atomic clusters and difficulty of atomic redistribution for their high GFA.<sup>[81-87]</sup>

For the metal–metalloid-type glassy alloys such as Fe(Co)–Nb–B etc., a network of atomic configurations consisting of trigonal prisms which are connected to each other through ‘glue’ atoms (usually Zr, Nb, Ta or lanthanide metals). Fe-based BMGs form primary crystals of complex f.c.c.-Fe<sub>23</sub>B<sub>6</sub> phase with large lattice parameter of 1.1 nm and a unit volume consisting of 96 atoms.<sup>[74]</sup>

Pd-based BMGs do not satisfy the three empirical rules proposed by Inoue.<sup>[20]</sup> Structural investigations have shown that Pd–Cu–Ni–P BMGs consist of two large clusters, one is a

trigonal prism capped with three half-octahedra for the Pd–Ni–P and the other a tetragonal dodecahedron for the Pd–Cu–P region, as shown in **Figure 2.10**.<sup>[20,74]</sup> The coexistence of these two large different clusters appears to play a crucial role in the stabilisation of the supercooled liquid in the Pd–Ni–Cu–P alloy, as is evident from the difference in GFA between Pd–Ni–Cu–P and Pd–Ni–P. This is attributed to the strong bonding nature of metal–metalloid atomic pairs and the difficulty of rearrangement the two different clusters.

### 2.3.4 Crystallisation

The crystallisation of a BMG requires a substantial redistribution of the component elements across the liquid. The highly dense, randomly packed structure of the BMG in its supercooled state results in extremely low atomic mobility, thus making the redistribution of atoms on a large scale difficult. BMGs offer a large experimentally accessible temperature/time window to investigate the nucleation and growth of crystals in the supercooled liquid state. Investigations of the crystallisation processes in BMGs have been carried out by numerous research groups (Vitreloys and Pd–Ni–Cu–P have been studied extensively) in an attempt to develop an understanding of: (i) the nucleation and growth of crystals in the metallic supercooled liquid; (ii) the glass-forming ability, and (iii) thermal stability of metallic glasses as well as the production of bulk nanocrystalline and composites using controlled crystallisation.<sup>[88-106]</sup> Common features of the nucleation and growth of crystals in BMGs are a high number density of nuclei and sluggish growth kinetics.<sup>[94-101]</sup> Nucleation in the entire supercooled liquid region cannot be sufficiently described by one single nucleation mechanism. Mechanisms such as high heterogeneous nucleation rates, quenched-in nuclei, phase separation in the supercooled liquid prior to crystallisation, homogeneous nucleation considering linked fluxes of interface attachment and diffusion in the liquid to the cluster neighborhood have been applied to describe the high density of nuclei.<sup>[27]</sup>

Crystallisation at low temperature (near  $T_g$ ) requires a large number of pre-existing nuclei.<sup>[88-106]</sup> For example, the number of nucleation events was found to increase from near  $10^8 \text{ m}^{-3}$  for samples annealed near melting temperature to approximately  $10^{23} \text{ m}^{-3}$  for samples annealed in the vicinity of  $T_g$  for a variety of BMGs.<sup>[27]</sup> This indicates that the locations of maxima in nucleation and growth rate differ significantly. In Vitreloy 1, the growth rate maximum occurs at 985 K, which is much higher than that of the nucleation rate at 840 K.<sup>[97]</sup> Therefore, the nuclei formed in a supercooled liquid have marked different growth rates during constant heating and cooling of the alloy<sup>[97,109-108]</sup> (phenomenon seen in **Figure 2.10a** and **b**)).

The isothermal transformation kinetics of a material is usually analysed using the well-known Johnson-Mehl-Avrami-Kolmogorov (JMAK) <sup>[57,110-113]</sup> equation:

$$X_v(t) = 1 - \exp[-k(t - \tau)^n] \quad (2.11)$$

where  $X_v(t)$  is the transformed volume fraction,  $\tau$  the incubation time taken as the time interval between the specimens reaching the annealing temperature and the start of the transformation,  $n$  is the Avrami exponent, reflecting the characteristics of nucleation and growth during crystallisation, and  $k$  is a reaction rate constant which is a function of annealing temperature<sup>[57]</sup> which is described by:

$$k = k_o \exp(-E_c / RT) \quad (2.12)$$

where  $k_o$  is a constant and  $E_c$  is the apparent activation energy for crystallisation. The values of  $k$  and  $n$  can be determined using the relationship:

$$\log[\ln 1/(1 - X_v)] = n \log k + n \log(t - \tau) \quad (2.13)$$

In order to investigate the details of the crystallisation process, the local Avrami exponent  $n(X_v)$  <sup>[114]</sup> can be calculated using the following relation:

$$n(X_v) = \frac{\delta \log[-\ln(1 - X_v)]}{\delta \log(t - \tau)} \quad (2.14)$$

The value of  $n(X_v)$  provides information on the nucleation and growth behaviour for a given crystallised volume fraction. In various studies on BMGs, significant variations in the local Avrami exponent and local activation energy for crystallisation demonstrates that crystallisation kinetics may vary at different stages. In most cases, it is agreed that Avrami exponents lie between 2.5 and 3.0 in the wide range  $0.1 < X_v < 0.85$ , indicating that the main crystallisation process is governed by three-dimensional growth at an increasing nucleation rate. When the crystallised fraction reaches 0.9,  $n$  is often close to 3.0, thereby indicating that nucleation is saturated and the nucleation rate is zero after initial nucleation. It is also suggested that the activation energy for growth is possibly larger than the activation energy for nucleation for various the BMGs studied.<sup>[107-109]</sup> Ranganathan and Heimendahl<sup>[115]</sup> have proposed that the activation energy for crystallisation of amorphous solids can be expressed as the sum of

nucleation and growth activation energies by the following relation:

$$E_C = (aE_N + bE_G)/n \quad (2.15)$$

where  $a$  and  $b$  are positive constants related to the Avrami exponents and  $a + b = n$  ( $n$  is again the Avrami exponent),  $E_N$  and  $E_G$  are the nucleation and growth activation energy, respectively. Considering that the nucleation rate is increasing, this means that the value of  $a$  in Eq. (2.15) increases and the value of  $b$  decreases, since  $E_C$  is decreasing in the main crystallisation process (for  $0.1 < X_V < 0.85$ ).

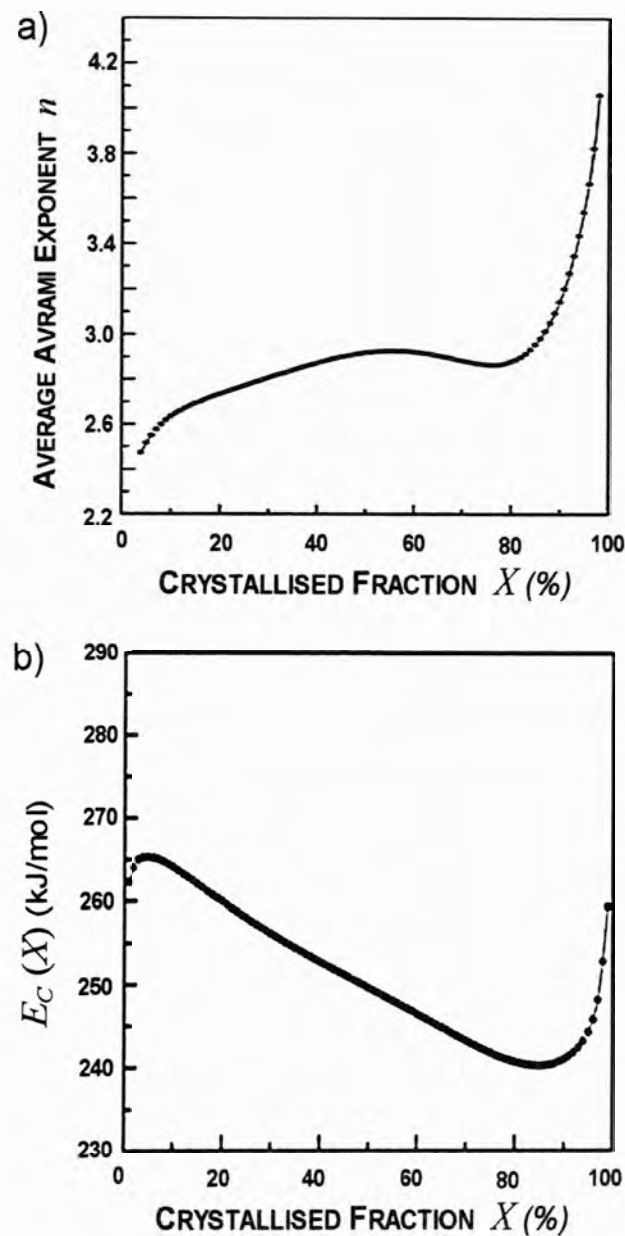


**Figure 2.10:** a) Variation of the Avrami exponent with crystallised fraction in Zr-Cu-Al-Ni BMG, b) Variation of the activation energy during crystallisation process of Zr-Cu-Al-Ni BMG.<sup>[108]</sup>



The well known Kissinger equation<sup>[116]</sup> may be used to analyse the crystallisation kinetics and determine the activation energy of the crystallisation reaction (and the glass transition) for characteristic temperatures at a given heating rate (non-isothermal event), given by:

$$\ln\left(\frac{\beta}{T_p^2}\right) = -\frac{E_C}{RT_p} + \text{constant} \quad (2.16)$$

where  $\beta$  is the heating rate,  $E_C$  is the activation energy for crystallisation,  $T_p$  is the characteristic or peak crystallisation temperature and  $R$  is the universal gas constant. Using the linear relation between  $\beta/T_p^2$  and  $1/T_p^2$ , the activation energy of crystallisation can be calculated.

The Avrami exponents ( $n$ ) for isochronal heating (constant heating rate conditions) may be calculated using the Ozawa method,<sup>[117]</sup> where the crystallised volume fraction,  $X_v$  can be expressed by:

$$X_v = 1 - \exp\left[-\left(k \frac{T - T_i}{\beta}\right)^n\right] \quad (2.17)$$

where again,  $k$  is a reaction rate constant and  $T_i$  an initial temperature. The value of  $n$  can be obtained from the plot of  $\log[-\ln(1 - X_v)]$  against  $\log \beta$ . However, there may be differences in the values of  $n$  compared to isothermal heating conditions due the variation of the diffusivity of the atoms (and hence their kinetics) during isochronal treatment as stabilisation times are very short.<sup>[117]</sup>

## 2.4. PARAMETERS USED TO DETERMINE GLASS-FORMING ABILITY

There is no single parameter that can accurately correlate glass-forming ability or alloy stability to a specific value in all alloy systems, with general trends often corresponding well in some alloy systems yet not so well in others. An alloy is regarded as having a high glass-forming ability (GFA) if crystallisation upon cooling below  $T_g$  can be suppressed, using a relatively low cooling rate e.g. Zr, Pd and Ln-based BMGs have critical cooling rates from 100 to 0.1 °C/s, hence have high GFA.

### 2.4.1 Reduced Glass Transition Temperature

In 1969, Turnbull<sup>[14,15]</sup> predicted the following ratio, referred to as the reduced glass transition temperature given by:

$$T_{rg} = \frac{T_g}{T_m} \quad (2.18)$$

This parameter is dependent on  $T_g$  and  $T_m$  of an alloy, and can be used as a criterion for determining the GFA (in binary systems).<sup>[14]</sup> According to Turnbull's criterion, a liquid with  $T_g/T_m = 2/3$  becomes somewhat impervious to crystallisation and can only crystallise within a narrow temperature range. Such a liquid can be supercooled at a relatively low cooling rate into the glassy state.<sup>[15]</sup> This ratio is derived from the requirement that viscosity must be high at a temperature between the melting point and the glass transition temperature.<sup>[118]</sup> Since the viscosity at the glass transition temperature is constant, the higher the  $T_g/T_m$  ratio, the higher the viscosity at the nose of the TTT curve, and the smaller the critical cooling rate ( $R_C$ ).<sup>[119]</sup>

**Figure 2.11a)** shows the relationship between the critical cooling rate, ( $R_C$ ) maximum sample thickness ( $Z_C$ ) and reduced glass transition temperature ( $T_g/T_m$ ) for a number of BMG systems.<sup>[20]</sup> (More recently,  $T_m$  has been represented by  $T_l$  in this ratio for liquid properties).

### 2.4.2 Supercooled Liquid Region

Using similar logic, Inoue<sup>[20]</sup> pointed out the relationship between  $R_C$ ,  $Z_C$  and the temperature interval of a supercooled liquid defined by the difference between the crystallisation temperature ( $T_X$ ), and glass transition temperature ( $T_g$ ) i.e.

$$\Delta T_X = T_X - T_g \quad (2.19)$$

A larger temperature interval indicates a higher stability of the supercooled liquid. The relationship between  $R_C$ ,  $Z_C$  and  $\Delta T_X$  can be clearly seen in **Figure 2.11b)**.

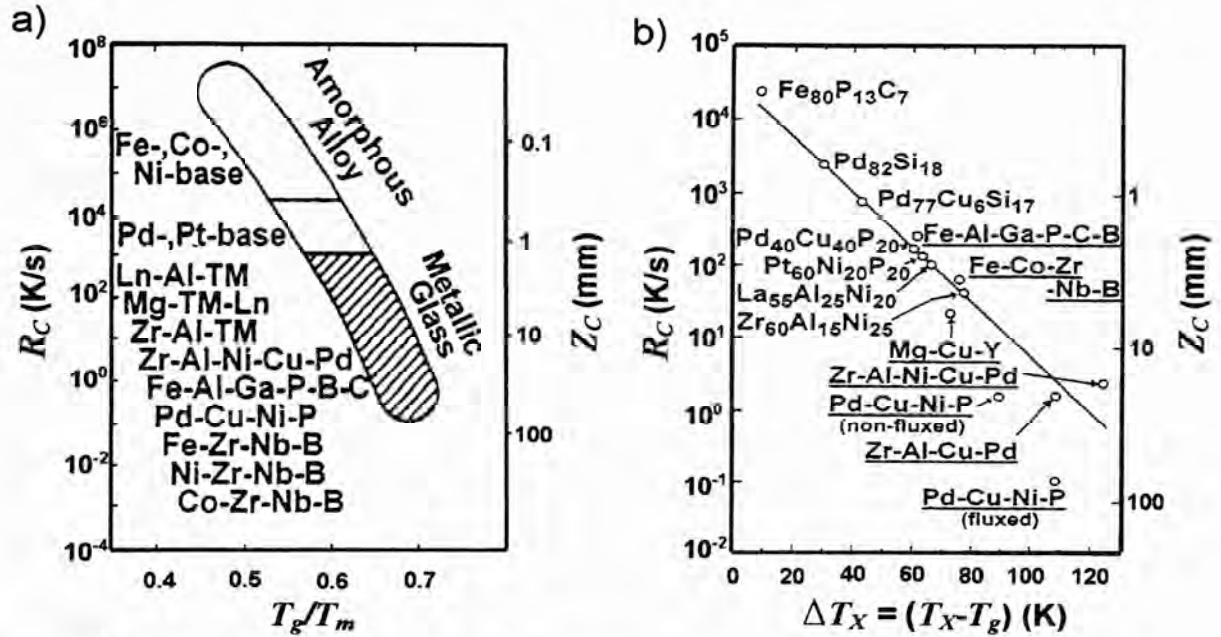


**Figure 2.11:** a) Relationship between the critical cooling rate,  $R_C$ , maximum sample thickness,  $Z_C$  and reduced glass transition temperature ( $T_g/T_m$ ) for BMGs.<sup>[20]</sup> b) Relationship between  $R_C$ ,  $Z_C$  and the SCL region ( $\Delta T_X = T_X - T_g$ ) for BMGs.<sup>[20]</sup>

$\Delta T_X$  values as large as 100 °C in some alloys implies that these glasses are relatively stable upon reheating; this parameter is considered to be a measure of glass stability defined as a glass's resistance to devitrification when reheated above its glass transition temperature,<sup>[120]</sup> whereas GFA is specified as the ease by which a melt is cooled to form an amorphous structure. This explains why  $\Delta T_X$  may correspond to a high GFA in some BMG-forming systems yet fails in other systems.

### 2.4.3 Fractional Departure

Lu and Liu<sup>[120]</sup> recently proposed that the GFA of alloys can be scaled using the following dimensionless parameter,  $\gamma$ , which is based on thermodynamic crystallisation processes during cooling and reheating of a supercooled liquid:

$$\gamma = \frac{T_X}{T_g + T_l} \quad (2.20)$$

where  $T_X$  is the onset crystallisation temperature and  $T_l$  the liquidus temperature. Lu and Liu also formulated the following relationship between the  $\gamma$ -value and the critical cooling rate,  $R_C$ , ( $R_C$  is in given in °C/s) regardless of the alloy system:

$$R_C = 5.1 \times 10^{21} \exp(-117.19\gamma) \quad (2.21)$$

Figure 2.12a) shows this relationship with respect to various metallic glasses. The statistical correlation parameter  $R^2$  for this plot was found to be 0.91 for the regression line of this graph, showing that there is a strong correlation between  $R_C$  and  $\gamma$ . However, the correlation between  $R_C$  and  $T_g/T_m$  was found to be weaker with a  $R^2 = 0.73$  (Figure 2.12b)).

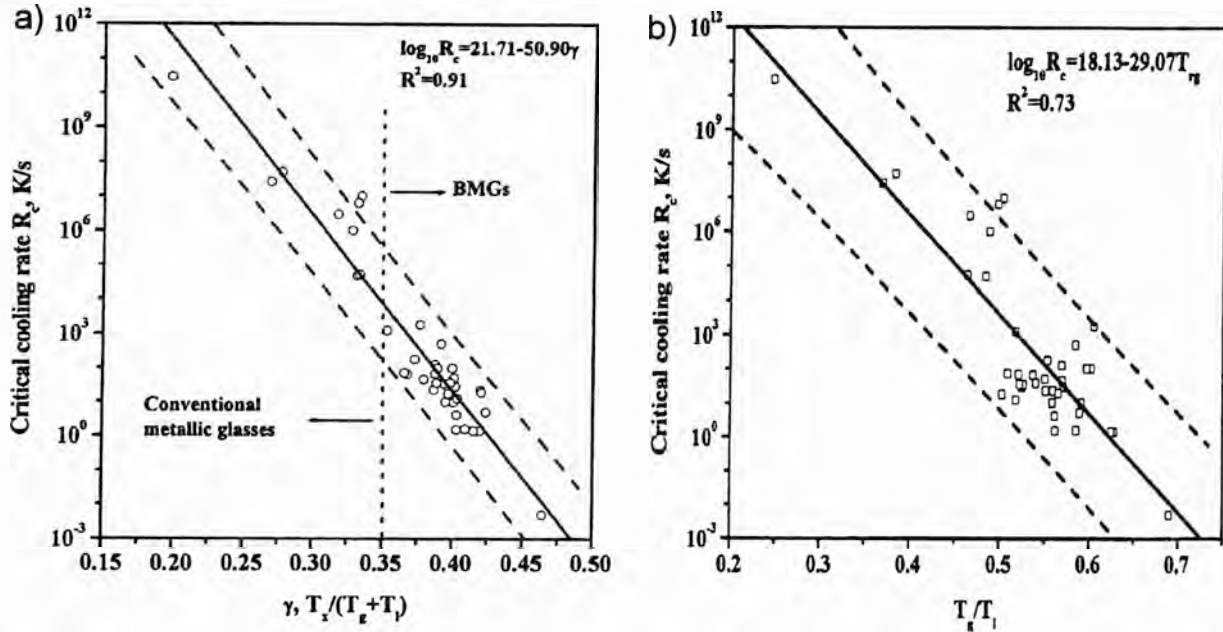


**Figure 2.12:** a) The correlation between  $\gamma$  and critical cooling rate  $R_C$ .<sup>[120]</sup> b) Critical cooling rate as a function of  $T_g/T_m$ .<sup>[120]</sup>

Lu and Liu<sup>[120]</sup> also plotted the critical section thickness ( $Z_C$  in mm) of a considerable number of BMGs as a function of  $\gamma$  and estimated the critical thickness of any BMG as:

$$Z_C = 2.8 \times 10^{-7} \exp(41.7\gamma) \quad (2.22)$$

The fit of Eq. (2.22) to the experimental data can be seen in Figure 2.13a). Based on theoretical calculations using the fragility concept and the nucleation theory for a model glass-forming system, Fan et al.<sup>[121]</sup> proposed the following dimensionless criterion,  $\phi$ , for determining the glass-forming ability of an alloy system:

$$\phi = T_{rg} \left( \frac{\Delta T_X}{T_g} \right)^a \quad (2.23)$$

where  $\Delta T_X$  is normalised by  $T_g$ , and  $a$  is a constant.

The parameter  $\phi$  was plotted against critical casting rate for a range of BMGs, where it was found that for all glasses  $a = 0.143$  and  $R_C$  can be estimated by:

$$R_C = 10^{8.638 \pm 0.475 - (18.0 \pm 1.055)\phi} \quad (2.24)$$

The fit of Eq. (2.24) to the experimental data can be seen in **Figure 2.13b**.

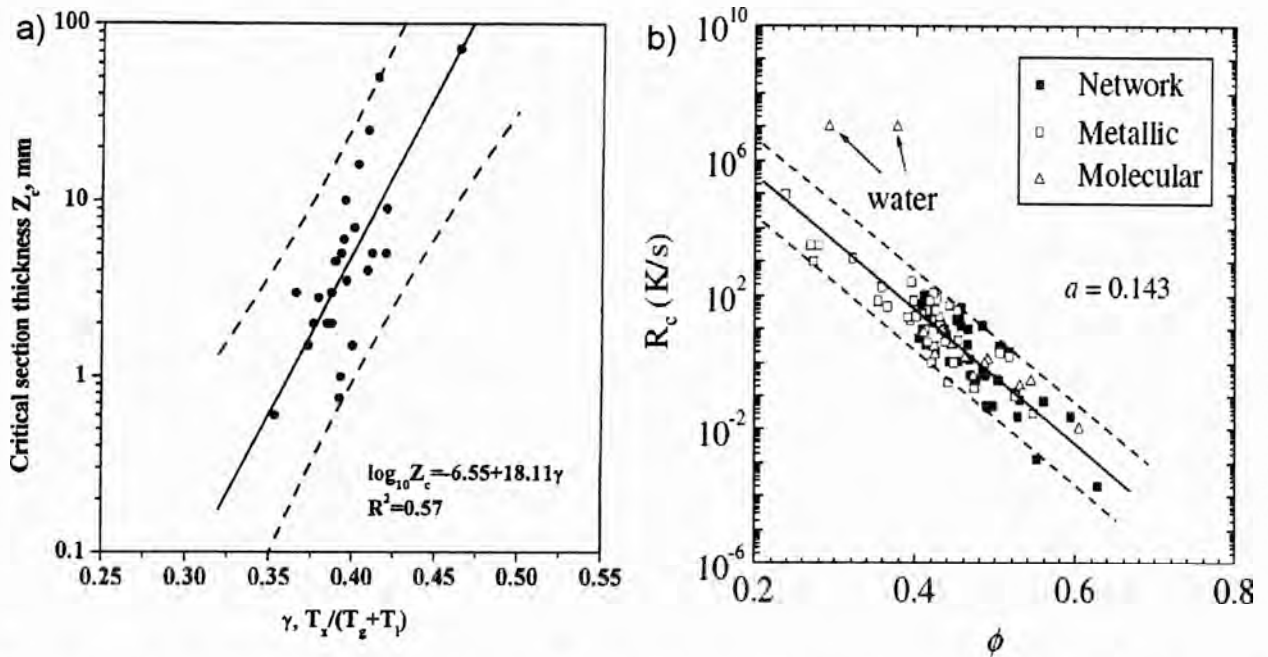


**Figure 2.13:** a) Critical section thickness  $Z_C$  as a function of  $\gamma$  for typical BMGs.<sup>[120]</sup> b) Critical cooling rate  $R_C$  as a function of  $\phi$  for typical glasses.<sup>[121]</sup>

#### 2.4.4 Order Parameter

By knowing the heat of crystallisation and the heat of fusion (usually found using differential scanning calorimetry), the order parameter,  $\phi$ , of an alloy in the solid state can be identified as:

$$\phi = 1 - \Delta H_X / \Delta H_f \quad (2.25)$$

where  $\Delta H_X$  and  $\Delta H_f$  are the heat of crystallisation and heat of fusion, respectively. For complete ordering of the alloy,  $\phi = 1$ , which corresponds to a fully crystalline state. If the solid alloy has atomic arrangements identical to the liquid state at the liquidus temperature, then  $\Delta H_X = \Delta H_f$  and  $\phi = 0$ ; this extreme situation corresponds to complete disordering of the atoms (identical to the liquid state).<sup>[122]</sup>

### 2.4.5 Time-Temperature-Transformation and C-Curve Estimation

Takeuchi et al.<sup>[75]</sup> have developed a model specific to BMGs in which the specific composition/atomic characteristics and viscosity are used for the estimation of the time required for the onset of crystallisation for a given temperature, given by the following relation:

$$t = \frac{9.3\eta}{k_B T} \left[ \frac{X_v a_o^9}{f^3 N_v} \exp\left(\frac{1.07}{T_r^3 \Delta T_r^2}\right) \left\{ 1 - \exp\left(-\frac{\Delta H_f^m \Delta T_r}{RT}\right) \right\}^{-3} \right]^{\frac{1}{4}} \quad (2.26)$$

where  $\eta$  is the viscosity,  $k_B$  the Boltzmann constant,  $T$  the absolute temperature,  $X_v$  the fraction of crystal formed in time  $t$ ,  $a_o$  the mean atomic diameter,  $f$  the fraction of sites at the melt/crystal interface at which atom transfer can occur, and  $N_v$  the volume concentration of atoms. In addition,  $T_r = T/T_m$  is the reduced temperature defined by  $T$  normalised with respect to the melting temperature  $T_m$ ,  $\Delta T_r = 1 - T_r$  the reduced undercooling of the melt,  $\Delta H_f^m$  the molar heat of fusion, and  $R$  the gas constant. In calculating,  $X_v$  is fixed at  $10^{-6}$ , and  $f$  is assumed to be proportional to  $\Delta T_r$  such that  $f = 0.2 \Delta T_r$ . This equation can be divided into three representative functions;

$$f_1(a_o, N_v) = \left[ \frac{9.3}{k_B} \left( \frac{1.25 \times 10^{-4} a_o^9}{N_v} \right)^{\frac{1}{4}} \right] \quad (2.27)$$

which represents physical quantities (on an atomic scale) specific to the BMG composition,

$$f_2(T_r) = \left[ \frac{1}{T_r \Delta T_r^{3/4}} \exp\left(\frac{1.07/4}{T_r^3 \Delta T_r^2}\right) \exp\left\{ \frac{2}{5} \left( \frac{T_r}{\Delta T_r} \right)^{\frac{3}{4}} \right\} \right] \quad (2.28)$$

which represents the reduced temperature factors associated with the calculation, and

$$f_3(\eta_r) = \frac{\eta}{T_m} = \frac{\eta_o \exp(D^* T_o / T - T_o)}{T_m} \quad (2.29)$$

which represents the reduced viscosity term. In the course of deriving Eq. (2.28), the  $\Delta H_f^m$  term, which is theoretically unpredictable, is approximated by Richard's law ( $\Delta H_f^m / RT_m = 1$ ). The multiple of these three functions for a given temperature estimates the time required for the onset of crystallisation at that temperature, hence the position of the C-curve in a TTT diagram.



## 2.5. PREPARATION OF BULK METALLIC GLASSES FROM A MELT

In the past, several different methods of rapid quenching from (i) the melt (melt spinning, melt atomization) or (ii) vapour phase (vapour deposition) have been used to achieve the glassy state. To avoid crystallisation, the quenching process in these techniques has to be done on a timescale much shorter than that for the nucleation and growth of the competing crystalline phases.

With respect to BMGs, there are two basic techniques used to produce bulk products, namely solidification and consolidation. Solidification techniques involve the quenching of the alloy from the molten state, and include: water quenching, copper-mould casting, arc melting, unidirectional melting, squeeze casting/splat quenching, evacuation casting, high-pressure die-casting and more recently, strip casting. Some examples of products produced from a melt are shown in **Figure 2.14**. Consolidation techniques involve the hot pressing and warm extrusion of atomised amorphous powders (usually produced by melt spinning or melt atomisation methods) in the supercooled liquid region.



**Figure 2.14:** A number of BMG components formed by direct casting.<sup>[123]</sup>



### 2.5.1 Arc-Melting

It has been reported that the quaternary and quinary alloys in the Zr-Al-TM (TM = Co, Ni, Cu) system can be amorphised using localised arc melting on a copper hearth.<sup>[124]</sup> Due to the heterogeneous nucleation initiated from incomplete melting at the base of the sample in contact with the copper hearth, the suppression of the Zr<sub>2</sub>TM crystalline phase was found to be difficult. However, the inner region of the heat-affected zone was found to be amorphous. Three different zones: outer equiaxed, columnar dendritic and metastable single phase were observed within the crystalline region.

### 2.5.2 Unidirectional Zone Melting

Unidirectional zone melting equipment with an arc-type heat source has been used to produce a continuous bulk amorphous Zr<sub>60</sub>Al<sub>10</sub>Ni<sub>10</sub>Cu<sub>15</sub>Pd<sub>5</sub> alloy.<sup>[125]</sup> The pre-alloyed Zr<sub>60</sub>Al<sub>10</sub>Ni<sub>10</sub>Cu<sub>15</sub>Pd<sub>5</sub> ingot was moving at a speed of 5.7 mm/s on the copper hearth under argon atmosphere. The use of the arc electrode as a heat source made direct measurement of the cooling rate difficult for that Zr-based alloy. The cooling rate was estimated as  $1.9 \times 10^2$  °C/s which was high enough to achieve an amorphous phase in the particular alloy. A completely amorphous phase was observed with the exception of the bottom and side edge regions in contact with the copper hearth. The resulting Zr-based amorphous alloy had a thickness of 10 mm, a width of 12 mm and a length of ~ 170 mm.<sup>[125]</sup>

### 2.5.3 Conventional Copper Mould Casting

This method of casting is identical to that found in the common foundry, whereby the charge material is melted in a suitable crucible and manually poured under the influence of gravity into a mould. In the case of BMGs, permanent copper moulds have been used to achieve high cooling rates, usually under atmospheric conditions (i.e. in air). A number of simple sample geometries have been produced using this method of casting such as rods, plates, wedges and cones.<sup>[126-128]</sup>

### 2.5.4 Water Quenching

Since water quenching of melts held in quartz tubes generates high critical cooling rates, this method has been regularly used in the production of amorphous alloys.<sup>[124,129-135]</sup> Using this method, Inoue and co-workers have produced bulk amorphous cylinders of Pd-Cu-Ni-P of diameter 72 mm and length 75 mm<sup>[129]</sup> and Zr-Al-Ni-Cu of diameters of 5 to 16 mm and length 150 mm.<sup>[124]</sup> These alloys were found to have the same  $T_g$  -,  $\Delta T_X$  -,  $T_X$  - and  $\Delta H_X$  -values for the corresponding melt-spun ribbons of 30 µm thickness.<sup>[131]</sup> Fully amorphous samples with

diameters of 12 mm have also been achieved for a  $\text{Mg}_{65}\text{Cu}_{15}\text{Ag}_5\text{Pd}_5\text{Y}_{10}$  alloy by water quenching.<sup>[132]</sup>

Recently, Li reported a method called the J-quenching technique, in which both untreated  $\text{Fe}_{40}\text{Ni}_{40}\text{P}_{14}\text{B}_6$  and fluxed  $\text{Fe}_{40}\text{Ni}_{40}\text{P}_{14}\text{B}_6$  melts held in a fused silica tube can be quenched in water or brine to produce an amorphous structure.<sup>[134]</sup> In this technique, the  $\text{Fe}_{40}\text{Ni}_{40}\text{P}_{14}\text{B}_6$  material, is placed in a silica tube arrangement (**Figure 2.15**). The tube is then connected to a mechanical pump and evacuated, then filled with high purity argon gas. After this, the whole system is transferred to a furnace. The melt is heated to 1177 °C (liquidus of  $\text{Fe}_{40}\text{Ni}_{40}\text{P}_{14}\text{B}_6$  is 927 °C) using high frequency induction. The system is held at this temperature for 5 min before removal from the furnace and quenched in iced brine water to produce an amorphous rod sample.<sup>[134]</sup>

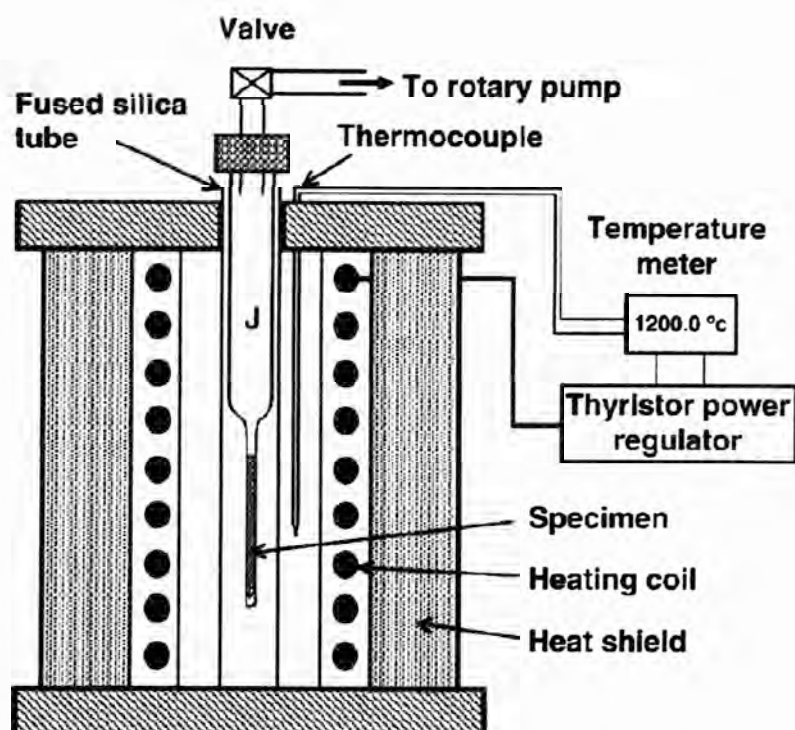


**Figure 2.15:** A schematic diagram of the J-quenching technique, made up of two fused silica tubes of different diameters.<sup>[134]</sup>

Amorphous  $\text{Zr}_{41.25}\text{Ti}_{13.75}\text{Ni}_{10}\text{Cu}_{12.5}\text{Be}_{22}$  (Vitreloy 1) coil springs with wire diameters of 4 mm and 6 mm and coil diameter of 40 mm have been fabricated by the water quenching method using a quartz tube specially designed by Qui and Ren.<sup>[135]</sup> The coiled quartz tube was connected to a larger quartz tube with an inner diameter of 18 mm, as shown schematically in **Figure 2.16**. The ingots were placed at the bottom of the larger quartz tube above the spring tube. The open end

of the large quartz tube was connected to a three-way switching valve. The tube could then be evacuated with a pump or pressurised. The connected tubes were first pumped to a vacuum of  $1 \times 10^{-3}$  Pa and then flushed three times with argon gas to further remove residual oxygen. The quartz tube containing the alloy ingots was lowered into a resistive tube furnace set at a temperature of 950 °C. When the temperature was stabilised, the sample was held for 8 min. A positive pressure of ~ 200 kPa argon gas was applied above the melt. After 2 min, the sample was quickly lowered and quenched into a saturated NaCl solution, producing the solid spring shown in **Figure 2.17**.

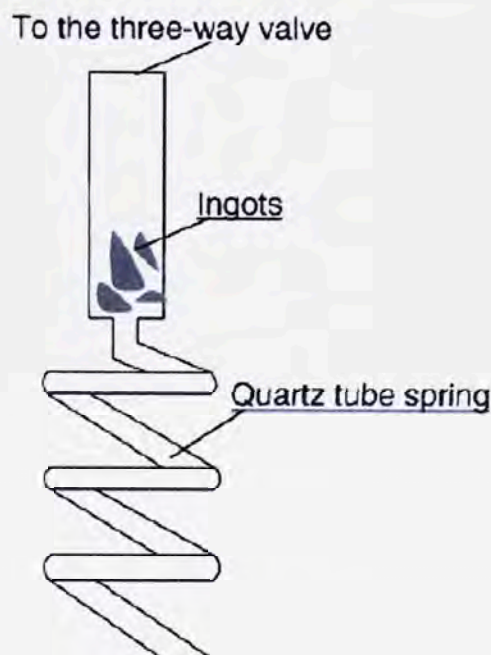


**Figure 2.16:** A schematic representation of the quartz tube setup used in the fabrication of a BMG coil spring.<sup>[135]</sup>

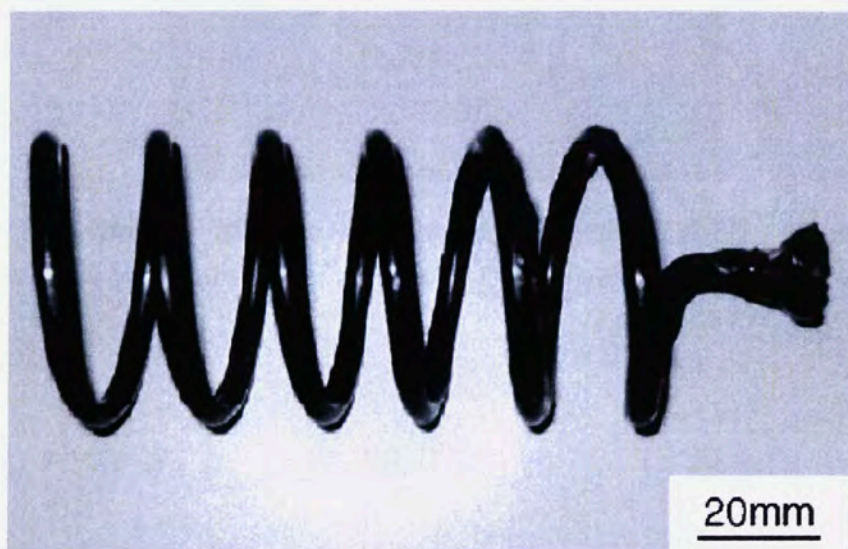


**Figure 2.17:** Appearance of the  $Zr_{41.25}Ti_{13.75}Ni_{10}Cu_{12.5}Be_{22}$  (Vitreloy 1) coil spring with a wire diameter of 4 mm and coil diameter of 40 mm fabricated by the water quenching method.<sup>[135]</sup>



### 2.5.5 Vacuum Casting into a Copper Mould

$\text{Zr}_{55}\text{Al}_{10}\text{Ni}_5\text{Cu}_{30}$  BMGs have been produced by casting into a cylindrical geometry with diameters up to 16 mm and a length of 70 mm by drawing the melt into a copper mould.<sup>[136]</sup> The evacuation force was produced by the rapid movement of a piston that was positioned at the centre of the mould. No significant crystalline phase was observed on either the outer surface or inner region of the samples. It was also noted that the casting was free of voids and cavities. It was found that the resulting cast samples showed similar values of  $T_g$ ,  $T_X$  and  $\Delta T_X$  and mechanical strength as the corresponding melt spun alloys. The size of the veins on the fracture surface were found to be about ten times larger than those of the ribbon sample, indicating high deformability of the cast samples.

Xing and co-workers were able to produce wedges of  $\text{Zr}_{52.5}\text{Cu}_{17.9}\text{Ni}_{14.6}\text{Al}_{10}\text{Ti}_5$  BMG which can be seen in **Figure 2.18** by arc melting a solid ingot in a water-cooled copper hearth and using a vacuum to draw the molten metal into a copper wedge die.<sup>[137]</sup>

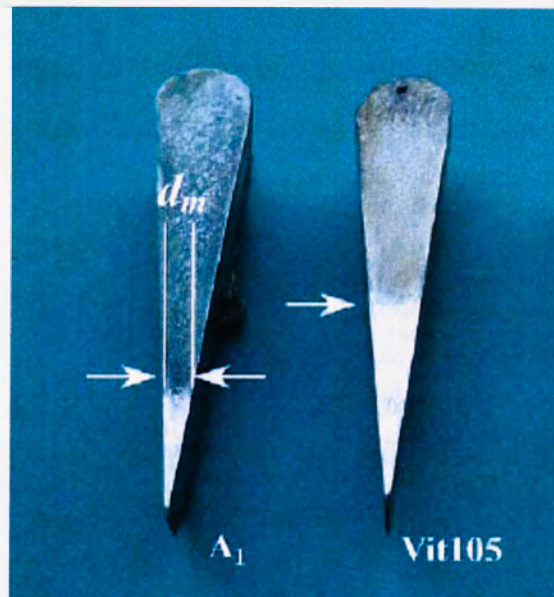


**Figure 2.18:** Appearance of the relative glass-forming ability of bulk amorphous  $\text{Zr}_{60}\text{Cu}_{20}\text{Ni}_8\text{Al}_7\text{Hf}_3\text{Ti}_2$  ( $A_1$ ) and  $\text{Zr}_{52.5}\text{Cu}_{17.9}\text{Ni}_{14.6}\text{Al}_{10}\text{Ti}_5$  (Vit105) alloy wedges produced by vacuum casting.<sup>[137]</sup>



### 2.5.6 Injection Casting into a Copper Mould

Possibly the most widely used method in recent times of preparing BMG samples from a melt is by applying a positive pressure, either by a mechanical plunger or a gas over pressure to force the molten alloy into a mould. This method has been used by many research groups in order to fabricate BMG samples with high structural integrity from numerous alloy systems in various geometric configurations.

Forming complex parts using the injection casting method is relatively easy in high glass-forming systems such as the Pd-Ni-Cu-P and Vitreloy groups, as large superheats can be applied and critical cooling rates are relatively low. Other systems such as Fe-, Ni- and Mg-based BMGs have proven to be more difficult to cast. An example of a difficult and complex component produced by this casting method is the ring cast by Wua et al.,<sup>[138]</sup> with an outer diameter of 10 mm, inner diameter of 6 mm and thickness of 1 mm, **Figure 2.19a**).

A schematic representation of the casting equipment shown in **Figure 2.19b**) is typical of that used for injection casting. In this example,  $\text{Fe}_{75.5}\text{Ga}_3\text{P}_{10.5}\text{C}_4\text{B}_4\text{Si}_3$  alloy ingots were placed in a quartz crucible with an orifice of 1.5 mm in diameter. After complete melting using high frequency induction heating, the alloys were injected into the copper mould at 1050 °C under an argon pressure of 176 kPa.

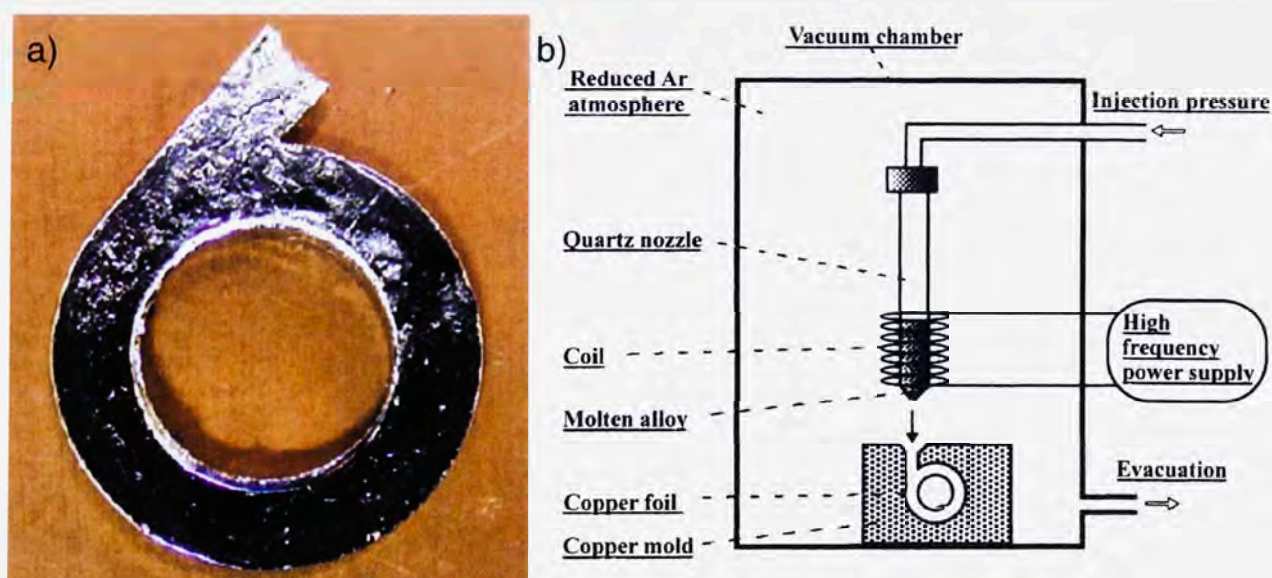


**Figure 2.19:** a) As cast 10 mm  $\text{Fe}_{75.5}\text{Ga}_3\text{P}_{10.5}\text{C}_4\text{B}_4\text{Si}_3$  BMG ring of inner diameter 6 mm and thickness 1 mm by Wua et al.<sup>[138]</sup> b) A schematic illustration of the (typical) copper mould/injection casting equipment used to produce a  $\text{Fe}_{75.5}\text{Ga}_3\text{P}_{10.5}\text{C}_4\text{B}_4\text{Si}_3$  BMG ring.<sup>[138]</sup>



### 2.5.7 Strip Casting

Twin-roll strip casting (in air) has been used to fabricate sheet products of Fe-, Zr- and Cu-base BMGs by Lee and co-workers.<sup>[139-141]</sup> Simulation of the solidification behaviour of these alloys during twin-roll casting shows that a suitable cooling rate can be achieved by this casting technique to form an amorphous structure throughout the entire thickness of the sheet.

Alloys having quite different glass-forming abilities have been cast using a horizontal twin-roll strip caster at POSTECH. These include  $\text{Zr}_{41.2}\text{Ti}_{13.8}\text{Cu}_{12.5}\text{Ni}_{10}\text{Be}_{22.5}$  alloy (Vitreloy 1) with  $R_C$  of  $\sim 1^\circ\text{C/s}$ <sup>[26]</sup> and  $\text{Cu}_{47}\text{Ti}_{33}\text{Zr}_{11}\text{Ni}_6\text{Sn}_2\text{Si}_1$  alloy with  $R_C$  of  $\sim 250^\circ\text{C/s}$ .<sup>[142]</sup> After melting, the molten alloy is transferred into a tundish where the metal is fed through a slot type ceramic nozzle used to achieve a uniform flow across the width of the rolls. The rolls were made of Cu-0.7 wt% Be and cooled by circulating water through holes inside the rolls. By using water-cooled Cu as the roll material, this particular strip caster can generate a faster solidification rate than those used in steel fabrication. Previous studies showed that a solidification rates up to  $1000^\circ\text{C/s}$  can be achieved for Al and Mg alloys using the present strip casting configuration.<sup>[143-147]</sup> As the molten metal feeds through the two rotating rolls (**Figure 2.20**), a solid shell forms near the contact region between the melt and rolls.

Lee and co-workers have also examined the viability of both vertical and horizontal twin roll strip casting of Fe-based amorphous alloys with the results suggesting that it is possible to obtain amorphous structures using this casting method.<sup>[140-141]</sup> These results indicate that this process is viable for the continuous fabrication of sheets of BMGs with a wide range of critical cooling rates.

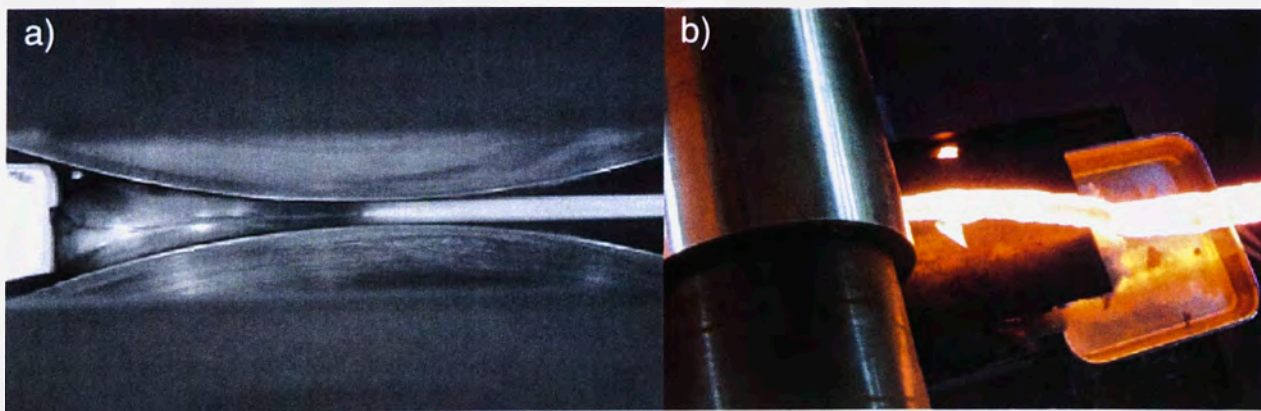


**Figure 2.20:** a) Thermal image of the roll gap area of the horizontal strip caster at POSTECH.<sup>[139]</sup> b) Photograph of the manufacturing of an Fe-Ni-Cr-Si-B BMG sheet.<sup>[140]</sup>



## 2.6. PROPERTIES OF BULK METALLIC GLASSES

With more BMG systems being developed continuously, one can expect the discovery of many new and unique properties, allowing their expansion into a range of specialty commercial components.

### 2.6.1 Modulus, Strength and Hardness

In general, BMGs have higher tensile strengths and lower Young's Moduli than their corresponding crystalline alloys. **Figure 2.21** summarises the work of Ashby and Greer<sup>[148]</sup> who compared the elastic limit and Young's modulus of BMGs with 1500 other useful commercial alloys. The shaded zone in this figure shows the fundamental boundary of the accessible region of the plot, limited by the theoretical strength ( $\sigma_y = E/20$ ), which the metallic glasses approach more closely than any other bulk metallic material. The contours given in **Figure 2.21** show the property combinations or material indices  $\sigma_y/E$  (yield strain) and  $\sigma_y^2/E$  (resilience). The use of such indices is described elsewhere.<sup>[149]</sup> Here, the metallic glasses excel, having a larger yield strain and the ability to store more elastic energy per unit volume than any of the other materials on the diagram.

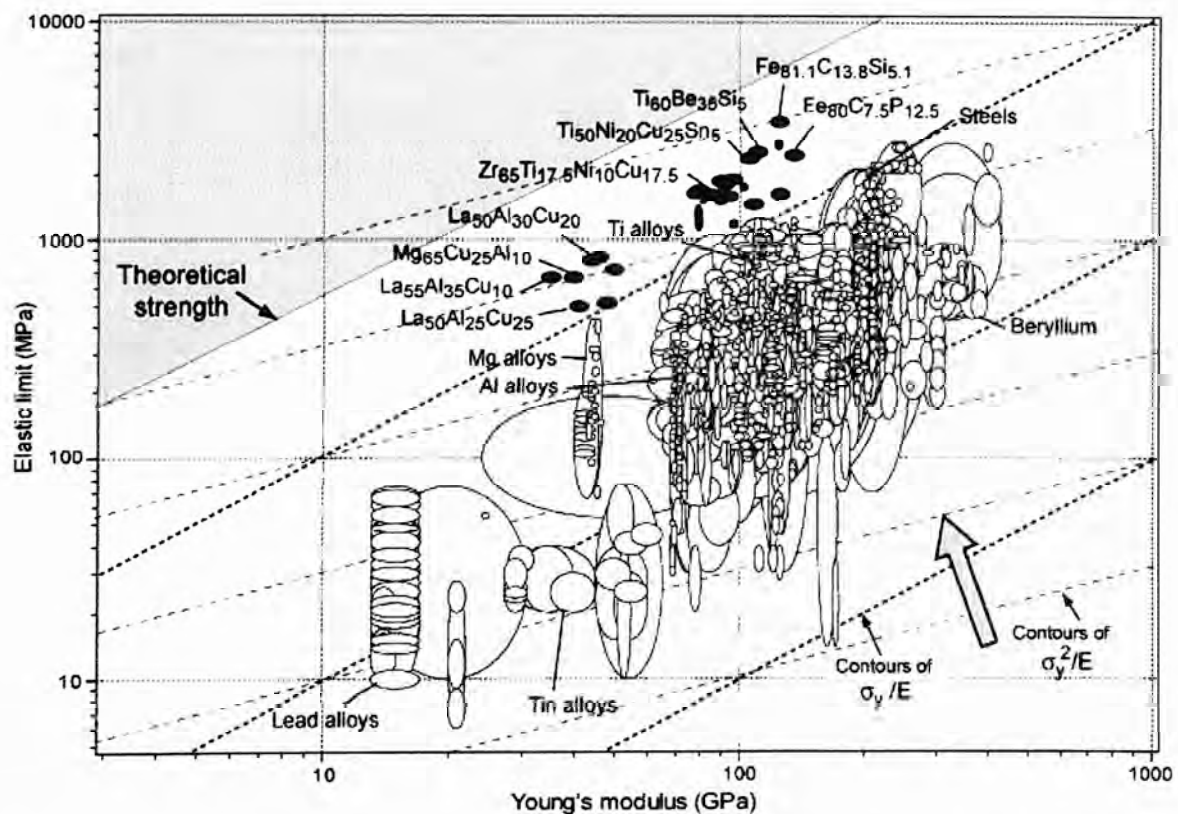


**Figure 2.21:** Elastic limit,  $\sigma_y$ , plotted against modulus,  $E$ , for 1500 metals, alloys, metal matrix composites and metallic glasses. The contours show the yield strain  $\sigma_y/E$  and the resilience  $\sigma_y^2/E$ .<sup>[148]</sup>



**Figure 2.22** shows the relationship between Young's modulus ( $E$ ), tensile fracture strength ( $\sigma_y$ ) for a large range of commonly produced BMGs.<sup>[41]</sup> The stiffest and strongest of these to date is the amorphous  $\text{Co}_{43}\text{Fe}_{20}\text{Ta}_{5.5}\text{B}_{31.5}$  alloy, which exhibits an ultra-high fracture strength (in compression) of 5.2 GPa and Young's modulus of 268 GPa.<sup>[41]</sup> It can be seen in this figure that the tensile fracture strength show a near linear relationship with  $E$ . A slope of 0.002 corresponds to the elastic strain limit of BMGs. A similar trend is also evident for ordinary crystalline alloys shown in the figure, but the slope of the linear region for BMGs is much steeper than that of the crystalline alloys, thereby indicating larger elastic limits for BMGs compared to the crystalline alloys.<sup>[150,151]</sup> The linearity of this relationship is attributed to the formation of an ideally homogenised solid solution over the entire composition range.

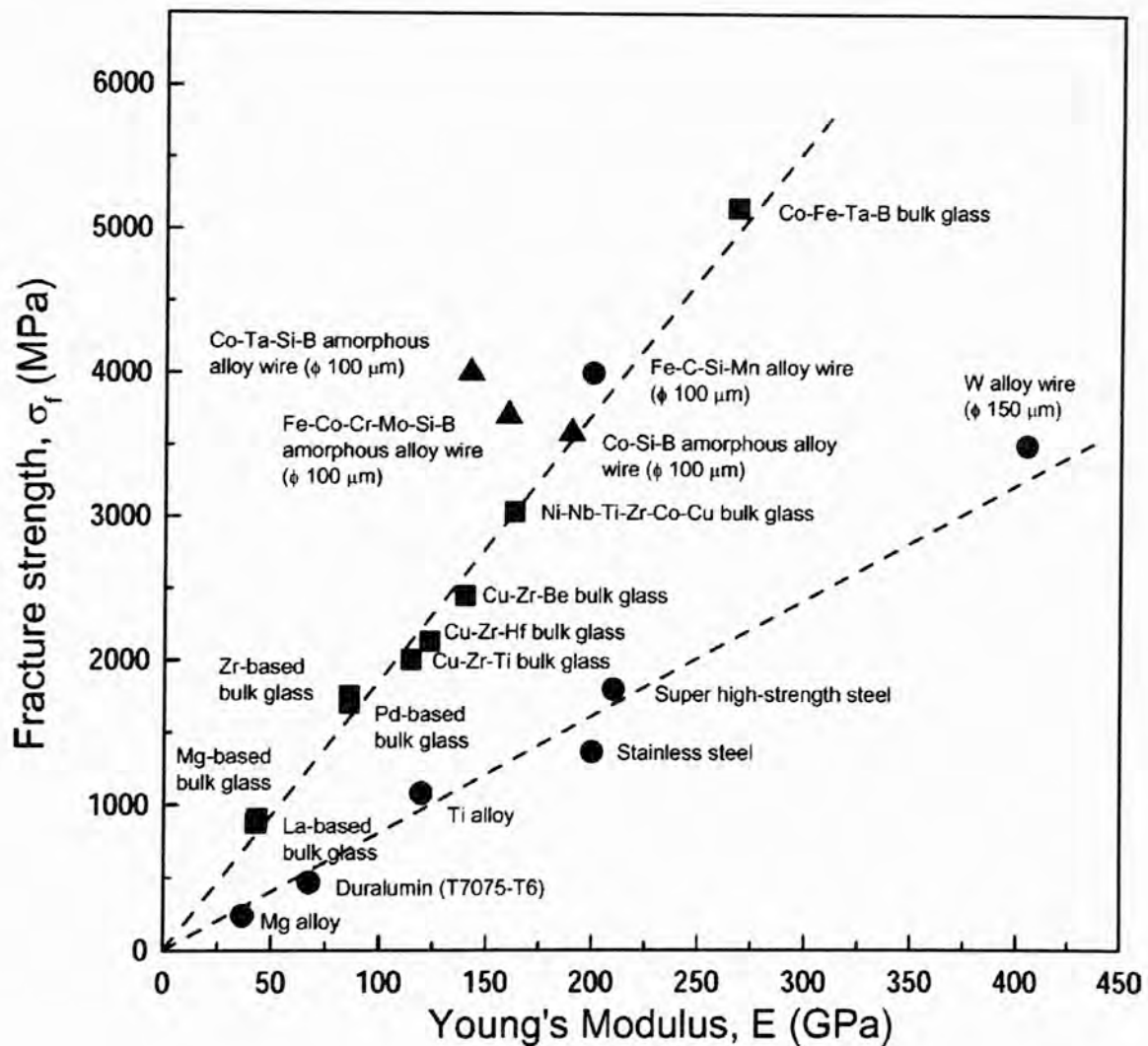


**Figure 2.22:** The relationship between Young's modulus and tensile fracture strength for BMGs with diameters over 2 mm (■); some amorphous wires (▲) (100  $\mu\text{m}$ ), and conventional crystalline alloys (●).<sup>[41]</sup>

Under tensile loading, typical crystalline metals exhibit substantial plastic strain, resulting in high fracture toughness and impact resistance. However, metallic glasses under tensile load show little global plasticity of the sample as a whole. Hence, these materials are generally considered to be “brittle”.<sup>[25]</sup> A comparison between  $Zr_{60}Al_{10}Ni_{10}Cu_{20}$  BMG and the crystalline Ti-6Al-4V alloy was made by Kakiuchi and co-workers<sup>[152,153]</sup> who demonstrated the superiority in mechanical properties of amorphous alloys over crystalline alloys. **Figure 2.23** highlights the high elastic strain limit and general toughness of a  $Zr_{60}Al_{10}Ni_{10}Cu_{20}$  BMG in comparison to the commercial Ti-6Al-4V crystalline alloy.

Inoue and co-workers have measured the three-point bending flexural stress and deflection curves of Zr-Al-Ni-Cu and Zr-Ti-Al-Ni-Cu BMGs. These materials have high flexural strength values of 3.0 - 3.9 GPa which are 2.0 - 2.5 times higher than those for crystalline Zr- and Ti-based alloys. Furthermore, BMGs have relatively large deflection values above 0.4 mm.<sup>[158]</sup>

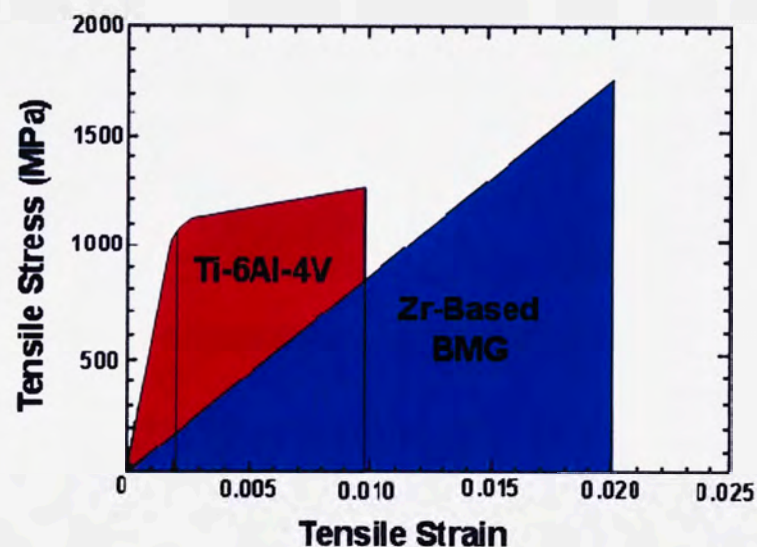


**Figure 2.23:** Tensile stress-strain curves of a  $Zr_{60}Al_{10}Ni_{10}Cu_{20}$  BMG and crystalline Ti-6Al-4V alloy.<sup>[153]</sup>

This significant difference in mechanical properties is attributed to the difference in deformation and fracture mechanisms between BMGs and crystalline alloys. Plastic deformation in metallic glasses is generally associated with inhomogeneous flow in highly localised shear bands,<sup>[25,154-157]</sup> as shown in **Figure 2.24**.

Even under slower strain rates, a veined fracture surface indicates a decrease in glass viscosity. Due to the highly localised nature of flow and the lack of microstructural features to divert the flow, shear band formation typically leads to catastrophic (brittle) failure in metallic glasses. The



localisation of shear is associated with possible strain-softening mechanisms and thermal softening as well as the absence of strain-hardening (working hardening) mechanisms.<sup>[25]</sup> Fractographic evidence from tensile experiments (**Figure 2.25**) suggests that, under high strain rate conditions, local melting occurs during unstable fracture.<sup>[159]</sup>

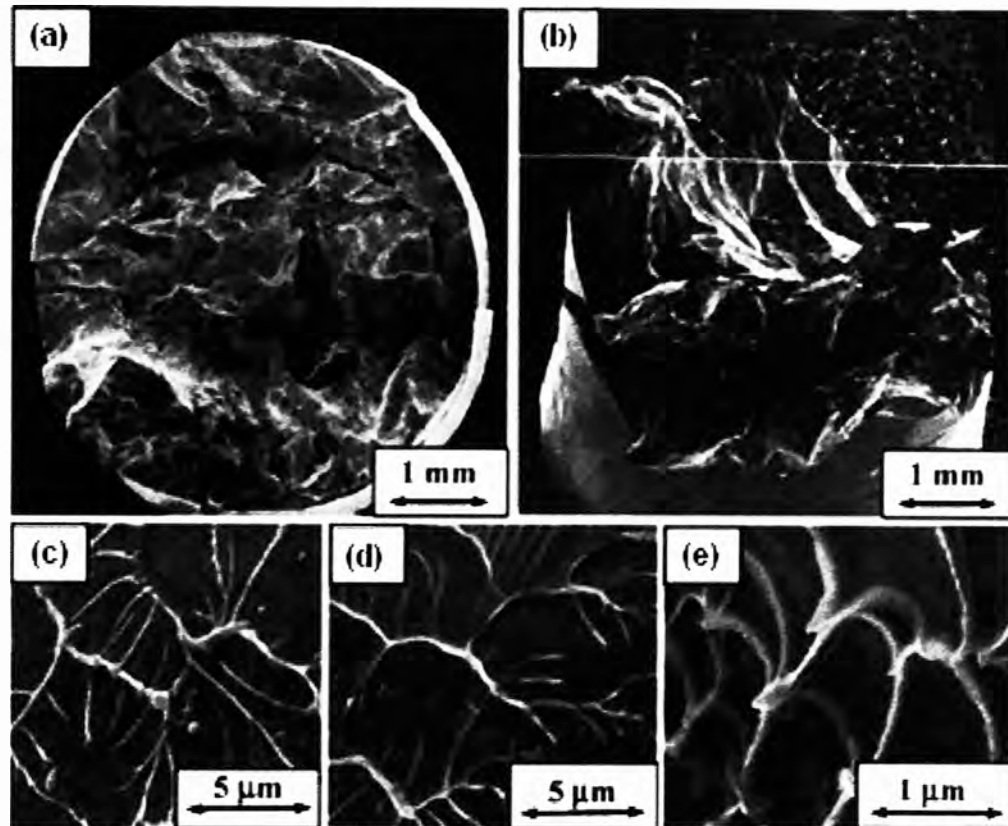


**Figure 2.24:** SEM images of the tensile fracture surface of a  $Zr_{50}Cu_{40}Al_{10}$  BMG.<sup>[156]</sup>

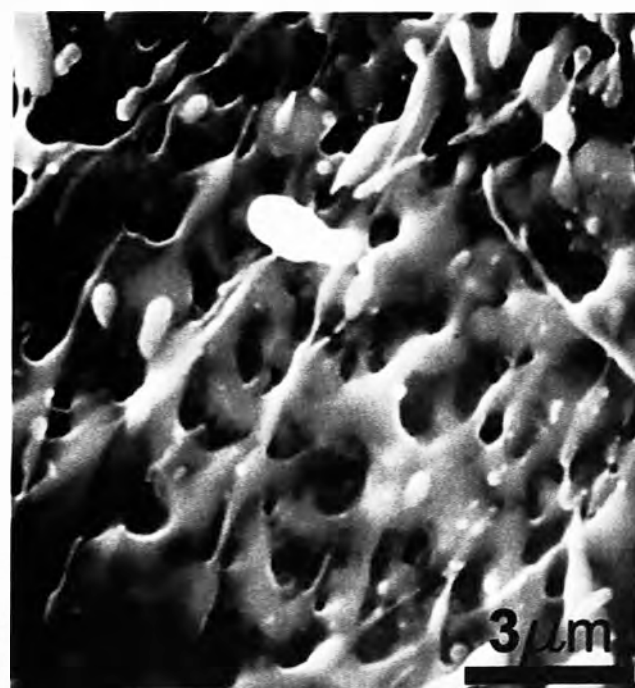


**Figure 2.25:** Fracture surface of a high strain rate tensile sample which exhibits a cup-and-cone type fracture. The small droplets are indicative of localised melting.<sup>[159]</sup>



they have small process zone sizes ( $d < 1$  mm) because  $\sigma_y$  is so large. In terms of  $d$ , a brittle metallic glass (e.g.  $\text{Fe}_{40}\text{Ni}_{40}\text{P}_{14}\text{B}_6$ ) shows poorer performance than conventional silicate glasses. The high toughness of some metallic glasses appears to be at variance with their near-zero ductility, which arises from shear localisation.<sup>[148]</sup>

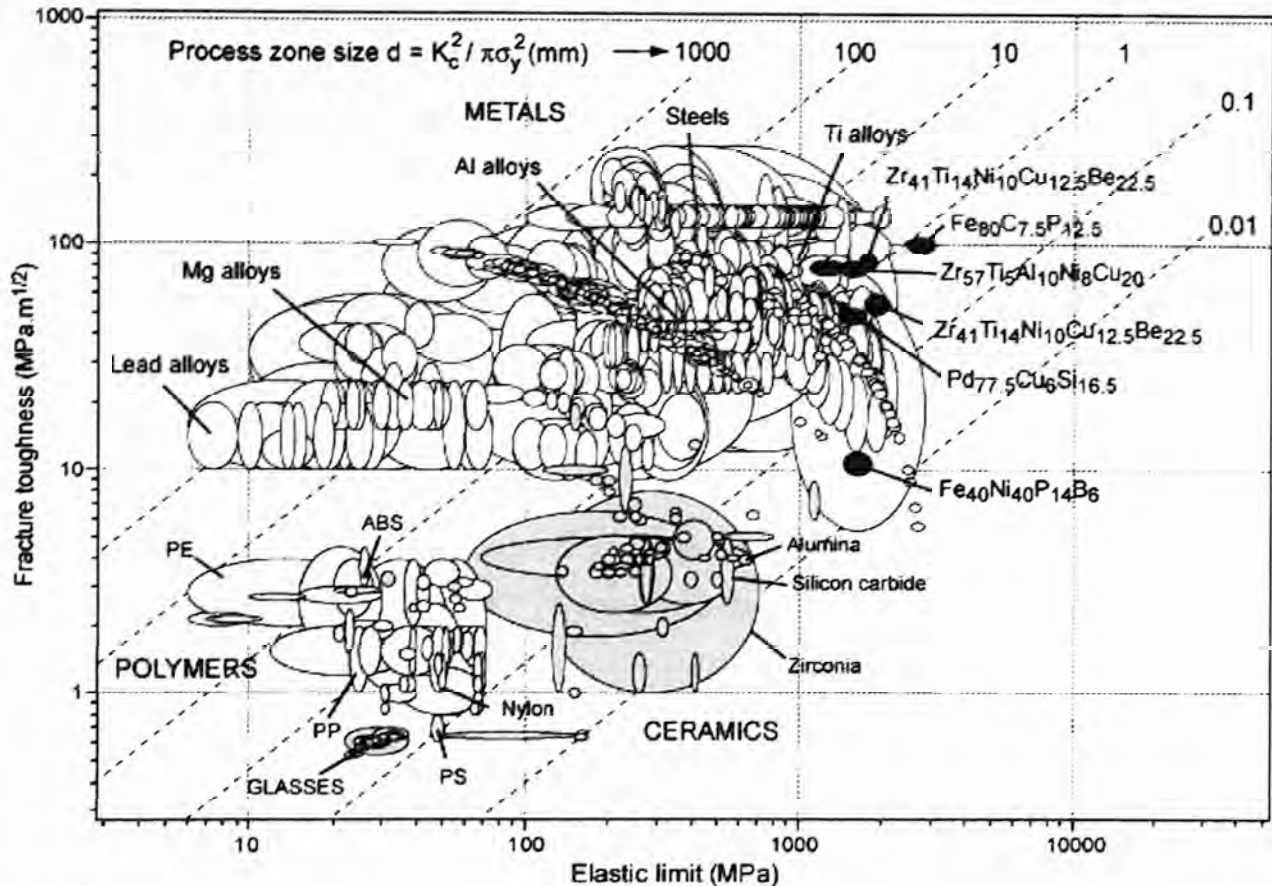


**Figure 2.27:** Fracture toughness and elastic limit for the same materials. The contours show the process-zone size  $d$  (mm).<sup>[148]</sup>

The  $K_C$ -values of Zr-based amorphous alloys with a thickness of 3 mm have been measured to be 55  $\text{MPa}\sqrt{\text{m}}$  for the Zr-Ti-Be-Ni-Cu,<sup>[160]</sup> 67  $\text{MPa}\sqrt{\text{m}}$  for  $\text{Zr}_{55}\text{Al}_{10}\text{Ni}_5\text{Cu}_{30}$  and 70  $\text{MPa}\sqrt{\text{m}}$  for  $\text{Zr}_{55}\text{Al}_{10}\text{Ni}_5\text{Cu}_{29}\text{Nb}_1$ .<sup>[78]</sup> These values are comparable to  $K_C$ -values for age-hardened Al-based alloys (24-36  $\text{MPa}\sqrt{\text{m}}$ )<sup>[161]</sup> and commercial Ti-based alloys (54-98  $\text{MPa}\sqrt{\text{m}}$ ).<sup>[161]</sup> It is also interesting to point out that  $K_C$ -values decrease to around 1  $\text{MPa}\sqrt{\text{m}}$  for Zr-Ti-Be-Ni-Cu amorphous alloys containing nanocrystalline particles,<sup>[162]</sup> yet Zr-Al-Ni-Cu BMGs containing nanocrystalline particles exhibit a marked improvement in  $K_C$  to  $\sim 160$   $\text{MPa}\sqrt{\text{m}}$ ,<sup>[163]</sup> which exceeds that of conventional Ti- and alloy steels. In a series of fracture toughness experiments, Flores and co-workers examined the plastic strain field at a crack tip using a single-edge notched tension sample. A stable damage zone of branched cracks was achieved within the classical plastic zone (**Figure 2.28**).<sup>[164]</sup>



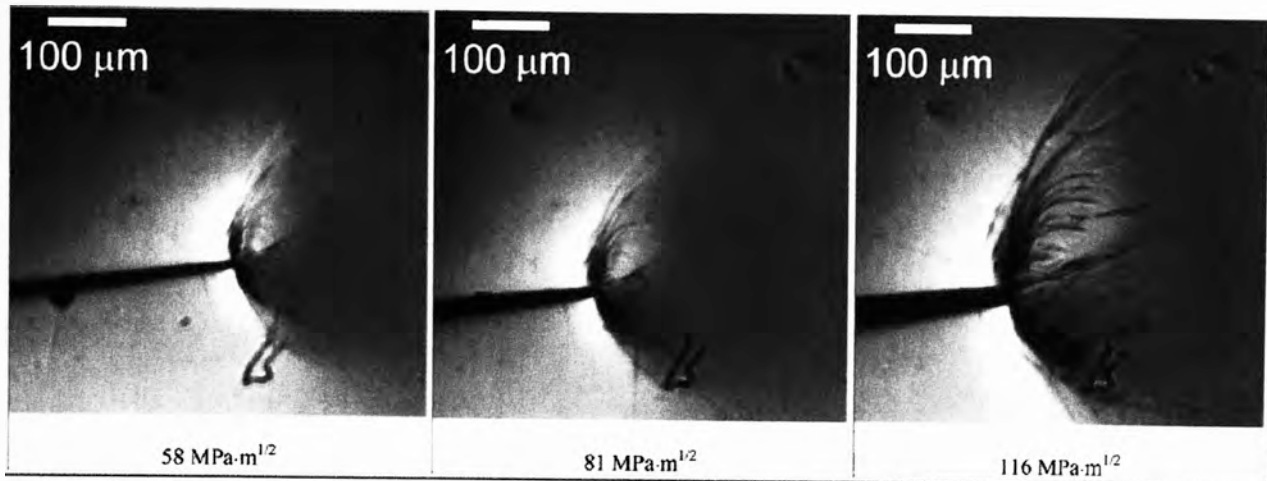


**Figure 2.28:** Optical microscope images of the crack tip in a single-edge notched tension sample during a fracture toughness experiment. Stress intensities at the crack tip are given.<sup>[164]</sup>

The softening of the fracture surface has led several researchers to conclude that shear band formation is associated with localised heating.<sup>[164,165]</sup> In addition to the heating associated with plastic deformation, a cooling zone was also recorded ahead of the crack tip, which is consistent with thermo-elastic cooling effects.<sup>[164,165]</sup> These results indicate that BMGs have high plastic deformability even near the crack tip. These data were obtained using sheet specimens with a thickness of 3.0 mm.

Compared to fracture toughness, an impact test is a qualitative property. Inoue et al. examined the compositional dependence of Charpy impact fracture energy for Zr-based BMGs.<sup>[74,158]</sup> They found that, for cast Zr-based BMG alloy sheets with a thickness of 2.5 mm, the impact fracture energy is in the range of 110-140 kJ/m<sup>2</sup>.

Raghavan and co-workers also impact tested Vitreloy 1 ( $\text{Zr}_{41.2}\text{Ti}_{13.75}\text{Cu}_{12.5}\text{Ni}_{10}\text{Be}_{22.5}$ ) over a range of temperatures (123-423 K) and alloy treatments to examine if these materials exhibit a ductile-to-brittle transition. Their results show an abrupt reduction in impact toughness when the testing temperature is lowered to below 150 K, implying that BMGs, similar to crystalline alloys, exhibit a ductile-to-brittle transition temperature. Fractographic observations indicated a transition in the fracture mode from ductile vein-like morphology above the transition to a cleavage-dominant fracture mode below it.<sup>[166]</sup>

### 2.6.3 Fatigue, Resilience and Damping Capacity

The fatigue limits in BMG systems investigated to date are comparable to those of crystalline alloys. Considering the tensile fracture strength of BMGs is about double that of the crystalline alloys, the fatigue endurance stress level is also much higher for BMGs. **Figure 2.29** summarises the bending and rotating beam fatigue strength as a function of number of cycles to failure for bulk amorphous  $\text{Zr}_{65}\text{Al}_{10}\text{Ni}_{10}\text{Cu}_{15}$ <sup>[78]</sup> and  $\text{Pd}_{40}\text{Cu}_{30}\text{Ni}_{10}\text{P}_{20}$ <sup>[167]</sup> alloys, respectively, together with the data under tensile stress conditions for melt-spun  $\text{Pd}_{80}\text{Si}_{20}$ ,<sup>[168]</sup>  $\text{Ni}_{75}\text{Si}_8\text{B}_{17}$ <sup>[169]</sup> and  $\text{Co}_{75}\text{Si}_{10}\text{B}_{15}$ <sup>[169]</sup> amorphous ribbons. Here, the fatigue limit is defined as the ratio of the minimum fatigue strength after 107 cycles over the static bending or tensile fracture strength. The bending fatigue strength is as high as 1000 MPa at cycles of  $3 \times 10^4$  for a  $\text{Zr}_{65}\text{Al}_{10}\text{Ni}_{10}\text{Cu}_{15}$  BMG.

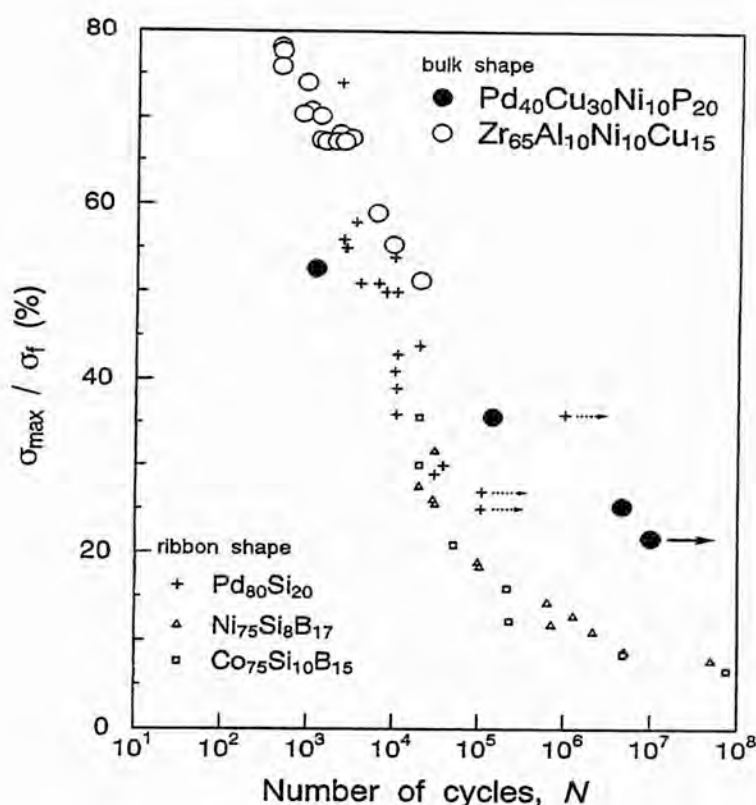


**Figure 2.29:** Maximum bending and rotating beam fatigue stress as a function of cyclic number up to failure for  $\text{Zr}_{65}\text{Al}_{10}\text{Ni}_{10}\text{Cu}_{15}$  and  $\text{Pd}_{40}\text{Cu}_{30}\text{Ni}_{10}\text{P}_{20}$  BMGs. Data for melt spun Pd-, Ni- and Co-based amorphous ribbons under tensile stress conditions are also shown.<sup>[20]</sup>

Fatigue and fracture toughness tests of the Vitreloy BMG have cast some doubt on the material's prospects for use in tougher, industrial applications that require long-term performance. Standard stress-strain fatigue tests also show that Vitreloy has an extremely low resistance to crack initiation and that a crack propagates rapidly once formed. It has also been found that the difference in BMGs and crystalline structures does not play a dominant role in the



propagation velocity of fatigue cracks, although the deformation and fracture behaviour under uniaxial loading is markedly different to crystalline alloys<sup>[74]</sup>.

**Figure 2.30** shows the resilience,  $\sigma_y^2/E$  and loss coefficient,  $g$  (a measure of the mechanical damping or energy loss in an elastic load cycle).<sup>[149]</sup> High resilience correlates with low loss coefficient, reflecting the contribution of local plastic flow to energy loss. The metallic glasses are considered exceptional with respect to their combination of high resilience and low damping and prove to be attractive materials for vibrating-reed systems such as gyroscopes, fast-acting springs and applications requiring transmission of elastic waves.<sup>[148]</sup>

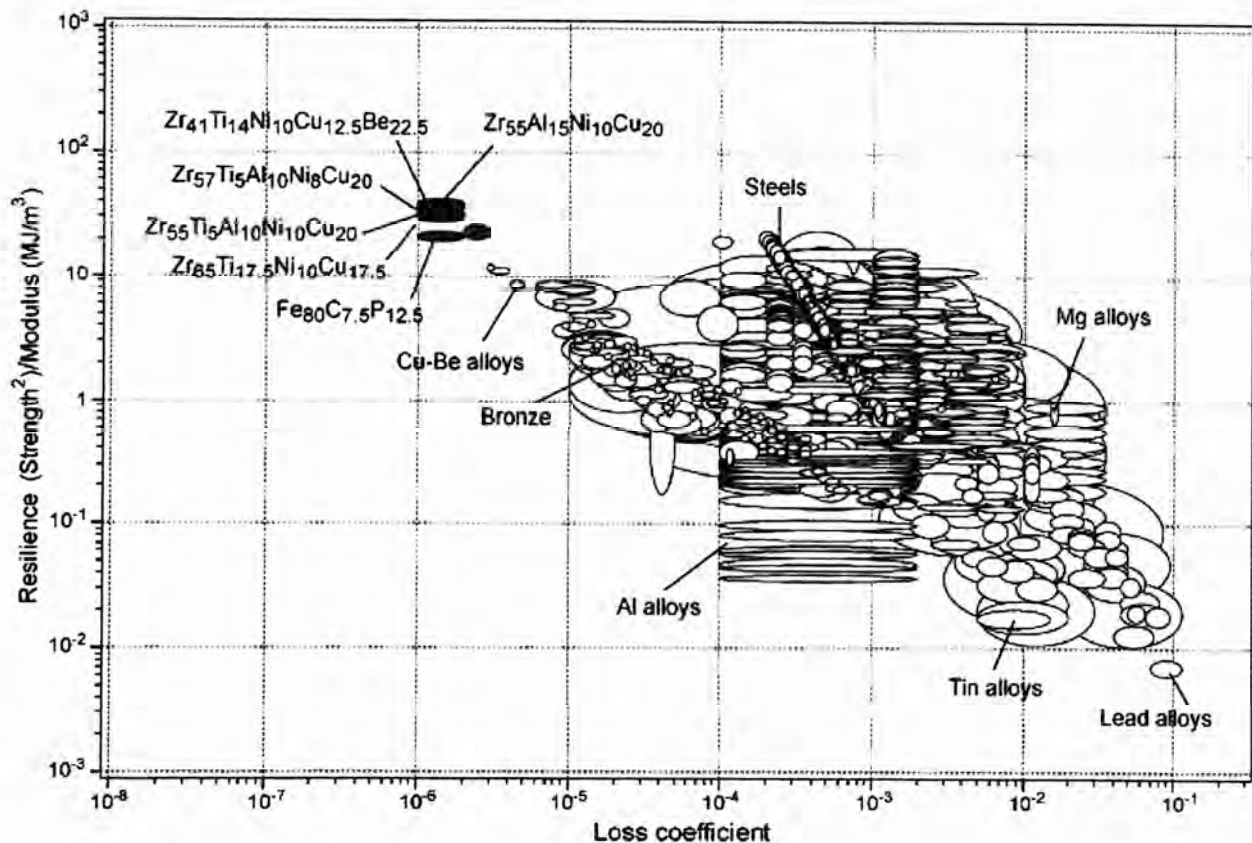


**Figure 2.30:** Resilience  $\sigma_y^2/E$  and loss coefficient  $g$  for the same materials as in **Figure 2.26**.<sup>[148]</sup>

#### 2.6.4 Superplastic Properties of Bulk Metallic Glasses

Forming BMG parts through viscous flow in the supercooled liquid state is both a viable and favourable process. The viscous flow behaviour of Zr-, La- and Pd-based BMGs has been investigated extensively. With such high formabilities, not only common small machine components can be fabricated with BMGs, but micro-machine components can be made through microforming.<sup>[170]</sup> Metallic glasses, when deformed in the SCL region, exhibit extraordinarily large strains. An example is given in **Figure 2.31**, in which a La<sub>55</sub>Al<sub>25</sub>Ni<sub>20</sub> alloy is

strained to 20,000% in the supercooled liquid region.<sup>[171]</sup> Another example is given in **Figure 2.32**, where, similar to thermoplastics a  $Zr_{44}Ti_{11}Cu_{10}Ni_{10}Be_{25}$  BMG has been ‘blow moulded’ in the SCL region into a shaped die.<sup>[172]</sup>

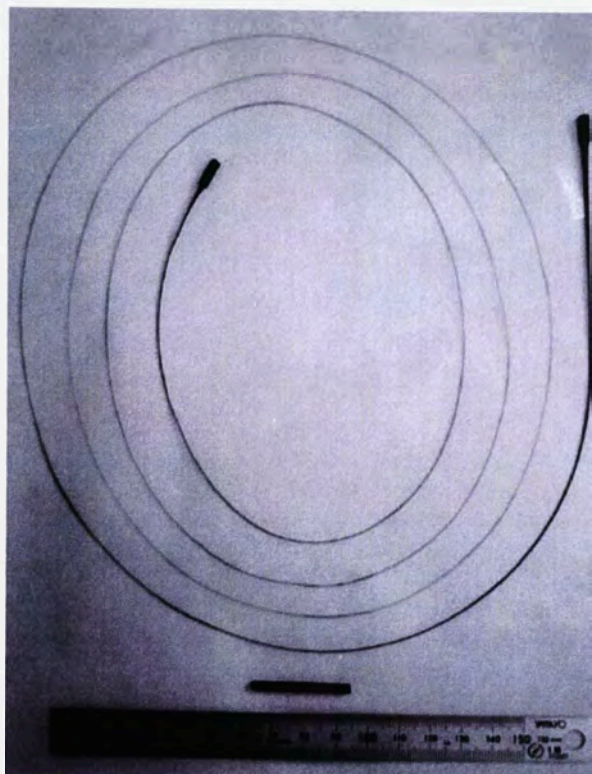


**Figure 2.31:** A  $La_{55}Al_{25}Ni_{20}$  BMG deformed in tension to 20,000% in the SCL region.<sup>[171]</sup>

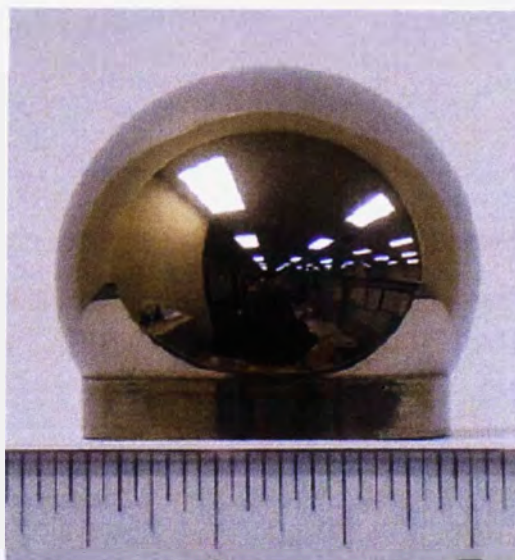


**Figure 2.32:** A  $Zr_{44}Ti_{11}Cu_{10}Ni_{10}Be_{25}$  BMG deformed by ‘blow moulding’ in the SCL region.<sup>[172]</sup>

In studying the formability of BMGs, numerous research groups<sup>[69,173-182]</sup> have reported that when deformed in the SCL region these alloys behave like Newtonian fluids. The achievement of Newtonian flow is an important factor in material formability as it indicates the point at which material flow is homogeneous throughout the entire sample and unaffected by strain rate.



**Figure 2.33** shows the relationship between log flow stress and log strain rate for  $Zr_{65}Al_{10}Ni_{10}Cu_{15}$  ( $T_g = 653$  K)<sup>[175]</sup> and  $La_{55}Al_{20}Ni_{25}$  ( $T_g = 473$  K)<sup>[176]</sup> under uniaxial tension.

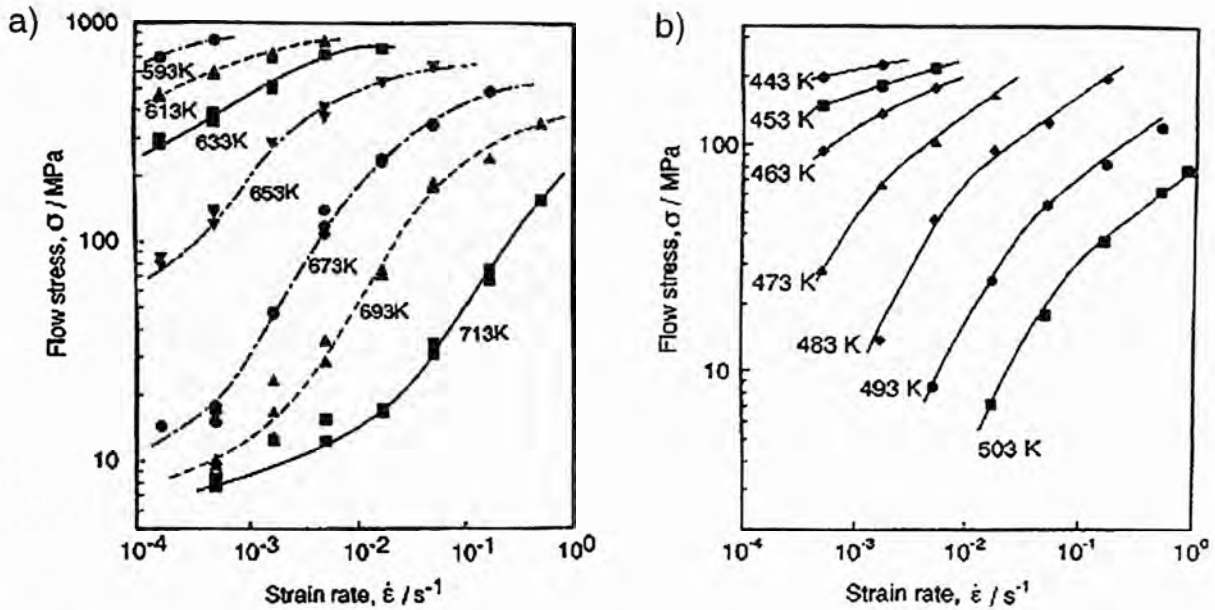


**Figure 2.33:** Relationship between flow stress and strain rate for a)  $Zr_{65}Al_{10}Ni_{10}Cu_{15}$  and b)  $La_{55}Al_{20}Ni_{25}$  BMGs deformed at various temperatures.<sup>[175,176]</sup>

For some portions of these plots it can be seen that flow stress is proportional to strain rate, indicating Newtonian flow conditions. This linear relation between flow stress ( $\sigma_f$ ) and strain rate ( $\dot{\epsilon}$ ) in the SCL region is expressed by:

$$\sigma_f = K\dot{\epsilon}^m \quad (2.30)$$

The slope of the linear relation corresponds to the strain-rate sensitivity exponent ( $m$ ), where an  $m$ -value of unity indicates ideal Newtonian flow, that is, a material that deforms homogeneously and superplastically.<sup>[69,175-179]</sup>

The flow behaviour of a BMG in the SCL region is usually described in terms of a proportionality constant or apparent viscosity,  $\eta$ , using the following relation:<sup>[69,173]</sup>

$$\eta = \frac{\tau}{\dot{\gamma}} \quad (2.31)$$

where  $\tau$  and  $\dot{\gamma}$  are shear stress and shear strain rate respectively.

For uniaxial loading, Eq. (2.29) can be expressed as: <sup>[69,173-178]</sup>

$$\eta = \frac{\sigma_f}{3\dot{\epsilon}} \quad (2.32)$$

where the factor of 3 relates applied uniaxial flow stress  $\sigma_f$  and strain rate  $\dot{\epsilon}$  to the apparent viscosity. As an example, the resulting viscosities of the  $Zr_{65}Al_{10}Ni_{10}Cu_{15}$  and  $La_{55}Al_{20}Ni_{25}$  BMGs are plotted as a function of strain rate in **Figure 2.34**.

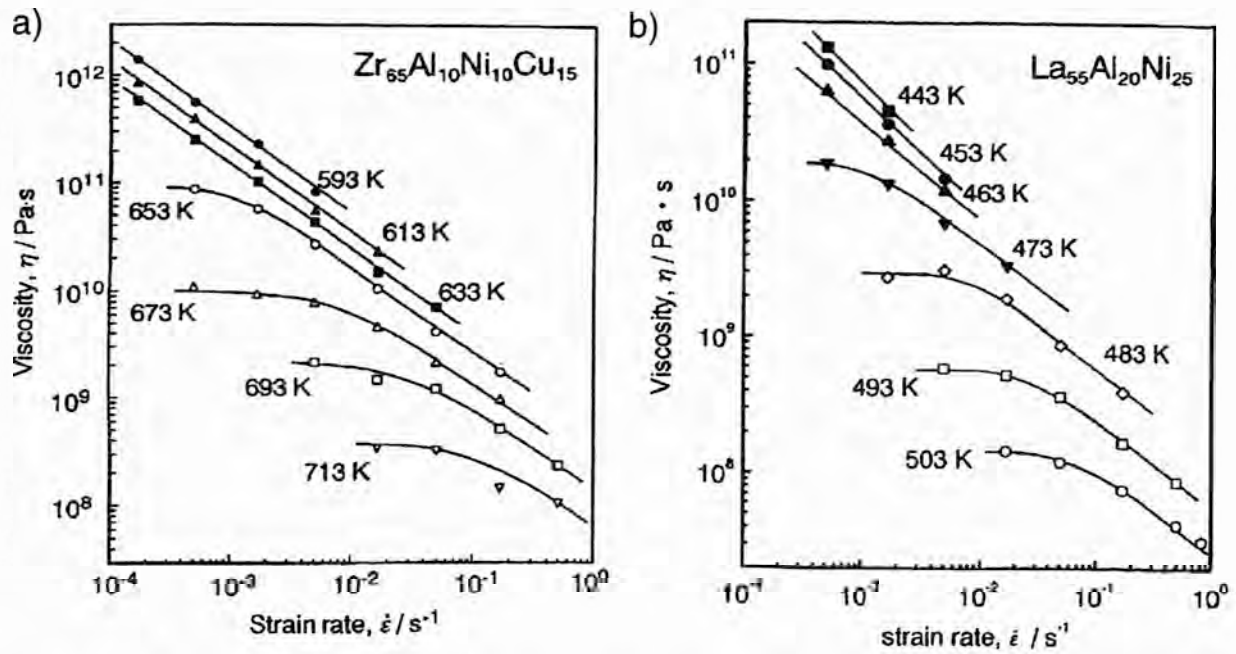


**Figure 2.34:** Viscosity as a function of strain rate for a)  $Zr_{65}Al_{10}Ni_{10}Cu_{15}$  and b)  $La_{55}Al_{20}Ni_{25}$  BMGs deformed at various temperatures. <sup>[175,176]</sup>

**Figure 2.34** shows that the viscosity in the SCL region becomes independent of strain rate (Newtonian) at higher temperatures and lower strain rates. As the strain rate increases, viscosity becomes dependent on strain rate and decreases in a linear fashion (on a log scale), indicating that the deformation mechanism changes from Newtonian to non-Newtonian flow. The independence of viscosity with strain rate is important for practical use when working BMGs in the SCL region.

Two theories discussing the transition from Newtonian to non-Newtonian behaviour have been proposed: one involves the transition state theory of intrinsic plastic flow of glass, <sup>[183]</sup> and the other, with concurrent nanocrystallisation. <sup>[184]</sup> With respect to the latter, Nieh et al. proposed that non-Newtonian behaviour is associated with stress-driven nanocrystallisation during deformation. This suggests that when a metallic glass contains aggregates of nanocrystals



dispersed in an amorphous structure, it deforms superplastically by grain boundary sliding, where the  $m$ -value is expected to be between 0.5 and 1.<sup>[184,185]</sup>

Inoue et al.<sup>[175,176]</sup> attempted to locate the ideal conditions for maximum elongation in BMGs.

**Figure 2.35** shows the relationship between elongation at different test temperatures and strain rate for  $Zr_{65}Al_{10}Ni_{10}Cu_{15}$  and  $La_{55}Al_{20}Ni_{25}$  amorphous alloys, together with data for ductility of the deformed samples. Maximum elongations of ~ 350 % for the Zr-based alloy and 1800% for the La-based alloy were achieved, with both alloys maintaining good bending ductility. These results were found to lie within the SCL region and the strain rate lies within the Newtonian flow region. The decrease in elongation in the lower strain-rate region is believed to be due to the progress of an incipient-stage reaction of crystallisation, while that at the higher strain-rates is believed to result from the rapid increase in flow volume generated during flow deformation.<sup>[175,176]</sup>

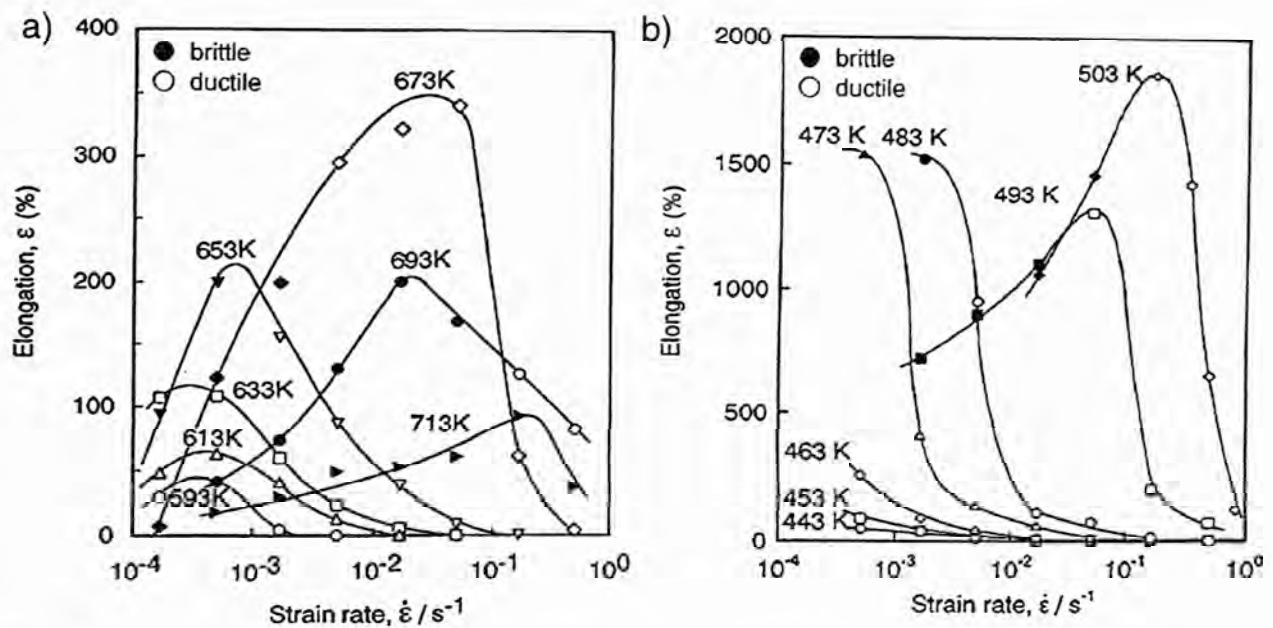


**Figure 2.35:** Relationship between elongation and strain rate for a)  $Zr_{65}Al_{10}Ni_{10}Cu_{15}$  and b)  $La_{55}Al_{20}Ni_{25}$  amorphous alloy ribbons with a thickness of 20  $\mu m$  deformed at various temperatures.<sup>[20]</sup>

Elongation is expected to increase dramatically for BMGs of large cross-sections. It has been reported that elongation reaches about 15,000% for cylindrical specimens of diameter 1.5 mm<sup>[179]</sup> and about 1,000,000% for cylindrical specimens of diameter 5 mm.<sup>[20]</sup> It is also important to note that specimens subjected to heavy tensile deformation also maintain good bending ductility. Deformation data of a range of BMGs in the supercooled liquid region from a number of research groups is given in **Table 2.2**.<sup>[171]</sup>

**Table 2.2:** Deformation data of a range of BMGs in the SCL region. <sup>[171]</sup>

Alloys (in at.%)	$T_g$ (K)	$T_x$ (K)	$m$ value	Ductility <sup>a</sup>
La <sub>55</sub> Al <sub>25</sub> Ni <sub>20</sub>	480	520	1	1800 (T)
Zr <sub>65</sub> Al <sub>10</sub> Ni <sub>10</sub> Cu <sub>15</sub>	652	757	0.8–1.0	340 (T)
Pd <sub>40</sub> Ni <sub>40</sub> P <sub>20</sub>	578–597	651	0.4–1.0	1260 (T)
Zr <sub>52.5</sub> Al <sub>10</sub> Ti <sub>5</sub> Cu <sub>17.9</sub> Ni <sub>14.6</sub>	358	456	0.45–0.55	650 (T)
Zr <sub>55</sub> Cu <sub>30</sub> Al <sub>10</sub> Ni <sub>5</sub>	683	763	0.5–1.0	N/A (C)
La <sub>60</sub> Al <sub>20</sub> Ni <sub>10</sub> Co <sub>5</sub> Cu <sub>5</sub>	451	523	1.0	N/A
Pd <sub>40</sub> Ni <sub>40</sub> P <sub>20</sub>	589	670	0.5–1.0	0.94 (C)
Zr <sub>65</sub> Al <sub>10</sub> Ni <sub>10</sub> Cu <sub>15</sub>	652	757	0.83	750 (T)
Zr <sub>55</sub> Al <sub>10</sub> Cu <sub>30</sub> Ni <sub>5</sub>	670	768	0.5–0.9	800 (T)
Ti <sub>45</sub> Zr <sub>24</sub> Ni <sub>7</sub> Cu <sub>8</sub> Be <sub>16</sub>	601	648	N/A	1.0 (T)
Cu <sub>60</sub> Zr <sub>20</sub> Hf <sub>10</sub> Ti <sub>10</sub>	721	766	0.3–0.61	0.78 (C)
Zr <sub>52.5</sub> Al <sub>10</sub> Cu <sub>22</sub> Ti <sub>2.5</sub> Ni <sub>13</sub>	659	761	0.5–1.0	>1.0 (C)
Zr <sub>41.25</sub> Ti <sub>13.75</sub> Ni <sub>10</sub> Cu <sub>12.5</sub> Be <sub>22.5</sub>	614	698	0.4–1.0	1624 (T)

<sup>a</sup> “T” and “C” stand for tension and compression, respectively.

Both the time and temperature of deformation that generates extremely large elongations in a La<sub>55</sub>Al<sub>20</sub>Ni<sub>25</sub> amorphous alloy have been examined in comparison with the associated isothermal temperature-time-transformation behaviour of the alloy.<sup>[20]</sup> The deformation temperatures and times are located in the higher temperature and longer time region as compared with the onset temperature and time line for crystallisation. It was suggested that this discrepancy indicates that Newtonian flow under appropriate deformation conditions causes a degradation of the crystallisation reaction, namely, deformation-induced stabilisation of the supercooled liquid. The mechanism for this deformation-induced stabilisation is not clear, though it is suggested that it may be due to the suppression of the incipient reaction for crystallisation as well as of the accumulation of flow volumes introduced by non-Newtonian deformation.<sup>[20]</sup>

A common physical-based model for the investigating the deformation behaviour of BMGs in the supercooled region is the free-volume model developed initially for liquids by Cohen and Turnbull<sup>[186,187]</sup> and extended by Spaepen<sup>[180]</sup> for plastic flow of metallic glasses. Free volume is defined as excess volume owing to the disordered state of the atomic configuration, where plastic deformation is attributed to atomic jumps into neighbouring holes or flow defects that exceed a critical size, to accommodate strain.<sup>[180]</sup> Spaepen showed that the flow behaviour of a metallic glass may be given as:<sup>[180]</sup>

$$\dot{\gamma} = \dot{\gamma}_0 \sinh \frac{\tau V}{2k_B T} \quad (2.33)$$

where  $\dot{\gamma}$  the shear strain rate,  $\dot{\gamma}_0$  a frequency factor,  $\tau$  is the shear stress,  $k_B$  Boltzmann's constant, and  $T$  is the absolute temperature.  $V$  is an activation volume, where  $V = \gamma_0 \Omega_f$ .

Here  $\gamma_o$  is the local strain and  $\Omega_f$  the shear site of volume. The steady-state flow stress can be prescribed according to the transition state theory of flow stress originally suggested by Spaepen<sup>[180]</sup>, for uniaxial flow, i.e.:

$$\dot{\epsilon} = \dot{\epsilon}_o \sinh \frac{\sigma_f V}{2\sqrt{3}k_B T} \quad (2.34)$$

where  $\dot{\epsilon}_o$  is a frequency factor, defined as a measure of the effective number of attempts per unit time to overcome a particular energy barrier, and expected to be constant for a given deformation temperature,<sup>[188]</sup>  $\dot{\epsilon}$  the uniaxial strain rate and  $\sigma_f$  the uniaxial flow stress.

### 2.6.5 Corrosion Resistance

The tendency of a metal to passivate depends on alloy composition (electrochemistry of individual atomic species) and solution chemistry. Amorphous alloys consist of chemically homogeneous single-phase solid solutions, which do not contain crystalline defects which can act as nucleation/galvanic sites for corrosion.<sup>[189]</sup> The chemically homogeneous single phase nature of amorphous alloys provides the formation of a uniform passive film without 'weak points' with respect to corrosion.<sup>[189,190]</sup> It has been suggested that, for amorphous alloys exhibiting excellent corrosion properties, the passive films that form are very stable and repassivate quickly if the film is damaged.<sup>[191,192]</sup> The new Fe-based BMGs (or amorphous steel) exhibit non-ferromagnetic properties, contain minimal or zero chromium content, outperform current Naval steels in mechanical properties, and have corrosion resistance comparable to current Naval steels, deeming them more than sufficient for use as practical corrosion resistant materials.<sup>[193]</sup> As a further example, the corrosion resistance of the present Al-based amorphous alloys in HCl and NaOH solutions is about 70 and 240 × respectively, higher than that for conventional high strength Al-based crystalline alloys.<sup>[194,195]</sup> Also, amorphous Al-refractory metal alloys are corrosion resistant in 1 M HCl and amorphous Cr alloys are spontaneously passive in 12 M HCl; these materials show far better corrosion resistance in comparison with their crystalline alloy counterparts. These amorphous Al-refractory metal alloys also have an extraordinarily high hot corrosion resistance. Their sulphidisation resistance at higher temperatures is far higher than any other known metallic materials and their oxidation resistance is comparable to chromia- or alumina-forming alloys.<sup>[196]</sup> It has also been reported that the corrosion loss in a NaCl solution for amorphous Mg-Cu-Ln alloys is about 30% of that for the commercial AZ91 alloy.<sup>[197]</sup>

## 2.7. SUMMARY AND SCOPE OF THESIS

It is clear from published literature, including those presented in **SECTION 2** that there is a distinct lack of research, development and data pertaining to the casting conditions and processes of lightweight BMGs. It is also apparent that, due to the brittle nature of BMGs, the majority of mechanical testing of such materials has been carried out in compression rather than tension. This thesis describes the development of methods for producing lightweight BMG castings of reproducible high quality and the utilisation of these castings to determine both the thermal and elevated temperature tensile properties of such alloys. The experimental work and associated discussion in this thesis is divided into three distinct sections as to show the evolution and development of the methods used in the production of lightweight BMGs.

The first part of the experimental program, **SECTION 3** concentrates on the production techniques and characteristic properties of Mg-based BMGs (specifically  $\text{Mg}_{65}\text{Cu}_{25}\text{Y}_{10}$ ). It presents the evolutionary steps involved in the production of simple gravity cast samples required for initial experimental testing to the development and in house construction of sophisticated injection casting equipment used for the rapid production of  $\text{Mg}_{65}\text{Cu}_{25}\text{Y}_{10}$  BMG samples. This section also describes a novel technique for fabricating tensile specimens from the as-cast alloys which were used for studying elevated temperature deformation behaviour. The data generated from this study was analysed with respect to current flow theory of BMGs.

**SECTION 4** concentrates on the production techniques and characteristic properties of Ca-based BMGs (specifically  $\text{Ca}_{65}\text{Mg}_{15}\text{Zn}_{20}$ ). This section presents further evolution of the techniques and apparatus necessary for producing this type of BMG. Similar to **SECTION 3**, the elevated temperature deformation properties of the  $\text{Ca}_{65}\text{Mg}_{15}\text{Zn}_{20}$  BMG are explored through tensile testing, and the data generated assessed and analysed with respect to current flow theory of BMGs.

A general discussion of the results given in **SECTIONS 3** and **4** is given in **SECTION 5**, which provides a comparison between  $\text{Mg}_{65}\text{Cu}_{25}\text{Y}_{10}$  and  $\text{Ca}_{65}\text{Mg}_{15}\text{Zn}_{20}$  BMGs in terms of glass stability, castability and elevated temperature deformation behaviour with an emphasis on characteristics favourable for industrial-scale component casting and fabrication. This section is followed by the major conclusions of the findings in this thesis.



## SECTION 3 - PRODUCTION AND PROPERTIES OF A MAGNESIUM-BASED BMG

### 3.1. BACKGROUND

Magnesium alloys exhibit the lowest density of all the metallic construction materials. Magnesium is the eighth most abundant element in the earth's crust and the third most plentiful element dissolved in seawater, is of relative low cost to produce and is relatively easy to recycle.<sup>[198]</sup> It is these properties that have sparked recent interest in the utilisation of magnesium-based alloys as a replacement for denser materials. Applications of conventional crystalline magnesium alloys have been limited due to their low mechanical strength, poor ductility, poor ignition and corrosion resistance. Currently, the major processing routes for magnesium alloy components are high-pressure die casting and near-net-shape casting.

Magnesium-based bulk metallic glasses (BMGs) are a relatively new family of materials that exhibit high specific strength at ambient temperature, extraordinary ductility/superplasticity at slightly elevated temperatures, outstanding wear resistance and hardness, superior corrosion resistance to their crystalline counterparts and may be partially crystallised to achieve strength and ductility values higher than that of the completely amorphous structure.<sup>[199]</sup>

The first report of a glass-forming system containing magnesium was discovered by Calka et al. in 1977 by melt spinning Mg-30at%Zn alloy<sup>[9]</sup>. This was followed by similar findings for splat quenched  $\text{Mg}_{81}\text{Ga}_{19}$ <sup>[200]</sup>,  $\text{Mg}_x(\text{Cu})_{9-42}$  and  $\text{Mg}_x(\text{Ni})_{8-25}$ <sup>[201]</sup> binary systems and the ternary Mg–Ni–Ce system.<sup>[202]</sup> Mg-based BMGs with critical thicknesses in the order of millimetres have since been discovered in the Mg–TM–RE (TM = Cu, Ni, Zn; RE = Ce, La, Y, Nd, Ga, Ca),<sup>[42,203-209]</sup> Mg–Cu–Y–M (M = Al, Ag, Zn)<sup>[210-212]</sup> and Mg–Cu–Ag–Pd–Y alloy systems<sup>[213]</sup>.

Magnesium-based BMGs have been produced by both conventional, vacuum and high-pressure die-casting methods. Having a wide supercooled liquid (SCL) region and high glass-forming ability (GFA), these alloys have been cast in sections of 25 mm in diameter for the  $\text{Mg}_{54}\text{Cu}_{26.5}\text{Ag}_{8.5}\text{Gd}_{11}$  BMG alloy<sup>[212]</sup>. It is a known fact that, within the field of amorphous alloys, alloy composition can radically affect the properties of the product, which can be seen in **Table 3.1** for a range of Mg-base BMGs.

**Table 3.1:** Critical thickness and thermal properties of selected Mg-based BMGs.

ALLOY (at.%)	$Z_C$ (mm)	$T_g$ (°C)	$T_X$ (°C)	$\Delta T_X$ (°C)	$T_m$ (°C)	$T_l$ (°C)	$T_{rg}$	REF
Mg <sub>65</sub> Cu <sub>25</sub> Y <sub>10</sub>	4-7*	147	212	65	465	-	0.558	[214]
Mg <sub>57</sub> Cu <sub>30</sub> Al <sub>3</sub> Y <sub>10</sub>	1	142	180	38	452	-	0.572	[128]
Mg <sub>58.8</sub> Cu <sub>30</sub> Al <sub>1.2</sub> Y <sub>10</sub>	2	148	181	33	452	-	0.581	[128]
Mg <sub>65</sub> Cu <sub>20</sub> Zn <sub>5</sub> Y <sub>10</sub>	6	131	183	52	465	-	0.580	[210]
Mg <sub>65</sub> Cu <sub>20</sub> Ag <sub>5</sub> Y <sub>10</sub>	5	151	203	52	414	466	0.590	[211]
Mg <sub>65</sub> Cu <sub>15</sub> Ag <sub>10</sub> Y <sub>10</sub>	6	155	192	41	413	421	0.632	[211]
Mg <sub>65</sub> Cu <sub>15</sub> Ag <sub>5</sub> Pd <sub>5</sub> Y <sub>10</sub>	7	164	199	35	434	-	0.618	[215]
Mg <sub>65</sub> Cu <sub>7.5</sub> Ni <sub>7.5</sub> Ag <sub>5</sub> Zn <sub>5</sub> Y <sub>10</sub>	9	157	186	29	421	455	0.591	[216]
Mg <sub>60</sub> Cu <sub>29</sub> Y <sub>10</sub> Si <sub>1</sub>	1.5	122	166	44	497	-	0.513	[128]
Mg <sub>65</sub> Cu <sub>20</sub> Y <sub>10</sub> B <sub>5</sub>	-	147	197	50	439	463	0.571	[217]
Mg <sub>65</sub> Cu <sub>25</sub> Gd <sub>10</sub>	8	150	211	61	406	467	0.572	[127]
Mg <sub>65</sub> Cu <sub>20</sub> Ag <sub>5</sub> Gd <sub>10</sub>	11	154	192	38	400	422	0.614	[127]
Mg <sub>54</sub> Cu <sub>26.5</sub> Ag <sub>8.5</sub> Gd <sub>11</sub>	<b>25</b>	-	-	-		-		[212]
Mg <sub>65</sub> Cu <sub>20</sub> Ni <sub>5</sub> Gd <sub>10</sub>	5	-	-	61	403	513	0.544	[218]
Mg <sub>75</sub> Cu <sub>15</sub> Gd <sub>10</sub>	2.5	148	179	31	-	460	0.574	[219]
Mg <sub>75</sub> Cu <sub>10</sub> Ni <sub>5</sub> Gd <sub>10</sub>	3	153	197	44	-	499	0.552	[219]
Mg <sub>65</sub> Cu <sub>7.5</sub> Ni <sub>7.5</sub> Ag <sub>5</sub> Zn <sub>5</sub> Y <sub>5</sub> Gd <sub>5</sub>	14	161	199	38	412	446	0.604	[216]
Mg <sub>65</sub> Cu <sub>25</sub> Tb <sub>10</sub>	5	142	210	68	443	460	0.580	[208]
Mg <sub>65</sub> Cu <sub>25</sub> Tb <sub>7</sub> Y <sub>3</sub>	5	143	215	72	444	463	0.580	[208]
Mg <sub>65</sub> Cu <sub>25</sub> Er <sub>10</sub>	3	149	207	58	468	493	0.570	[220]
Mg <sub>65</sub> Cu <sub>15</sub> Ag <sub>10</sub> Er <sub>10</sub>	6	154	192	38	433	560	0.610	[220]
Mg <sub>57</sub> Cu <sub>31</sub> Y <sub>6.6</sub> Nd <sub>5.4</sub>	14	154	218	64	434	505	0.549	[221]
Mg <sub>70</sub> Ni <sub>15</sub> Nd <sub>15</sub>	1.5	194	216	22	469	571	0.650	[221]
Mg <sub>75</sub> Ni <sub>15</sub> Nd <sub>10</sub>	2.8	177	197	20	444	516	0.630	[222]
Mg <sub>65</sub> Ni <sub>20</sub> Nd <sub>15</sub>	3.5	186	228	42	470	531	0.630	[222]
Mg <sub>70</sub> Zn <sub>25</sub> Ca <sub>5</sub>	3	<b>125</b>	135	10	398	-	0.590	[42]
Mg <sub>67.5</sub> Zn <sub>27.5</sub> Ca <sub>5</sub>	4	133	145	12	375	-	0.628	[42]

**Key**

$Z_C$  = Critical Thickness,  $T_g$  = Glass Transition Temperature,  $T_X$  = Crystallisation Temperature,  $\Delta T_X$  = Supercooled Liquid Region,  $T_m$  = Melting Temperature,  $T_l$  = Liquidus Temperature,

The material chosen for study in this part of the thesis was the  $\text{Mg}_{65}\text{Cu}_{25}\text{Y}_{10}$  BMG, as it is a well known glass former, has a large, experimentally accessible supercooled liquid region and relatively low density compared to other BMG systems.

### 3.2. ALLOY PREPARATION

The starting materials used in preparing the  $\text{Mg}_{65}\text{Cu}_{25}\text{Y}_{10}$  alloy were high purity metals: magnesium (99.9 wt.%), copper (99.9 wt.%) and yttrium (99.999 wt.%). Considering that the melting points of Cu (1065 °C) and Y (1522 °C) are well above that of Mg (650 °C) and holding Mg at high temperatures results in evaporation (due to the low vapour pressure of this metal) and possible oxidation, it was decided that the nominal alloy composition be reached by preparing a Cu-Y master alloy. The composition of this master alloy was calculated to be  $\text{Cu}_{71.43}\text{Y}_{28.57}$  at.% (as indicated in **Figure 3.1**) based on the ratio of Cu to Y present in the nominal  $\text{Mg}_{65}\text{Cu}_{25}\text{Y}_{10}$  alloy. Appropriate amounts of Cu and Y were prepared to give a total mass of 20g of the desired composition. The base elements were arc melted using a tungsten electrode under the protection of varigon (5 vol.%  $\text{H}_2$  in Ar) gas mixture to give 20g buttons of  $\text{Cu}_{71.43}\text{Y}_{28.57}$  alloy. These buttons were remelted four times to generate a homogeneous alloy and were subsequently mechanically polished to remove surface scum and oxide.

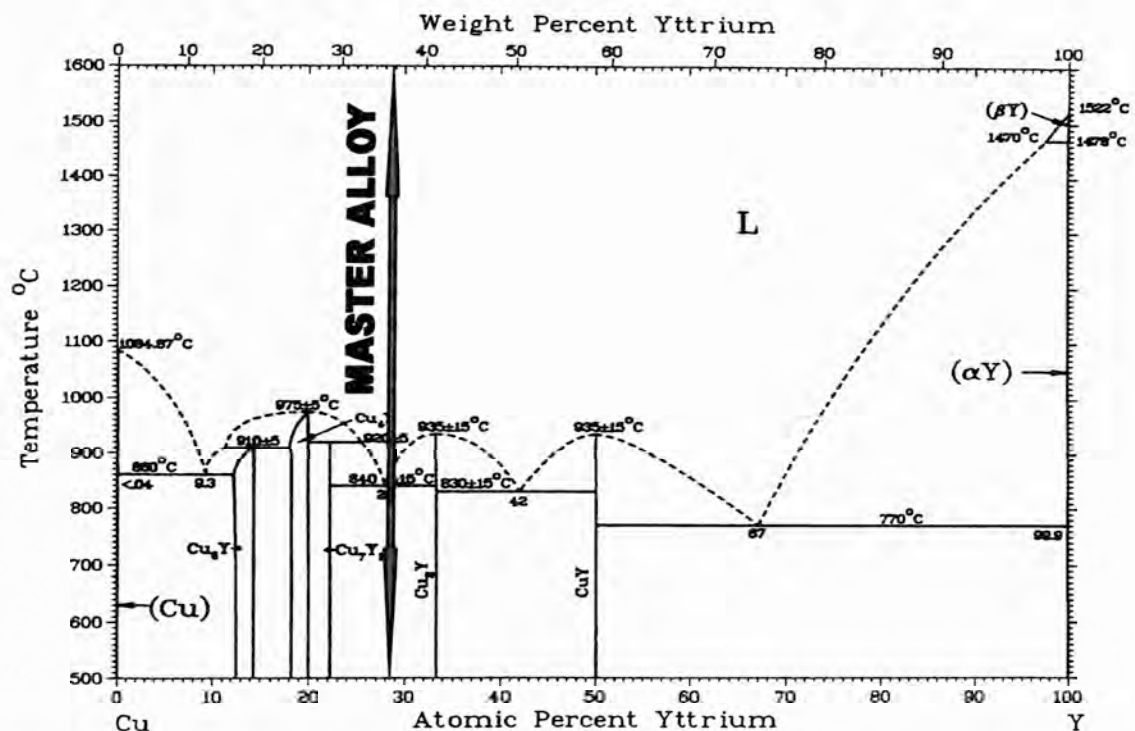


**Figure 3.1:** Equilibrium phase diagram of the Cu-Y system, indicating the location of the  $\text{Cu}_{71.43}\text{Y}_{28.57}$  at.% master alloy.<sup>[223]</sup>



The appropriate amount of magnesium was also mechanically cleaned and placed in boron nitride-coated graphite crucible. A boron nitride coating was used as it is considered inert in molten magnesium, and also creates a barrier between the melt and the reactive graphite crucible. A graphite crucible was used for improving the ease of removal of residual charge material from the melting vessel and due to its high thermal conductivity compared to other ceramic crucible materials. This crucible was then placed in a sealed 316 stainless steel chamber. Argon of 99.997 vol.% purity was circulated through the melting vessel at a rate of 80 cm<sup>3</sup>/min for protecting the charge from oxidation during each melting cycle. The charge temperature was measured using a K-type thermocouple inserted into a 316 stainless steel sheath incorporated into the lid of the melting vessel. Where this stainless steel sheath was in the vicinity of the melt, it was covered with a boron nitride-coated graphite sheath, as to aid with the removal of the vessel lid and clean up.

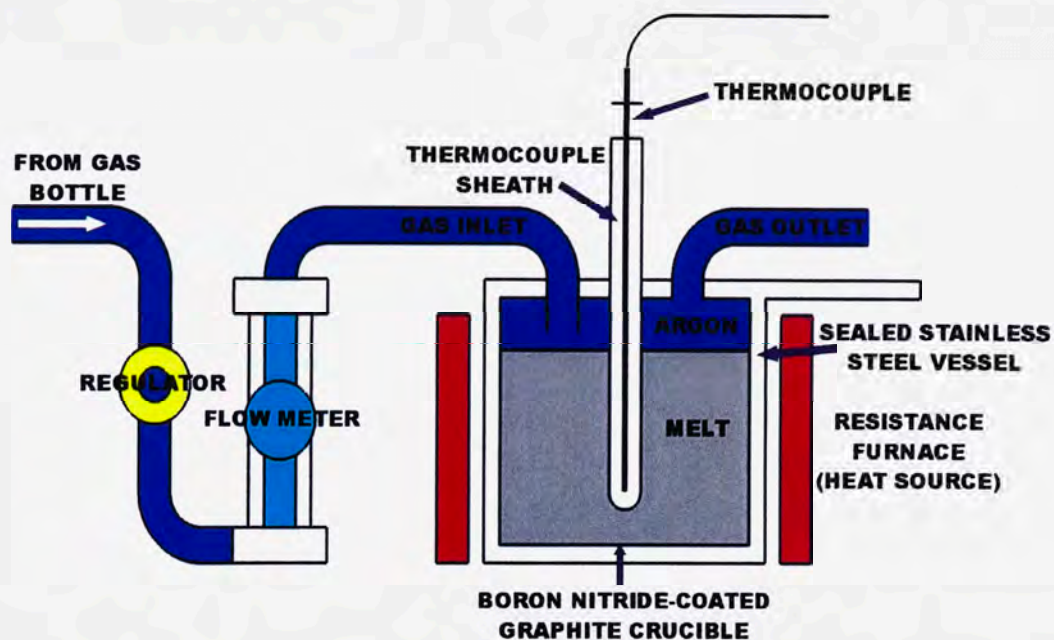


**Figure 3.2:** Schematic representation of the equipment used to prepare the  $Mg_{65}Cu_{25}Y_{10}$  alloy under a protective atmosphere.

The charge was heated to a temperature of 850 °C using a LABEC HTF90 resistance furnace for melting the  $Cu_{71.43}Y_{28.57}$  master alloy (eutectic temperature 840°C). The appropriate amount of  $Cu_{71.43}Y_{28.57}$  master alloy was added to the melt in a stepwise manner, stirring with a tungsten rod after each addition until completely dissolved to produce the final composition. The melt was then cooled to the desired casting temperature, shaken immediately prior to casting, then cast into the desired mould in an argon-flushed atmosphere, provided by an auxiliary argon line.



### 3.3. DETERMINATION OF CRITICAL THICKNESS, COOLING RATE AND THERMAL PROPERTIES OF THE $\text{Mg}_{65}\text{Cu}_{25}\text{Y}_{10}$ BMG

To determine the critical thickness ( $Z_C$ ) and the critical cooling rate ( $R_C$ ) of the  $\text{Mg}_{65}\text{Cu}_{25}\text{Y}_{10}$  alloy, a copper wedge mould, similar to that used by Inoue et al.<sup>[224]</sup> was constructed. This mould consists of two 25 mm thick copper plates, with a cavity of length 100 mm, width 40 mm and a maximum thickness of 10 mm (**Figure 3.3**). This allowed a wide range of cooling rates to be achieved. The mould was configured with thermocouple entry points for enabling the measurement of cooling rates at three individual positions. **Figures 3.3** and **3.4** show the position of each thermocouple within the mould. As shown in **Figure 3.4**, the surface of the cavity was polished using BRASSO® metal polish, aiding removal of the cast sample from the mould and for suppressing grain nucleation at the mould walls.

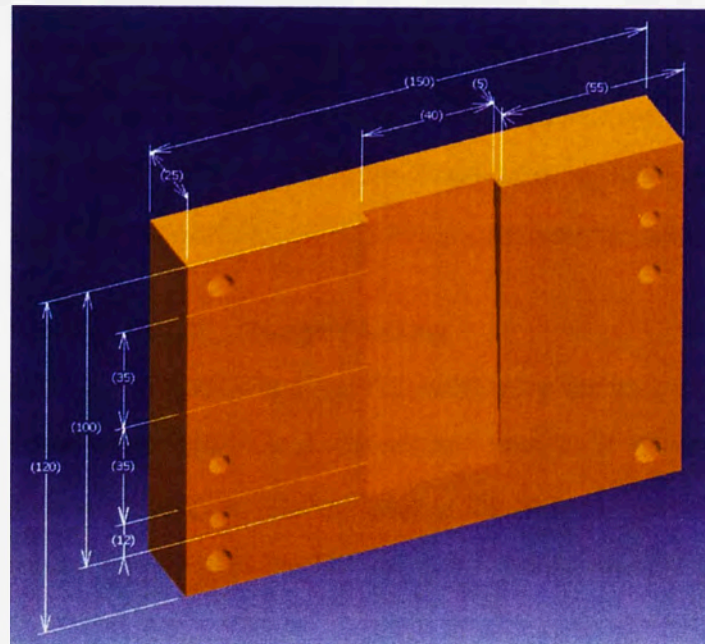


**Figure 3.3:** Schematic diagram showing half of the copper wedge mould (dimensions in mm).

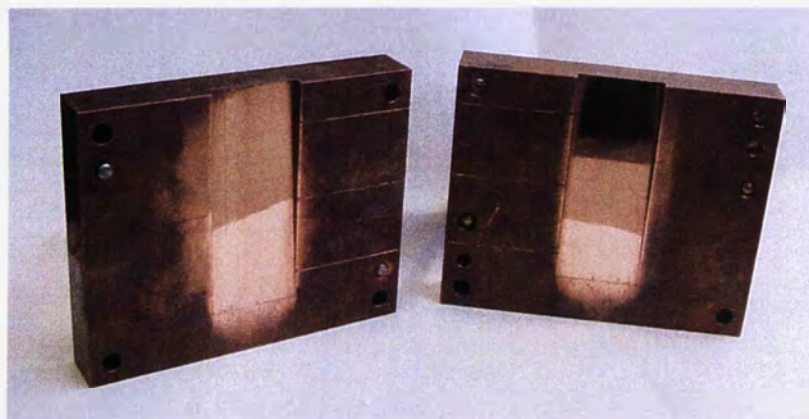


**Figure 3.4:** The wedge mould showing the 40 mm wide, 100 mm deep wedge with base of 10 mm, the highly polished mould cavity walls and thermocouple entry points.



### 3.3.1 Experimental Procedure

For the determination of critical thickness and cooling rate, the  $\text{Mg}_{65}\text{Cu}_{25}\text{Y}_{10}$  alloy was prepared by the method described in SECTION 3.2. Three 0.02mm K-type thermocouple wires were attached to the copper mould within the casting cavity at 12, 47 and 82mm from the wedge tip. The  $\text{Mg}_{65}\text{Cu}_{25}\text{Y}_{10}$  alloy melt was cooled to a temperature of 600 °C in the original boron nitride-coated graphite crucible under circulating argon and removed from the resistance furnace. The molten metal was hand poured into the copper wedge mould under an argon gas stream. Temperature data was gathered at time increments of 0.01 s using a DT800 dataTaker data logging unit. The mould was then separated and the wedge sample removed for further analysis. The wedge casting (**Figure 3.5**) was set in resin at room temperature so as not to crystallise any amorphous sections of the sample. The casting was then sectioned at various thicknesses and ground down to its centre so that the centre of the sample (the last portion of the sample to solidify) could be characterised with respect to an amorphous structure. Samples were analysed for amorphicity using a Phillips X'PERT MRD X-Ray Diffractometer and CuK $\alpha$  radiation (XRD). In order to determine the thermal properties of the alloy, sections of the wedge determined to be amorphous by XRD were examined using a TA 2010 differential scanning calorimeter (DSC) at various heating rates.

### 3.3.2 Evaluation of the $\text{Mg}_{65}\text{Cu}_{25}\text{Y}_{10}$ Wedge Casting

Attempts at producing an amorphous  $\text{Mg}_{65}\text{Cu}_{25}\text{Y}_{10}$  sample by conventional gravity casting in a copper wedge mould were successful and an as-cast sample is shown in **Figure 3.5**. The appearance of both the external and fracture surfaces of the as-cast wedges were highly reflective in the amorphous regions. The samples themselves were quite brittle and some shattered in the mould upon cooling or removal due to internal stresses related to rapid solidification.<sup>[225]</sup>

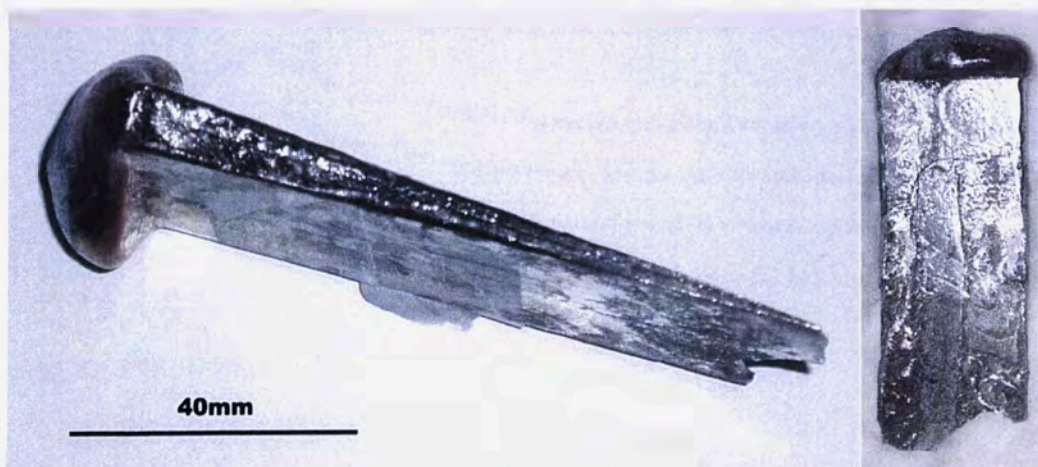


**Figure 3.5:** A  $\text{Mg}_{65}\text{Cu}_{25}\text{Y}_{10}$  gravity cast wedge to be sectioned and analysed for amorphicity.



The composition of the as-cast bars was determined using electron probe microanalysis (EPMA) and found to be  $\text{Mg}_{65}\text{Cu}_{25}\text{Y}_{10}$  (+/- 0.81at.% maximum for each element). The degree of crystallinity of the sample sections was characterised with an X-Ray Diffractometer using  $\text{CuK}\alpha$  radiation. The XRD traces for the given wedge thickness can be seen in **Figure 3.6**. A completely amorphous structure was generated within the wedge at a thickness of 3 mm, given by the characteristic broad amorphous crest and the absence of sharp crystalline peaks. Sections above this thickness were observed to have a partially crystalline interior and an amorphous outer region at the mould walls. This XRD data indicates that the critical thickness  $Z_C$  of the amorphous  $\text{Mg}_{65}\text{Cu}_{25}\text{Y}_{10}$  alloy for this particular casting procedure falls within the range 3 to 3.75 mm. To determine the characteristic thermal properties of the alloy, DSC was used to determine  $T_g$  (glass transition temperature),  $T_x$  (onset crystallisation temperature),  $T_m$  (alloy melting temperature) and  $T_l$  (alloy liquidus temperature). Isochronal DSC scans were carried out at heating rates ranging from 2 to 20 °C/min. It is pertinent to note that the majority of reported vales for the thermal properties of BMGs are quoted at a heating rate of 20 °C/min. The DSC results for the present work at a heating rate of 20 °C/min are shown in **Figure 3.7**.

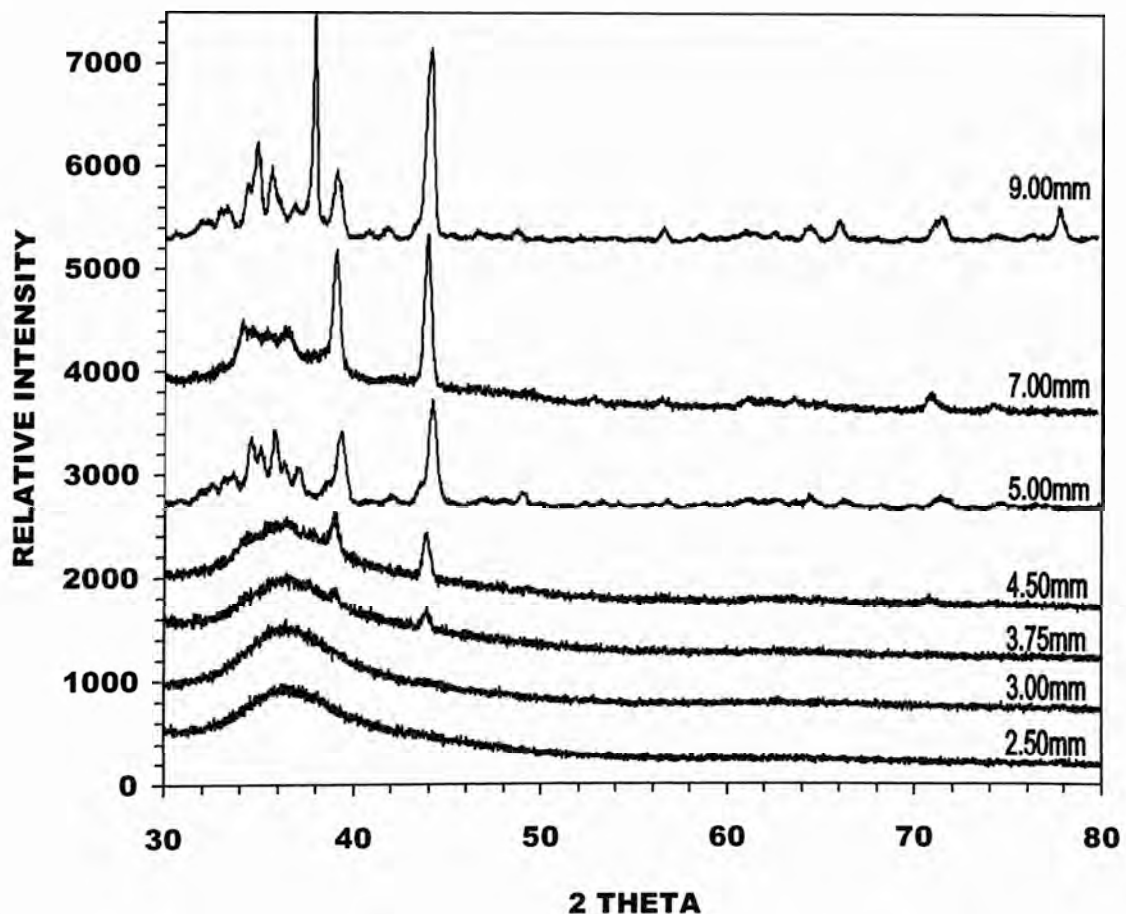


**Figure 3.6:** X-ray diffraction traces taken at various section thicknesses of the wedge casting.

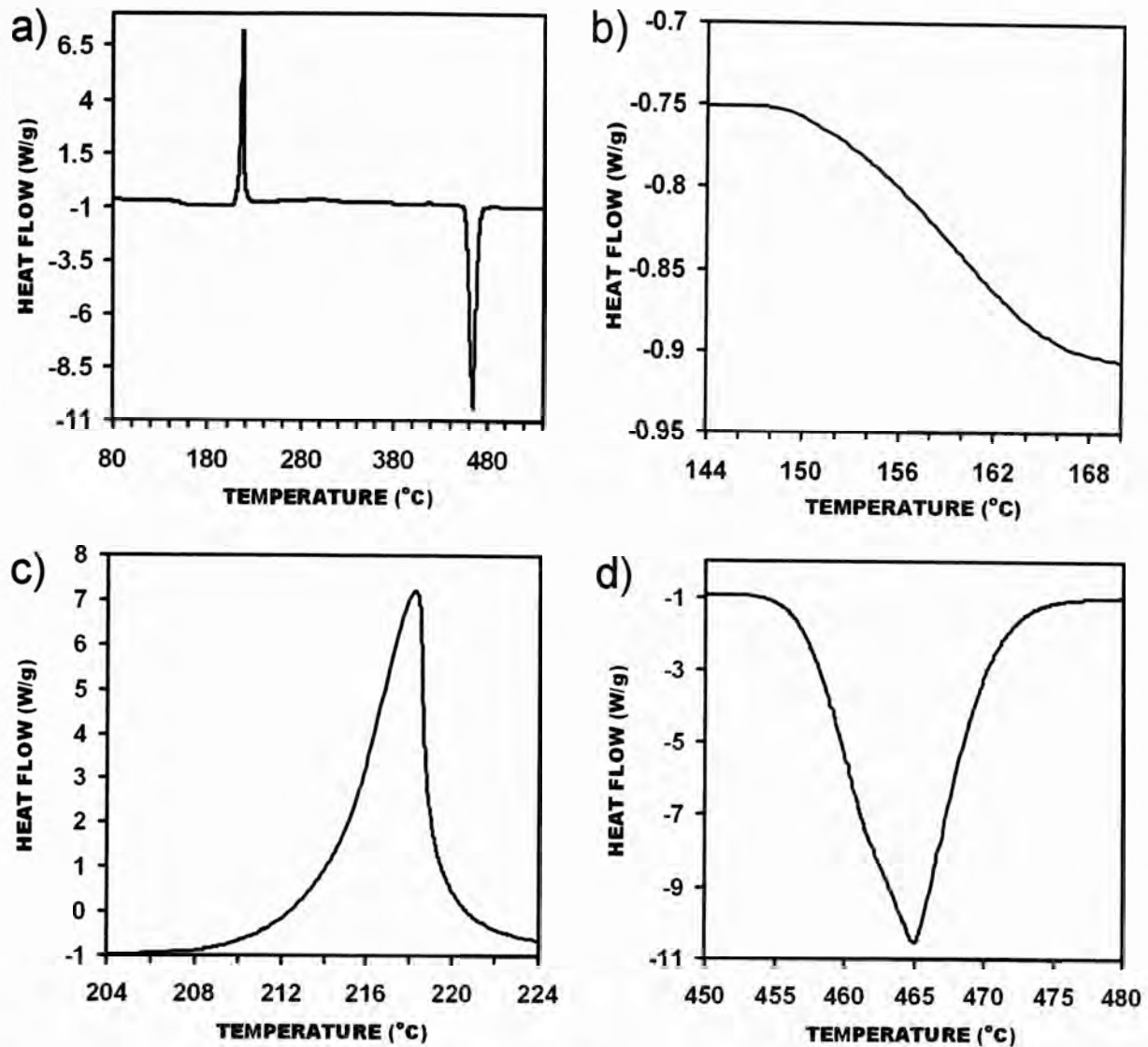


**Figure 3.7:** DSC results at a heating rate of 20 °C/min for gravity cast  $Mg_{65}Cu_{25}Y_{10}$  bulk metallic glass cast at 600 °C including: a) Complete DSC curve; b) magnification of  $T_g$  region; c) magnification of  $T_x$  region, and d) magnification of  $T_m$  and  $T_l$  region.

Like other amorphous materials, the glass transition (endothermic phenomenon) does not occur at a certain temperature, and is heating rate dependent.<sup>[60]</sup> For the present alloy, the temperature range was ~ 12 °C for heating rates in the range 2 to 20 °C/min. At a heating rate of 20 °C/min,  $T_g$  starts at 148 °C and is completed at 168 °C. The value of  $T_x$ , which is usually taken as a tangent to the crystallisation curve generates a value of ~213 °C (these values are similar to those reported by Inoue et al.<sup>[214]</sup>, as shown in **Table 3.1**), although it can be seen that the absolute starting point of the crystallisation reaction begins much earlier at around 206 °C. By definition, we have  $\Delta T_x = T_x - T_g$ , and these results yield a SCL region of ~ 65 °C.  $T_m$  and  $T_l$  were determined to be 453 °C and 480 °C respectively, which do not vary with heating rate. **Figure 3.8** shows the dependency of both  $T_g$  and  $T_x$  on heating rate. This data is analogous to Eq. (2.9), a variant of the VFT equation which combines the kinetics of glass transition to the equilibrium viscosity, both of which may be related glass stability/fragility.<sup>[60]</sup>



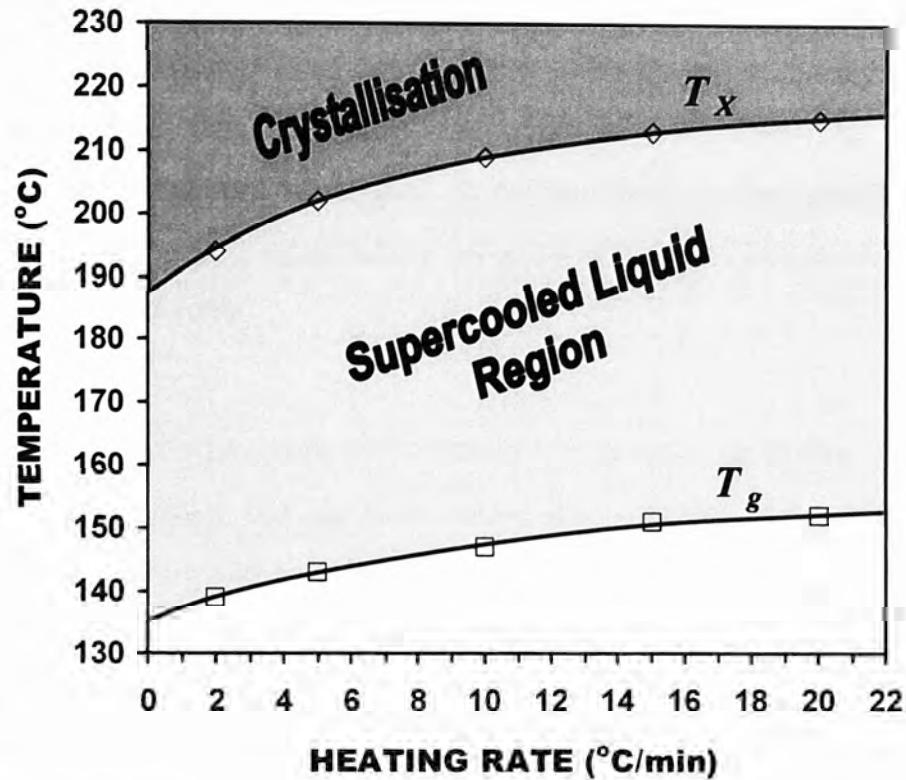


**Figure 3.8:** Results for  $T_g$  and  $T_X$  determined by DSC at heating rates from 2 to 20 °C/min for the  $Mg_{65}Cu_{25}Y_{10}$  alloy.

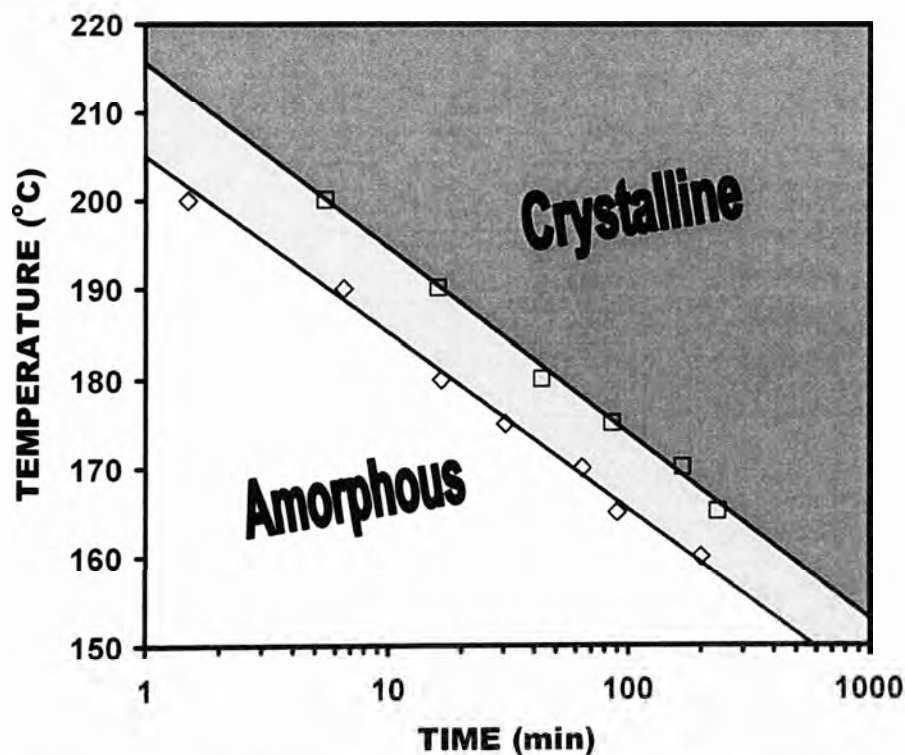


**Figure 3.9:** Time-Temperature-Transformation diagram for the transition from the non-equilibrium amorphous phase to the equilibrium crystalline structure for the  $Mg_{65}Cu_{25}Y_{10}$  alloy.

It can be seen in **Figure 3.8** that both  $T_g$  and  $T_X$  increases with increasing heating rate, with the crystallisation temperature affected more greatly, which, in turn yields a larger SCL region,  $\Delta T_X$ , suggesting that higher heating rates would prove more beneficial for hot working these materials. In conjunction with this work, isothermal annealing DSC was carried out at temperatures ranging from 160 °C to 200 °C to determine the allowable time frame for deformation/working in the SCL region before the onset of crystallisation and to provide insight into the kinetics of crystallisation.

**Figure 3.9** shows a Time-Temperature-Transformation diagram generated using isothermal annealing data. It is evident that the data follows an Arrhenius type trend, typical of the crystallisation reaction shown by Eq. (2.3),<sup>[57,58]</sup> where temperature plays a leading role in the nucleation rate and in accordance with Eq. (2.11)<sup>[110-113]</sup> and (2.12)<sup>[110-113]</sup>, depicting the rate of growth of these crystalline phases.

Using temperature/time data acquired by the three thermocouples in the wedge casting, three cooling curves were extrapolated from the casting temperature of 600 °C to the equilibrium mould temperature, which can be seen in **Figure 3.10**.

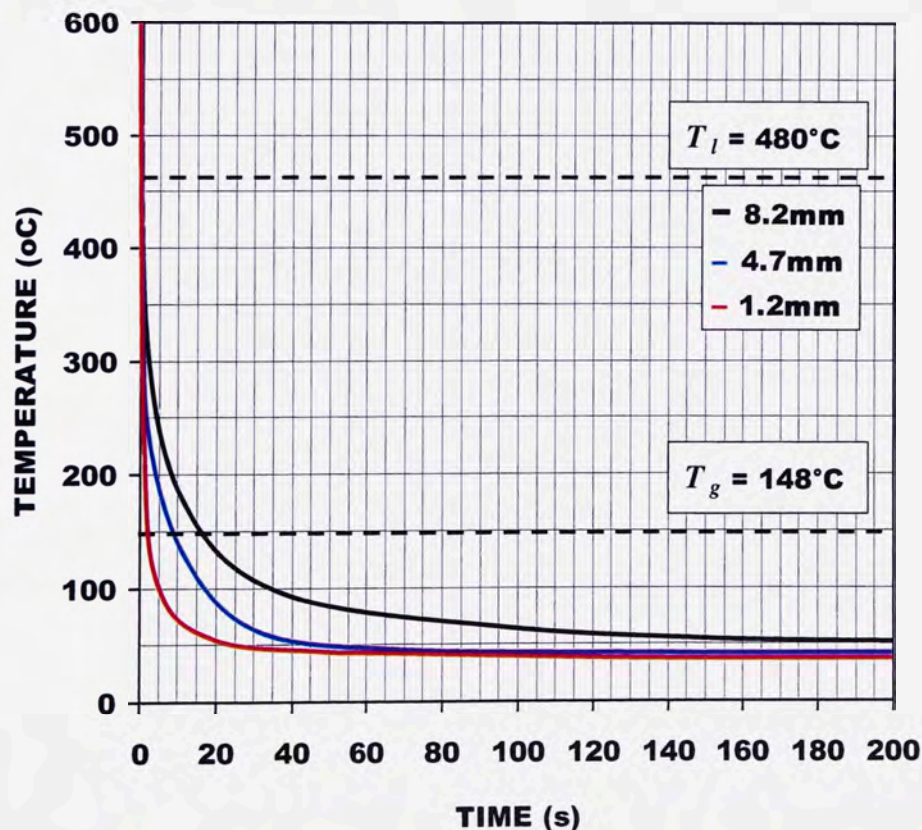


**Figure 3.10:** Cooling rate data from three K-type thermocouples in the wedge casting.

The critical cooling rate is defined as the minimum cooling rate required to supercool a liquid metal (amorphous structure) to a temperature at which atoms cannot rearrange themselves to form a crystalline structure, i.e. the cooling rate for the interval between  $T_l$  and  $T_g$ .<sup>[118,226]</sup> From this data, average cooling rates were determined at wedge thicknesses ( $Z$ ) of 1.2, 4.7 and 8.2 mm using the relation:<sup>[226,227]</sup>

$$\frac{dT}{dt} = \frac{T_l - T_g}{\Delta t} \quad (3.1)$$

where  $\Delta t$  is the time interval between  $T_l$  and  $T_g$ . An example of this determination and an enlarged figure of the region of interest between  $T_l$  and  $T_g$  is given in **APPENDIX A**. From these cooling rates, a master cooling rate curve was developed with respect to  $Z$  and is shown in **Figure 3.11**.

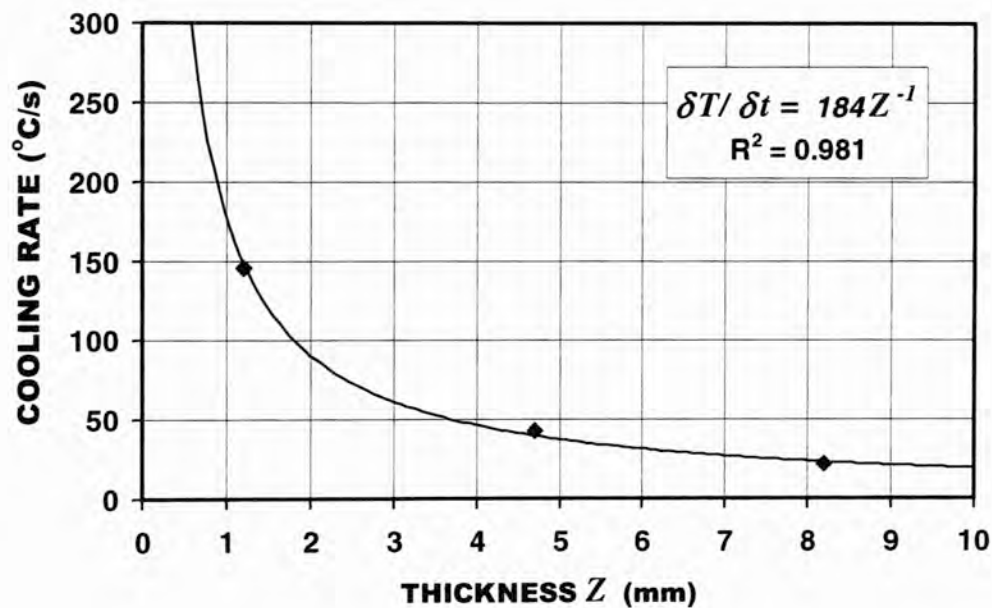


**Figure 3.11:** Calculated cooling rate data as a function of wedge thickness.

From this curve, it was determined that the cooling rate of the  $\text{Mg}_{65}\text{Cu}_{25}\text{Y}_{10}$  alloy during cooling from the liquidus temperature (480 °C) to the glass transition temperature (148 °C) can be approximately given by:

$$\frac{dT}{dt} \approx \frac{184(^{\circ}\text{C s}^{-1} \text{ mm}^{-1})}{Z(\text{mm})} \quad (3.2)$$



When molten metal is cooled in a cold metal mould of high thermal conductivity, heat flow is controlled by the interfacial resistance at the mould-metal interface.<sup>[228,229]</sup> The mould, being assumed to be infinite in extent remains at its original equilibrium temperature  $T_{MOULD}$  and the entire decrease in temperature is across the mould-metal interface. The total quantity of heat  $Q$  that transfers across the mould-casting interface in a time interval  $t$  is given by:<sup>[228,229]</sup>

$$Q = hA(T_{CAST} - T_{MOULD})t \quad (3.3)$$

where  $h$  is the interfacial heat transfer coefficient,  $A$  is the area of the interface and  $T_{CAST}$  and  $T_{MOULD}$  the casting and mould temperature, respectively. Now, the amount of heat present in a given volume of metal can be given by:<sup>[230]</sup>

$$Q = T_{CAST}VC_p\rho \quad (3.4)$$

where  $V$  is the volume of metal present in the mould,  $C_p$  the heat capacity and  $\rho$  the density of the metal. For descriptive purposes, the latent heat of fusion has been neglected as the quantity of material crystallising in the sample is unknown and the transition from liquid to supercooled liquid or an amorphous structure cannot be described by regular fusion. By combining Eqs. (3.3) and (3.4), and differentiating with respect to temperature and time generates:<sup>[231]</sup>

$$\frac{dT}{dt}VC_p\rho = -hA(T - T_{MOULD}) \quad (3.5)$$

Considering we are dealing with one half of the casting (as there is a mould interface where heat is being removed on both sides of the plate, we can apply Eq. (3.5) to the case of unidirectional cooling, where  $V/A = Z/2$ , ( $Z$  being the casting thickness), it can be seen that:

$$\frac{dT}{dt} = \frac{-2h(T - T_{MOULD})}{ZC_p\rho} \quad (3.6)$$

If it is assumed that  $h$ ,  $C_p$  and  $\rho$  are essentially constant for a given temperature interval, the rate of cooling is given as:

$$\frac{dT}{dt} \approx \frac{B}{Z} \quad (3.7)$$

where  $B$  is constant.



Equation (3.7) corresponds directly to the results shown in **Figure 3.11** and Eq. (3.2). Using this equation the approximate critical cooling rate range  $R_C$  of the amorphous  $Mg_{65}Cu_{25}Y_{10}$  alloy may be determined. Since the critical amorphous thickness lies between 3.0 and 3.75 mm for the current laboratory set up, the critical cooling rate range is 61.3 to 49.1 K/s which will lie within the range of reported cooling rate values of 50 to 100 °C/s.<sup>[60,232]</sup>

### 3.4. GRAVITY CASTING INTO A COPPER PLATE MOULD

Once the critical amorphous thickness was determined using samples produced with the copper wedge mould, a second copper plate mould was manufactured from 25 mm thick copper plates (**Figure 3.12** and **3.13**), along with a series of spacing shims (0.1, 0.5 and 1 mm) in an attempt to generate large flat samples of various thicknesses suitable for mechanical testing.

#### 3.4.1 Experimental Procedure

The molten metal was prepared with the method described in **SECTION 3.2** and poured by hand into the riser (funnelled section) of the plate mould under an argon-flushed atmosphere. The mould riser section was coated with boron nitride, which provided an insulating barrier for avoiding premature solidification in this region. Casting was carried out to generate plate sample thicknesses of 2-3 mm. A large number of casting temperatures and cavity venting configurations were investigated, as well as pre-heating of the mould in an attempt to fill the entire mould cavity. The degree of crystallinity of sections of the as-cast samples were analysed by XRD.

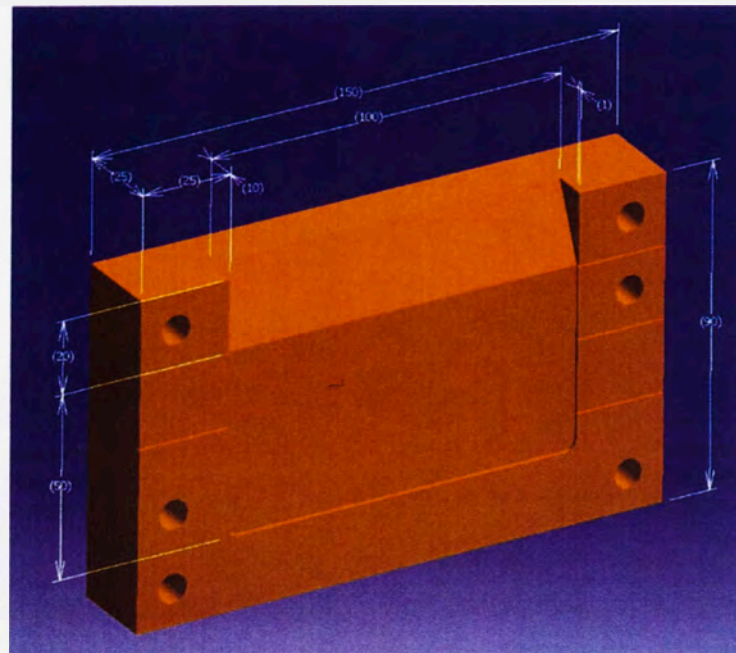


**Figure 3.12:** Schematic diagram of the copper plate mould showing cavity size and dimensions.



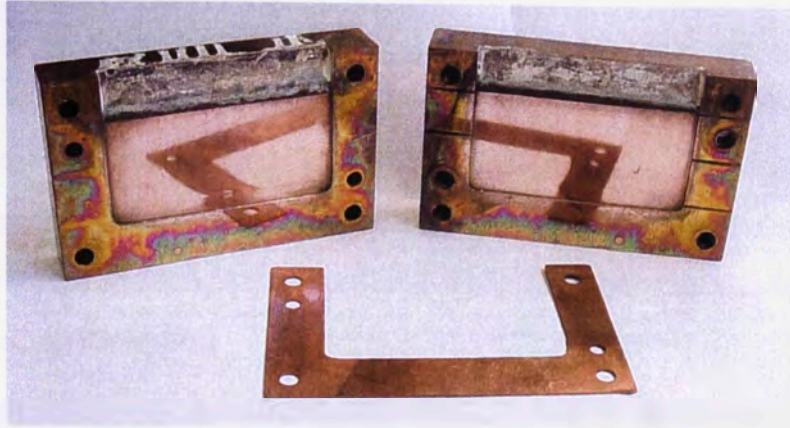


**Figure 3.13:** The copper plate mould with a 1 mm shim. Note the boron nitride coating on the riser (funnel region) and the polished surface finish of the mould walls.

### 3.4.2 Evaluation of the $\text{Mg}_{65}\text{Cu}_{25}\text{Y}_{10}$ Plate Casting

The production of plate material suitable for mechanical testing was partly successful. However, due to the high cooling rates, complete filling of the mould cavity was not possible, as depicted in **Figure 3.14a)**. As a result, casting sections of irregular shape were generated (**Figure 3.14b)**). Similar to the wedge shaped castings, there was the inherent problem of internal stresses within the as-cast samples during rapid cooling which resulted in spontaneous cracking of the castings. Such a phenomenon has been observed in other BMG systems in the production of large plates<sup>[225]</sup> Based on these results, it is almost impossible to generate large flat plate samples of the  $\text{Mg}_{65}\text{Cu}_{25}\text{Y}_{10}$  BMG by conventional gravity casting.

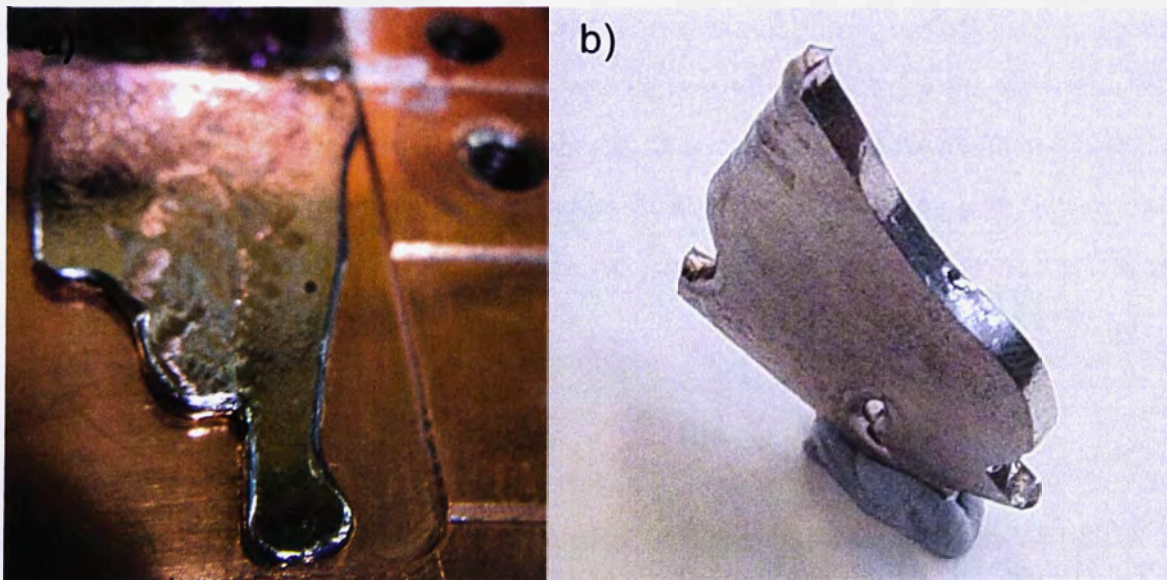


**Figure 3.14:** a) Photograph depicting the incomplete filling of the mould cavity and b) an irregular shaped amorphous shard of 3mm thickness produced using the copper plate mould.



Stable sections of these irregular shaped castings were fashioned into regular shapes ready for further preparation or testing. In an attempt to produce standard tensile specimens, plate material was cut in the appropriate profile using a water jet cutter. As can be seen in **Figure 3.15**, this method of preparing tensile test pieces resulted in a poor surface finish, which in some cases degraded the structural integrity of the sample and the cut on a tapered edge producing a non-uniform cross section. Both of these defects generated samples that were not suitable for reliable tensile testing.



**Figure 3.15:** A tensile specimen of 3mm thickness produced by water jet cutting.

### **3.5. DEVELOPMENT OF THE INVERTED INJECTION DIE CASTING TECHNIQUE FOR THE PRODUCTION OF BMG SAMPLES**

Due to the substantial difficulties associated with conventional gravity casting for the production of high quality BMGs, a program of research was carried out to develop a die casting facility for consistent production of large amounts of material. This method of casting was selected due to its likelihood for producing high quality samples of a range of desirable geometries that are needed to reduce material wastage due to overflowing moulds, large runner/gating configurations and irregular casting shapes.

#### **3.5.1 Background Work**

Preparing BMG samples from the melt by injection die casting is common among research groups. It is usually carried out by applying a positive pressure, either by a mechanical plunger or a gas over pressure to force molten metal through a small hole into a mould. According to published data, the resulting specimens produced by this route are of reasonable structural

integrity and can be formed in numerous alloy systems in various geometric configurations. A schematic representation of the casting equipment was given in **Figure 2.19b**)<sup>[138]</sup> which is typical of that used for die casting of BMG components.

When injecting molten metal through a small hole or nozzle, in a downward direction, it is inevitable that gravity will play a roll in the destabilisation of the metal flow front on its approach to the mould. It is also likely that the stream of molten metal will be considerably narrower than the pattern in the mould. This type of set up can only begin to fill the mould after it has hit a wall within the mould, which in turn creates numerous amounts of new reflection flow fronts within the mould. In effect, the molten metal stream must 'back fill' the mould. In regular die casting, this is not a major problem as cooling rates are quite low. However, when casting into a copper mould where cooling rates are high, the molten metal stream may not have time to entirely 'back fill' the mould cavity, thereby generating defects such as voids and cold shuts.

To avoid these foregoing casting problems, a completely new type of casting technique, specific to BMGs, was designed in this thesis. It is a low-pressure injection die caster that uses compressed argon gas to force molten metal through a silica tube into a copper mould. A schematic representation of a prototype system is shown in **Figure 3.16**. There are several advantages in using this injection configuration over conventional casting systems for the production of BMGs. The 'upside down' (inverted) casting configuration was proven to be advantageous as it negates the need for tipping the crucible or the presence of a valve or plug in the bottom of the melting crucible for the release of molten metal into the mould. By forcing molten metal up the silica tube into the mould, it is possible to utilise the positive effects of surface tension and gravity to naturally stabilise the metal flow front on its approach to the mould, as opposed to injecting the melt in a downward stream. There is also the benefit of taking a sample from the centre of the melt, as opposed to sampling from the top of the melt when pouring or from the bottom when using a plug or valve. There are also no valve or plug blockage complications with this method of casting. It is also pertinent to note that the diameter of the silica tube used to transport the metal into the mould is larger than that of the pattern being generated in the mould. Hence, the cross section of the flow front is always decreasing, as compared to the use of a small diameter stream of molten metal to fill a larger cross section cavity, where the metal stream must 'back fill' the mould cavity which was found to lead to cold shuts or incomplete cavity filling at the cavity entrance. Furthermore, the



'nozzle' as such, which is the final reduction in cross-section as the liquid metal approaches the mould pattern is actually incorporated in the mould pattern for providing a smooth transition into the final geometry.

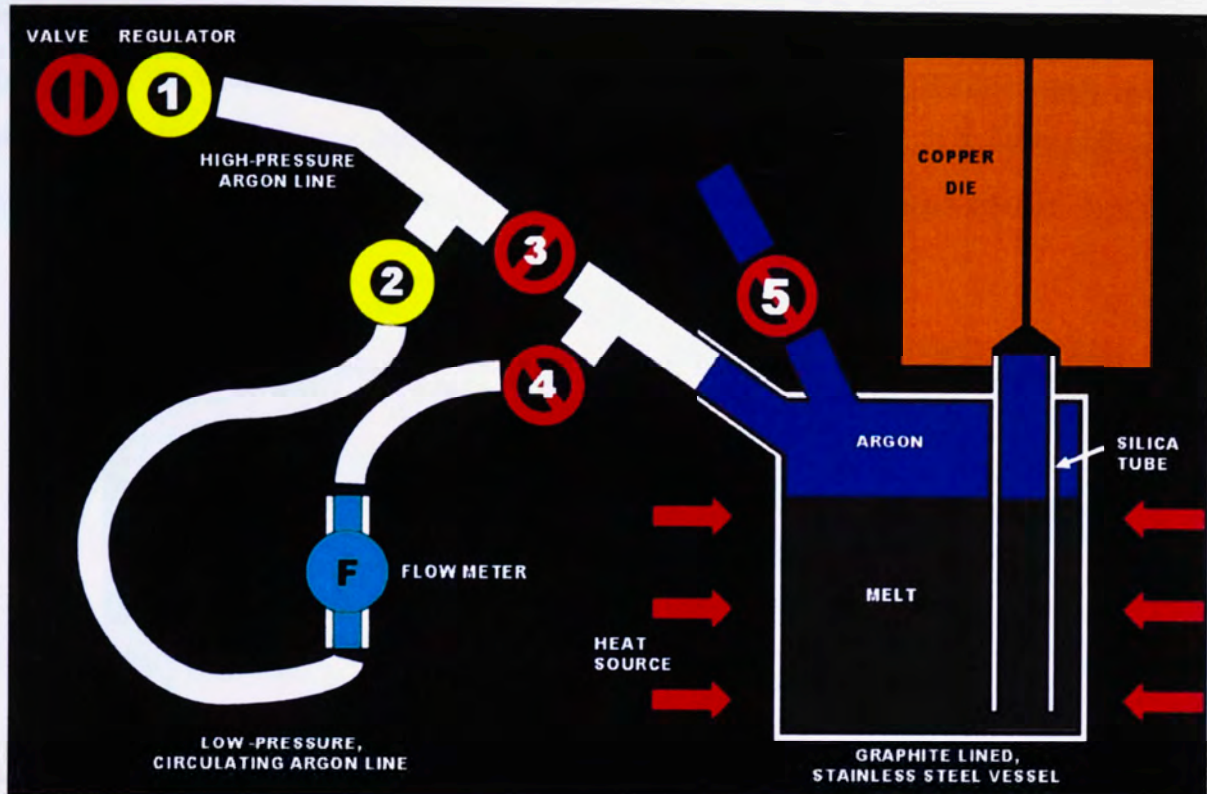


**Figure 3.16:** Schematic representation of the low-pressure die casting apparatus developed for large-scale production of BMG samples.

### 3.5.2 Casting Methodology

The low-pressure die-casting apparatus shown schematically in **Figure 3.16** uses pressurised argon from a gas bottle which is regulated through the regulator labeled **1** (this is the nominated casting injection pressure). The charge material is added to a preheated, sealed vessel that has been purged with argon gas. The unit is then heated to the desired casting temperature under circulating argon which is provided by opening the valve labeled **4** via the circulating argon line with regulating valve labeled **2** and a flow meter. Exhaust gasses are handled by opening valve **5**. Once the desired temperature is reached, the copper mould and silica tube unit are attached to the chamber. All gas valves are closed, the chamber is sealed and the high pressure gas line is opened by opening the valve labeled **3**, thereby forcing the molten metal up the silica tube and into the copper die to create the sample. Once the sample is obtained, the high pressure valve (**3**) is closed, the exhaust valve (**5**) is opened, the circulating argon valve (**4**) is opened and the copper mould and silica arrangement are removed from the vessel. Additional charge material can be added to the remaining melt and the process can be repeated.



### 3.6. PRELIMINARY DIE CASTING INVESTIGATIONS

A prototype iron pressure vessel (**Figure 3.17**) was constructed with appropriate plumbing inlets and outlets according to the injection method outlined in **SECTION 3.5**. Both the inner and outer shell of the casting unit was coated with boron nitride for avoiding iron pick up in the melt and corrosion of the vessel. The charge material is melted inside the vessel to a specified superheat temperature, followed by the introduction of pressurised argon into the chamber for allowing the melt to be injected into a copper mould with a 3 mm diameter cavity (**Figure 3.18**).



**Figure 3.17:** *Prototype injection caster constructed out of cast iron irrigation fittings with appropriate plumbing fixtures.*



**Figure 3.18:** *The tube or rod die. The die was originally twice the length given in this figure but was subsequently modified (cut in half) for aiding gas evacuation and for ensuring complete filling of the cavity.*



### 3.6.1 Experimental Procedure

Molten  $\text{Mg}_{65}\text{Cu}_{25}\text{Y}_{10}$  alloy prepared by the method outlined in SECTION 3.2 was hand cast at  $\sim 600^\circ\text{C}$  into the mould under an argon-flushed atmosphere to produce a number of cast rods of 10 mm in diameter and 150 mm in length. Surface oxide was removed and the rods cut to appropriate lengths for ease of introduction into the injection caster via the mould attachment orifice. The charge material was added to the injection vessel, which was purged with argon gas, sealed and melted at  $600^\circ\text{C}$  under an argon atmosphere circulating at a rate of  $80\text{ cm}^3/\text{min}$ . The charge temperature was monitored by using a K-type thermocouple inserted into a steel sleeve incorporated in the top of the injection vessel. The charge material was cooled to a given injection temperature and the desired overpressure applied to the chamber using the valve sequence described in SECTION 3.5.2.

### 3.6.2 Preliminary Die-Casting Results and Analysis

Using the injection method described above, both rod and tubular samples were successfully produced in this prototype die-caster. The careful control of both pressure and temperature during casting allowed the production of either solid rod samples or novel amorphous tubes (Figure 3.19 and 3.20). The latter were generated by using higher injection pressures, which resulted in molten metal flowing rapidly up the mould cavity walls, sealing the mould vent before all of the gas in the cavity could be evacuated by the molten metal front thereby generating an amorphous tube. It was found that tubes of various wall thicknesses could be generated by varying the injection pressure. For lower injection pressures, high quality rod samples were produced as shown in Figure 3.20a). The measurement of both sample length and wall thickness as a function of casting temperature and pressure allowed the generation of a processing map with respect to these casting variables.



**Figure 3.19:** Injection die-cast amorphous  $\text{Mg}_{65}\text{Cu}_{25}\text{Y}_{10}$  samples generated using the tube die.



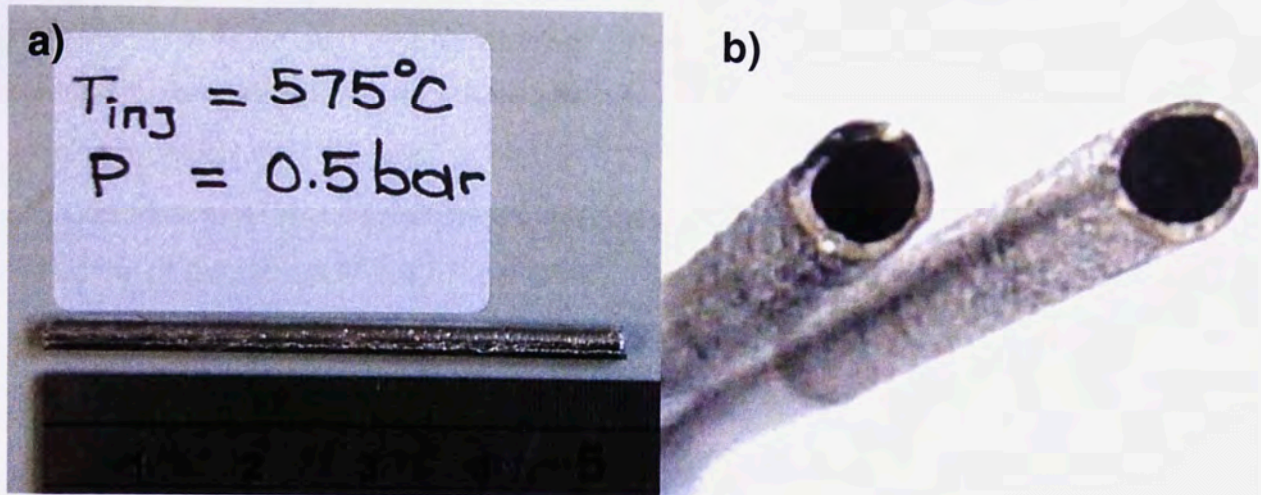


**Figure 3.20:** a) The largest solid rod sample produced using the prototype die caster shown in Figure 3.17. b) The production of novel magnesium-based amorphous tubes of 3 mm in diameter and 0.4 mm wall thickness.

**Figure 3.21** shows the effect of temperature and pressure on the production of tubular BMGs showing that long (100 mm), thin-walled (< 0.4 mm thickness) tubular samples can be generated for a range of casting conditions, as shown in the processing map.

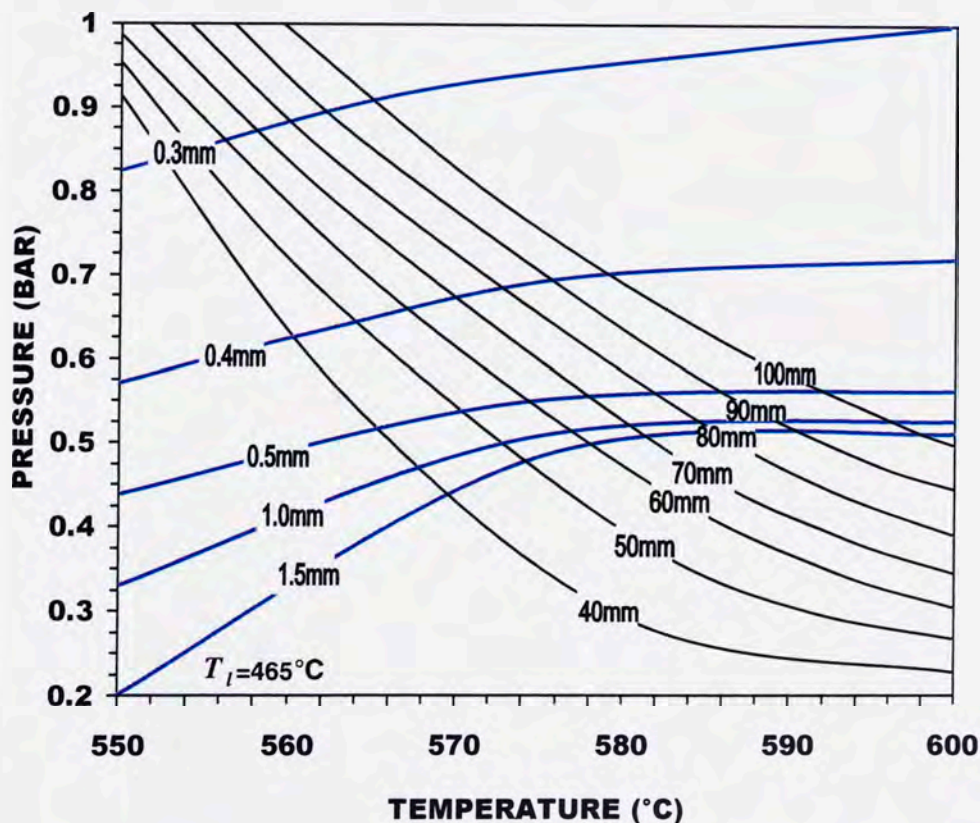


**Figure 3.21:** Processing map showing BMG sample wall thickness (0.3-1.5 mm) and length (40 - 100 mm) as a function of casting pressure and temperature.



A major aim of the thesis was the reliable production of a large number of high quality BMG samples suitable for elevated temperature tensile testing. In an attempt to produce these samples, a copper mould was constructed with a cavity in the shape of a standard tensile specimen, which may be seen in **Figure 3.22**. In this work, numerous gating and venting configurations were investigated but the ultimate outcome was unsuccessful for two reasons: (i) the cavity of the die could not be sufficiently filled to produce a complete sample (even after several gating and venting modifications), and (ii) due to the nature of the material, upon cooling, the sample would break somewhere along the gauge length due to shrinkage, since it was held in the cavity by the two large tabs on either end. Due to these problems, further development of the die caster and an alternative method of producing tensile test samples was devised.

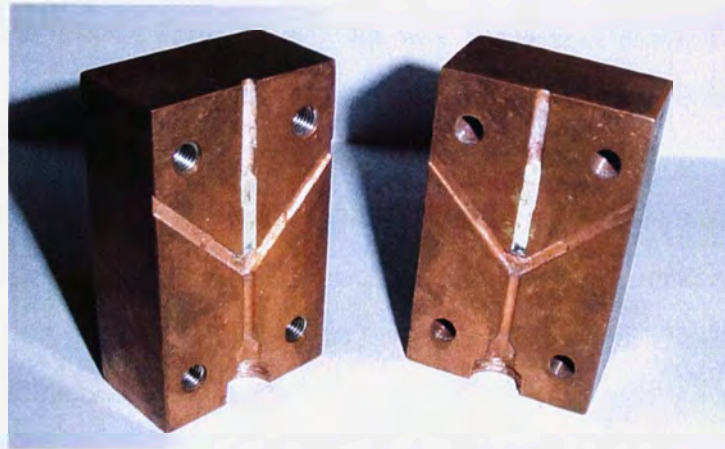


**Figure 3.22:** The so-called 'dog-bone' die, which consists of a standard tensile specimen pattern of diameter 3 mm and gauge length 12.3 mm. Note the numerous modifications made to the gas exit tract.



**Figure 3.23:** Unsuccessful injection-cast tensile test samples generated using the 'dog bone' die of **Figure 3.22**.



### 3.7. IMPROVEMENT OF THE INVERTED INJECTION DIE CASTING TECHNIQUE FOR THE $\text{Mg}_{65}\text{Cu}_{25}\text{Y}_{10}$ BMG

SECTION 3.6 described a reliable, repetitive low-pressure die-casting technique for producing high quality rods of  $\text{Mg}_{65}\text{Cu}_{25}\text{Y}_{10}$  BMG by optimising the casting parameters. The objective in this part of the work was to establish the optimal combination of casting parameters for reducing the variation in quality from a minimum number of casting experiments. It was found that charge temperature, injection pressure/injection velocity were important parameters for controlling the length, porosity and degree of crystallinity in the as-cast samples. For this series of experiments, a new, more permanent injection casting unit was constructed. **Figure 3.24** shows the configuration of the casting unit showing a gas-tight chamber constructed using AISI 316 stainless steel with appropriate gas inlets and outlets. The unit uses a copper ring for sealing and a boron nitride coated graphite crucible liner to prevent iron pick-up in the melt. The new unit uses the same principles and methodology shown in **Figure 3.16**. Once it had been established that injection die casting was the most suitable method of producing a large number of BMG castings for a variety of mechanical, thermal and chemical tests, a generic casting geometry was chosen which was dictated by both the critical sample thickness of the BMG and the width of an standard ASTM tensile test piece (which could later be ground from these samples). After careful consideration, a casting geometry of thickness 3.15 mm (to be ground to a 3 mm gauge diameter) and width 7 mm and maximum achievable length (125 mm die length) was chosen.

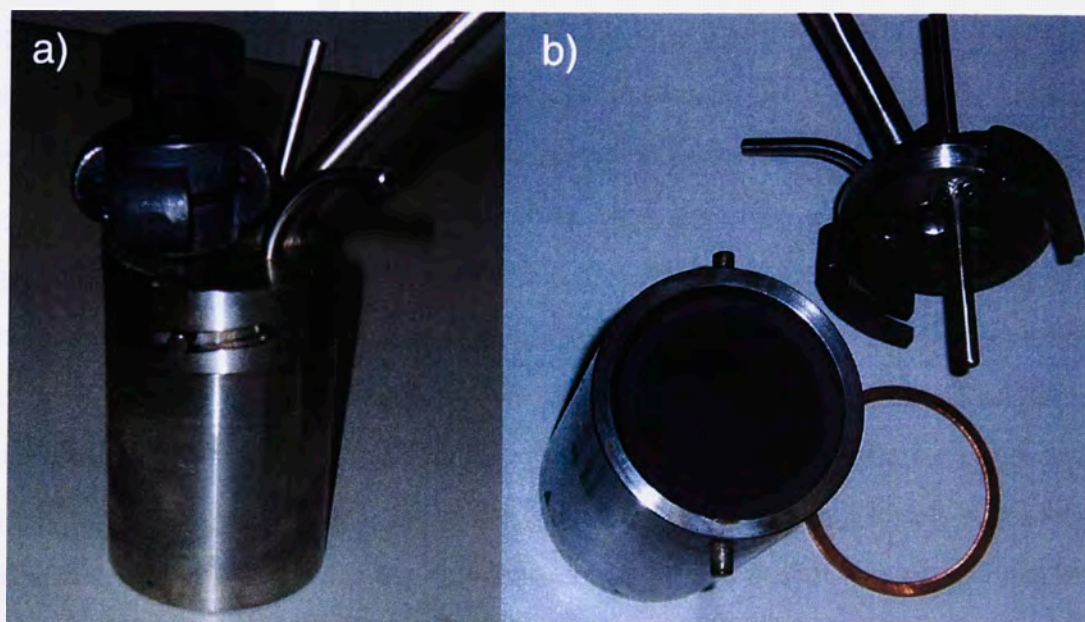


**Figure 3.24:** Photograph of a) assembled injection die casting unit with stopper and b) disassembled showing graphite crucible and copper sealing ring prior to boron nitride coating.



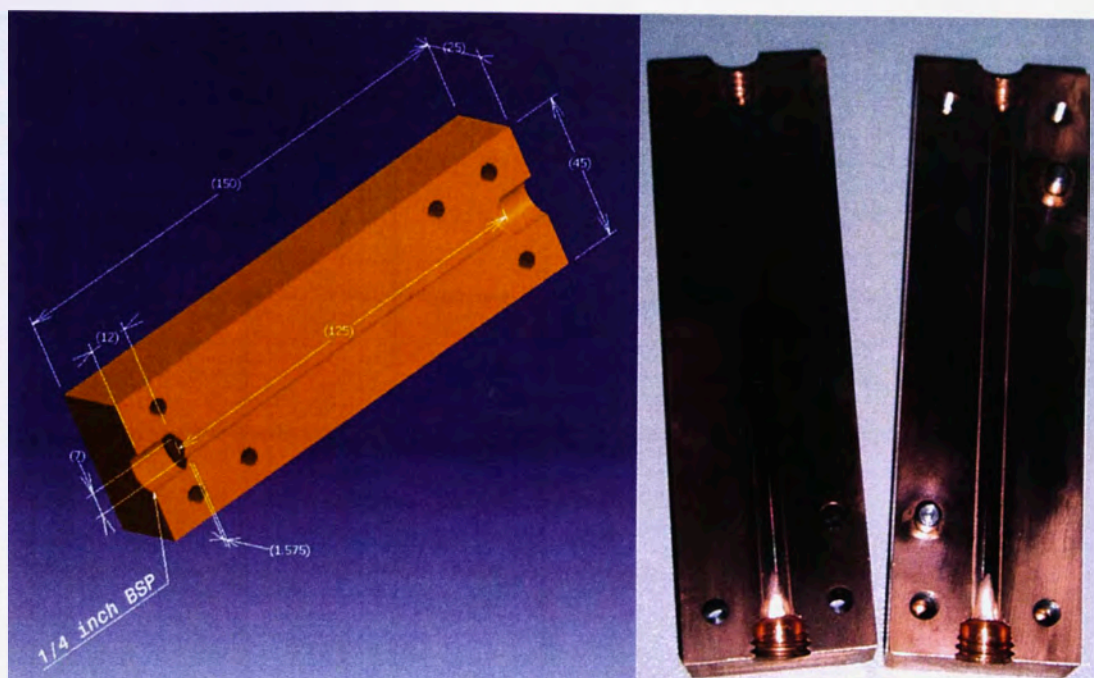


**Figure 3.25:** Dimensions and fitting sizes of the new 3.15 x 7 x 125 mm copper mould.

### 3.7.1 Experimental Procedure

As described in **SECTION 3.2**, molten  $\text{Mg}_{65}\text{Cu}_{25}\text{Y}_{10}$  alloy was cast by hand  $\sim 600\text{ }^{\circ}\text{C}$  into a steel mould under an argon-flushed atmosphere to produce numerous rods of 10 mm in diameter and 150 mm in length. Surface oxide was removed and the rods were cut to a more appropriate length as to be easily introduced into the injection caster via the mould attachment orifice. The charge material was added to the injection vessel, which was purged with argon gas (purity 99.997 vol.%) for 10 minutes, sealed and heated to  $600\text{ }^{\circ}\text{C}$  under an argon atmosphere circulating at a rate of  $80\text{ cm}^3/\text{min}$ . The charge temperature was monitored by a K-type thermocouple that was inserted into a steel sleeve incorporated in the top of the injection vessel. The charge material was cooled to a given injection temperature and the desired overpressure applied to the chamber using the valve sequence described in **SECTION 3.5.2**. The various casting experiments carried out in this part of the work are given in **Table 3.2**. Between each casting cycle, further charge material was added to maintain a constant melt level of 90% of the maximum chamber capacity. For consistency, die casting was carried out only on a downward heating cycle (chamber was cooled to the chosen injection temperature rather than heated to it). The melt injection temperature was monitored accurately by a K-type thermocouple and noted during each experiment. This was critical for ensuring the prescribed amount of superheat was applied during casting. The resulting samples were weighed and measured to determine their bulk density and length achieved for each experiment (**Table 3.2**). The composition of the as-cast bars was determined using electron probe microanalysis (EPMA) and found to be  $\text{Mg}_{65}\text{Cu}_{25}\text{Y}_{10}$  ( $\pm 0.81\text{ at.}\%$  maximum for each element).



**Table 3.2:** The range of casting temperatures and pressures used for casting  $\text{Mg}_{65}\text{Cu}_{25}\text{Y}_{10}$  samples and their corresponding results.

		CASTING TEMPERATURE (°C)														
		490	495	500	505	510	520	530	540	550	560	565	570	575	585	
P R E S S U R E  (BAR)	1.0	L = 125mm MF = 100% DN = <5%														
	0.8	L = 125mm MF = 100% DN = 37%														
	0.7	L = 109mm MF = 82% DN = 40%	L = 12mm MF = 10% DN = 100%	L = 125mm MF = 100% DN = <5%												
	0.6	L = 80mm MF = 64% DN = 35%		L = 125mm MF = 100% DN = 37%			L = 125mm MF = 100% DN = 44%						L = 125mm MF = 100% DN = 71%			
	0.5	L = 65mm MF = 52% DN = 86%	L = 78mm MF = 62% DN = 95%	L = 89mm MF = 71% MF = 71%	L = 104mm MF = 83% DN = 90%	L = 110mm MF = 88% DN = 91%	L = 125mm MF = 100% DN = 93%	L = 125mm MF = 100% DN = 95%	L = 125mm MF = 100% DN = 93%	L = 125mm MF = 100% DN = 93%	L = 125mm MF = 100% DN = 95%	L = 125mm MF = 100% DN = 96%	L = 125mm MF = 100% DN = 95%	L = 125mm MF = 100% DN = 100%	L = 125mm MF = 100% DN = 100%	
	0.4			L = 69mm MF = 55% DN = 100%			L = 100mm MF = 80% DN = 100%				L = 118mm MF = 95% DN = 100%	L = 120mm MF = 96% DN = 100%		L = 18mm MF = 14% DN = 100%	L = 125mm MF = 100% DN = 98%	L = 125mm MF = 100% DN = 100%
	0.3											L = 104mm MF = 83% DN = 100%			L = 106mm MF = 85% DN = 100%	L = 109mm MF = 87% DN = 100%

Key: L = sample length MF = mould filling % DN = casting density %

Grey regions indicate an inconsistent result due to experimental error.

### Injection Die Casting Results and Analysis

The principal casting variables studied in this part of the work were injection pressure/velocity, melt temperature and melt depth. Die-casting parameters are known to be interdependent and constantly in conflict. In practice, the injection process starts by setting up both the melt temperature and the injection pressure, with the operator determining experimentally the optimum injection parameters to produce a high quality, reproducible casting. Recent topical studies<sup>[233-235]</sup> have indicated that the mechanical properties of a die-cast product are related principally to the die temperature, the metal velocity at the gate, and the applied casting pressure. The combination of die temperature, the mould filling capacity of the molten metal, the geometrical complexity of the parts and cooling rate during die casting all affect the integrity of the cast component. If these parameters are not controlled adequately, various defects within the finished component are expected to be generated.

A majority of flow-related casting defects are caused by either trapped gases or premature solidification. Ideally, the liquid metal should displace the cavity gas ahead of the flow front as the cavity fills. The general objective is to fill the cavity evenly from the runner to the vents without creating gas pockets or sealing the vents before the gas escapes. While computational fluid dynamics has seen increasing application for cavity filling in die casting over the last decade,<sup>[233-237]</sup> most methods based on computational modeling are too unwieldy for use in routine die and process design, hence the prevailing method for correcting flow problems in die-casting continues to be by trial-and-error.

During the experimental program using the casting unit shown in **Figure 3.24**, it was found that the melt depth dramatically affected the reproducibility of results. A lower melt level inherently means that there is more gas in the injection system (specifically the silica feeder tube) to be displaced by the advancing molten metal. By having more gas in the system, the propensity for the mould vent to seal before all the gas in the system is evacuated is much higher, hence the likeliness of generating a hollow casting is much higher. The optimum results were achieved when the melt depth was close to maximum. The melt level was therefore held at 90% of the maximum chamber capacity for all experiments, this level would then rise upon the immersion of the silica feeder tube, keeping the amount of gas in the tube and hence the injection system to a minimum. A number of casting results and the corresponding injection casting conditions can be seen in **Figure 3.26a)** to **i)**.





**Figure 3.26:** A range of amorphous  $\text{Mg}_{65}\text{Cu}_{25}\text{Y}_{10}$  samples produced by injection casting for a given combination of melt injection temperature and casting pressure.



It was found that the degree of crystallinity of the present alloy was dependent on both the cooling rate within the copper mould and mould temperature. It was discovered in the earlier work that casting above 650 °C increases the probability of nucleating crystalline structures, as the cooling rate was not effectively steep enough to produce a completely amorphous structure. Consequently, melt superheat was kept to a minimum. The degree of crystallinity was determined both by X-ray diffraction (Philips MRD diffractometer) (**Figure 3.27**) and transmission electron microscopy (Philips CM200 97 TEM). TEM foils, as seen in **Figure 3.28**, were manufactured using focused ion beam milling (FEI XP200 machine), with a final milling current of 5 keV. For these casting conditions, an amorphous structure was confirmed by XRD and TEM whereby samples showed no diffraction peaks in the X-ray spectra and, despite over-exposure, no crystallites in TEM foils. It was found that low current ion beam milling did not affect the amorphous structure of the  $Mg_{65}Cu_{25}Y_{10}$  samples.<sup>[238]</sup>

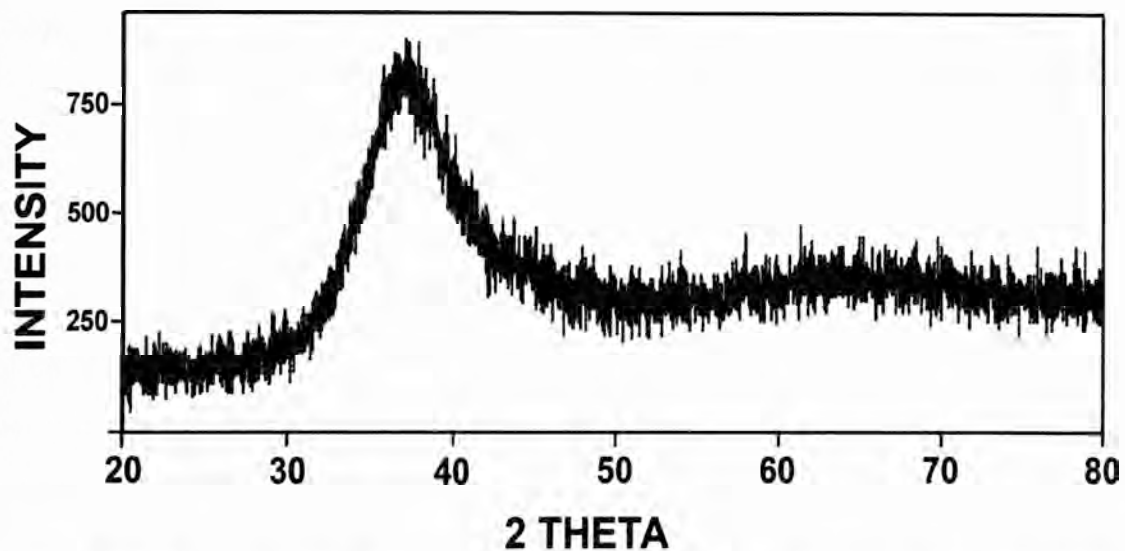


**Figure 3.27:** XRD spectrum for the centre section of a 3.15 mm thickness  $Mg_{65}Cu_{25}Y_{10}$  sample cast at 585 °C showing a typical amorphous halo.

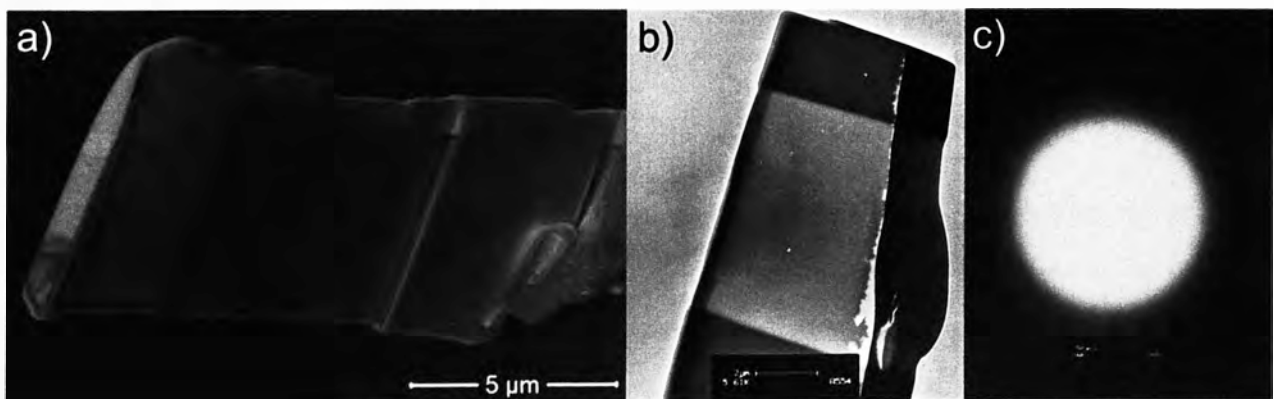


**Figure 3.28:** Images of  $Mg_{65}Cu_{25}Y_{10}$  a) SEM image of foil produced using focused ion beam milling (FIB) b) TEM image of foil and c) Selected area electron diffraction pattern showing no indication of crystals.

Pressure was a major experimental variable in this work. However, much of the work in the field of die casting is explained in terms of fluid velocity, so calculations were made to determine this parameter for various casting conditions so that a comparison may be made for different casting systems. By using the pressure boundary condition on the flow front, calculated from a Bernoulli integral of the momentum equation.<sup>[239]</sup>

$$P_1 + \frac{1}{2}\rho v_1^2 = P_2 + \frac{1}{2}\rho v_2^2 + \rho gh \quad (3.8)$$

and assuming that the applied pressure was instantaneous and constant, the movement of the flow front was determined by a traditional volume of fluid approach i.e.  $A_1 v_1 = A_2 v_2$  to give an approximate melt flow velocity ( $v_F = v_2$ ) upon entry to the die for a particular injection pressure ( $P_{INJ} = P_1$ ), that is:

$$v_F = \sqrt{\frac{2(P_1 - P_2 - \rho gh)}{\rho[1 - (A_2/A_1)^2]}} \quad (3.9)$$

where  $\rho$  is the density of the liquid metal (3260 kg/m<sup>3</sup>),  $P_2 = P_o$  the atmospheric pressure,  $h$  the silica draw tube height (0.06 m),  $A_1$  the cross-sectional area of the melt surface (1.78×10<sup>-3</sup>m<sup>2</sup>) to which the pressure is applied and  $A_2$  the cross-sectional area of the silica draw tube (6.09×10<sup>-5</sup>m<sup>2</sup>). The cross sectional area of the rectangular mould shown in **Figure 3.25** is 2.1×10<sup>-5</sup>m<sup>2</sup>, which is used to determine the final velocity of the melt entering the mould.

This method of calculation gives a maximum possible velocity entering the mould channel, neglecting friction effects of the silica tube wall and energy losses associated with flow system restrictions. An example of these calculations is given in **APPENDIX B**.

### 3.7.2 Cavity Filling

The cavity-filling problem in die casting involves transient, inertia-dominated, free surface flow within a narrow cavity. The velocities are prescribed at the entrance to the runner and the pressure boundary conditions on the free surface depend on the rate at which the excess gas escapes through the vents. Most of the energy dissipation occurs at the gates, where the liquid metal enters the cavity from the runner.<sup>[237]</sup> Since the liquid metal flow velocities ( $v_F$ ) in die-casting usually range from 10 to 100 m/s. As long as temperatures remain well above the liquidus temperature, the kinematic viscosity of the liquid alloy (~5 Pa.s<sup>[63]</sup>) is comparable to that

of water at about 6-10 Pa.s. The fluid flow behaviour can be determined by the associated Reynolds Number (  $Re$  ):<sup>[240]</sup>

$$Re = \frac{\rho v_F D}{\eta} \quad (3.10)$$

where  $\rho$  is the fluid density,  $v_F$  the fluid velocity,  $D$  the channel diameter and  $\eta$  the fluid viscosity.

Although the cavity cross-section in die casting is usually small in both dimensions (typically <10 mm), the combination of a high injection velocity and a low viscosity at high injection temperatures generally generates a Reynolds Number in excess of 5000. Furthermore, fluid flow in die casting is strongly dominated by inertia when well above the critical viscosity/freezing temperature. It is therefore reasonable to neglect the effect of viscosity at these higher temperatures and assume that the flow is both inviscid and incompressible. Even at injection speeds normally associated with slow-fill processes such as squeeze casting (<1 m/s),  $Re$  is still large enough to validate this assumption. The same high  $Re$  values that motivate the assumption of an inviscid fluid also suggest turbulent flow of the melt. Despite its complexity, turbulent mixing actually promotes a blunt time-averaged velocity profile through the cavity thickness, which is more consistent with bulk fluid motion than laminar flow.<sup>[237]</sup>

Conversely, the increased dissipation of turbulent flow may affect the solution in other ways. In a series of flow visualisation experiments, Booth and Allsop<sup>[241]</sup> varied the injection speeds from 5 to 50 m/s in a variety of cavity and gating configurations and observed no significant change in the fill patterns. Evidently, whatever the difference turbulence makes, it has a negligible effect on the bulk kinematics of flow. This is a clear indication that inertia forces generally prevail despite the presence of turbulent dissipation. Moreover, the very short fill times in die casting do not allow small-scale statistical turbulence to develop fully. This makes it very difficult to justify any model that goes beyond a simple inviscid fluid.<sup>[236,237]</sup>

Premature solidification in the mould is usually avoided by reducing the rate of die cooling (heating the die) or increasing the metal injection velocity. In the present work, the cooling rate of the die is a critical parameter for obtaining an amorphous sample. Therefore, to counter the effects of the high die cooling rate it was deemed necessary to increase the temperature of the melt (superheat) and select an appropriate injection velocity. However, insufficient casting



velocities and rapid cooling rates were found to result in incomplete filling of the die, as indicated in **Figure 3.26a**).

**Figure 3.29** shows the effect of both casting pressure/velocity and melt temperature on the propensity for the alloy to fill the mould cavity. It is clear, particularly for lower casting pressures, that the mould filling capability of the system is highly dependent on injection temperature. In **Figure 3.29**, it can be seen that at any given pressure, the contour lines generated from data points become further apart at an increasing rate with respect to the temperature axis.

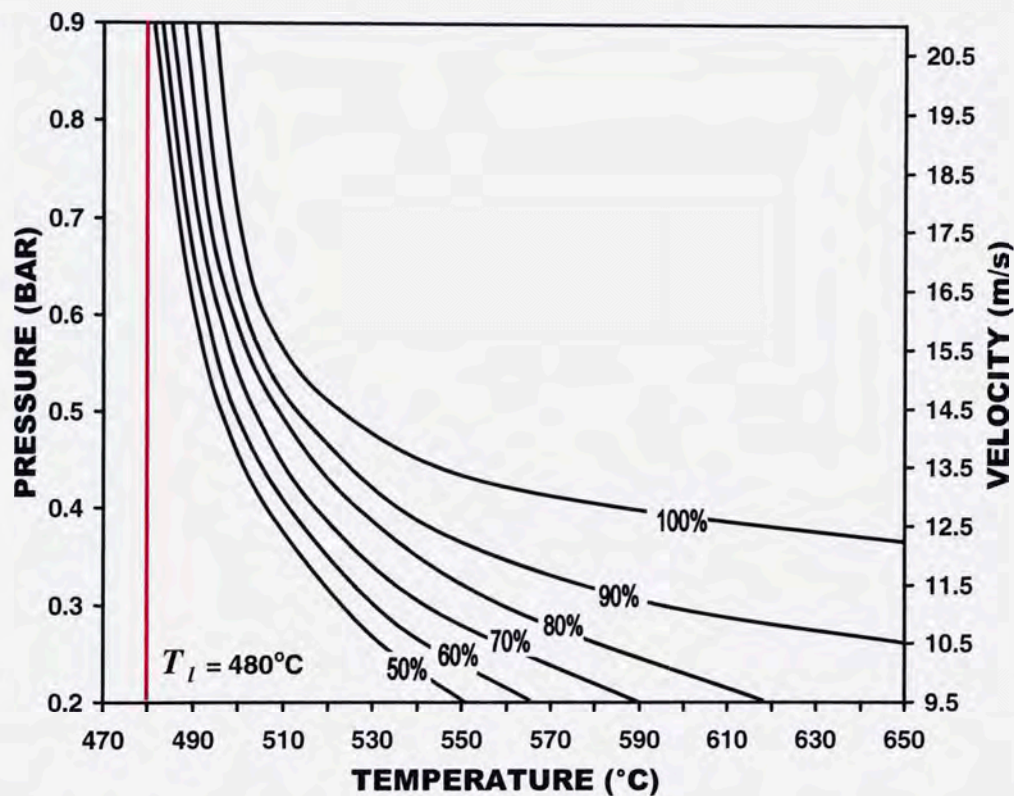


**Figure 3.29:** Contour representation of the injection results showing the percentage mould filling capacity (length of sample) for a given combination of melt temperature and casting pressure/velocity.

The viscosity of a BMG, which determines the fluidity of the molten metal whilst flowing in a mould cavity, is highly temperature dependent (as indicated by Eq. (2.8)). For an initial melt temperature,  $T_i$ , the flow of liquid into a cold channel of high thermal conductivity at a constant temperature,  $T_{MOULD}$ , will result in the metal decreasing in temperature via interfacial heat transfer to the channel. This reduction in temperature will result in an increase in the viscosity of the liquid (Eq. (2.8)), whereby, at some critical temperature  $T_C$ , there is a critical viscosity  $\eta = \eta_C$  where flow is no longer possible.

Using the simple analysis of Flemings,<sup>[242]</sup> an element of liquid metal entering a channel at a flow velocity,  $v_F$ , will result in the loss of heat into the channel with the instantaneous longitudinal temperature distribution in the liquid given schematically in **Figure 3.30**. Superimposed on this figure is the expected change in viscosity with temperature (Eq. (2.8)) where a critical casting length,  $L_C$ , is reached at  $\eta = \eta_C$ .

As described in **SECTION 3.3.2** for wedge casting, for a channel of thickness  $Z$ , where it is assumed that there are negligible frictional effects between the liquid and channel wall and heat flux is interface-controlled, then heat leaving the liquid volume element is equal to heat entering the channel:

$$\frac{dT}{dt} V C_P \rho = -hA(T - T_{MOULD}) \quad (3.11)$$

where  $h$  the interfacial heat transfer coefficient,  $C_P$  and  $\rho$  the heat capacity and density of the liquid metal, respectively,  $T$  and  $T_{MOULD}$  the melt and channel temperature, respectively. Again, if Eq. (3.11) is applied for the case of unidirectional cooling, where  $V/A = Z/2$ , it can be seen that the rate of temperature change of the flowing metal is given as:

$$\frac{dT}{dt} = \frac{-2h(T - T_{MOULD})}{Z C_P \rho} \quad (3.12)$$

The time,  $t_r$ , for the liquid volume element to move from  $x = 0$  to  $x = L_C$  (where stagnation occurs since  $\eta = \eta_C$ ) is:

$$t_r = \frac{L_c}{v_F} \quad (3.13)$$

Integrating Eq. (3.13) from  $t = 0$  to  $t = t_r$  and combining with Eq. (3.12) gives:

$$\frac{v_F Z \Delta T}{2 L_c} = \frac{h(T_i - T_{MOULD})}{C_P \rho} \quad (3.14)$$

where  $T_i$  is the temperature of the melt as it enters the channel. The right hand side of Eq. (3.14) is essentially constant which gives  $L_c \propto (v_F \Delta T)_c$  for a given channel cross-section and for a melt that does not crystallise.<sup>[242]</sup> Hence, for a given value of  $L_C$ , the critical liquid flow velocity is inversely proportional to the degree of superheat above the critical temperature,  $T_C$ , which corresponds to  $\eta = \eta_C$ . **Figure 3.29** demonstrates this inverse relationship between  $v_F$  and  $\Delta T$ .

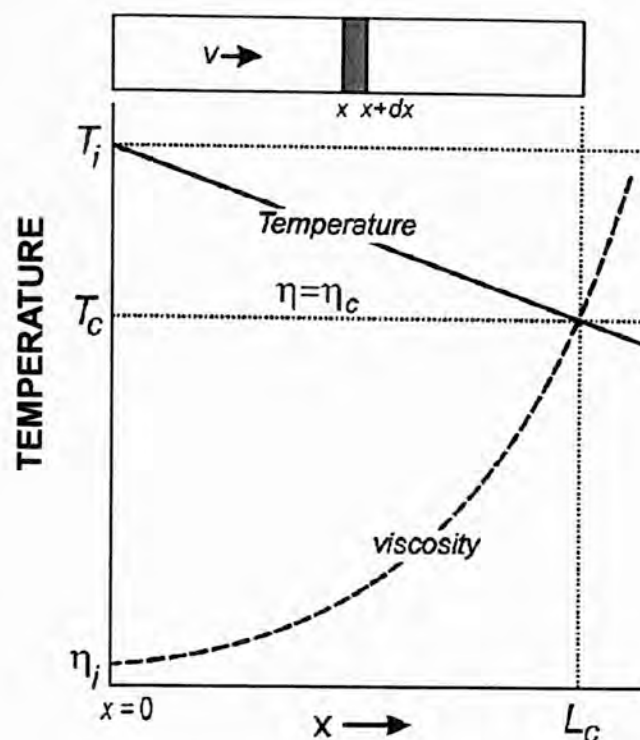


**Figure 3.30:** The temperature drop in liquid metal of initial temperature,  $T_i$ , flowing through a channel. Based on Eq. (2.8), the viscosity increase associated with this temperature drop is also shown. At the critical temperature  $T = T_c$  where  $\eta = \eta_c$ , flow will cease at  $x = L_c$ .

### 3.7.3 Voids, Porosity and Surface Defects in As-Cast Samples

If liquid metal cools too rapidly as it flows, it may partially solidify before the cavity is completely filled, which can lead to a number of casting defects, including degradation in surface quality, general porosity and cold shuts, all of which may reduce the structural soundness of the casting. It was observed that low casting pressures and high casting temperatures resulted in the majority of the argon gas in the injection system escaping through the mould vent ahead of the fluid front. However, if the vent was sealed by the advancing metal before the gas escaped, or if the metal encircled portions of the gas as it flowed, the resulting casting would contain a certain degree of porosity. Since the liquid metal is assumed to be incompressible, the pressure in the cavity gas cannot affect the metal velocities as long as it is all contained in a continuous pocket. Once two or more separate air pockets form, the flow front pressure may no longer be uniform and the relative pressure between distinct air pockets begins to affect the fluid flow front.<sup>[236,237]</sup> Furthermore, if the charge material was injected too rapidly (high pressure/velocity), the entire length of the die cavity was covered but a hollow section or 'shell' structure was generated within the sample, as shown in **Figures 3.26b)** and **c)**. (Similar to the overpressures utilised to create the amorphous tubes, **Figure 3.20**). The effect of both liquid metal flow velocity (and pressure) and melt temperature on the density of an as-cast sample is given in **Figure 3.31**.



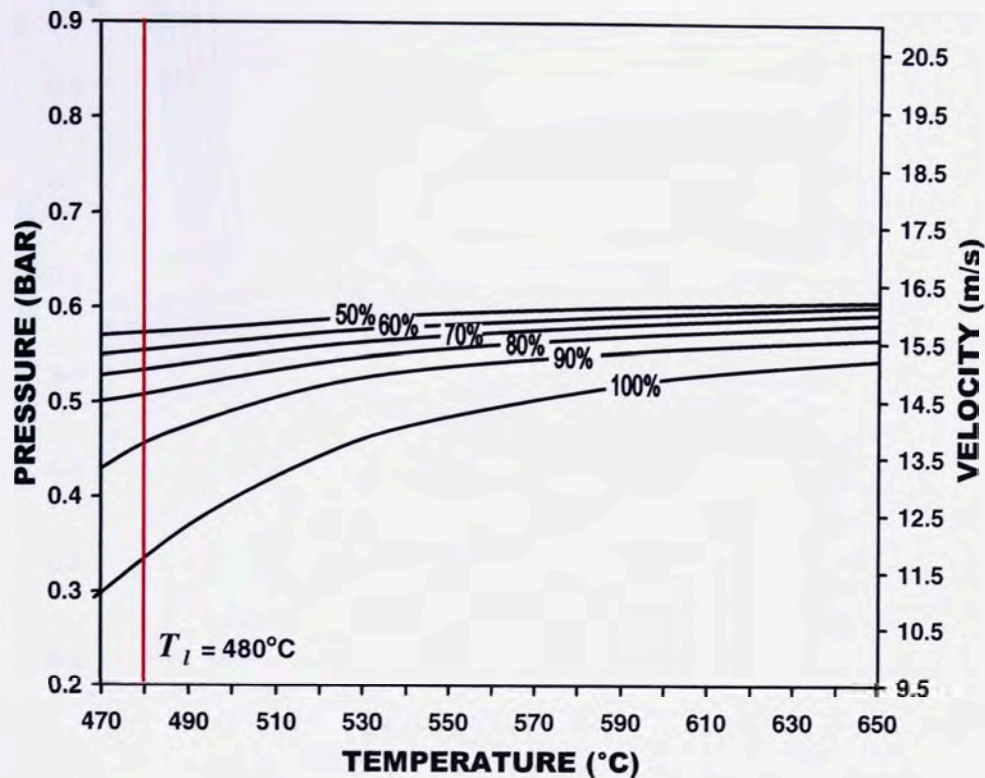


**Figure 3.31:** Contour representation of the injection results showing the density (percentage) of castings with respect to porosity and/or a hollowed structure for a given melt temperature and pressure/velocity.

It has been shown that an inhomogeneous metal layer is formed on the surface of Mg-alloy die castings when cast at a high temperature and flow rapidly in contact with a mould wall, and that this layer generates a surface warping defect.<sup>[243]</sup> This appears to be the case with the present alloy, as shown in **Figure 3.26c**). Here, rapid freezing of the metal in contact with the copper mould creates ‘flow-like’ striations on the surface of the finished product. It is also important to note that the spontaneous cracking of amorphous  $\text{Mg}_{65}\text{Cu}_{25}\text{Y}_{10}$  samples observed when gravity casting of flat plate sections was not an issue during injection die casting. Unlike the samples produced by gravity casting, the die-cast samples also exhibited a certain degree of toughness and could be bent and dropped without fracture. The mechanical instability problem appears to have been eradicated by continuously applying pressure (the injection pressure) to the casting as it cools, which is inherent to this low-pressure injection process. This phenomenon is possibly due to a certain degree of induced structural relaxation during cooling. The pressure/velocity–temperature diagrams given in **Figures 3.29** and **3.31** provide a useful representation of the desirable parameters needed for producing high quality amorphous bars of the present alloy. **Figure 3.32** shows these diagrams in combination to generate an overall processing map that provides information on the optimum conditions for generating amorphous, fully dense BMG samples that completely fill the mould cavity.



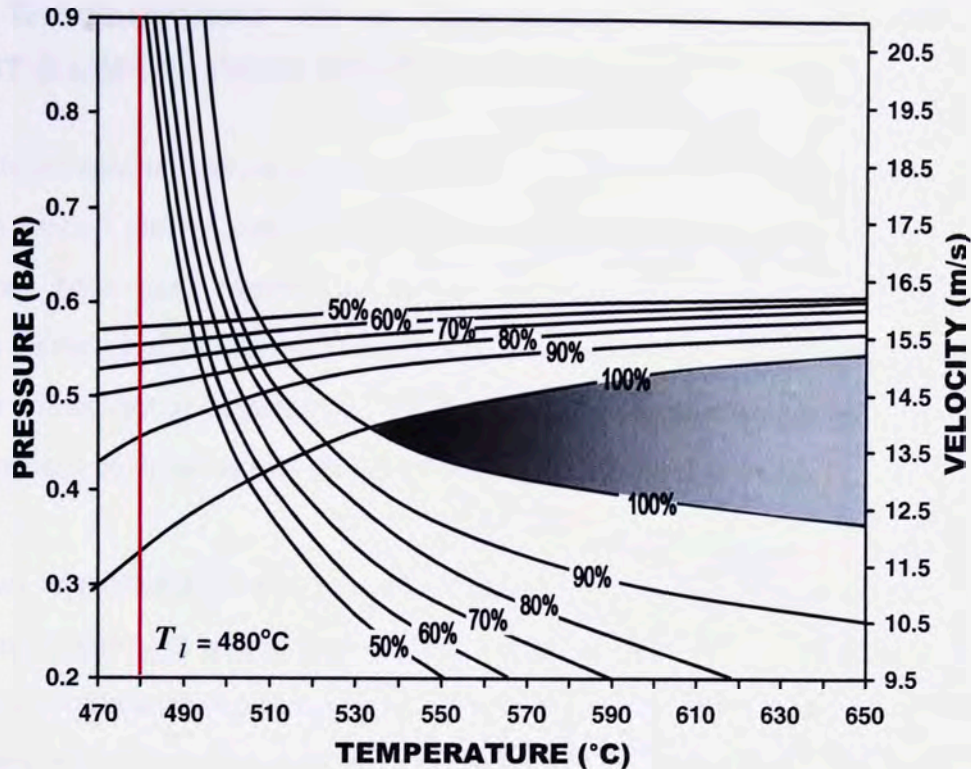


**Figure 3.32:** Processing map showing the effect of casting pressure/velocity and melt temperature on mould filling capacity and sample density. The shaded zone indicates the optimum processing window for generating the highest quality BMG samples.

It can be seen that the desirable processing window (shaded zone) is reasonably large and a sound casting is expected for a range of processing parameters. Based on this diagram, the optimum combination of melt temperature and casting pressure to generate a sound casting is 560–580 °C and 0.4–0.5 bar, respectively, as demonstrated by the as-cast samples shown in **Figure 3.26h)** and i). The processing map of **Figure 3.32** was utilised successfully to consistently produce a large number of high quality BMG samples shown in **Figure 3.33**.

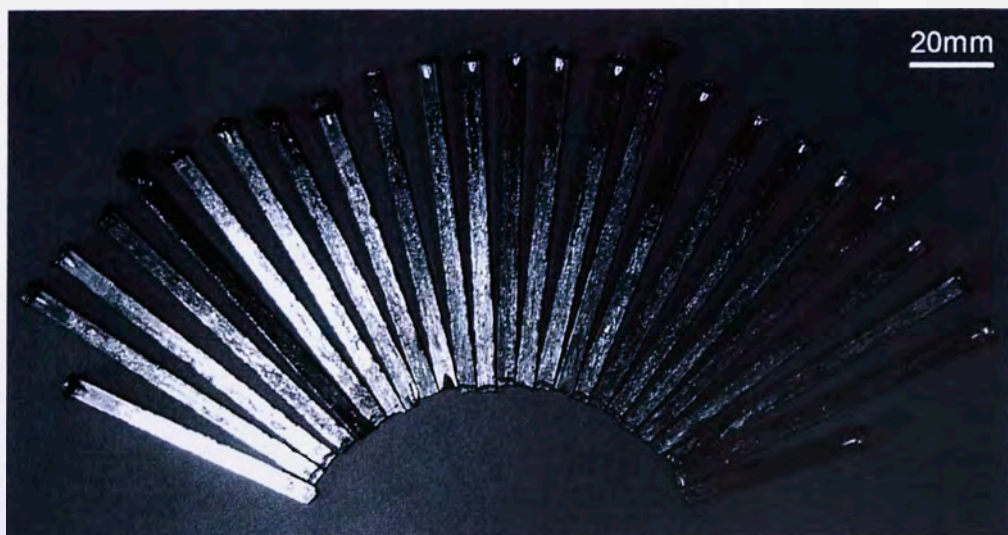


**Figure 3.33:** A number of full length, fully dense  $Mg_{65}Cu_{25}Y_{10}$  BMG samples produced by low-pressure injection die-casting. (Temperature = 585°C and Pressure = 0.5 bar).



### 3.8. DEVELOPMENT OF A TECHNIQUE FOR PRODUCING TENSILE TEST SAMPLES FROM DIE-CAST BMGS

Despite extensive investigations on the mechanical properties of BMGs since 1960s, most studies have been carried out by compressive testing at room temperature.<sup>[244]</sup> A limited number of investigations have been reported on tensile deformation of BMGs using non-standard test specimens (usually in ribbon form). In the ternary Mg-Cu-Y system, all deformation studies to date have been carried out in compression.<sup>[245,246]</sup> In order to standardise testing techniques, tensile test specimens in compliance with ASTM-B8 were generated in this thesis.

It was shown in SECTION 3.6.2 that injection die casting was not suitable for the direct production of the complex geometry of a typical tensile test sample in the  $\text{Mg}_{65}\text{Cu}_{25}\text{Y}_{10}$  alloy. Hence, a novel preparation device was constructed for producing tensile test samples (**Figure 3.34**). The apparatus was designed specifically to grind rectangular as-cast samples of dimensions 7 mm × 3.15 mm into a 'dog bone' shaped sample of diameter 3 mm and gauge length 12.3 mm in accordance with ASTM-B8 for tensile testing (**Figure 3.35**). The apparatus uses a copper lap of diameter 120 mm, with an outer diameter profile that matches the longitudinal profile of the desired tensile test specimen (**Figure 3.34b**), which is engrained with #600 grade diamond powder. The sample is held in a set of collet-style grips and spun counter directionally to the copper lap. It can be spun at variable speeds to produce standard tensile specimens of the required dimensions. The samples are prepared to a near mirror finish (with negligible surface striations) and are sufficient for tensile testing. **Figure 3.36** shows a number of  $\text{Mg}_{65}\text{Cu}_{25}\text{Y}_{10}$  BMG tensile test samples produced by this technique.

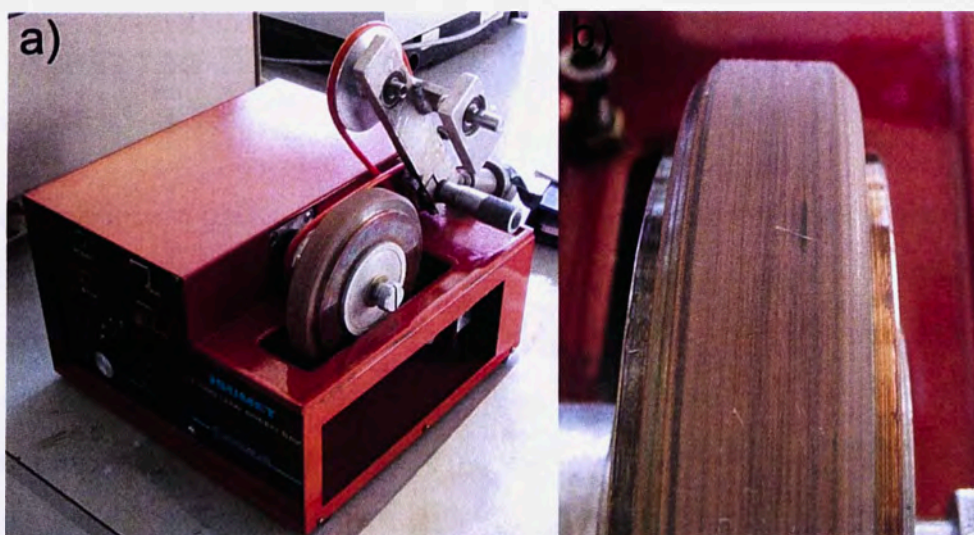


**Figure 3.34:** a) Variable-speed tensile specimen grinder and b) the profiled copper grinding wheel with engrained #600-grade diamond powder.



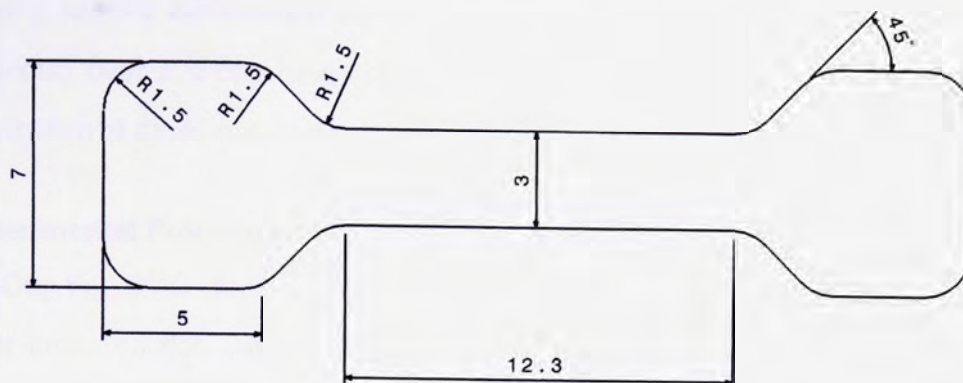


**Figure 3.35:** The dimensions of the ground ASTM-B8 compliant tensile test samples.

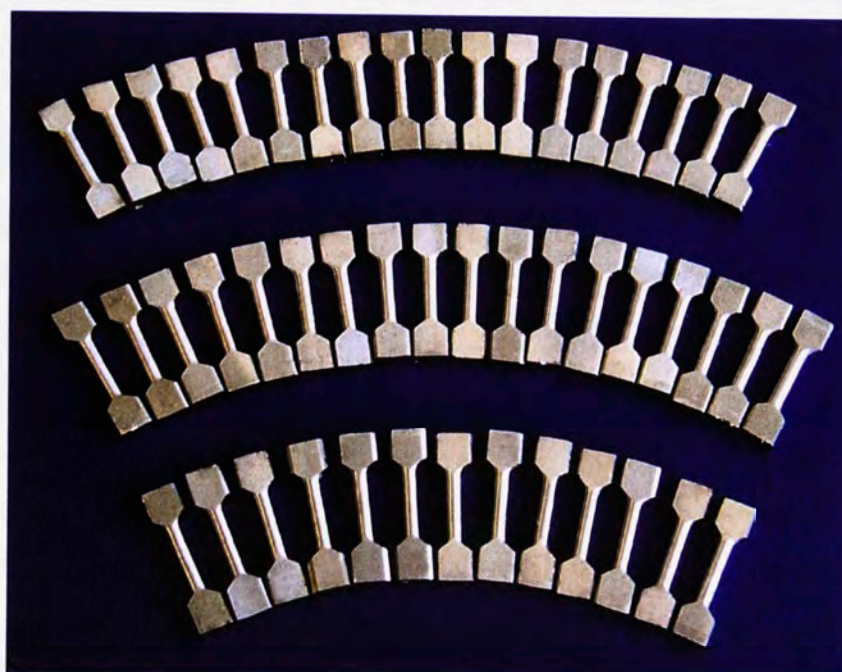


**Figure 3.36:** A number of completed  $Mg_{65}Cu_{25}Y_{10}$  BMG samples prepared for tensile testing.

### 3.9. ELEVATED TEMPERATURE MECHANICAL BEHAVIOUR OF THE $Mg_{65}Cu_{25}Y_{10}$ BMG

In the supercooled liquid (SCL) region, there is a drastic decrease in material viscosity (see e.g. SECTION 2.6.4). This phenomenon has attracted substantial attention in industry due to the increased ability in near-net-shape forming of these materials into complex components. From an engineering viewpoint, an understanding of the deformation behaviour of BMGs in the SCL region would prove beneficial for future applications of such materials. This part of the thesis describes the elevated temperature flow behaviour (uniaxial tension) of the Mg-base BMG using the standardised tensile test samples shown in **Figure 3.36**). The data generated from these tests allowed the development of deformation maps with respect to temperature and strain rate



for identifying specific deformation behaviour (of particular interest and importance, Newtonian flow behaviour) over a broad range of testing conditions that may prove useful for near-net-shape fabrication of these materials.

### 3.9.1 Experimental Procedure

The  $\text{Mg}_{65}\text{Cu}_{25}\text{Y}_{10}$  BMG tensile test samples were produced from injection-cast bars of rectangular cross section using the grinding technique described in SECTION 3.8. The ASTM standardised tensile test samples (Figure 3.36) were deformed in air using an MTS 810 hydraulic tensile machine equipped with a 1kN load cell and an MTS 651 Environmental Chamber for high temperature testing. A built-in Eurotherm 2024 temperature controller was employed to maintain constant temperature within  $\pm 1^\circ\text{C}$ . However, since the built-in thermocouple was at the inside corner of the furnace chamber, an additional K-type thermocouple was positioned in close proximity to the specimen to monitor the temperature at the specimen surface. A schematic diagram of the equipment used for this part of the thesis is given in Figure 3.37. The MTS 651 Environmental Chamber was preheated to each preset temperature prior to mounting the specimens. Due to the fact that  $T_g$  is not a unique physical property of the BMG (see Figure 3.8), the heating rate of all samples was kept constant at  $5^\circ\text{C}/\text{min}$  after reaching  $140^\circ\text{C}$ . During heating, the tensile samples were held at a constant load of 5N which was necessary for allowing for the expansion of the stainless steel draw bars so as not to crush the sample upon heating. Tensile testing commenced after the sample was stabilised for  $\sim 5$  min at the selected test temperature.

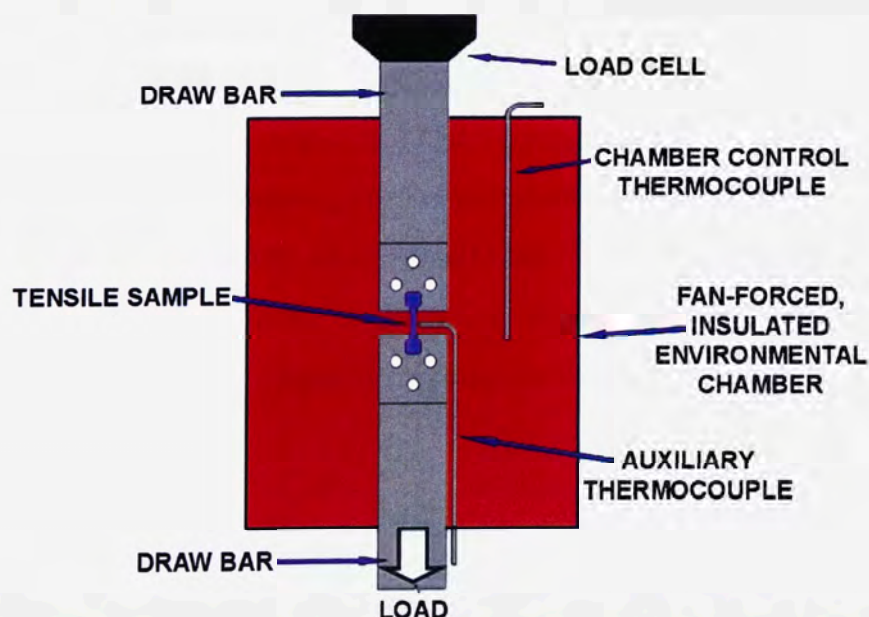


**Figure 3.37:** Schematic representation of the equipment used to perform elevated temperature tests on the  $\text{Mg}_{65}\text{Cu}_{25}\text{Y}_{10}$  BMG samples.

### 3.9.2 Constant Strain Rate Tensile Testing

The tensile deformation behaviour of the die-cast  $\text{Mg}_{65}\text{Cu}_{25}\text{Y}_{10}$  BMG within the SCL region (150-170 °C) was examined at constant strain rates ranging from  $10^{-3}$  to  $10^{-1} \text{ s}^{-1}$ . The maximum strain to failure of these samples was in excess of 1300% which was limited only by the maximum travelling distance of the tensile testing unit.

Isothermal annealing DSC experimental results carried out at temperatures ranging from 160 to 200 °C (**Figure 3.9**) were used to determine the allowable time frame for tensile testing before the onset of crystallisation. Using this data it was determined that testing should be carried out at temperatures at or below 170 °C to avoid crystallisation within the experimental time frame, hence constant strain rate tensile testing was carried out at temperatures from 150 to 170 °C in increments of 5 °C.

**Table 3.4** provides a summary of results for the BMG including peak load ( $L_P$ ), flow stress ( $\sigma_f$ ), maximum strain ( $\epsilon_{\text{MAX}}$ ) and elongation (**Elong**). Samples were observed to have failed in either a brittle type manner with elongations <2.3% or continued to flow plastically until failure. Brittle and Non-Newtonian flow regimes are marked in **Table 3.4** as dark grey and light grey, respectively, with the other values indicating Newtonian flow conditions.

For some samples that flowed in a homogeneous, plastic manner, a stress overshoot, which is a typical indication of non-Newtonian flow conditions<sup>[60,247]</sup> was observed. This phenomena has also been observed in other BMG systems by Kawamura et al.<sup>[247]</sup> and is generally attributed to the change in atomic-mobility at the yield point with increasing strain rate, and its gradual return to an equilibrium state during stress relaxation.<sup>[60,185,247]</sup> Following this overshoot was a yield drop to a lower equilibrium flow stress. The flow stress of samples was determined using the methodology described in **APPENDIX C**. The general strain-induced softening phenomenon after an initial peak stress is explained by an increase in the free volume of the amorphous structure and the generation of shear bands, which act as dislocation-like defects to accommodate strain.<sup>[20,25,27,248-250]</sup> Both of these effects contribute to a lower flow stress.<sup>[20,25,27,248]</sup>



**Table 3.4:** A summary of tensile test conditions and corresponding results for the  $\text{Mg}_{65}\text{Cu}_{25}\text{Y}_{10}$  BMG.

		CONSTANT STRAIN RATE ( $\text{s}^{-1}$ )						
		$1 \times 10^{-1}$	$5 \times 10^{-2}$	$2.5 \times 10^{-2}$	$1 \times 10^{-2}$	$7.5 \times 10^{-3}$	$5 \times 10^{-3}$	$1 \times 10^{-3}$
T E M P E R A T U R E  (°C)	170	$L_P = 618\text{N}$	$L_P = 407\text{N}$		$L_P = 121\text{N}$		$L_P = 46\text{N}$	$L_P = 6.7\text{N}$
		$\sigma_f = 87.4\text{MPa}$	$\sigma_f = 57.6\text{MPa}$		$\sigma_f = 17.1\text{MPa}$		$\sigma_f = 6.52\text{MPa}$	$\sigma_f = 0.95\text{MPa}$
		$\varepsilon_{\text{MAX}} = 161.5\text{mm}$	$\varepsilon_{\text{MAX}} = 161.7\text{mm}$		$\varepsilon_{\text{MAX}} = 161.0\text{mm}$		$\varepsilon_{\text{MAX}} = 83.1\text{mm}$	$\varepsilon_{\text{MAX}} = 65.7\text{mm}$
		<b>Elong</b> > 1313%	<b>Elong</b> > 1314%		<b>Elong</b> > 1309%		<b>Elong</b> = 676%	<b>Elong</b> = 534%
	165	$L_P = 813\text{N}$	$L_P = 505\text{N}$	$L_P = 188\text{N}$	$L_P = 147\text{N}$		$L_P = 80.4\text{N}$	$L_P = 14.3\text{N}$
		$\sigma_P = 115\text{MPa}$	$\sigma_P = 71.4\text{MPa}$	$\sigma_f = 46.5\text{MPa}$	$\sigma_f = 20.7\text{MPa}$		$\sigma_f = 11.4\text{MPa}$	$\sigma_f = 2.02\text{MPa}$
		$\varepsilon_{\text{MAX}} = 0.5\text{mm}$	$\varepsilon_{\text{MAX}} = 0.4\text{mm}$	$\varepsilon_{\text{MAX}} = 158.0\text{mm}$	$\varepsilon_{\text{MAX}} = 161.0\text{mm}$		$\varepsilon_{\text{MAX}} = 162\text{mm}$	$\varepsilon_{\text{MAX}} = 78.5\text{mm}$
		<b>Elong</b> = 4.10%	<b>Elong</b> = 3.30%	<b>Elong</b> > 1287%	<b>Elong</b> > 1309%		<b>Elong</b> > 1317%	<b>Elong</b> = 638%
	160				$L_P = 388\text{N}$		$L_P = 203\text{N}$	$L_P = 34.8\text{N}$
					$\sigma_f = 54.8\text{MPa}$		$\sigma_f = 28.7\text{MPa}$	$\sigma_f = 4.92\text{MPa}$
					$\varepsilon_{\text{MAX}} = 161.0\text{mm}$		$\varepsilon_{\text{MAX}} = 162\text{mm}$	$\varepsilon_{\text{MAX}} = 129\text{mm}$
					<b>Elong</b> > 1309%		<b>Elong</b> > 1317%	<b>Elong</b> = 1050%
	155					$L_P = 466\text{N}$	$L_P = 361\text{N}$	$L_P = 131\text{N}$
						$\sigma_P = 65.9\text{MPa}$	$\sigma_f = 51.1\text{MPa}$	$\sigma_f = 18.5\text{MPa}$
						$\varepsilon_{\text{MAX}} = 0.15\text{mm}$	$\varepsilon_{\text{MAX}} = 161.8\text{mm}$	$\varepsilon_{\text{MAX}} = 162.5\text{mm}$
						<b>Elong</b> = 1.2%	<b>Elong</b> > 1315%	<b>Elong</b> > 1321%
	150						$L_P \sim 168\text{N}$	$L_P = 327\text{N}$
							$\sigma_P \sim 23.8\text{MPa}$	$\sigma_f = 46.3\text{MPa}$
							$\varepsilon_{\text{MAX}} = 0.1\text{mm}$	$\varepsilon_{\text{MAX}} = 162.4\text{mm}$
							<b>Elong</b> = 0.81%	<b>Elong</b> > 1320%

**Key:**  $L_P$  = peak load  $\sigma_f$  = flow stress  $\varepsilon_{\text{MAX}}$  = maximum strain **Elong** = Elongation %

Brittle and Non-Newtonian flow regimes are marked in dark grey and light grey respectively, white cell values indicate Newtonian flow conditions.

### 3.9.3 The Effect of Deformation Temperature on Flow Behaviour

Plastic deformation of a metallic glass is believed to occur by two major modes.<sup>[251,252]</sup> At low temperatures, deformation is inhomogeneous and confined to a small number of very thin shear bands. Inside these bands, the shear strain and shear strain rate are very large. Inhomogeneous flow is an instability due to progressive softening believed to be a result of deformation-induced disordering, accompanied by shear-induced dilatation,<sup>[253-256]</sup> though the atomistic mechanism of the phenomenon is still under investigation.<sup>[180,257]</sup> At higher temperatures in the SCL region, deformation is considered homogeneous, whereby each volume element of the material undergoes the same strain. This behaviour generally generates exceedingly large elongations during tensile deformation. Typical results at a strain rate of  $5 \times 10^{-3} \text{ s}^{-1}$  for temperatures from 155 °C to 170 °C are shown in **Figure 3.38**.

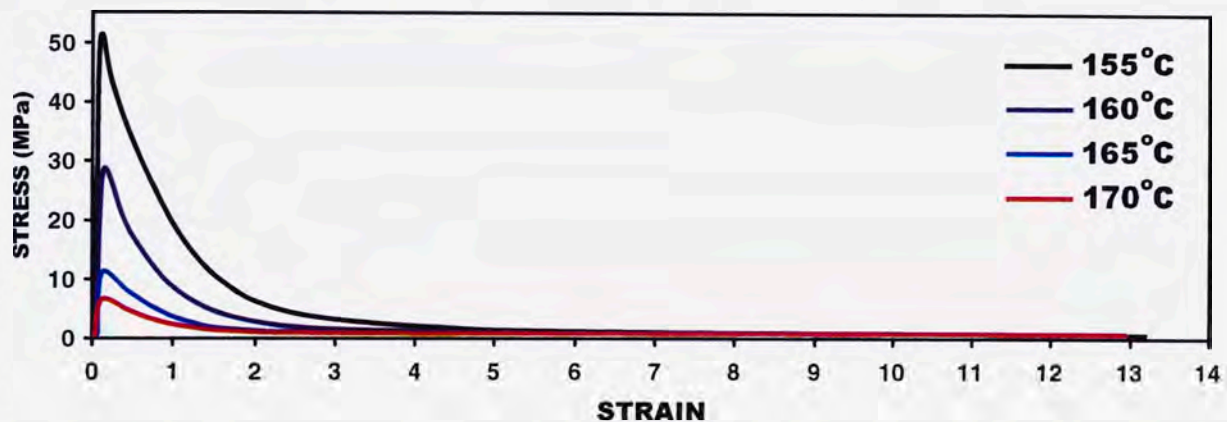


**Figure 3.38:** Stress-Strain curves for  $\text{Mg}_{65}\text{Cu}_{25}\text{Y}_{10}$  samples tested at a strain rate of  $5 \times 10^{-3} \text{ s}^{-1}$  for temperatures ranging from 155 °C - 170 °C.

A stress overshoot and yield drop to an extremely small flow stress were observed in some cases. Such flow softening behaviour of BMGs was originally observed by Inoue<sup>[130]</sup> and is similar to the phenomenon observed in polymer systems.<sup>[258]</sup> Kawamura et al.<sup>[247]</sup> investigated the stress overshoot in Zr-based metallic glasses and concluded that the stress overshoot occurred in a non-Newtonian flow state when the strain rate was increased. The stress overshoot was attributed to the change in atomic-mobility at the yield point, with increasing strain rate, and its gradual return to an equilibrium state during stress relaxation.<sup>[247]</sup> In this temperature range, the flow was homogeneous and failure occurred in a ductile manner and, as expected, flow stress increased as the test temperature was decreased. This result relates directly to the inherent increase in viscosity of the material with respect to a decrease in temperature, analogous to Eq. (2.8) when testing in the SCL region. The temperature dependence of sample ductility is also evident in **Table 3.4**, where the small strain to failure of



the brittle samples also increases with increased temperature. The overall form of the flow curves at various temperatures and strain rates are similar to that observed in a number of BMG forming systems including Pd,<sup>[259]</sup> Zr,<sup>[244]</sup> La,<sup>[174]</sup> Cu<sup>[185]</sup> and Ti<sup>[260]</sup> based BMGs for the tensile-deformed samples. **Figure 3.39** shows the change in flow stress as a function of testing temperature at various strain rates for all samples tested, highlighting the boundaries between Newtonian and non-Newtonian flow (to be discussed in detail anon) and a low temperature inhomogeneous region where brittle fracture occurs. (N.b. there is a distinct change in direction of curves in the non-Newtonian regime). In the homogeneous deformation zone (both Newtonian and non-Newtonian), most samples deformed to elongations considerably greater than 1000%, which was limited only by the travel distance of the tensile testing unit (**Figure 3.40**).

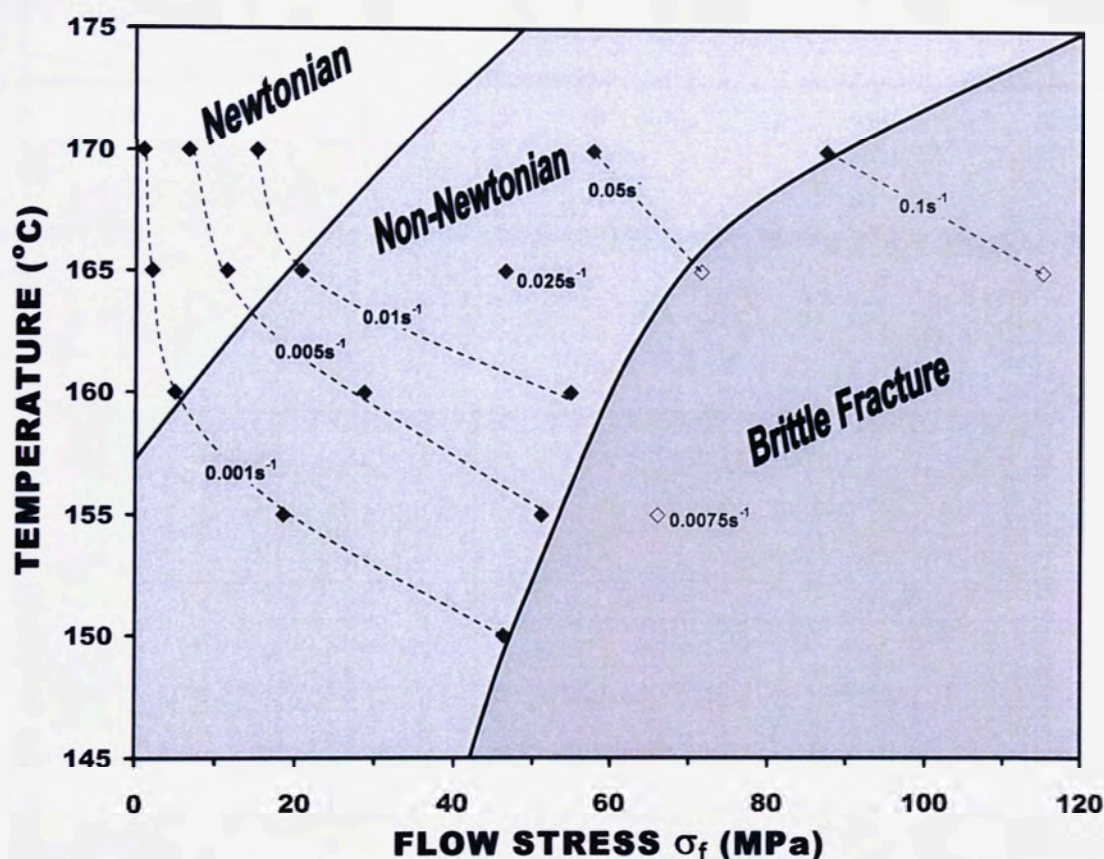


**Figure 3.39:** Effect of temperature on the flow stress at various strain rates.

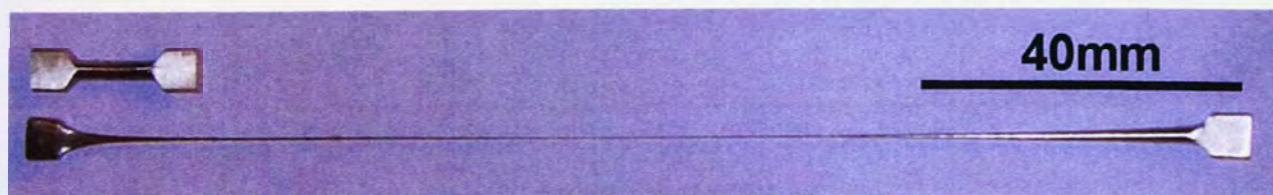


**Figure 3.40:** As-prepared and deformed ( $170\text{ }^{\circ}\text{C}$  at  $10^{-2}\text{ s}^{-1}$ ) tensile test samples showing an elongation in excess of 1300%.



### 3.9.4 The Effect of Strain Rate on Flow Behaviour

Typical stress/strain results at 170 °C for strain rates in the range of  $1 \times 10^{-3}$  to  $1 \times 10^{-1} \text{ s}^{-1}$  are shown in **Figure 3.41**, with **Figure 3.42** showing the effect of strain rate on flow stress for the entire sample range. Both figures indicate that the material flow stress decreases with decreasing strain rate.

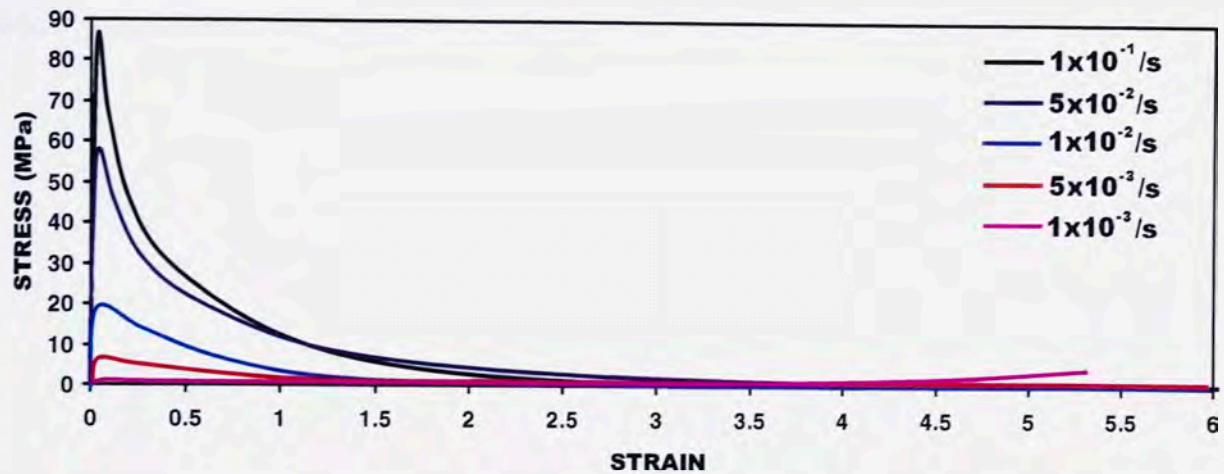


**Figure 3.41:** Effect of strain rate on flow stress during tensile testing of the  $Mg_{65}Cu_{25}Y_{10}$  BMG at 170 °C.

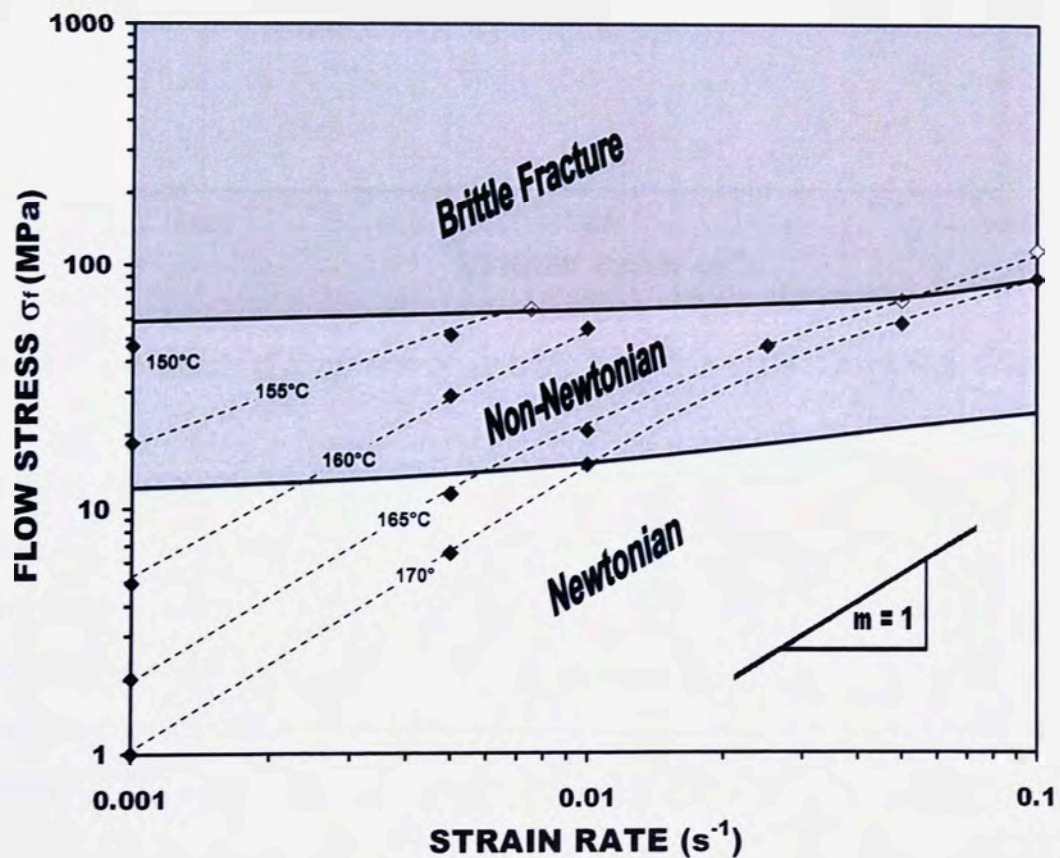


**Figure 3.42:** Effects of strain rate on flow stress at different temperatures for the  $Mg_{65}Cu_{25}Y_{10}$  BMG. ( $m = 1$  for Newtonian flow).<sup>[175-179]</sup>

As discussed in SECTION 2.6.4, the steady-state flow stress can be described according to the transition state theory of flow stress, where the relation between  $\sigma_f$  and  $\dot{\epsilon}$  under uniaxial constant strain rate loading conditions is given by Eq. (2.32), namely,  $\eta = \sigma_f / 3\dot{\epsilon}$ , with  $\eta$  defined as the apparent viscosity parameter.<sup>[69,173]</sup> Using this relationship, the viscosity of the material for the specific test conditions was calculated according to the tensile test results and can be seen in Figure 3.43, which exemplifies the strain-rate dependence of the flow stress at various temperatures for the  $Mg_{65}Cu_{25}Y_{10}$  BMG.

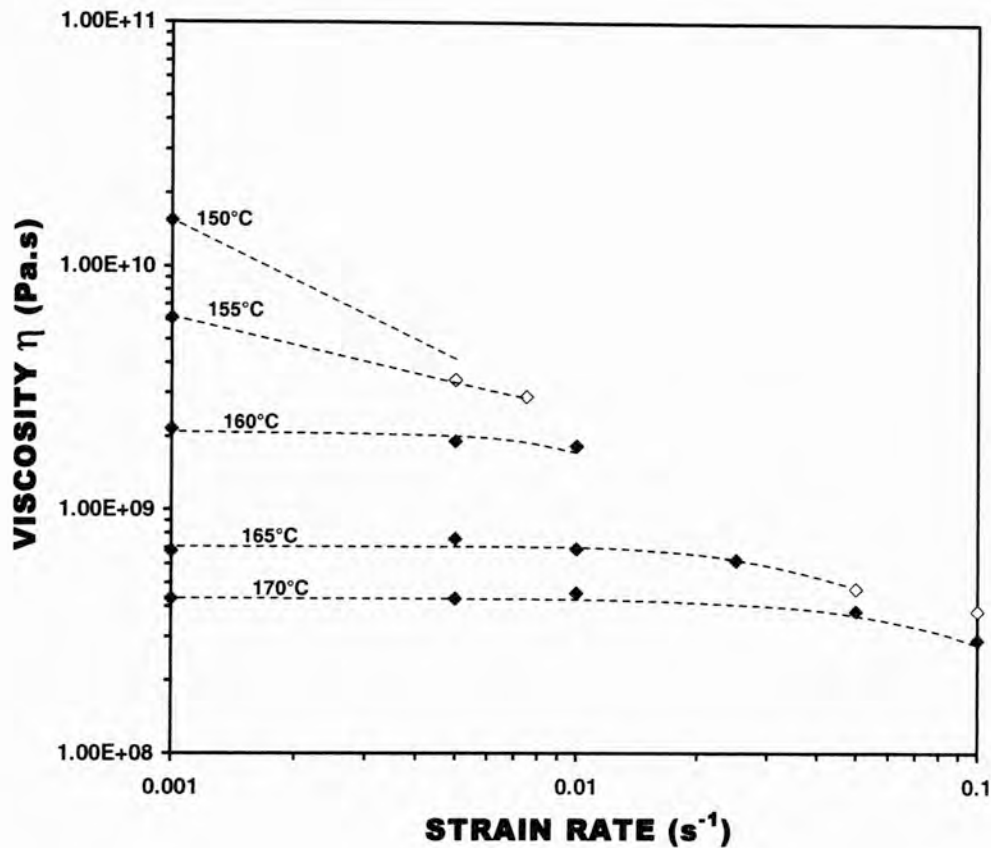


**Figure 3.43:** The effects of strain rate on viscosity in the SCL region for the  $Mg_{65}Cu_{25}Y_{10}$  BMG.

Here, it can be seen that the viscosity in the SCL region is independent of strain rate at lower strain-rates (suggesting Newtonian flow conditions) and temperatures between 160 °C and 170 °C, indicating Newtonian flow. As the strain rate increases, viscosity becomes dependent on strain rate and decreases in a linear fashion, indicating that flow conditions change from Newtonian to non-Newtonian, which is similar to the results found by Inoue and Kamawura indicated in Figure 2.34.<sup>[175,176]</sup>

### 3.9.5 Flow Characterisation of the $\text{Mg}_{65}\text{Cu}_{25}\text{Y}_{10}$ BMG using the Free Volume Model<sup>[180]</sup>

Free volume is defined as excess volume owing to the disordered state of the atomic configuration. The plastic deformation is attributed to atomic jumps into neighbouring holes or flow defects that exceed a critical size, to accommodate strain. Spaepen<sup>[180]</sup> showed that uniaxial flow behaviour of a metallic glass may be given by Eq. (2.34). Both the activation volume and frequency factor for a given deformation temperature were calculated from the experimental values of flow stress and strain rate using Eq. (2.34) (e.g. given in APPENDIX D). The results are given in Table 3.5. It can be seen that an increase in temperature results in an increase in the frequency of elementary defect jumps ( $\dot{\epsilon}_0$ ), with a corresponding decrease in the activation volume involved per atomic jump ( $V$ ). Here, the flow stress corresponds to the stress level for a given temperature at which the internal stresses are large enough to generate additional free volume, thereby resulting in a decrease in viscosity.

**Table 3.5:** Activation volume and frequency factor obtained from the experimental data fitted to equation (3.15).

Temperature (°C )	$\dot{\epsilon}_0$ ( s <sup>-1</sup> )	$V$ ( nm <sup>3</sup> )
160	$9.35 \times 10^{-4}$	0.331
165	$1.91 \times 10^{-2}$	0.329
170	$6.92 \times 10^{-2}$	0.268

Viscosity can also be defined in terms of the free-volume model by combining Eq. (2.32) with Eq. (2.34) to give:

$$\eta = \frac{\sigma_f}{3\dot{\epsilon}_0 \sinh(\sigma_f V / 2\sqrt{3} k_B T)} \quad (3.15)$$

Newtonian viscosity ( $\eta_N$ ) is expected at high temperatures and low stresses, so Eq. (3.15) can be rewritten as:<sup>[183,188]</sup>

$$\eta_N = \frac{2\sqrt{3}k_B T}{3\dot{\epsilon}_0 V} \quad (3.16)$$

Based on the work of Bletry et al.,<sup>[183,188]</sup> normalised viscosity ( $\eta/\eta_N$ ) can be determined by combining Eq. (3.15) with Eq. (3.16) to give:

$$\frac{\eta}{\eta_N} = \frac{\sigma_f V / 2\sqrt{3} k_B T}{\sinh(\sigma_f V / 2\sqrt{3} k_B T)} \quad (3.17)$$



Equation (3.17) was used to construct the viscosity master curve shown in **Figure 3.44** in terms of  $\eta/\eta_N$  as a function of  $\sigma_f V / 2\sqrt{3} k_B T$  for all homogeneous flow data (an example given in **APPENDIX D**). The master curve successfully demonstrates Newtonian flow in the supercooled state at higher temperatures and lower strain rates where normalised viscosity is unity, analogous to **Figure 3.42**. Conversely, higher strain rates resulted in a decrease in viscosity, showing a transition state from Newtonian flow to non-Newtonian flow. The critical strain rate for Newtonian flow was found to increase with increasing temperature. For example, deformation at a strain rate of  $10^{-2} \text{ s}^{-1}$  led to non-Newtonian flow at  $160^\circ\text{C}$  whereas, for the same strain rate, Newtonian flow was observed at  $170^\circ\text{C}$ .

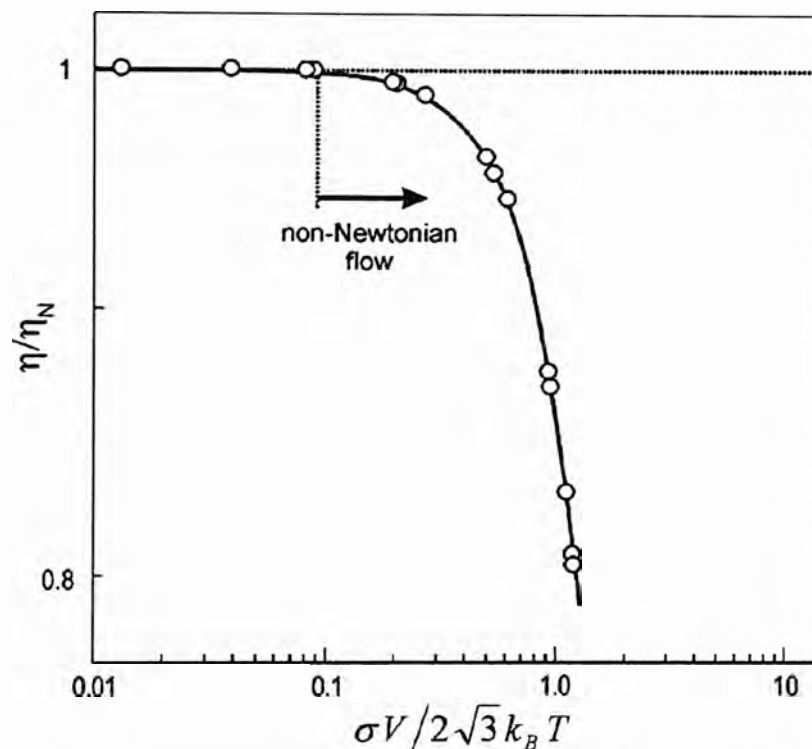


**Figure 3.44:** Master curve of normalised viscosity region for the  $\text{Mg}_{65}\text{Cu}_{25}\text{Y}_{10}$  BMG constructed using Eq. (3.17).

### 3.9.6 Fragility Determination of the $\text{Mg}_{65}\text{Cu}_{25}\text{Y}_{10}$ BMG Using the VFT Equation<sup>[60,66,67]</sup>

As discussed in **SECTION 2.3.2**, viscosity of a Newtonian fluid (i.e. a BMG in the Newtonian Flow regime) can be described using the VFT equation. Viscosity data generated from Newtonian flow results at  $170$ ,  $165$  and  $160^\circ\text{C}$ , was fitted using mathematical iteration to Eq. (2.8)  $\eta = \eta_o \exp[D^* T_o / (T - T_o)]$ , a variant of the VFT equation where  $T_o$  is the VFT-temperature at which the barriers with respect to flow would go to infinity and  $D^*$  is called the 'Fragility' parameter of the liquid. (**Figure 3.45**). By using iterative curve fitting for the three unknown constants using Origin Version 6.0, it was found that  $\eta_o = 3.031 \times 10^{-5} \text{ Pa.s}$ ,  $T_o = 257.97 \text{ K}$  and

$D^* = 21.64$ . These results are similar to those published by Busch et al.<sup>[60]</sup> for viscosity data generated by three point bending where  $\eta_o = 3 \times 10^{-5}$  Pa.s,  $T_o = 260$  K and  $D^* = 22.1$ .

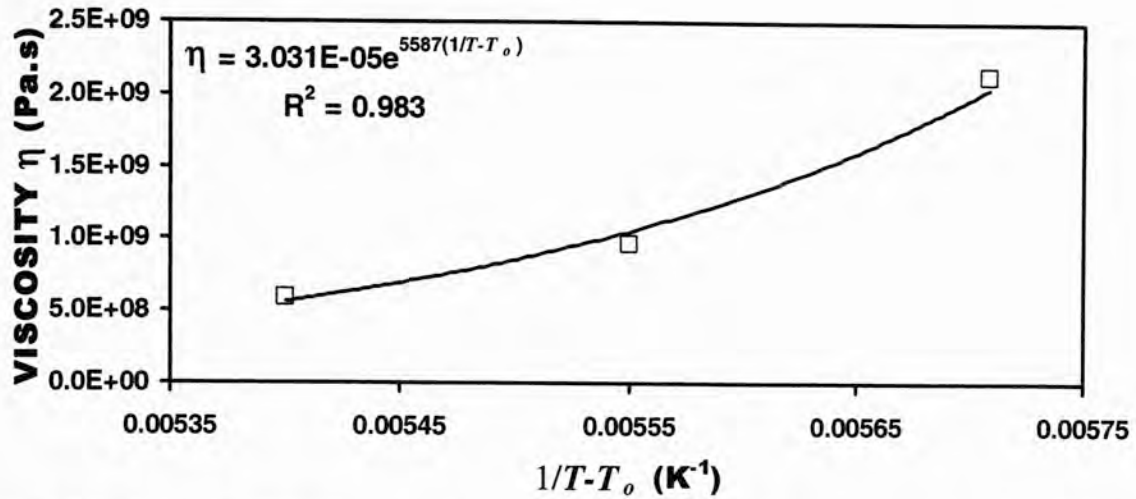


**Figure 3.45:** Curve fitted to viscosity data from the Newtonian flow regime using Eq. (2.8).

Another form of the VFT equation developed by Busch et al.<sup>[60]</sup> Eq. (2.10) combines the kinetics of glass transition to the equilibrium viscosity. Here, the dependence of  $T_g$  on the inverse of heating rate,  $\beta$ , is given by  $\beta^{-1} = \tau_o \exp [D^* T_o / (T - T_o)]$ . By using DSC data (Figure 3.8) to determine the onset of  $T_g$  and using the same mathematical iteration methodology, a curve was fitted (Figure 3.46) to these data points.

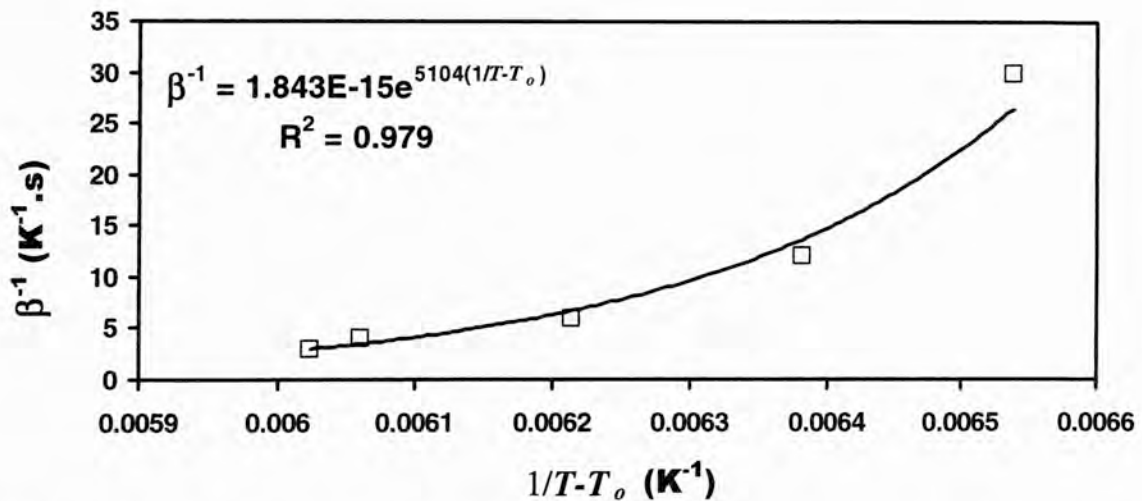


**Figure 3.46:** Curve fitted to heating rate and  $T_g$  onset data using the modified VFT Eq. (2.10).

The solution for the three unknown constants using Origin Version 6.0, found that  $\tau_o = 1.8 \times 10^{-15}$  Pa.s,  $T_o = 258.2$  K and  $D^* = 19.8$ . These results are comparable to those found using viscosity data in Figure 3.45. These values may now be used to compare the  $Mg_{65}Cu_{25}Y_{10}$  BMG to other glass-forming systems with respect to glass fragility for commercial applications.



### 3.9.6. Strain Rate Sensitivity and Superplastic Flow Behaviour of the $\text{Mg}_{65}\text{Cu}_{25}\text{Y}_{10}$ BMG

The independence of viscosity with strain rate has important practical consequences when working BMGs in the SCL region. The relationship between log flow stress ( $\sigma_f$ ) and log strain rate ( $\dot{\epsilon}$ ) in the SCL region for the  $\text{Mg}_{65}\text{Cu}_{25}\text{Y}_{10}$  BMG is shown in **Figure 3.42** and can be expressed by Eq. (2.30),  $\sigma_f = K\dot{\epsilon}^m$ , where the slope of a tangent to the curve for any given temperature data set corresponds directly to the strain-rate sensitivity ( $m$ ); an  $m$ -value of unity indicates ideal Newtonian flow,<sup>[175-179]</sup> whereby the material can be worked homogeneously with the highest degree of efficiency.<sup>[181,182]</sup> The variation of the  $m$ -value in the supercooled liquid region with respect to temperature and strain rate is shown in **Figure 3.47** (map construction method is shown in APPENDIX E). It can be seen in **Figure 3.47** that the variation in the strain rate sensitivity correlates well with conditions pertaining to Newtonian flow ( $m = 1$ ), non-Newtonian flow ( $0.6 < m < 1$ ) and brittle failure ( $m < 0.6$ ). It can be seen that these results correspond directly with the boundaries determined using the free volume model, thereby supporting current viscosity theory of BMGs and the free volume model for the  $\text{Mg}_{65}\text{Cu}_{25}\text{Y}_{10}$  BMG.

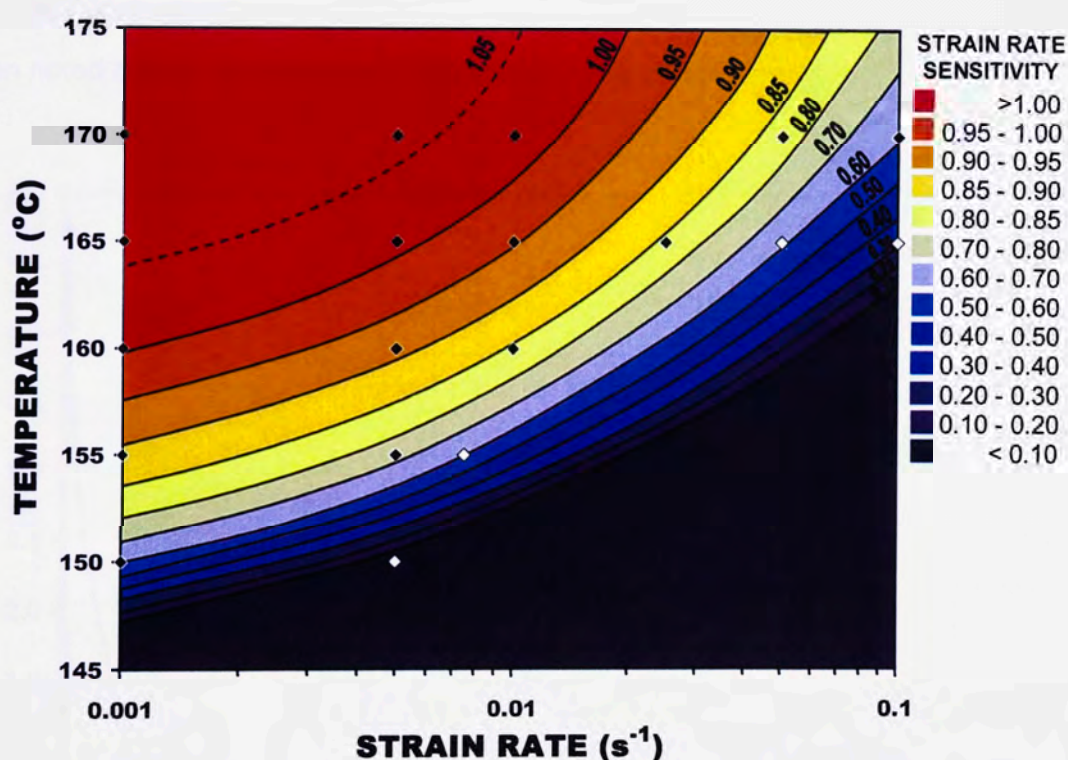


**Figure 3.47:** The variation of the strain rate sensitivity exponent ( $m$ ) in the supercooled liquid region with respect to temperature and strain rate.

It is of particular interest that the  $m$ -value for the present BMG approaches a value greater than unity in some cases above 165 °C. It is pertinent to note that  $m$ -values greater than unity are usually associated with microstructural instability.<sup>[261]</sup> Similar observations have been made in



the  $\text{Pd}_{40}\text{Ni}_{40}\text{P}_{20}$  BMG alloy, at temperatures higher in the SCL region where crystallisation is known to occur.<sup>[261]</sup> An  $m$  value greater than unity has also been observed in some ceramics deformed at high temperatures.<sup>[262]</sup>

### 3.9.7 The Effect of Temperature, Strain and Time on Plastic Flow

During tensile testing, the possibility of crystallisation was encountered both at higher test temperatures and lower strain rates (i.e. longer time at temperature). An eventual rise in flow stress is generally attributed to the strengthening effect of nano-crystallisation of the supercooled liquid, where the viscosity of the partially nanocrystalline solid is higher than that of a fully amorphous structure at elevated temperatures,<sup>[175,176]</sup> due to a composite effect.<sup>[185,263,264]</sup>

In a series of tests carried out at temperatures ranging from 160 to 170 °C and a strain rate of  $1 \times 10^{-3} \text{ s}^{-1}$ , there was a marked rise in flow stress prior to the predicted onset of (static) crystallisation (determined by isothermal DSC experiments), as shown in **Figure 3.48**. This rise in the flow stress prior to the onset of static crystallisation (indicated by the DSC curves in **Figure 3.48**) was attributed to deformation-induced crystallisation. An identical phenomenon has been noted during homogeneous deformation of other BMG systems.<sup>[69,183,244]</sup>

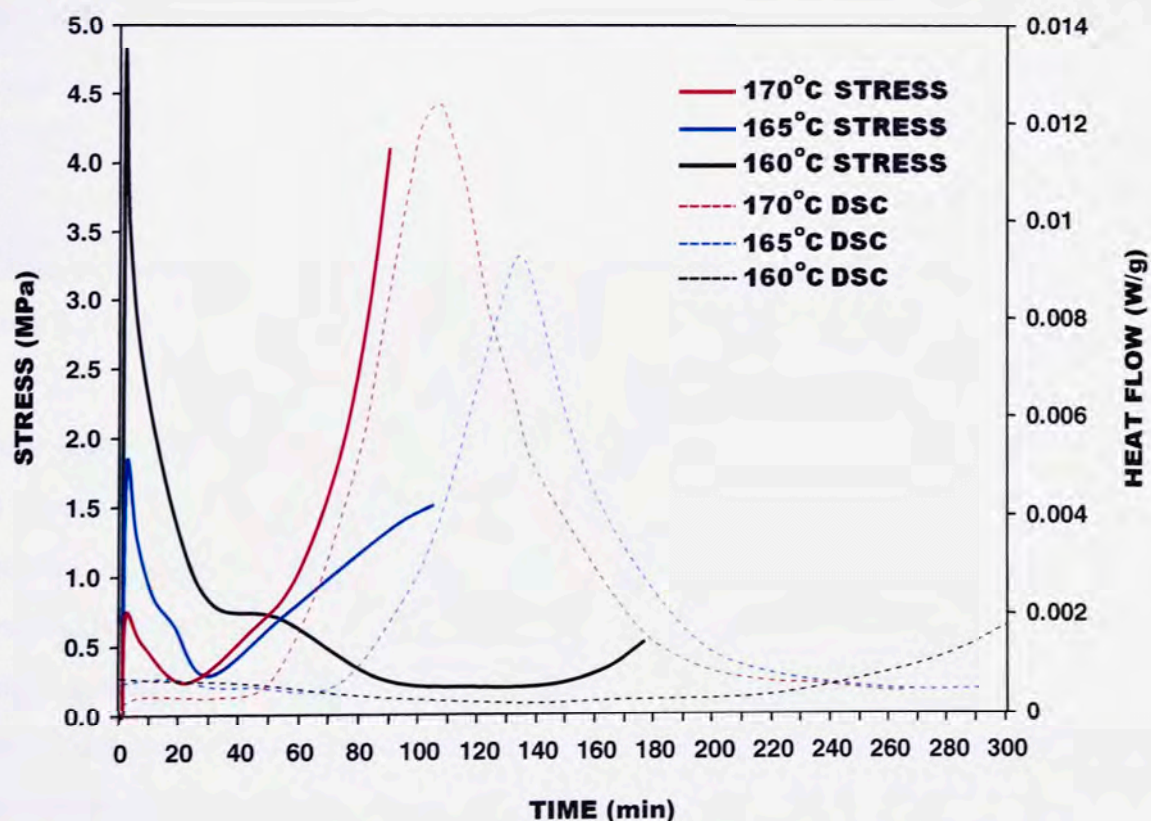


**Figure 3.48:** Stress –time plot of samples tested at a strain rate of  $10^{-3} \text{ s}^{-1}$ , showing the effect of dynamic (strain induced) crystallisation compared to static crystallisation (isothermal DSC curves) for the  $\text{Mg}_{65}\text{Cu}_{25}\text{Y}_{10}$  BMG.



There are two major mechanisms proposed for the reduction of crystallisation time during deformation in the SCL region.<sup>[265]</sup> The first mechanism is described as deformation-induced disordering, whereby the extent of atomic diffusion necessary for nucleation is enhanced due to the increase in free volume caused by plastic flow<sup>[265]</sup> (nucleation being diffusion related).<sup>[57]</sup>

The second mechanism is described as non-equilibrium phase separation caused by plastic deformation which is argued to generate local compositional changes resulting in regions exhibiting a reduced viscosity compared to that of the nominal composition. Such behaviour is expected to induce flow localisation in these low-viscosity regions causing further decomposition. Due to the thermodynamic instability of BMGs in the SCL region, phase separation into two or more slightly different supercooled liquids may occur and trigger primary crystallisation.<sup>[266-269]</sup>

A related phenomenon was also noted for samples tested at a temperature of 170 °C and strain rate of  $5 \times 10^{-3} \text{ s}^{-1}$ , where flow could be described as segmented or serrated, as shown in **Figure 3.49**.

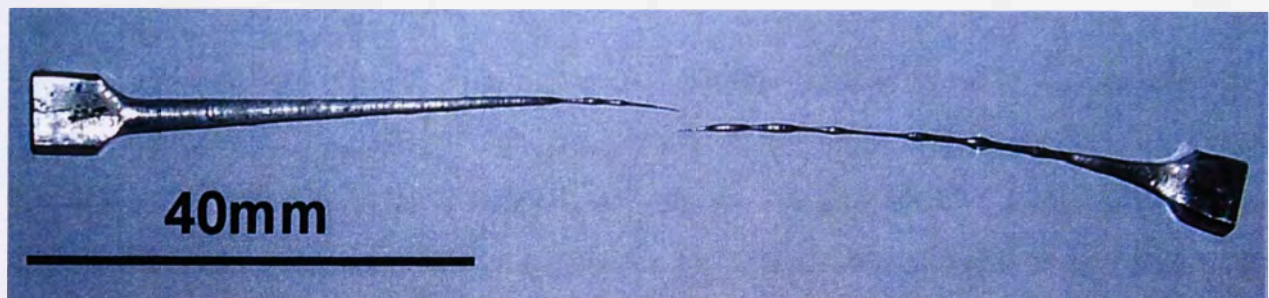


**Figure 3.49:** *Segmented or serrated flow in a sample tested at 170 °C and  $5 \times 10^{-3} \text{ s}^{-1}$ .*

**Figure 3.50** shows stress-strain and stress-time plots for samples tested at a temperature of 170 °C and strain rates of  $5 \times 10^{-3} \text{ s}^{-1}$  and  $1 \times 10^{-3} \text{ s}^{-1}$ , where it can be seen that such serrated flow behaviour is strain related rather than time dependent, although the strengthening effect (crystallisation) appears to be suppressed in the sample deformed at the higher strain rate. Similar serrated flow behaviour was observed during the deformation of  $\text{Zr}_{65}\text{Al}_{10}\text{Ni}_{10}\text{Cu}_{15}$  metallic glass. These fluctuations in flow stress were explained to be the result of interactions between nanocrystalline agglomerates in the amorphous matrix, whereby when these agglomerates collide, stress increases due to the increase in viscosity and conversely decreases as they glide past one another.<sup>[185]</sup>



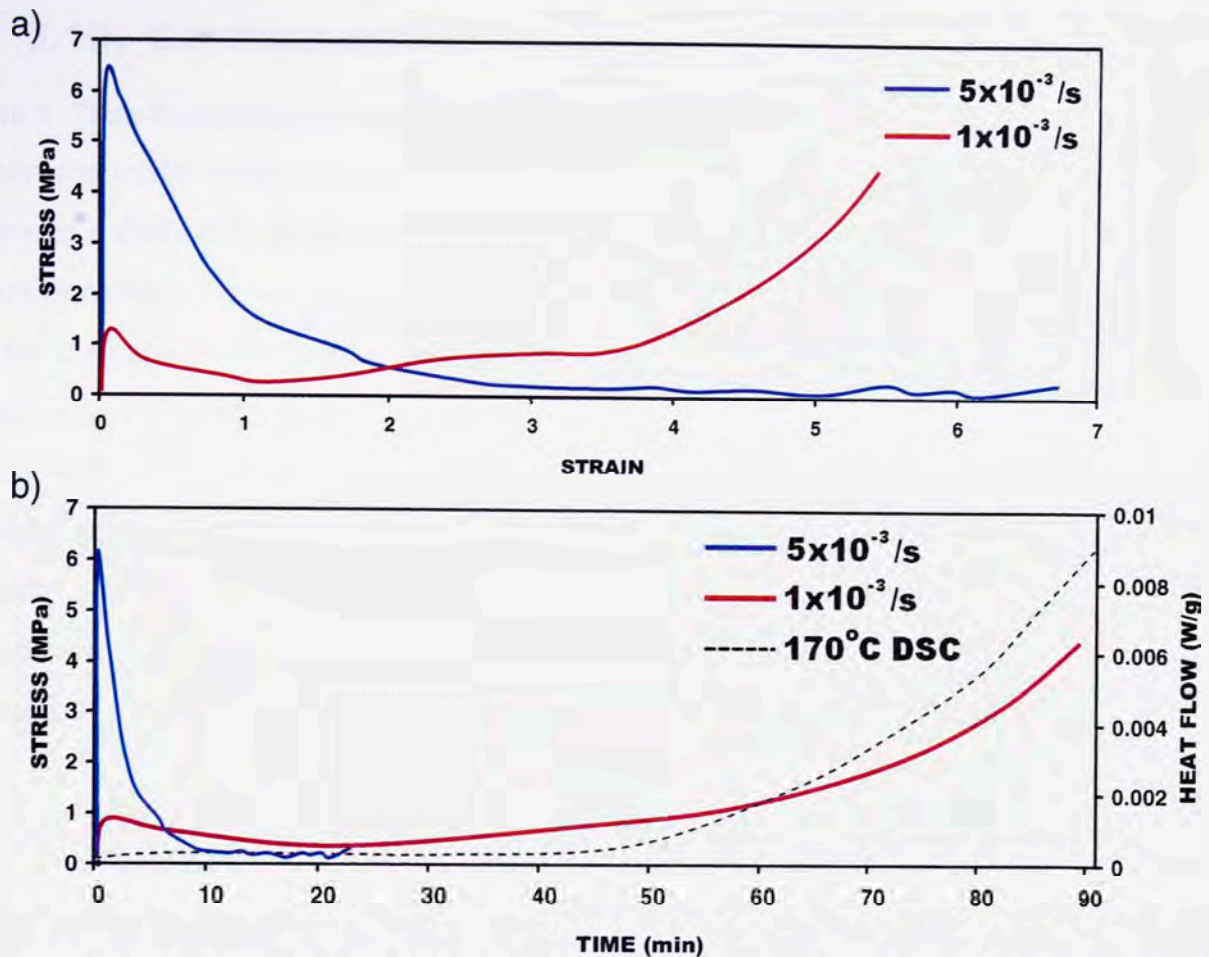


**Figure 3.50:** a) Stress-strain plot and b) Stress-time plot for samples tested at a temperature of 170 °C and at strain rates of  $5 \times 10^{-3} \text{ s}^{-1}$  and  $1 \times 10^{-3} \text{ s}^{-1}$ .

Temperature/time and crystallisation during deformation was also found to play an important role in the ductility of the BMG. At high strain rates (shorter test periods) at low temperatures in the SCL region, the samples remained fully amorphous and showed exceptional ductility (**Figure 3.51**). However, samples that experienced any degree of crystallisation during straining were found to fracture at elongations less than 1300% and had a tendency to break during post-test handling, indicating that the partially crystalline structure exhibited relatively poor ductility.

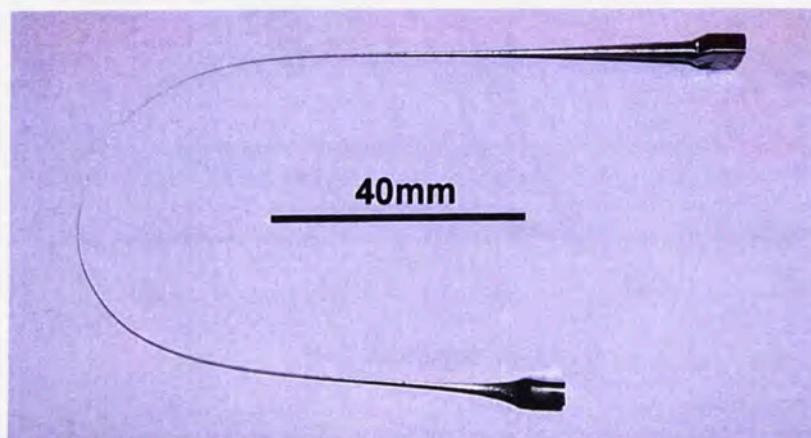


**Figure 3.51:** Tensile sample tested at a temperature of 160 °C and strain rate of  $5 \times 10^{-3} \text{ s}^{-1}$  showing extraordinary ductility and flexibility.



### 3.10. CRYSTALLISATION BEHAVIOUR OF THE $\text{Mg}_{65}\text{Cu}_{25}\text{Y}_{10}$ BMG

#### 3.10.1 Time-Temperature-Transformation Diagram Development

Using the model developed by Takeuchi et al.<sup>[75]</sup> (SECTION 2.4.5) to predict the position of the C-curve in a BMG TTT diagram with respect to the non-equilibrium supercooled liquid phase a transformation curve was constructed represented by the solid blue line in **Figure 3.52**. Included in the diagram are the liquidus (480 °C) and glass transition (148 °C) temperatures (solid red lines) and the onset (dashed black line) and completion (solid black line) of crystallisation according to isothermal annealing data (**Figure 3.9**). Also included in the diagram are the cooling curves from the wedge casting (**Figure 3.10**) of: (i) the amorphous 1.2 mm section (dotted black line); (ii) the partially crystalline 4.7 mm section (dashed black line), and (iii) the crystalline 8.2 mm section (solid black line). It can be seen that there is a strong correlation between the curve predicted by the Takeuchi model and the experimental data.

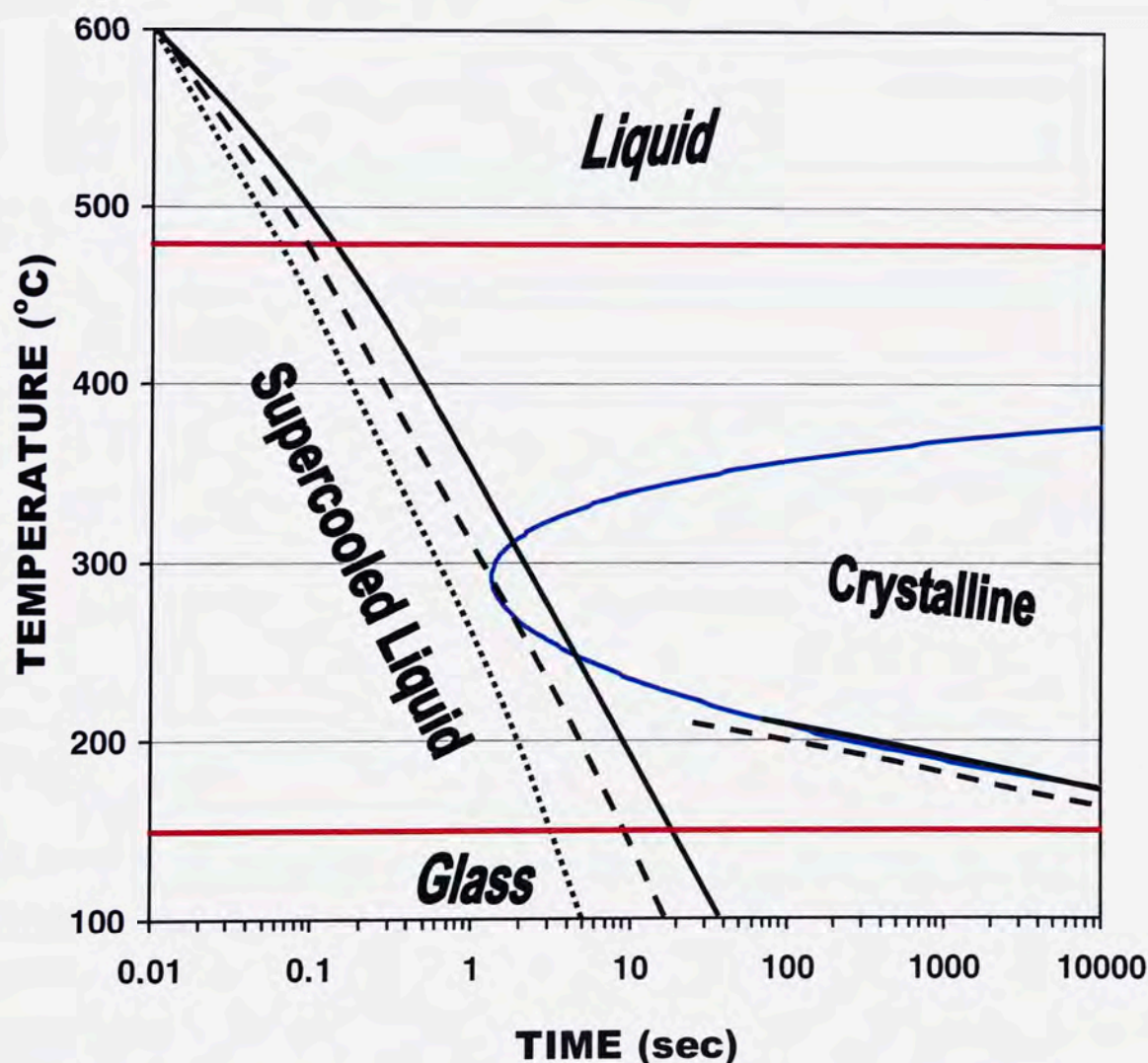


**Figure 3.52:** Time-temperature-transformation diagram including cooling curves from the wedge casting, isothermal annealing data showing the onset and completion of crystallisation at given temperatures and the C-curve predicted by the Takeuchi model.<sup>[75]</sup>



### 3.10.2 Preliminary Static Crystallisation Investigation

To determine the phases present and the order in which these phases appear during crystallisation, a series of annealing experiments were carried out on the  $\text{Mg}_{65}\text{Cu}_{25}\text{Y}_{10}$  BMG. Amorphous samples were annealed at a temperature of 230 °C for 3 and 9 minutes. These samples were then analysed using XRD to determine the different crystalline phases present (**Figure 3.53**). It has been demonstrated that the first phase to form is  $\text{Mg}_2\text{Cu}$ ; this is associated with the diffusivity of individual atomic species and directly related to atomic radius, whereby smaller atoms such as copper (~128 pm) may diffuse more readily through the amorphous structure. The formation of  $\text{Mg}_2\text{Cu}$  during crystallisation of  $\text{Mg}_{60}\text{Cu}_{30}\text{Y}_{10}$  between  $T_g$  and  $T_x$  was reported by Linderoth et al.,<sup>[270]</sup> which is supported in the present work. From this data it was determined that there are five possible phases likely to be present in the partially crystallised alloy, namely:  $\text{Mg}_2\text{Cu}$ , Mg,  $\text{Cu}_2\text{Y}$ ,  $\text{Mg}_{24}\text{Y}_5$  and residual amorphous  $\text{Mg}_{65}\text{Cu}_{25}\text{Y}_{10}$ .

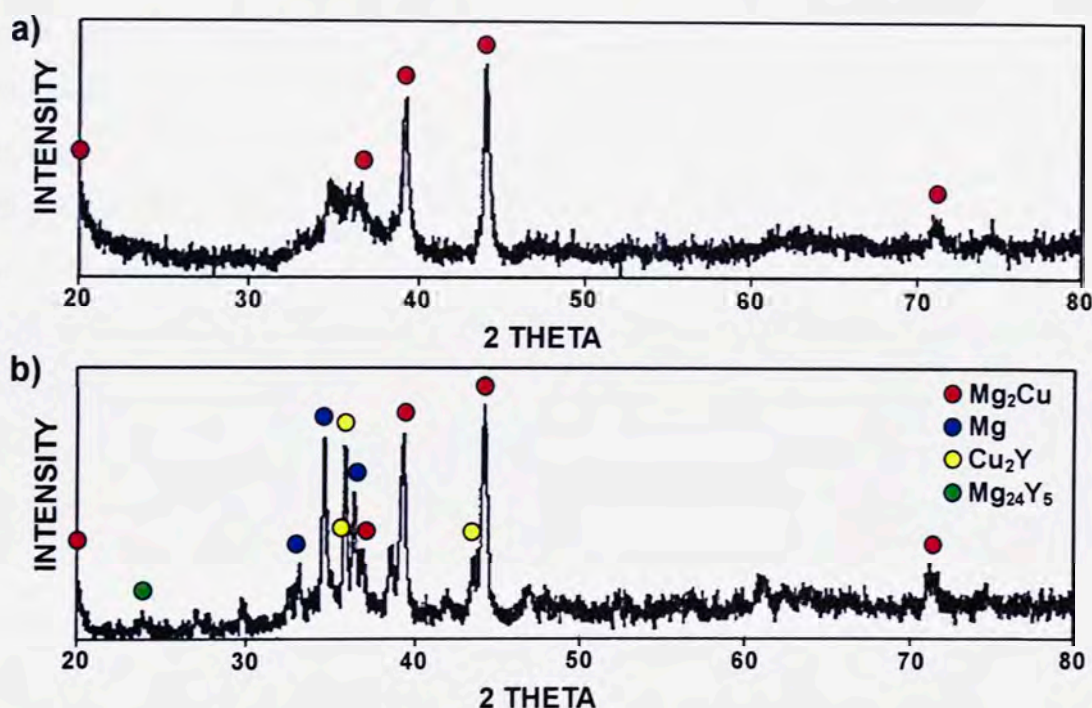


**Figure 3.53:** XRD traces from amorphous  $\text{Mg}_{65}\text{Cu}_{25}\text{Y}_{10}$  samples annealed for a) 3 min and b) 9 min at 230°C.

### 3.10.3 Transmission Electron Microscopy (TEM) and Atom Probe Tomography (APT)

In order to confirm that a nanocrystalline structure was generated during tensile straining, and for gaining an insight into the mechanisms associated with dynamic crystallisation in the  $\text{Mg}_{65}\text{Cu}_{25}\text{Y}_{10}$  BMG, a series of samples suitable for transmission electron microscopy (TEM) analysis and atom probe tomography (APT) were milled from various samples believed to contain crystallites using a focused ion beam. The 'micropost release' technique<sup>[271]</sup> involves milling a post from the sample with the area of interest at the tip, detaching it from the bulk, then

transferring, mounting and securing it to the edge of a TEM slot grid, which is then prepared for further analysis. APT is a microstructural characterisation technique that uses the principle of field ion evaporation (using a local electrode atom probe or LEAP) to remove atoms from a sample by applying a high electric field to the sample tip.<sup>[271]</sup> Once evaporated, the species and position (in 3-dimensions) of each individual atom can be identified with the aid of a time-of-flight mass spectrometer and a position sensitive detector.

#### 3.10.4 Sample Preparation for Atom Probe Tomography

Samples suitable for both TEM and APT analysis were prepared using a FEI XP200 dual beam FIB, which uses gallium ions to 'mill' (removal of material) a specimen of desired dimensions. The specific technique used to generate these samples is termed the 'micropost release technique', as developed by McGrouther et al.<sup>[271]</sup>

The initial step in the formation of a micropost is the milling of two cuts each made at 45° relative to the surface of the material and which converge at some depth below the surface as seen in **Figure 3.54a**). The length of these cuts is typically 50 µm. The spacing of the cuts and their depth (typically 0.5 µm) are carefully chosen so that they intersect, thereby creating a support bridge. Following this step, further milling/thinning of the sample at one end is carried out to create a 'tapered shank' type sample. This methodology results in the milling/removal of a relatively large volume of material, hence a relatively large ion beam current (7.0 nA) was used to minimise sample preparation time. A finished sample for this stage of preparation can be seen in **Figure 3.54b**), which indicates a sample tip size of around 260 nm.

The following step of sample preparation requires the sample to be removed from the bulk material. This is achieved by removing the bulk sample from the FIB chamber and using a micromanipulator. A hot-drawn glass needle (sharp tip) was used on the end of a robotic micromanipulator to break the sample away from the bulk material. The loosened sample was attracted to the glass needle by static forces, where it is then lifted and placed on to the smooth inner edge of a modified 1x2 mm copper TEM slot grid, as shown in **Figure 3.54c**). The modified TEM slot grid was placed back into the FIB where the base of the sample was welded in place using the in-situ platinum deposition gas injection system, as shown in **Figure 3.54d**). Exposing the post to a 30 keV annular mill produced a uniform circular cross section that is required to produce a symmetric electric field around the tip when using the LEAP. After annular milling, a 5 keV clean up mill with circular cross section (not annular) was used to remove material damaged by the 30 keV ion beam, which further sharpens the sample tip to a diameter



less than 50 nm. The tip finished with this mill can be seen in the SEM image in **Figure 3.54e**). Once the sample tip was sufficiently sharpened, further platinum was deposited around the base of the post to secure it to the grid, ready for both TEM and APT analysis.

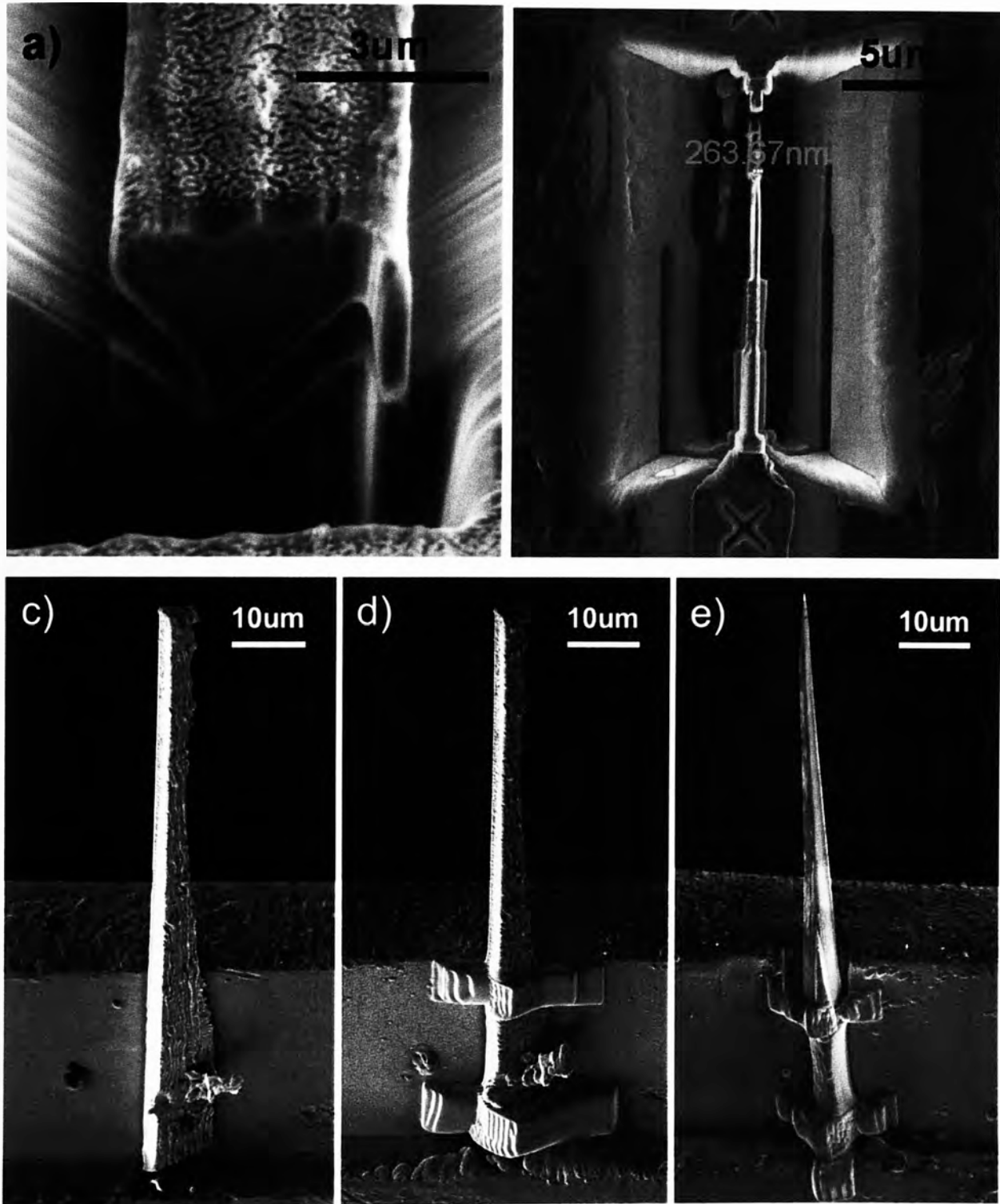


**Figure 3.54:** a) The two initial  $45^\circ$  cuts made relative to the bulk sample surface, b) a 'tapered shank' micropost milled from the initial 'support bridge', ready to be removed from the bulk sample, c) micropost placed on a modified copper TEM slot grid, d) platinum deposited over the micropost to hold it in place and e) finished atom probe tip after annular milling and 5 keV 'clean up' mill.

### 3.10.5 APT Sample Investigation by TEM

An analysis of the APT micropost samples using TEM showed that the samples held at temperatures of 170 -160 °C and strained at  $1 \times 10^{-3} \text{ s}^{-1}$  were indeed nanocrystalline. **Figure 3.55a)** shows a dark field TEM image of a  $\text{Mg}_{65}\text{Cu}_{25}\text{Y}_{10}$  micropost milled from the strained region of a tensile sample which had undergone an elongation of 534% tested at 170 °C at a strain rate of  $1 \times 10^{-3} \text{ s}^{-1}$ , where regions of nanocrystals that range in size from 20-60 nm were evident. **Figure 3.55b)** shows a similar image from the strained region of a tensile sample which had undergone an elongation of 638% during testing at 165 °C at a strain rate of  $1 \times 10^{-3} \text{ s}^{-1}$ , where nanocrystals of size 7-20 nm can be seen.

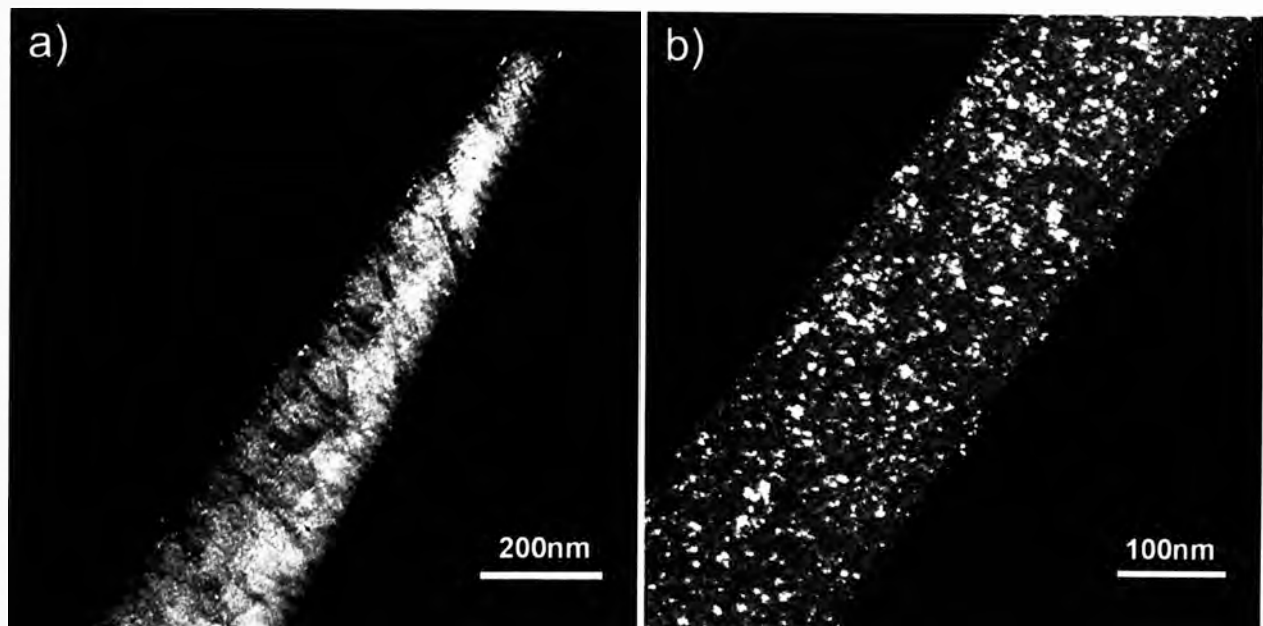


**Figure 3.55:** Dark field TEM micrographs of APT samples milled from the strained regions of tensile samples tested at a) 170 °C and b) 165 °C at a strain rate of  $1 \times 10^{-3} \text{ s}^{-1}$

**Figure 3.56** shows a bright field TEM micrograph of a micropost milled from the strained region (sample had undergone a strain of 1050%) of a sample tensile tested at 160 °C at a strain rate of  $1 \times 10^{-3} \text{ s}^{-1}$ . Here, nanocrystals ranging in size from 2-6 nm are evident. Also highlighted in this figure is the apparent depth of ion damage ( $\sim 5.8 \text{ nm}$ ) from the final 5 keV milling process and (inset) a diffraction pattern of the tip region, revealing a number of diffraction reflections indicative of crystallites, and, both broad and narrow halo ringlets around the transmitted electron beam characteristic of a primary amorphous phase and several altered amorphous regions, which may exhibit short range ordered atomic domains.

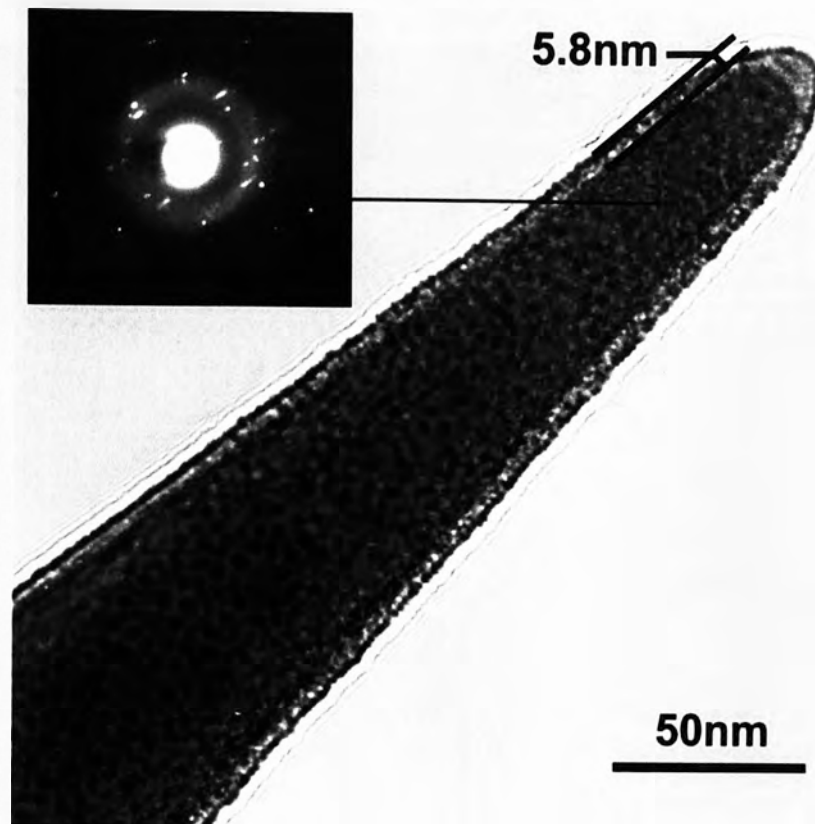


**Figure 3.56:** A bright field TEM micrograph of the APT tip milled using a focused ion beam from the strained region (1050% strain) of a tensile sample held at 160 °C and strained at a rate of  $1 \times 10^{-3} \text{ s}^{-1}$  for 180 minutes and (inset) the SAD pattern from the area indicated.

### 3.10.6 APT Analysis

As discussed previously, APT is a microstructural characterisation technique that uses the principle of field ion evaporation to remove atoms from a sample by applying a high electric field to the sample tip. To induce field ion evaporation, a voltage between the local electrode and sample, in the order of 10 kV is applied. Under these conditions, electric fields in the order of 20-40 V/nm can only be generated if an electrically conductive sample is produced in the shape of needle with a circular cross section, a taper angle of less than  $5^\circ$  and tip radius less than 50 nm. Once evaporated, the species and position (in 3-dimensions) of the atoms can be identified with the aid of a time-of-flight mass spectrometer and a position sensitive detector.

From the majority of samples tested, no atom probe data was obtained as the posts failed during the initial stages of analysis in the LEAP, usually due to the post breaking under the mechanical force generated by the applied electric field. **Figure 3.56** is a bright field TEM micrograph of the post from which the first reported APT results using the 'micropost release technique' have been obtained. **Figure 3.57** shows the APT results, which consist of over  $5 \times 10^7$  atoms, where the solvent atoms, magnesium, are removed from the data set for ease of analysis. Copper and yttrium atoms are represented by the green and red spheres, respectively.



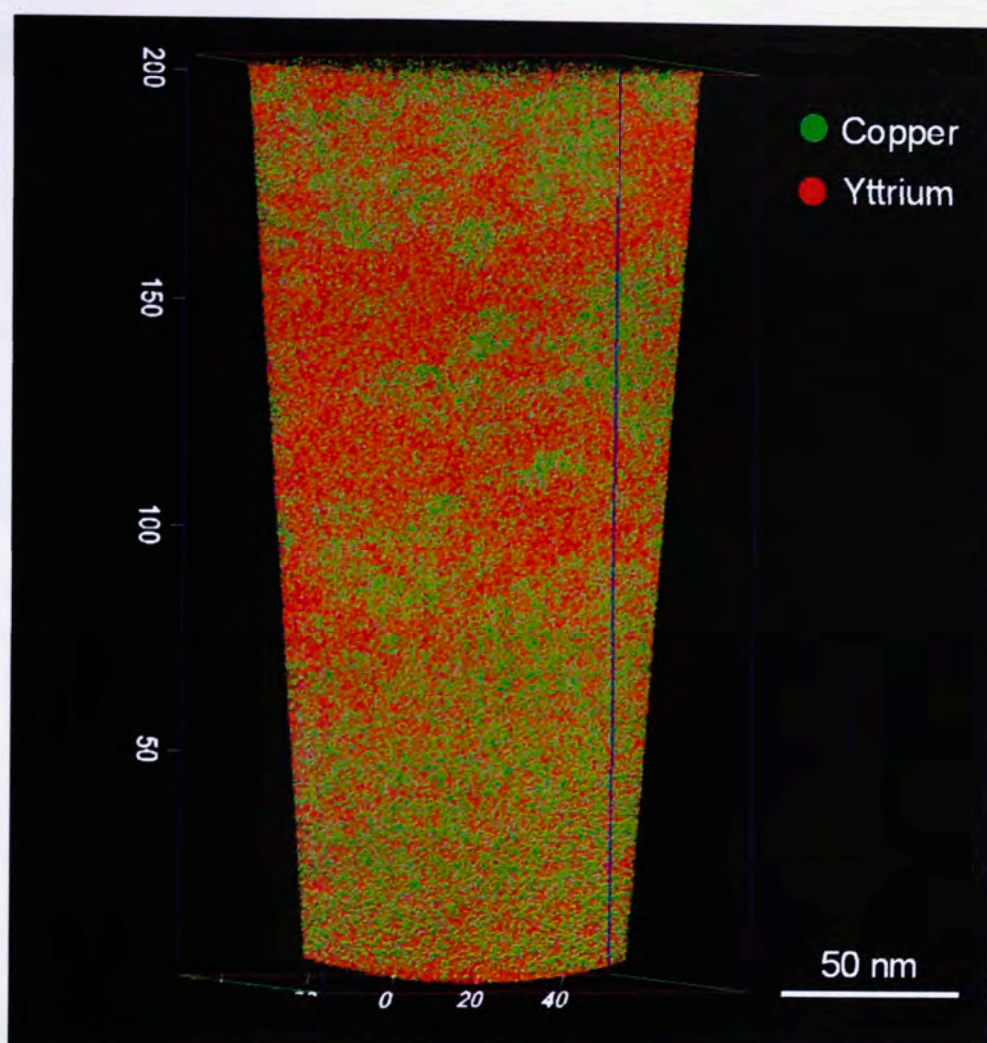


**Figure 3.57:** Atom probe data set consisting of around  $5 \times 10^7$  atoms taken from the APT tip shown in **Figure 3.56**. (Cell dimensions in nm).

From this data set (**Figure 3.57**), distinct nanocrystalline regions of high copper or yttrium concentrations are evident, indicating segregation either prior to or during crystallisation. If this is so in the former case, it would enforce the theory described in **SECTION 3.9.7**, whereby the reduction of crystallisation time during deformation is believed to be due to non-equilibrium phase separation into two or more slightly different supercooled liquids caused by plastic deformation this phenomenon is argued to trigger primary crystallisation.<sup>[266-269]</sup>

From the central region of this data set, a sample data set  $50 \times 50 \times 120$  nm was further analysed and shown in **Figure 3.58**. An iso-concentration surface set at a concentration of 15% Y is shown in red and defines a boundary between two distinct composition regions; these regions are likely to contain 2-6 nm diameter nanocrystals (as shown in the TEM image of the tip in **Figure 3.56**). Small regions devoid of copper atoms (green) indicate a high concentration of yttrium and/or magnesium.



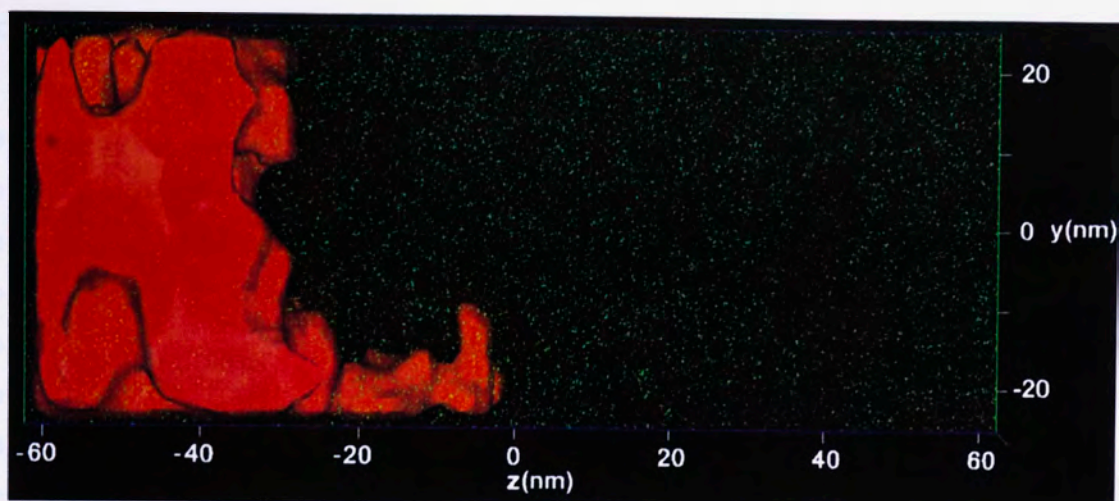


**Figure 3.58:** A sample data set ( $50 \times 50 \times 120$  nm) taken from the  $5 \times 10^7$  atoms set in **Figure 3.56**. An iso-concentration surface set at a concentration of 15% Y is shown in red, defining the boundary between two distinct regions.

From this sample data set, a composition sample of diameter 10 nm was taken from the region indicated in **Figure 3.59** (n.b. the existence of Cu (green) and Y (red) rich regions), from which an atomic composition analysis was carried out, as shown in **Figure 3.60**.

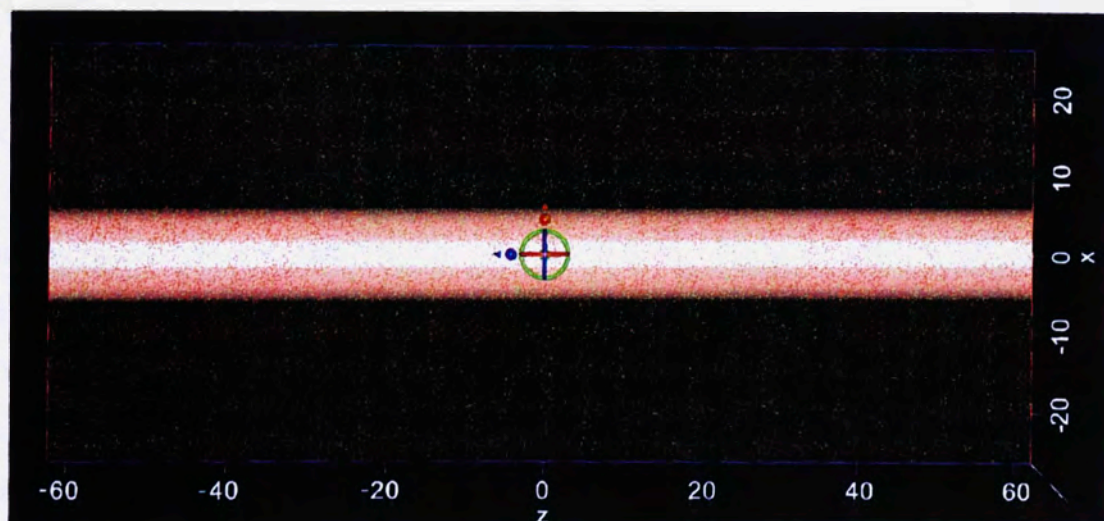


**Figure 3.59:** A composition sample of diameter 10nm taken from the sample data set in **Figure 3.58**.

From previous work (**SECTION 3.10.2**), it is known that at least five possible phases may be present in the partially crystallised sample:  $\text{Mg}_2\text{Cu}$ , Mg,  $\text{Cu}_2\text{Y}$ ,  $\text{Mg}_{24}\text{Y}_5$  and residual amorphous  $\text{Mg}_{65}\text{Cu}_{25}\text{Y}_{10}$ . However, if the theory of non-equilibrium phase separation into two or more slightly different supercooled liquids caused by plastic deformation<sup>[266-269]</sup> is tenable, the presence of amorphous phases of compositions varying slightly from the base  $\text{Mg}_{65}\text{Cu}_{25}\text{Y}_{10}$ ,



glass should exist, which may explain the presence of additional halo ringlets in the transmitted electron beam in the SAD pattern in **Figure 3.56** which are not evident in **Figure 3.28c**.

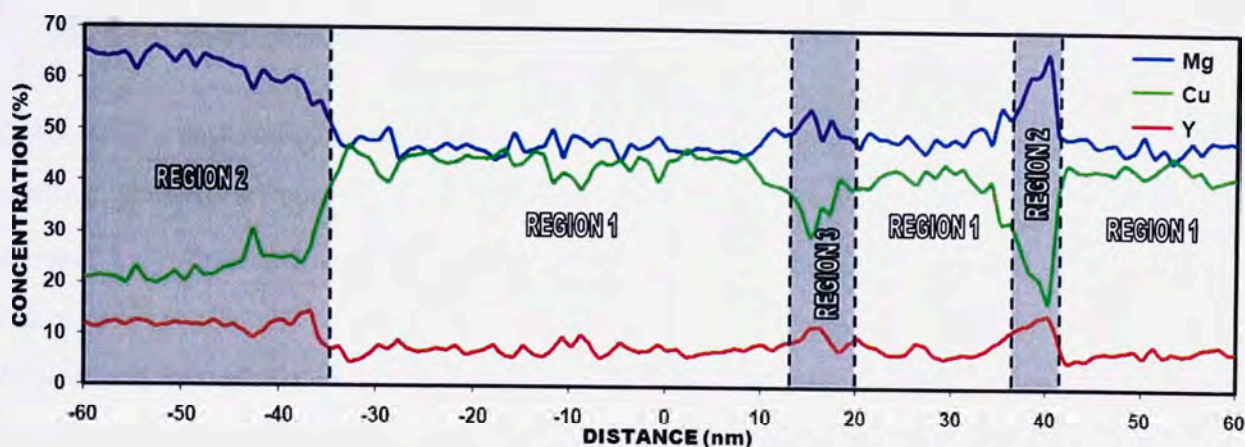


**Figure 3.60:** Atomic composition map generated from the region depicted in **Figure 3.59**.

Further analysis of **Figure 3.60** reveals that the areas in labelled Region 1 have an average composition of  $\text{Mg}_{50}\text{Cu}_{42}\text{Y}_{8.5}$ . This composition breaks down to  $\text{Mg}_{50}\text{Cu}_{25}$  (or twenty-five parts  $\text{Mg}_2\text{Cu}$  stoichiometry) and  $\text{Cu}_{17}\text{Y}_{8.5}$  (eight and one half parts  $\text{Cu}_2\text{Y}$ ). Based on static crystallisation knowledge (**SECTION 3.10.2** and literature data),<sup>[270]</sup>  $\text{Mg}_2\text{Cu}$  phase is expected to form first, (which is also related to the diffusivity of the smaller Cu atom of radius 128 pm).

Region 2 is associated with magnesium (atomic radius 160 pm) and yttrium (atomic radius 180 pm) rich regions, as depicted in the iso-concentration surface map in **Figure 3.58**. These regions approach an average atomic concentration of  $\text{Mg}_{65}\text{Cu}_{20}\text{Y}_{15}$ , which is similar to the nominal composition. This composition breaks down to  $\sim\text{Cu}_{20}\text{Y}_{10}$  (ten parts  $\text{Cu}_2\text{Y}$ ), one part  $\text{Mg}_{24}\text{Y}_5$ , and the remainder, forty-one parts crystalline Mg. Based on static crystallisation results and atomic diffusivity with respect to atomic radii, these regions are expected be the last to crystallise, and may contain residual amorphous regions close to  $\text{Mg}_{65}\text{Cu}_{25}\text{Y}_{10}$  stoichiometry, as suggested by the numerous diffuse rings seen in the SAD pattern in **Figure 3.56**.

Finally, region 3 shows a composition that lies between that of regions 1 and 2 of approximately  $\text{Mg}_{53}\text{Cu}_{35}\text{Y}_{12}$ . This region is expected to be a crystalline region exhibiting a transition in stoichiometry between region 1 and 2, or a region developing from the amorphous state similar to the original amorphous composition generated by non-equilibrium phase separation.



## SECTION 4 - PRODUCTION AND PROPERTIES OF A CALCIUM-BASED BMG

### 4.1. BACKGROUND

Calcium is a reactive alkaline earth metal and usually used in metallurgical processes as an alloying addition to purify iron melts by scavenging impurities<sup>[272]</sup> or in the refining of lead alloys.<sup>[273]</sup> Calcium has one of the largest atomic sizes among the elements (~197.6 pm) and has a low density (1540 kg/m<sup>3</sup>). Calcium-based amorphous alloys were first reported by St. Amand and Giessen in 1978.<sup>[10]</sup> They discovered a high glass-forming tendency in seven binary Ca-alloy systems occurring over broad composition ranges.

Ca-based BMGs are a relatively new and unique group of light-weight amorphous alloys. The first Ca-based BMGs were reported by Inoue and coworkers in 2002, where they produced fully amorphous rods with a maximum diameter of 4 mm for two ternary alloys, Ca<sub>57</sub>Mg<sub>19</sub>Cu<sub>24</sub> and Ca<sub>60</sub>Mg<sub>20</sub>Ag<sub>20</sub>,<sup>[36]</sup> and 7 mm for a quaternary alloy, Ca<sub>60</sub>Mg<sub>20</sub>Ag<sub>10</sub>Cu<sub>10</sub>,<sup>[37]</sup> by conventional copper mould casting techniques. More recently, numerous multi-component glass-forming systems based on Ca have been explored, such as the Ca-Al-(Mg, Zn, Cu, Ag),<sup>[274]</sup> Ca-Mg-(Zn, Cu, Ag, Ni),<sup>[227,275-277]</sup> and various combinations of these systems, which can be seen in **Table 4.1**. Ca-based BMGs are potential candidates for a range of applications as they exhibit a high glass-forming ability/stability as well as unique physical and chemical properties including low densities (2000-2200 kg/m<sup>3</sup>), relatively high compressive yield strengths (~350 MPa), low Young's moduli (17-20 GPa), low glass transition temperatures (100-130 °C), large supercooled liquid regions (22–66 °C) and superplastic behaviour within the supercooled liquid region. While most Ca-based crystalline alloys oxidise in air in a matter of days, many Ca-based metallic glasses are argued to maintain a metallic lustre long after casting.<sup>[278]</sup> They are also potential candidates for dissolvable biomedical applications due to their bio-compatible compositions.

In this part of the thesis, the Ca<sub>65</sub>Mg<sub>15</sub>Zn<sub>20</sub> alloy was selected for detailed analysis as it has been reported to have one of the lowest densities of all BMG systems, a maximum critical thickness of 15 mm at a solidification rate less than 20 °C/s when cast in a copper mould and displays a supercooled liquid region of 35 °C.<sup>[227]</sup> This material also shows potential in biomedical applications as a dissolvable type implant, since all elements in the alloy are compatible with the human body in large quantities.

**Table 4.1:** Critical thickness and various thermal properties of selected Ca-based BMGs.

ALLOY (at.%)	$Z_C$ (mm)	$T_g$ (°C)	$T_X$ (°C)	$\Delta T_X$ (°C)	$T_m$ (°C)	$T_l$ (°C)	$T_{rg}$	REF
Ca <sub>66.4</sub> Al <sub>33.6</sub>	1	255	267	12	560	590	0.634	[274]
Ca <sub>63</sub> Al <sub>32</sub> Cu <sub>5</sub>	2	230	257	27	535	570	0.623	[274]
Ca <sub>60</sub> Al <sub>30</sub> Ag <sub>10</sub>	2	210	258	48	508	525	0.618	[274]
Ca <sub>60</sub> Al <sub>30</sub> Mg <sub>10</sub>	2	235	250	15				[274]
Ca <sub>60</sub> Al <sub>30</sub> Zn <sub>10</sub>	1.5	225	257	32				[274]
Ca <sub>56.5</sub> Al <sub>28.5</sub> Mg <sub>10</sub> Cu <sub>5</sub>	3	220	247	27	490	525	0.646	[274]
Ca <sub>56.5</sub> Al <sub>28.5</sub> Mg <sub>10</sub> Ag <sub>5</sub>	3	215	242	27				[274]
Ca <sub>60</sub> Mg <sub>20</sub> Ag <sub>20</sub>	4							[36]
Ca <sub>60</sub> Mg <sub>20</sub> Ag <sub>10</sub> Cu <sub>10</sub>	7							[37]
Ca <sub>55</sub> Mg <sub>20</sub> Zn <sub>25</sub>	2	110	155	45	350	429	0.535	[275]
Ca <sub>60</sub> Mg <sub>15</sub> Zn <sub>25</sub>	6	106	154	32	336	377	0.507	[275]
Ca <sub>60</sub> Mg <sub>17.5</sub> Zn <sub>22.5</sub>	10	105	155	45	336	377	0.546	[275]
Ca <sub>62.5</sub> Mg <sub>17.5</sub> Zn <sub>20</sub>	10	102	139	35	336	367	0.595	[275]
Ca <sub>65</sub> Mg <sub>15</sub> Zn <sub>20</sub>	6-15	102	137	50	336	357	0.582	[227,275]
Ca <sub>70</sub> Mg <sub>10</sub> Zn <sub>20</sub>	<1	94	126	37	336	384	0.586	[275]
Ca <sub>40</sub> Mg <sub>25</sub> Cu <sub>35</sub>	4	126	163	37	377	407	0.587	[277]
Ca <sub>45</sub> Mg <sub>25</sub> Cu <sub>30</sub>	6	127	165	38	354	405	0.590	[277]
Ca <sub>50</sub> Mg <sub>25</sub> Cu <sub>25</sub>	9	127	166	39	354	382	0.611	[277]
Ca <sub>50</sub> Mg <sub>22.5</sub> Cu <sub>27.5</sub>	10	127	169	42	354	390	0.603	[277]
Ca <sub>55</sub> Mg <sub>25</sub> Cu <sub>20</sub>	8	125	155	30	354	395	0.596	[277]
Ca <sub>57</sub> Mg <sub>19</sub> Cu <sub>24</sub>	4							[36]
Ca <sub>58</sub> Mg <sub>18</sub> Cu <sub>24</sub>	6	115	153	38	355	394	0.582	[277]
Ca <sub>60</sub> Mg <sub>20</sub> Cu <sub>20</sub>	4	114	139	25	356	405	0.571	[277]
Ca <sub>65</sub> Mg <sub>15</sub> Cu <sub>20</sub>	4	110	136	26	357	409	0.562	[277]
Ca <sub>70</sub> Mg <sub>10</sub> Cu <sub>20</sub>	1	112	134	22	397	440	0.540	[277]
Ca <sub>70</sub> Mg <sub>10</sub> Ni <sub>20</sub>	13	158	180	22	-	410	0.631	[276]
Ca <sub>47</sub> Mg <sub>19</sub> Zn <sub>7</sub> Cu <sub>27</sub>	6	120	167	47	334	403	0.581	[278]
Ca <sub>50</sub> Mg <sub>20</sub> Zn <sub>5</sub> Cu <sub>25</sub>	10	126	168	42	338	381	0.610	[278]
Ca <sub>50</sub> Mg <sub>25</sub> Zn <sub>15</sub> Cu <sub>10</sub>	8	110	157	47	330	450	0.530	[278]
Ca <sub>50</sub> Mg <sub>15</sub> Zn <sub>10</sub> Cu <sub>25</sub>	10	122	161	39	327	405	0.583	[278]
Ca <sub>55</sub> Mg <sub>18</sub> Zn <sub>11</sub> Cu <sub>16</sub>	>10	100	166	66	330	363	0.586	[278]
Ca <sub>55</sub> Mg <sub>18</sub> Zn <sub>16</sub> Cu <sub>11</sub>	>10	111	164	53	331	352	0.614	[278]
Ca <sub>58</sub> Mg <sub>18</sub> Zn <sub>12</sub> Cu <sub>12</sub>	>10	100	155	55	328	355	0.594	[278]

## 4.2. FURTHER DEVELOPMENT OF THE INVERTED INJECTION DIE CASTING TECHNIQUE – INDUCTION HEATING

The Ca-based BMG studied in this thesis was produced using an entirely new casting facility developed and constructed in-house, and designed specifically for the production of lightweight BMGs. This unique facility utilises the same inverted (upside down) injection casting theory as the facility used to cast Mg-BMGs (SECTION 3.5). However, the major innovation was the incorporation of induction heating to melt the charge material. This die casting facility, shown in **Figures 4.1 to 4.3**, is capable of single step alloy preparation to a maximum temperature of 1300 °C, at a heating rate of 500 °C/min, which reduces alloy preparation time to the order of minutes. The facility is also capable of vacuum melting, melting under a dynamic gas atmosphere (reactive or inert gases), conventional gravity casting, 'inverted' injection casting, vacuum/suction casting or a combination of injection/vacuum casting. The facility's extremely fast heating rate and inert atmosphere capabilities are essential for the production of the  $\text{Ca}_{65}\text{Mg}_{15}\text{Zn}_{20}$  alloy due to the extremely reactive nature of molten calcium.

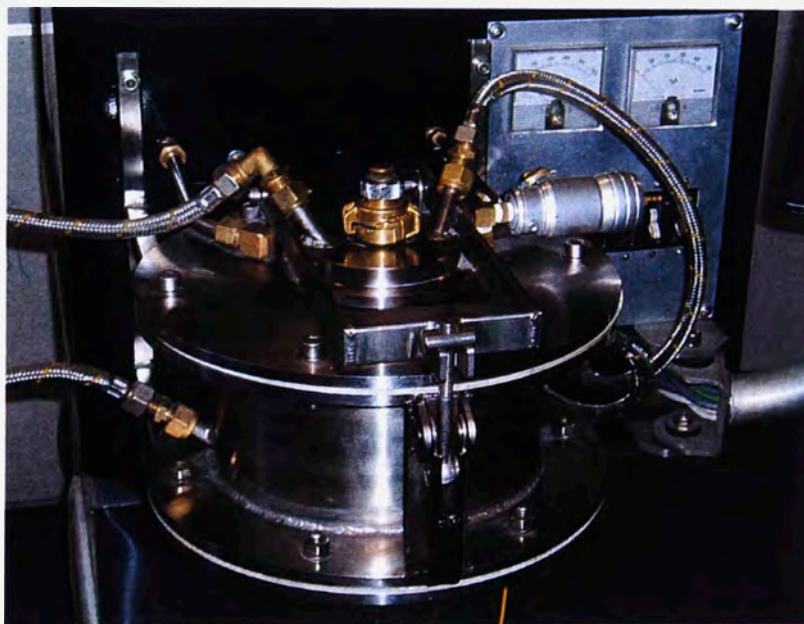


**Figure 4.1:** Photograph of the induction-heated die casting facility developed for the production of  $\text{Ca}_{65}\text{Mg}_{15}\text{Zn}_{20}$  and other lightweight BMG samples.

The several advantages of using an inverted injection casting configuration over conventional injection systems for the production of BMGs were discussed in SECTION 3.5.1. However, in the previous experimental work outlined in SECTION 3.7.2, it was found that, when using a small sealed heating chamber, the rapid application of a gas overpressure resulted in a rapid impulse and abrupt motion of the molten metal flow front; this resulted in an initial instability of the metal flow front that restricted its use to low injection pressures.



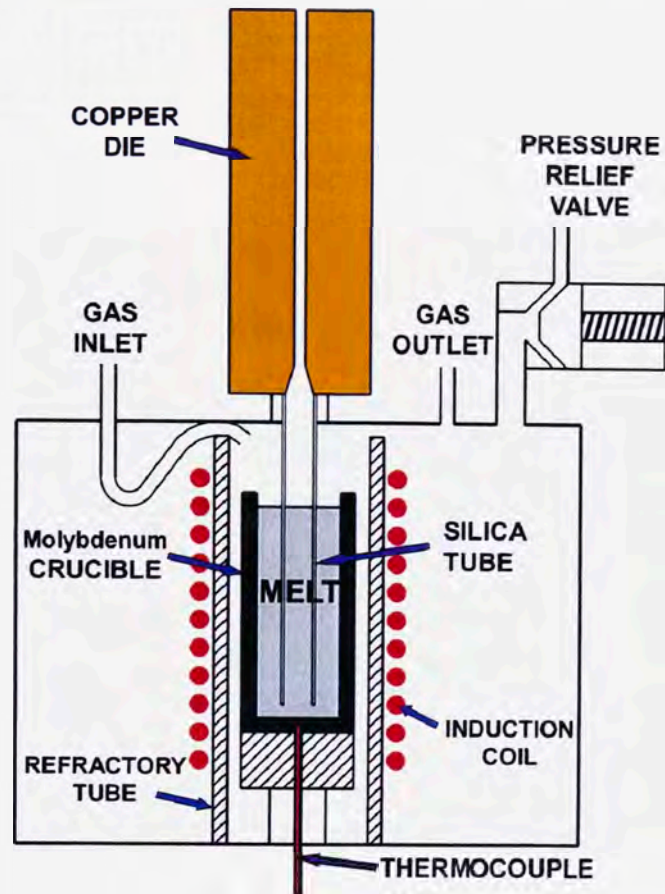


**Figure 4.2:** Schematic representation of the melting chamber of the die casting facility developed for casting BMGs.

In a further development of the casting facility, the volume of the heating chamber was increased substantially to accommodate an induction coil. This increase in chamber volume reduced the impulse (time taken for pressure to build up) of the applied gas overpressure which, in turn, created a lower acceleration of the molten metal flow front from rest, thereby allowing it to stabilise much earlier in its motion path up the filler tube into the copper die. This modification allowed higher injection pressures resulting in higher injection velocities of the flow front at the mould gate and in the mould pattern itself, subsequently resulting in more frequent complete filling of the mould cavity over a greater range of injection parameters when compared to the previous design (**Figure 3.24**). However, the increased pressure posed another problem within this process. In preliminary work, it was found that once the mould vent had been sealed, pressure would build up to the much higher injection pressure that, at higher casting temperatures, caused 'blow through' whereby any molten material remaining in the sample was ejected through the mould vent, leaving a hollowed sample. To avoid this problem, a variable pressure relief valve was fitted to the melting chamber, allowing the accurate control of the pressure build up.



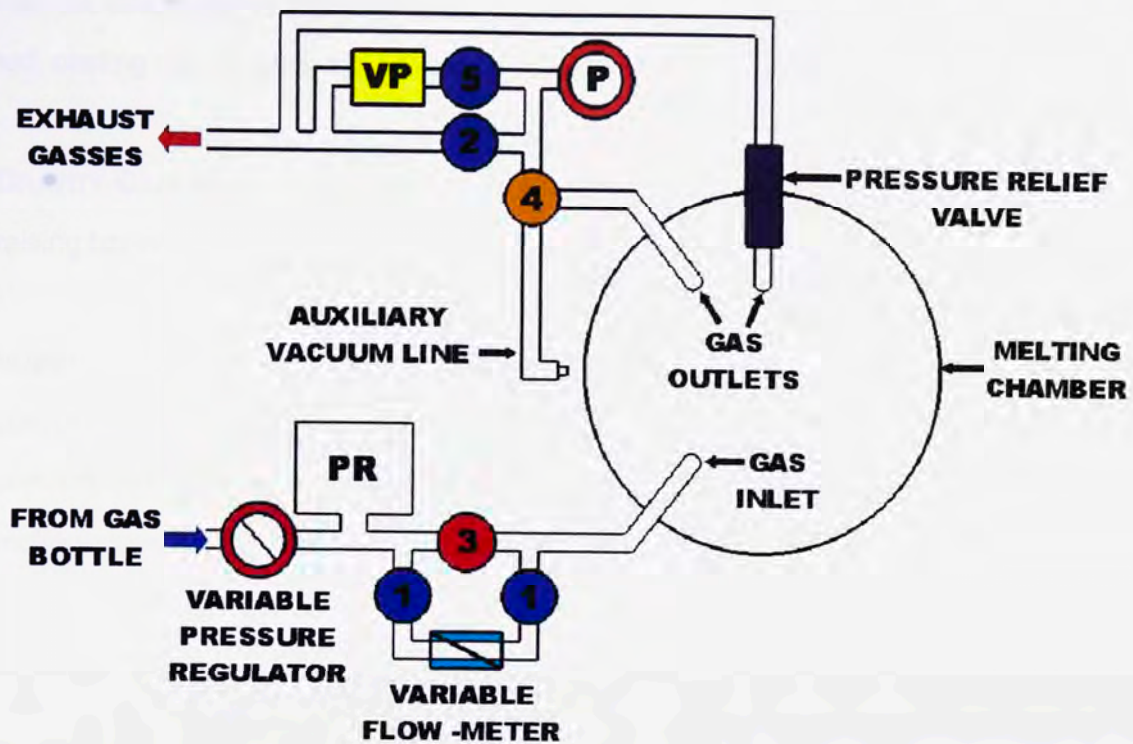


**Figure 4.3:** A comprehensive representation of the valve and gas plumbing configuration of the BMG die casting facility shown in Figure 4.1.

**Figure 4.3** shows a comprehensive diagram of the valve and gas plumbing configuration developed for enabling the casting facility to achieve such a large range of casting and melting capabilities (all valves described herein are solenoid valves, activated by electronic switches on a remote control station board). Here, highly pressurised gas (argon in this case) is supplied from a gas bottle to shield the melt and provide the force for injection casting. The desired injection pressure is governed via a VARIABLE PRESSURE REGULATOR (labelled). The region labelled **PR** is a pressure reservoir, which has a volume of approximately twenty times that of the melting chamber. This reservoir ensures that a constant pressure is supplied to the chamber upon injection casting. Prior to melting, the chamber is vacuum purged with argon. Assuming all solenoid valves are closed, this is achieved by first switching the two-way solenoid valve **4**, in the default gas outlet direction. The vacuum pump labelled **VP** is switched on and the valve labelled **5** is opened. The pressure gauge labelled **P**, which reads pressures in the range -100 to 150 kPa, indicates the pressure of the chamber as the vacuum is applied. Once a substantial vacuum is achieved, valve **5** is closed and the high flow volume gas inlet valve **3** is opened to fill the chamber with gas. This is repeated numerous times to ensure any residual oxygen is removed from the chamber during melting. Once the chamber has been purged and all valves are again closed, circulating gas may be applied to the melting chamber. This is achieved by simultaneously opening valves labelled **1** and **2**. The desired circulating gas flow rate is governed by the VARIABLE

FLOW METER, which can be adjusted from 0 to 200 cm<sup>3</sup>/min. Once the desired melt temperature is reached, casting can be carried out by one of the following methods:

- (i) **GRAVITY CASTING** – the crucible is removed from the chamber by using the incorporated raising bar and manually poured into the desired mould.
- (ii) **INJECTION CASTING** – this method was used in this thesis whereby the chamber access lid is opened, the desired mould is attached to the die-casting unit, valves **1** and **2** are closed simultaneously, and valve **3** is opened to apply the desired gas overpressure, forcing the molten metal up the silica tube into the mould. Once the mould is filled, valve **3** is closed, valves **1** and **2** are opened to return the chamber to atmospheric pressure and continue protecting the melt, the mould is removed from the chamber and the access lid is replaced.
- (iii) **VACUUM CASTING** – a vacuum is generated by the vacuum pump **VP** which draws the molten metal up the silica tube into the mould. This is achieved by leaving valves **1** and **2** open as to maintain atmospheric pressure in the chamber, with all other valves remaining closed. Casting is carried out by attaching the AUXILIARY VACUUM LINE to the vent of the desired mould. Valve **4** is moved from its default position to the direction of the auxiliary vacuum line. The vacuum pump **VP** is switched on, the chamber access lid is opened, and the mould is attached to the die-casting unit. During casting, valve **5** is opened which draws the molten metal into the mould. The pressure supplied by the vacuum pump is constant, so the velocity (constant) of the molten metal in the mould is governed by variable flow meter set up.
- (iv) **COMBINED VACUUM AND INJECTION CASTING** – the two pressure differentials now work in tandem to fill the mould cavity. This method is generally used for very thin castings to aid in rapid gas evacuation and cavity filling. Casting is carried out by attaching the AUXILIARY VACUUM LINE to the vent of the desired mould. Valve **4** is moved from its default position to the direction of the auxiliary vacuum line. The vacuum pump **VP** is switched on and the chamber access lid opened, then the mould is attached to the die-casting unit. For casting, valves **1** and **2** are closed and valves **3** and **5** are opened simultaneously, as to apply the preset injection pressure and vacuum for filling the mould cavity.

The pressure at which the chamber is held, once the mould is filled, is determined by the one-way, variable pressure relief valve, which is plumbed back into the exhaust gasses line.



### 4.3. ALLOY PREPARATION

A two-stage melting and casting procedure was carried out for the preparation of the  $\text{Ca}_{65}\text{Mg}_{15}\text{Zn}_{20}$  alloy. A  $\text{Ca}_{80}\text{Mg}_{20}$  (99.9 wt%) master alloy, Zn (99.9 wt.%) and Ca (99.8 wt.%) raw materials were used for the charge preparation. All materials were mechanically cleaned immediately prior to melting to minimise the amount of the fast forming oxide film of the Ca-based materials. The balance of Ca was placed in the bottom of a molybdenum crucible, followed by the balance of zinc and approximately 1/3 the balance of master alloy. The melting chamber was evacuated and purged with argon gas (99.997 vol.%) five times, followed by the circulation of argon gas for 20 min at a rate of  $200 \text{ cm}^3/\text{min}$ . The charge was induction heated to  $700^\circ\text{C}$  and held for 5 min, stirred using a tungsten rod then cooled to room temperature. The remainder of the master alloy was added to the crucible, heated to  $700^\circ\text{C}$  and held for 5 min, stirred then cooled to the desired injection temperature, where it was held for 1-2 min and again stirred using a tungsten rod immediately prior to injection casting.

Based on the binary phase diagrams given in **Figures 4.4-4.6**,<sup>[279-281]</sup> it can be seen that melting the alloy in this order allows the preparation temperature to be kept as low as possible for minimising the evaporation of the more volatile constituents. Among the constituents, zinc will melt first with a melting point of  $419^\circ\text{C}$ . It can be seen in **Figure 4.4**<sup>[279]</sup> that, at the maximum ratio of calcium to zinc for this composition, i.e.  $\text{Ca}_{76.5}\text{Zn}_{23.5}\text{at}\%$  (from  $\text{Ca}_{65}\text{Zn}_{20}\text{at}\%$ ), moving from 100% zinc will result in all calcium dissolving at a temperature below  $700^\circ\text{C}$  since all eutectic temperatures are below  $700^\circ\text{C}$ . **Figure 4.5**<sup>[280]</sup> shows that the melting point of the  $\text{Ca}_{80}\text{Mg}_{20}\text{(wt}\%)$  master alloy is  $\sim 470^\circ\text{C}$ , which is also well below our preparation temperature of  $700^\circ\text{C}$ ; this will aid in the dissolving of pure calcium. **Figure 4.6**<sup>[281]</sup> indicates that all combinations of magnesium and zinc will have a melting point below  $700^\circ\text{C}$ .

**Figure 4.7**<sup>[275]</sup> shows the ternary phase diagram for the present alloy; there is a ternary eutectic reaction at a composition of  $\text{Ca}_{64}\text{Mg}_{14}\text{Zn}_{22}$  with a corresponding melting temperature of  $336^\circ\text{C}$ . The presence of the deep ternary eutectic in this area provides a strong liquidus temperature gradient in the selected composition area, which leads to an expected high GFA of the alloy composition.<sup>[5]</sup> According to the phase diagram, the glass-forming alloy  $\text{Ca}_{65}\text{Mg}_{15}\text{Zn}_{20}$  has a near ternary eutectic composition that lies just in the Ca phase field and shows the smallest difference between the liquidus and solidus temperatures of alloys studied within this system (**Table 4.2**).

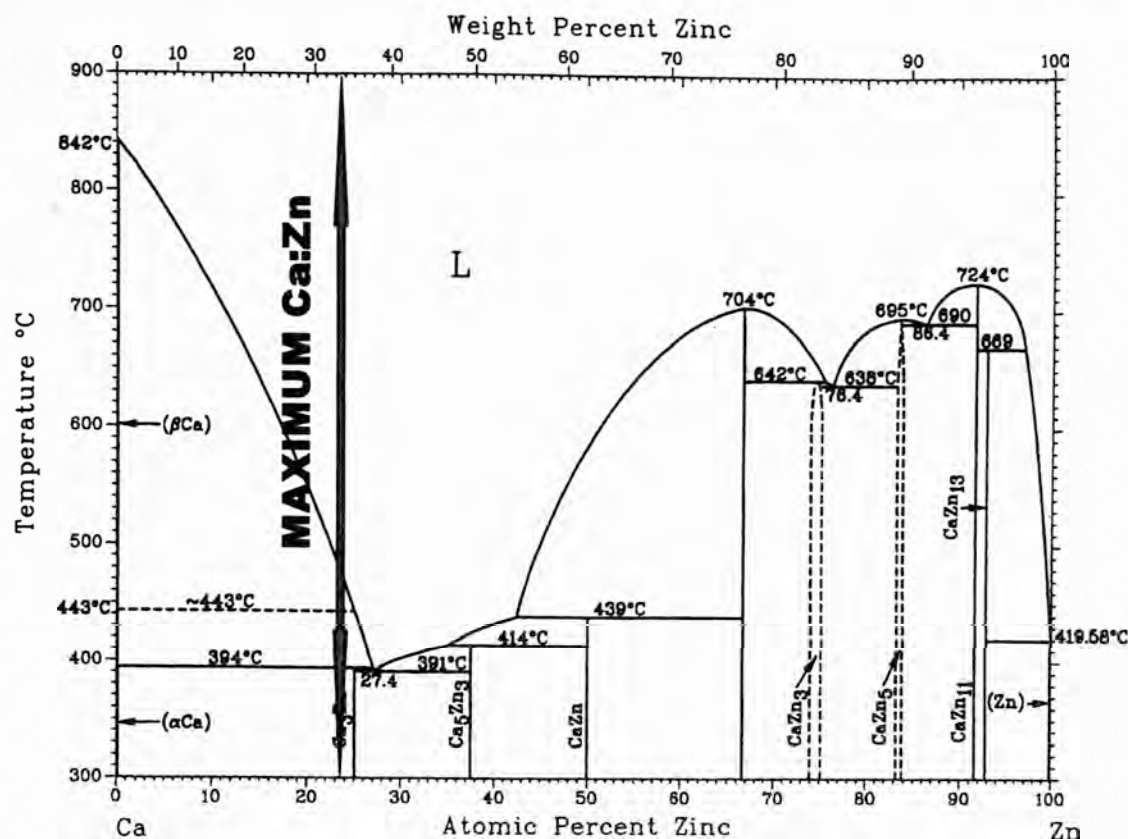


**Figure 4.4:** Equilibrium binary phase diagram of the Ca-Zn system, indicating the maximum Ca:Zn ratio possible for the  $\text{Ca}_{65}\text{Mg}_{15}\text{Zn}_{20}$  alloy.<sup>[279]</sup>

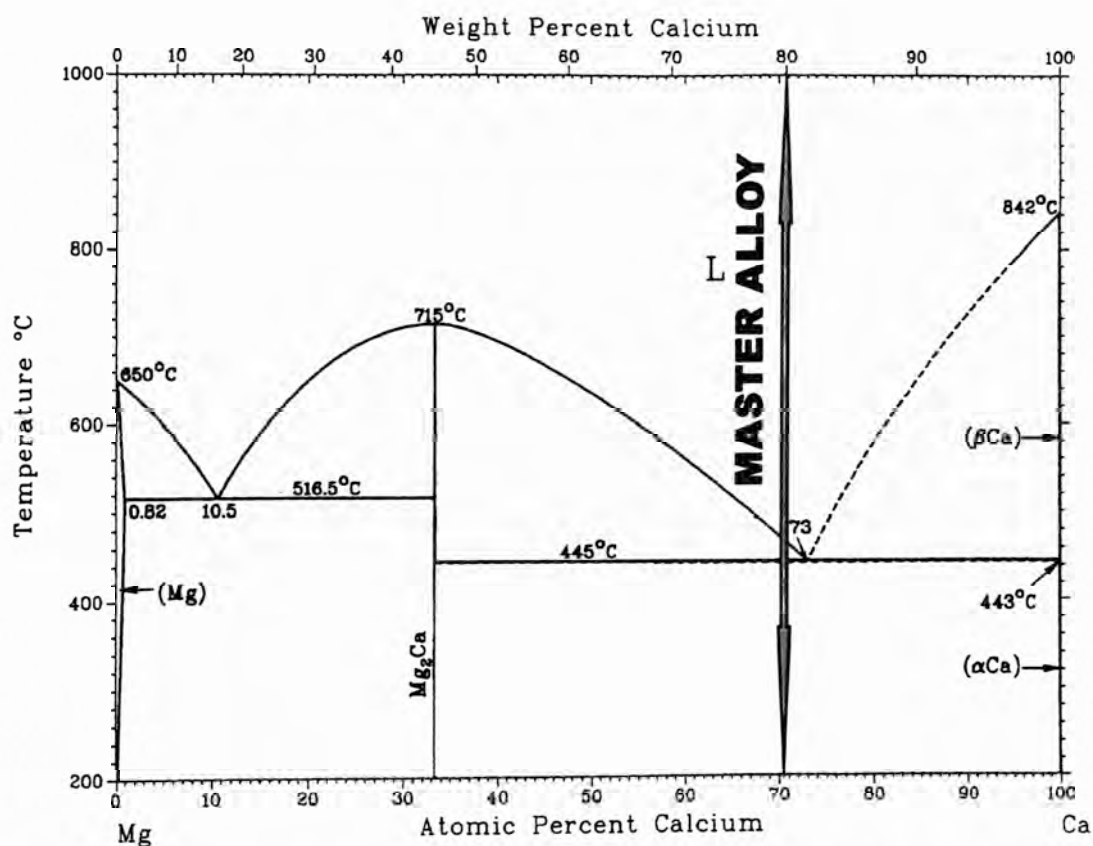


**Figure 4.5:** Equilibrium binary phase diagram of the Ca-Mg system, indicating the location of the  $\text{Ca}_{80}\text{Mg}_{20}$  wt% master alloy.<sup>[280]</sup>

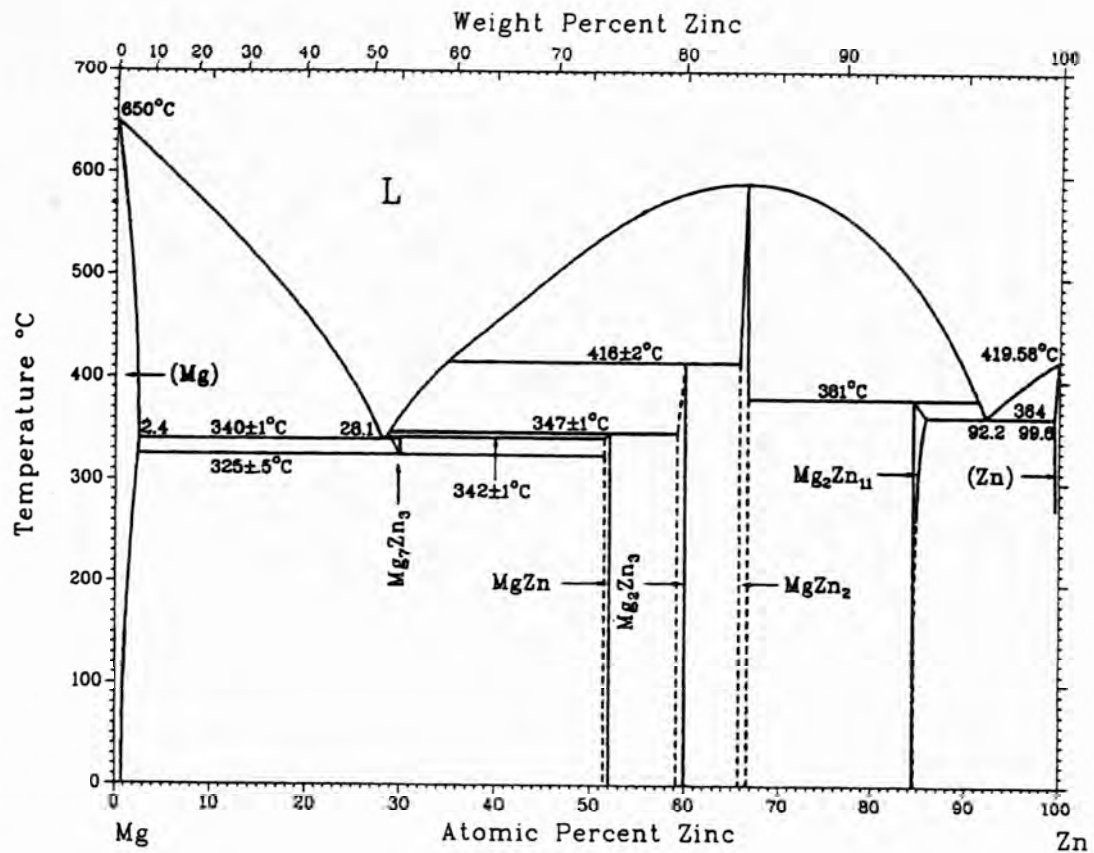


Figure 4.6: Equilibrium binary phase diagram of the Mg-Zn system.<sup>[281]</sup>

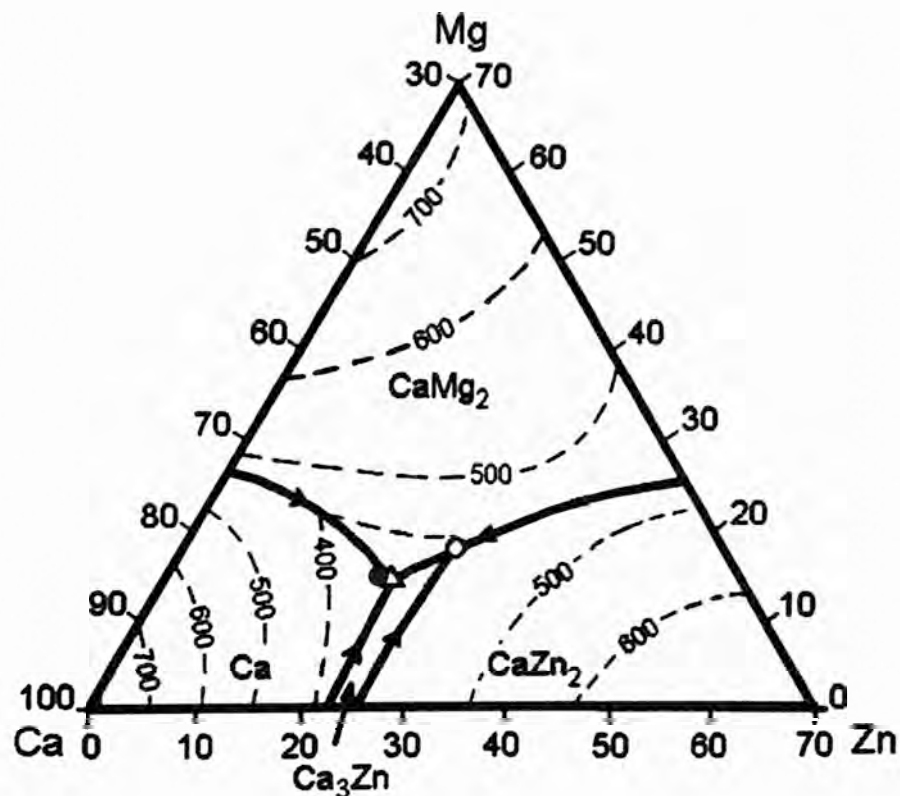
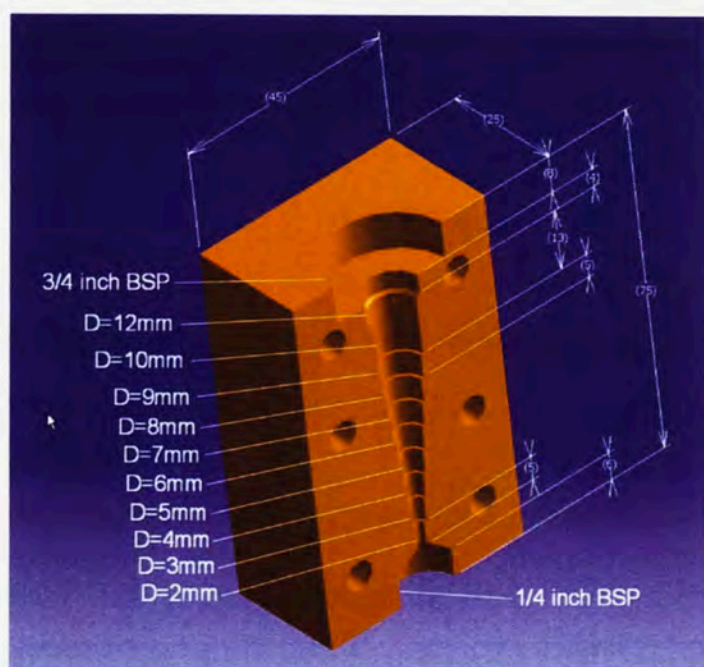


Figure 4.7: The liquid surface of the Ca-Mg-Zn ternary equilibrium phase diagram showing the nominal composition of the alloy studied in this thesis (redrawn Senkov and Scott)<sup>[275]</sup>



#### 4.4. DETERMINATION OF CRITICAL THICKNESS, COOLING RATE AND THERMAL PROPERTIES OF THE $\text{Ca}_{65}\text{Mg}_{15}\text{Zn}_{20}$ BMG

For the determination of the maximum amorphous thickness and critical cooling rate, a copper graduated cylinder mould was constructed, with sample diameters ranging from 2-10 mm, which can be seen in **Figure 4.8** and **Figure 4.9**. This allowed a wide range of cooling rates to be achieved. To enable the measurement of cooling rates, insulated K-type thermocouple wires of diameter 0.02 mm were introduced to the mould cavity via the mould split at various diameters. Using these thermocouples, the variation in the metal cooling rate for given diameters was determined, enabling the calculation of the critical cooling rate of the  $\text{Ca}_{65}\text{Mg}_{15}\text{Zn}_{20}$  BMG.



**Figure 4.8:** Workshop drawing of the copper mould used to produce  $\text{Ca}_{65}\text{Mg}_{15}\text{Zn}_{20}$  alloy samples of varying diameters.

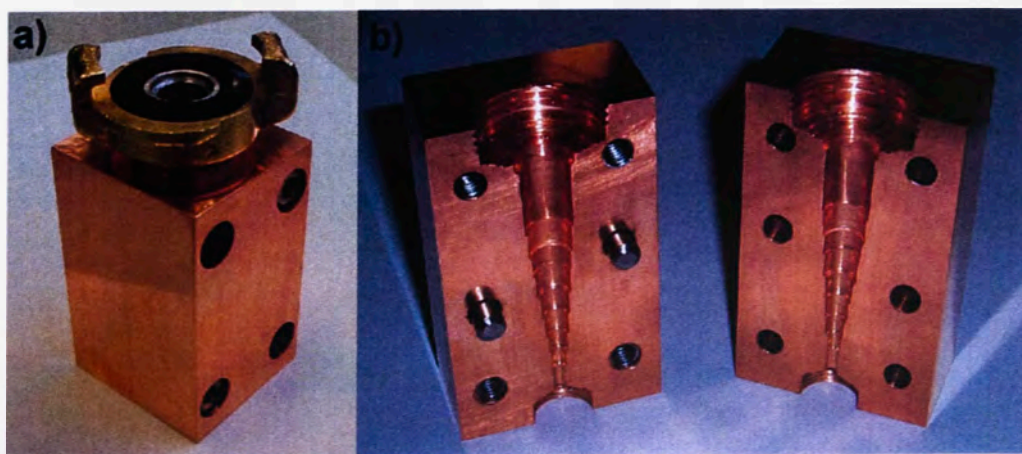


**Figure 4.9:** Photos of the copper graduated cylinder mould a) assembled and b) split.



#### 4.4.1 Experimental Procedure

For the determination of critical thickness and cooling rate, the  $\text{Ca}_{65}\text{Mg}_{15}\text{Zn}_{20}$  alloy was prepared using the melting sequence described in SECTION 4.3 and casting methodology of SECTION 4.1–(ii) **INJECTION CASTING**. Four K-type thermocouple wires of diameter 0.02 mm (for fast response times) were incorporated into the mould cavity at diameters of 4, 6, 8 and 10 mm for determining the variation in cooling rate of the alloy during casting. On the final melting cycle, the alloy was cooled to 420 °C, held for 1 min and stirred using a tungsten rod. The graduated cylinder copper mould was attached to the die-casting unit and the charge material injected into the mould at an overpressure of 1.5 Bar to generate the sample. Temperature data was gathered at time increments of 0.01 s using a DT800 dataTaker data logging unit. The composition of the as-cast sample was determined to be  $\text{Ca}_{65}\text{Mg}_{15}\text{Zn}_{20} \pm 0.28\text{at.}\%$  by electron probe microanalysis (EPMA) using a Cameca SX50 microanalyser and X-Ray fluorescence (XRF) using a Philips PW2400 XRF and UniQuant analysis software. The resulting sample was segmented along its centre (the last portion of the sample to solidify) and analysed for crystalline phases using a Phillips X'PERT MRD X-Ray Diffractometer and  $\text{CuK}\alpha$  radiation. In order to determine the thermal properties of the alloy, such as  $T_g$ ,  $T_X$ ,  $T_m$  and  $T_i$ , sections of the cylinders found to be amorphous by XRD were examined using a TA 2010 differential scanning calorimeter at various heating rates.

#### 4.4.2 Evaluation of the $\text{Ca}_{65}\text{Mg}_{15}\text{Zn}_{20}$ Graduated Cylinder Casting

Attempts at producing an amorphous  $\text{Ca}_{65}\text{Mg}_{15}\text{Zn}_{20}$  sample by injection casting into the graduated cylinder mould were successful and a typical as-cast sample is shown in **Figure 4.10**.

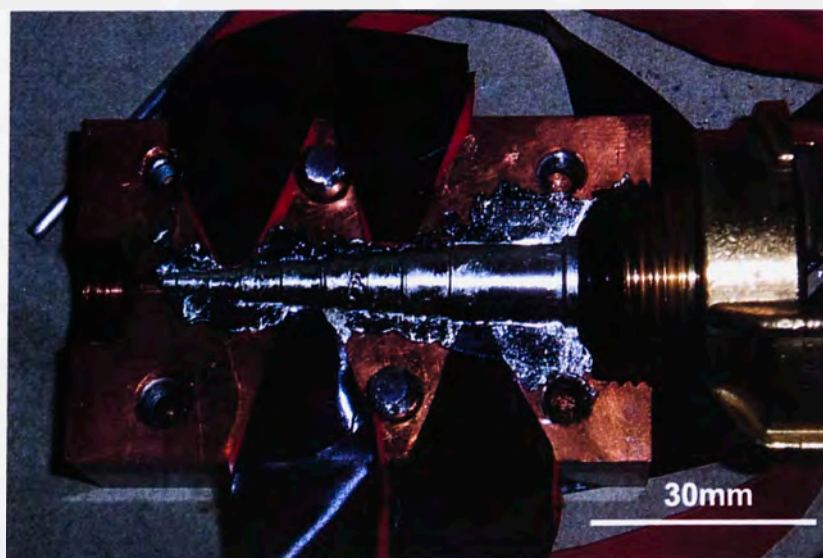


**Figure 4.10:** Photograph of a  $\text{Ca}_{65}\text{Mg}_{15}\text{Zn}_{20}$  sample cast at 420 °C and 1.5 Bar overpressure using the graduated cylinder mould with insulated thermocouples in situ.

The graduated cylindrical samples were sectioned along their centre-line for further analysis. The degree of crystallinity of the sample sections was determined by XRD. The XRD traces for the given sample diameter can be seen in **Figure 4.11**.

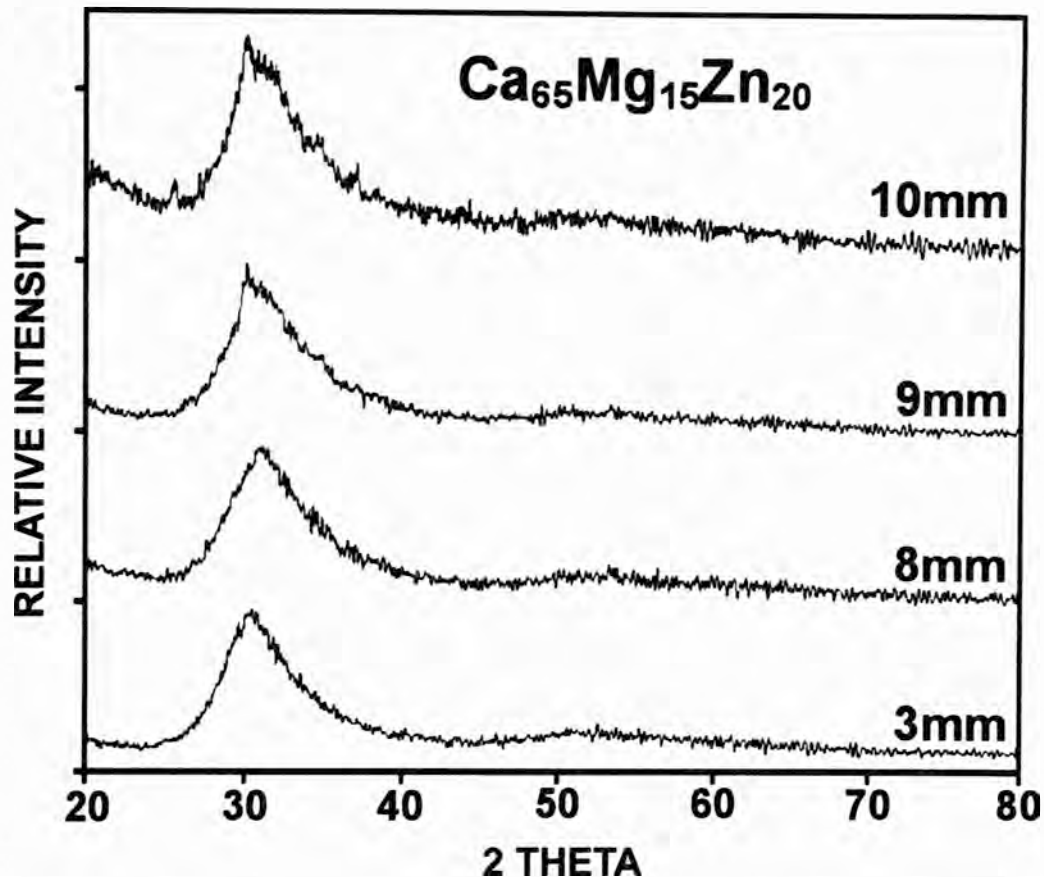


**Figure 4.11:** X-Ray diffraction patterns taken from centre sections of  $\text{Ca}_{65}\text{Mg}_{15}\text{Zn}_{20}$  cylinders of different diameters following casting at 420 °C.

A completely amorphous structure was generated at a sample diameter of up to 8 mm, given by the characteristic broad amorphous crest and the absence of sharp crystalline peaks. Sections above this thickness were observed to have a partially crystalline interior and an amorphous annulus. This XRD data indicates that the critical diameter  $D_C$  of the amorphous  $\text{Ca}_{65}\text{Mg}_{15}\text{Zn}_{20}$  alloy for this particular casting procedure is 8-9 mm. To determine the characteristic thermal properties of the amorphous alloy DSC was used to determine  $T_g$ ,  $T_X$ ,  $T_m$  and  $T_l$  on 3 mm sections of the as-cast material. Isochronal DSC scans were performed at heating rates ranging from 5 to 20 °C/min. The thermal properties for the  $\text{Ca}_{65}\text{Mg}_{15}\text{Zn}_{20}$  BMG at heating rate of 20 °C/min cast at a temperature of 420 °C are shown in **Figure 4.12**.



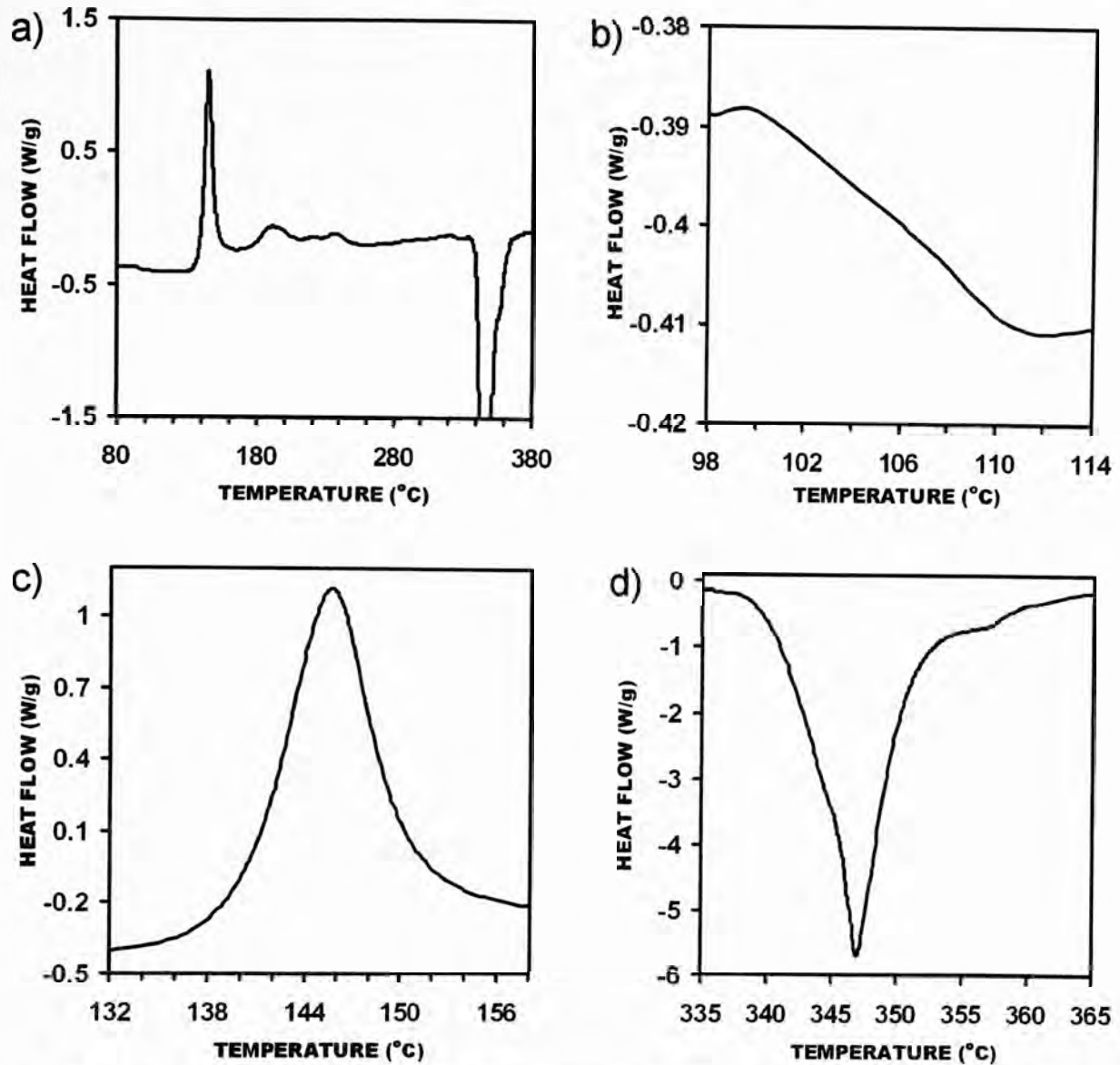


**Figure 4.12:** a) Complete DSC Curve for low-pressure die-cast  $\text{Ca}_{65}\text{Mg}_{15}\text{Zn}_{20}$  BMG cast at 420 °C and magnifications of b)  $T_g$ , c)  $T_X$  and d)  $T_m$  and  $T_l$  regions.

Similar to the Mg-base BMG, the glass transition temperature varied with heating rate. For the Ca-base BMG, the temperature range was  $\sim 12$  °C for heating rates in the range 5 to 20 °C /min. At a heating rate of 20 °C/min,  $T_g$  starts at 100 °C and is completed at 110 °C. Taking the midpoint of the tangent between these two points (using Thermal Advantage Version 1.1a) Software) yields a value of  $T_g$  of 105 °C, which is similar to that reported by Senkov et al.<sup>[275]</sup> as shown in **Table 4.2**. The value of  $T_X$ , which is usually taken as a tangent to the crystallisation curve, generates a value of  $\sim 137$  °C (again comparable to values in **Table 4.2**), although it can be seen that the absolute starting point of the crystallisation reaction begins much earlier at around 132 °C. By definition, we have  $\Delta T_X = T_X - T_g$ , resulting in a SCL region of  $\sim 32$  °C.  $T_m$  and  $T_l$  were determined to be 337 °C and 357 °C respectively, which do not vary with heating rate.

**Figure 4.13** illustrates the dependency of both  $T_g$  and  $T_X$  on heating rate. Here, it can be seen that there is very little variation of the thermal characteristics of the glass over the given range of heating rates. The variation of  $T_g$  and  $T_X$  with respect to heating rate is related to glass stability/fragility, whereby a lower heating rate dependence indicates a more fragile glass.<sup>[60]</sup> This behaviour is described by Eq. (2.10), a variant of the VFT equation that combines the kinetics of glass transition to the equilibrium viscosity.<sup>[60]</sup>

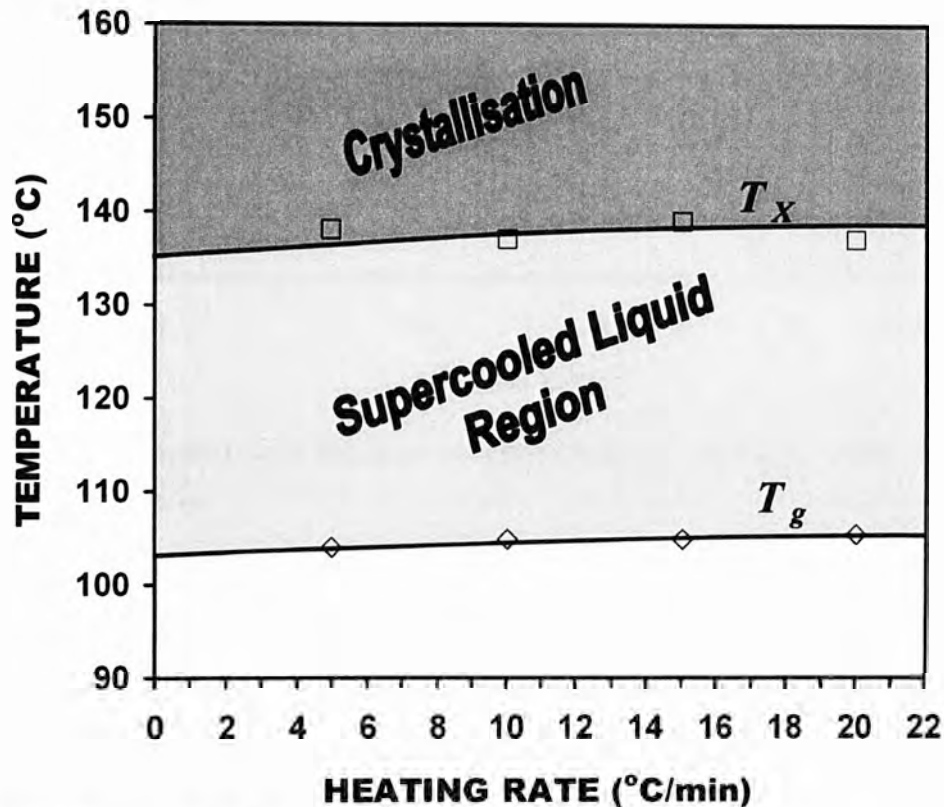


**Figure 4.13:** DSC results for  $T_g$  and  $T_X$  at heating rates from 5 - 20 °C/min.

**Figure 4.14** shows isothermal DSC results for the temperature range 135 - 110 °C, presented in a Time-Temperature-Transformation diagram. It can be seen from the isothermal DSC data that, when the  $\text{Ca}_{65}\text{Mg}_{15}\text{Zn}_{20}$  BMG is held at temperatures near and greater than 125 °C (greater than half of the SCL region), the onset and completion time of the crystallisation reaction becomes quite short, again indicating a fragile/less stable glass. This is somewhat analogous to the observation made previously, whereby the thermal characteristics of the glass with respect to heating rate also indicate a fragile glass. Another indication of poor glass stability is the size of the SCL region<sup>[20,121,185]</sup>. For the present alloy,  $\Delta T_X$  (~32 °C) is quite small relative to other BMGs with such high critical casting thickness).<sup>[282]</sup>

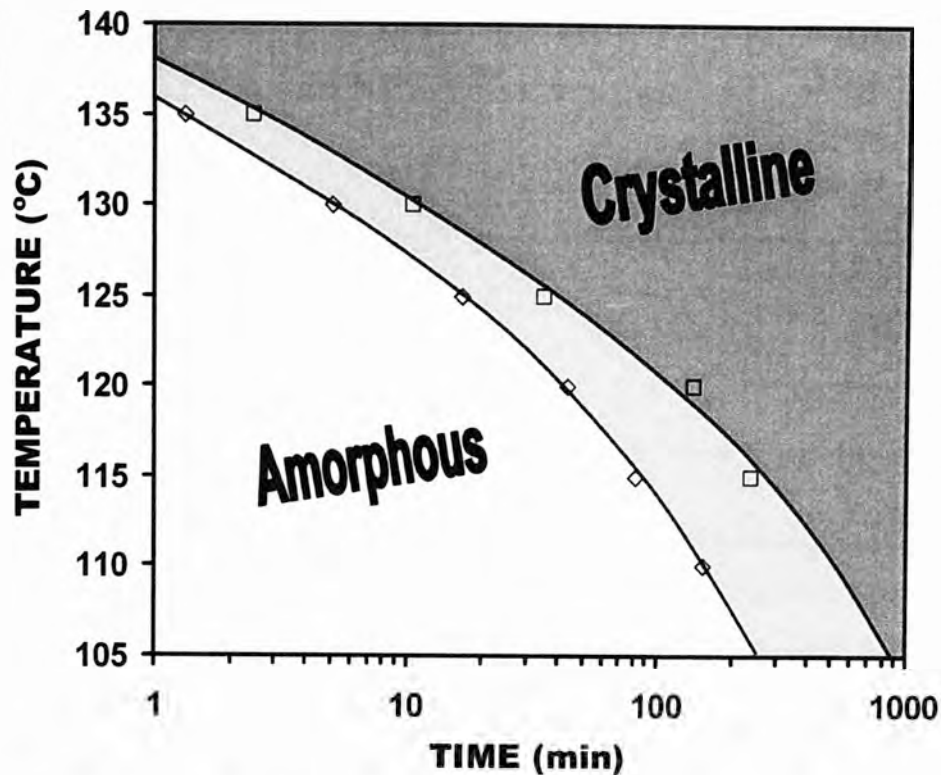


**Figure 4.14:** An annealing time-temperature-transformation diagram, which follows a non-Arrhenius type relationship.

It can be seen that the data presented in **Figure 4.14** does not follow the expected Arrhenius type relationship expected for a crystallisation reaction. This behaviour may be explained using the VFT relation, Eq. (2.8),<sup>[60]</sup> which describes the change in viscosity as a function of temperature and liquid fragility i.e.  $\eta = \eta_0 \exp[D^*T_0 / (T - T_0)]$ . We can see both from the VFT equation and experimental observations (**Figure 2.6b**) that a more fragile liquid will deviate further from Arrhenius-type viscosity behaviour. It is also known that viscosity (which is inversely proportional to diffusivity, **SECTION 2.3.2**), has conventionally been regarded as a kinetic factor controlling the jumping and rotation rates of atoms or molecules across the nucleus-liquid interface,<sup>[15,22,60-63]</sup> which is a determining factor in both the nucleation rate (Eq. (2.3)) and growth (Eq. (2.11)) of crystalline phases.

Temperature/time data acquired by the four K-type thermocouple wires were recorded at a capture rate of 100 points per second and averaged for three repeats of the same experiment with an injection temperature of 420 °C and gas over pressure of 1.5 Bar. These results are given in **Figure 4.15**. From the data given in **Figure 4.15**, the linear cooling rates of the  $\text{Ca}_{65}\text{Mg}_{15}\text{Zn}_{20}$  alloy from the liquidus temperature (357 °C) to the glass transition temperature (105 °C), for diameters of 4, 6, 8 and 10 mm were determined using Eq. (3.1).



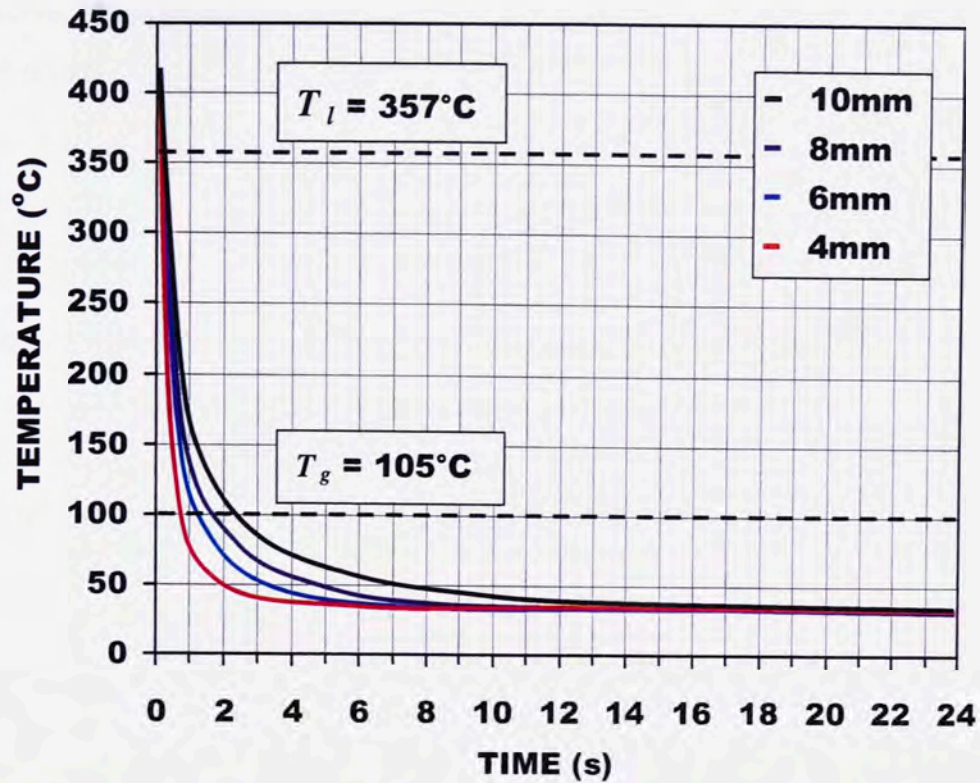


**Figure 4.15:** Averaged temperature/time data taken from the 0.02 mm K-type thermocouple wires captured at time increments of 0.01 s at sample diameters of 4, 6, 8 and 10 mm for three repeated casting experiments at 420 °C.

Using the cooling rates determined by Eq. (3.1), cooling rate as a function of sample diameter is shown in **Figure 4.16**.

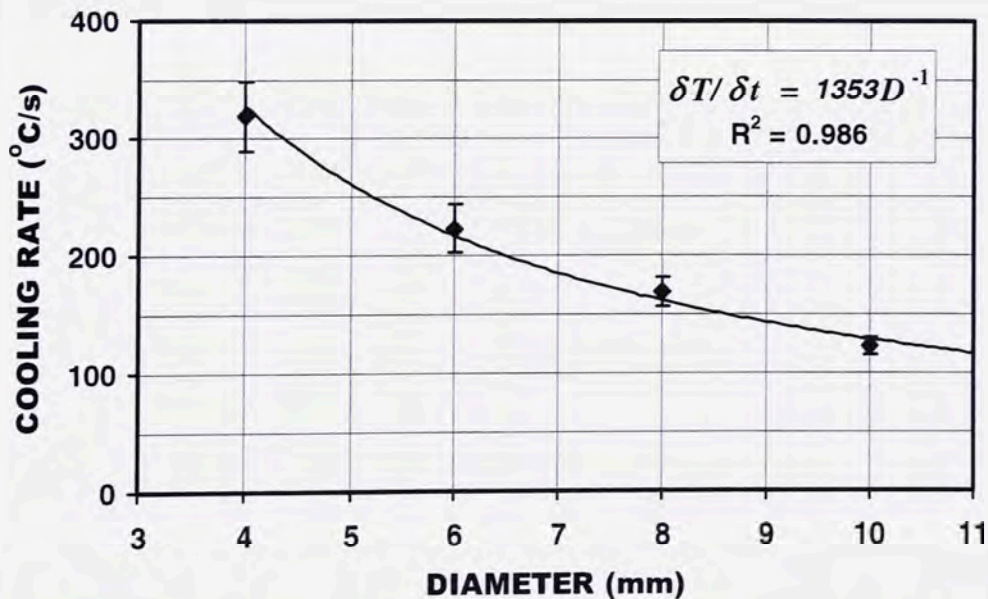


**Figure 4.16:** Cooling rate data taken between the liquidus temperature of 357 °C and the glass transition temperature of 105 °C by 0.02 mm K-type thermocouple wires at mould diameters of 4, 6, 8 and 10 mm. Errors are taken as half the range of the given data points for three individual samples.

From this curve, the approximate average cooling rate for a sample of diameter between 4 and 10 mm is given as:

$$\frac{dT}{dt} \approx \frac{1353(Ks^{-1}mm^{-1})}{D(mm)} \quad (4.1)$$

This equation can be compared with a simple energy balance of the process. Since the cavity in the mould has a circular cross section of various diameters, by assuming that the heat flux is interface-controlled (neglecting frictional effects between the casting and mould wall), the heat leaving the volume element (casting) is equal to heat entering the mould which may be described by:<sup>[242]</sup>

$$\rho C_P \frac{dT}{dt} \left( \frac{\pi D^2}{4} dx \right) = -h(T - T_{MOULD})(\pi D dx) \quad (4.2)$$

where  $D$  is the channel diameter,  $h$  the interfacial heat transfer coefficient,  $C_P$  and  $\rho$  the heat capacity and density of the liquid metal, respectively, and  $T$  and  $T_{MOULD}$  the casting and channel temperature, respectively. Rearranging Eq. (4.2) gives the rate of temperature change of the casting:

$$\frac{dT}{dt} = -\frac{4h(T - T_{MOULD})}{C_P \rho D} \quad (4.3)$$

By assuming that  $h$ ,  $C_P$  and  $\rho$  remain relatively constant for a given temperature interval (given as  $A$ ), results in an inverse relation between cooling rate and casting diameter, i.e.:

$$\frac{dT}{dt} = \frac{A}{D} \quad (4.4)$$

This relation corresponds directly to that observed in the experimental cooling behaviour of the  $Ca_{65}Mg_{15}Zn_{20}$  alloy in Eq. (4.1), indicating that at temperatures close to the liquidus temperature cooling is governed by interfacial heat transfer.

Since the maximum amorphous diameter of the  $Ca_{65}Mg_{15}Zn_{20}$  BMG was 8-9 mm, in accordance with Eq. (4.1) the critical cooling rate is computed to be 170-150 °C /s. These results also indicate that the critical amorphous thicknesses achieved in copper mould casting of BMGs are

not necessarily an indicator of glass stability. There are some discrepancies in the literature as to the reproducibility of critical thickness measurements for the  $\text{Ca}_{65}\text{Mg}_{15}\text{Zn}_{20}$  BMG. In 2003, Park and Kim reported a critical thickness of over 15 mm by casting from a graphite crucible in air and a critical cooling rate of  $20\text{ }^{\circ}\text{C/s}$ <sup>[227]</sup> for the same  $\text{Ca}_{65}\text{Mg}_{15}\text{Zn}_{20}$  BMG. Also apparent in the work of Park and Kim<sup>[227]</sup> was the response time of their thermocouples that appears to be much slower than those used in this thesis (**Figure 4.15**).

In 2005, Senkov and Scott reported a critical thickness of 6 mm for the same alloy composition by casting from a Quartz vessel into a water-cooled copper mould.<sup>[275]</sup> Such discrepancies between laboratories for this particular alloy may be due to a number of variables. One such variable could be the purity of the initial charge material. The purity of starting materials used by Park and Kim are similar to those used by Senkov and Scott, i.e. 99.9 wt.% purity materials in all cases. In the case of the current work, raw materials of inferior purity (i.e. industrial purity Ca 99.8 wt% and Ca/Mg 99.8 wt%) were used, with the major impurity found to be sodium; this is a typical impurity in the electrolytic processing of calcium.<sup>[273]</sup> The presence of sodium may affect the glass-forming ability in two ways: either as (i) an atomic addition to the amorphous matrix (further employing the ‘confusion principle’),<sup>[44]</sup> or (ii) as a scavenging addition, which removes other impurities such as oxygen, hydrogen and carbon from the melt. Generally, the preparation and control of such an alloy composition would prove quite difficult due to the reactive nature and volatility of the alloy constituents.

Another likely reason for the discrepancies in the reported data may be the difference in experimental conditions which include crucible material, casting temperature and mould cooling capacity or configuration. Between groups, there were three different melting crucible materials used for casting: graphite, quartz (silica) and molybdenum. In the case of the graphite crucible it has been suggested<sup>[275]</sup> that there may have been a reaction/dissolution between carbon and the alloy during melting cycles, which, when compared to other data suggests that carbon at this concentration may in fact enhance GFA. In the case of a silica vessel, it was found that there was some reaction with or dissolution of the melting vessel walls as Si was an impurity found in elemental trace analysis,<sup>[284]</sup> which would be expected as both Mg and Ca have a higher affinity for oxygen than Si. In this case Si may have affected GFA. There have been numerous reports in other BMG forming systems where microalloying with small atoms such as carbon or silicon can individually, or when used in combination with larger atoms, enhance or reduce the glass-forming ability of a standard composition.<sup>[285,286]</sup>



As for the molybdenum crucible used in this thesis, molybdenum is considered to be a refractory metal and the terminal solid solubility of molybdenum is estimated to be negligible in calcium.<sup>[287]</sup> It has also been published that molybdenum does not alloy with magnesium<sup>[288]</sup> and from thermodynamic calculations has a solubility limit of 0.015 at.% in molten zinc at temperatures above 575 °C.<sup>[289]</sup> Trace elemental analysis using EPMA and XRF failed to detect Mo in the as-cast structure. In this thesis a silica tube was used for transporting the molten metal to the copper mould. It was found that no obvious reaction occurs with the tube wall when casting at 420 °C. Residual alloy left in the feeder tube retained a metallic luster with no discolouration, and was easily removed from the tube. There was also no Si detected in the as-cast alloy by EPMA or XRF i.e. the reaction time between the melt and tube wall appears to be insufficient.

There has been little data published concerning the effect of melt superheat immediately prior to casting into a copper mould on GFA. As will be revealed later in this thesis (**SECTION 4.5.2**) melt superheat is a critical parameter when aiming to achieve an amorphous structure when copper mould casting. In the present work, an as-cast sample of diameters ranging from 2-10 mm (**Figure 4.10**) that entirely filled the mould cavity without premature solidification was achieved at an injection temperature as low as 420 °C. In the current work, it is noted that upon cooling of the cast sample,  $T_g$  was reached by all sections of the mould in less than 2.5 s and an equilibrium temperature of ~30 °C was reached after 20 s, as seen in **Figure 4.15**. It was also noted in the same experimental work that through 25mm of solid copper the thermocouple reaction upon simply touching the mould with your hands (~36 °C) was seen instantaneously in live data acquisition. This would suggest that water cooling a copper mould (as was done by Senkov and Scott),<sup>[275]</sup> should improve the cooling capacity of the system.

The volume of copper in the copper cooling moulds will also affect the cooling/quenching ability of a system, as well as the dimensions of the mould cavity. The moulds used in all three works have similar dimensioned cavity angles/step sizes and step lengths per increase in diameter/thickness, although the mould used by Park and Kim<sup>[227]</sup> to achieve an amorphous thickness of 15 mm has a much larger starting and finishing diameter. With respect to a conical or graduated/stepped mould, a longer mould will give a different result to a shorter one due to the cooling effects of the sections immediately above and below a particular diameter. Generally, a longer mould would be expected to give a more accurate result as it is closer to an infinitely long section of that diameter or thickness.

## 4.5. INJECTION DIE CASTING OF $\text{Ca}_{65}\text{Mg}_{15}\text{Zn}_{20}$ BMG

In this section of the thesis, the original  $3.15 \times 7 \times 125$  mm rectangular copper mould used in **SECTION 3.7 (Figure 3.25)** to produce  $\text{Mg}_{65}\text{Cu}_{25}\text{Y}_{10}$  BMG bars was modified to fit the new induction-heated injection die casting unit. Here, a similar methodology to that used previously was employed to create multiple identical sized samples of the  $\text{Ca}_{65}\text{Mg}_{15}\text{Zn}_{20}$  BMG alloy. The three principal variables studied in this part of the work were: (i) melt temperature; (ii) injection pressure/velocity, and (iii) pressure relief. The melt injection temperature was found to determine both the viscosity of the molten metal and the degree of crystallinity of the casting, whereas the injection pressure determined the molten metal flow front velocity and velocity at the mould gate. The pressure relief was used to determine the maximum pressure achievable in the melt chamber, hence, the pressure at which the solidifying sample is held whilst cooling.

### 4.5.1 Experimental Procedure

The preparation of molten  $\text{Ca}_{65}\text{Mg}_{15}\text{Zn}_{20}$  alloy was carried out using the melting sequence described in **SECTION 4.3** and casting methodology of **SECTION 4.1– (ii) INJECTION CASTING**. On the final melting cycle, the alloy was cooled to the desired casting temperature, the copper mould was attached to the die-casting unit and the charge material injected into the mould at the desired overpressure to obtain the sample. Incremented temperatures in the range 410 - 600 °C and injection pressures in the range 1.5 - 2.2 Bar were used to produce samples of rectangular cross-section  $3.15 \times 7$  mm and lengths up to 125 mm using the methodology described in **SECTION 4.2** for injection casting. Relief pressures of 0.5-1.0 Bar were used in a number of preliminary experiments to determine its effect on surface quality and mould wall replication. The range of temperatures and pressures used in this part of the thesis together with length and sample density results are given in **Table 4.2**. The composition of the as-cast bars was determined to be  $\text{Ca}_{65}\text{Mg}_{15}\text{Zn}_{20} \pm 0.22\text{at.}\%$  by EPMA. Similar to the Mg-base BMG, samples were analysed for the presence of crystalline phases by XRD.

**Table 4.2:** The range of casting temperatures and pressures used for casting  $\text{Ca}_{65}\text{Mg}_{15}\text{Zn}_{20}$  samples and the corresponding results.

		CASTING TEMPERATURE (°C)													
		410	420	430	440	450	460	470	480	490	500	510	525	550	600
<b>P</b> <b>R</b> <b>E</b> <b>S</b> <b>S</b> <b>U</b> <b>R</b> <b>E</b>  (BAR)	2.2				L = 125mm DN = 99.1%						L = 125mm DN = 99.8%	L = 125mm DN = 99.8%			
	2.0	L = 112mm DN = 95.2%	L = 125mm DN = 96.1%	L = 125mm DN = 97.8%	L = 125mm DN = 99.1%	L = 125mm DN = 99.1%	L = 125mm DN = 99.3%	L = 125mm DN = 99.4%	L = 125mm DN = 99.4%		L = 125mm DN = 99.8%	L = 125mm DN = 99.8%		L = 125mm DN = 57.6%	L = 125mm DN = 45.8%
	1.8		L = 111mm DN = 94.9%	L = 125mm DN = 96.7%		L = 125mm DN = 98.5%			L = 125mm DN = 99.4%	L = 125mm DN = 99.7%	L = 125mm DN = 99.8%				
	1.6								L = 125mm DN = 99.1%	L = 125mm DN = 99.3%					
	1.5				L = 108mm DN = 94.1%	L = 125mm DN = 96.0%		L = 125mm DN = 98.0%		L = 125mm DN = 99.1%	L = 125mm DN = 99.1%		L = 125mm DN = 99.7%	L = 125mm DN = 99.8%	

**Key:** L = sample length DN = casting density % (with respect to the density of a fully dense casting).

Light grey regions indicate incomplete mould filling; dark grey regions indicate a partially crystalline microstructure (by XRD).



#### 4.5.2 Effect of Injection Temperature on As-Cast $\text{Ca}_{65}\text{Mg}_{15}\text{Zn}_{20}$ Samples

For the current setup, injection temperature was considered to be the determining experimental parameter with respect to obtaining an amorphous structure. The highest temperature at which the  $\text{Ca}_{65}\text{Mg}_{15}\text{Zn}_{20}$  bars were cast was 600 °C. Here it becomes apparent that in the case of the  $\text{Ca}_{65}\text{Mg}_{15}\text{Zn}_{20}$  BMG that the casting temperature  $T_{\text{CAST}}$  affects the internal structure of the as-cast samples. It is quite obvious from both the XRD patterns in **Figure 4.17a)** and the observed fracture surface seen in **Figure 4.17b)** that this particular sample displays a crystalline core. Injection temperatures were dropped until a critical injection temperature was found at which a completely amorphous structure was achieved at a thickness of 3.15 mm. From these results, the critical casting temperature for obtaining an amorphous structure was found to be 525 °C, where the amorphous structure was confirmed by XRD and showed no crystallite diffraction peaks in the X-ray spectra.

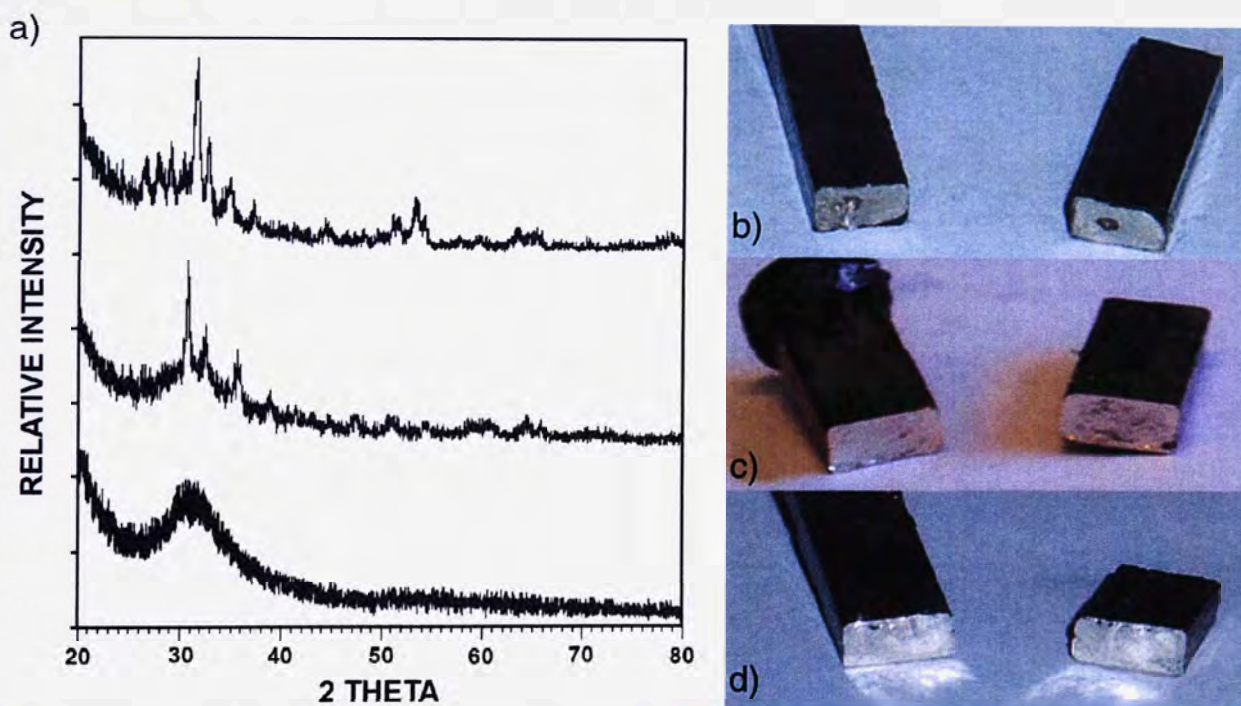


**Figure 4.17:** a) X-ray Diffraction patterns taken from the centre regions of the 3.15 x 7mm as cast bars and fracture surfaces of samples cast at b) 600 °C showing a crystalline interior and thin amorphous skin, c) 550 °C showing a crystalline interior and thick amorphous skin and d) 525 °C showing a highly reflective homogeneous amorphous structure throughout its cross section.

This behaviour cannot be explained in terms of Eqs. (3.3) and (3.6), since they only describe the cooling rate near or at the casting/mould interface. The reasoning behind this type of behaviour can only be explained by (i) an excessive thermal gradient within the mould; (ii) a significant thermal gradient within the casting itself, or a combination of the two.<sup>[229]</sup> Considering that the

thermal conductivity of copper is approximately four times greater than that of any of the alloy constituents used, and the volume of the copper mould is much greater than the volume of the casting, it far more likely that there is a significant thermal gradient within the casting, which would explain the transition from an amorphous skin to crystalline core.

This information suggests that, particularly at higher casting temperatures, the thermal conductivity of the casting is also a determining factor in producing a fully amorphous structure of a given thickness  $Z$ . So, assuming that the copper mould retains a constant temperature ( $T_{MOULD}$ ), which was validated by the reasoning above, the fact that when casting well above  $T_l$  (in this case 243 °C superheat) the temperature gradient within the casting will affect its structure. **Figure 4.18** gives a representation of such a cooling event from the centre of a BMG ( $Z/2$ ) where interface resistance is dominant, where at;  $t = 0$ ,  $T_{Z/2} = T_{CAST}$ .

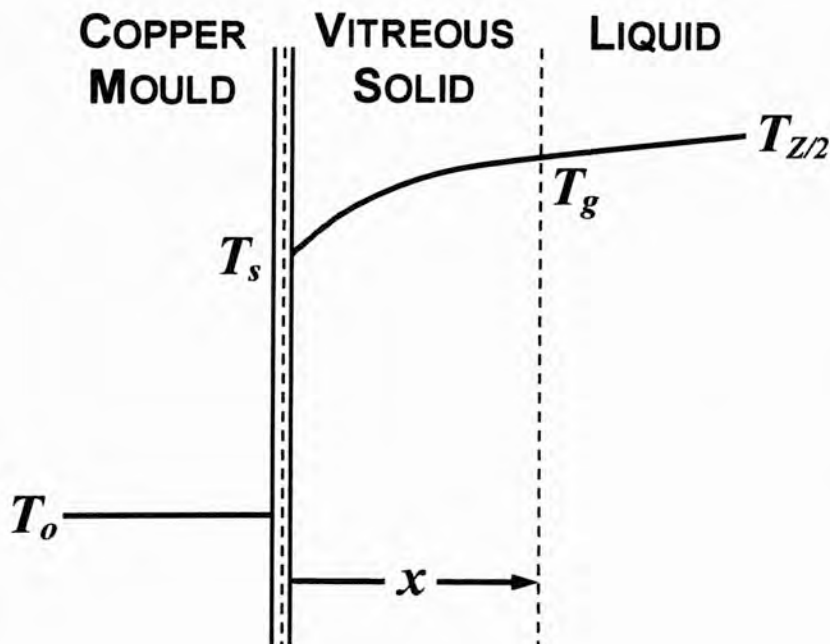


**Figure 4.18:** A representation of the temperature distribution within a BMG casting during cooling with a predominating interface resistance.

The numerical analysis of the system can be further simplified by approximating the temperature profile within the cooling casting as a linear function, the heat flux at the casting/mould interface can be given as:

$$q' = k \frac{T_{Z/2} - T_{MOULD}}{Z/2} \quad (4.5)$$



Also, for the interface:

$$q' = h(T_s - T_{MOULD}) \quad (4.6)$$

Equation (4.5) is Fourier's law of conduction, where  $k$  is the heat transfer coefficient of the casting and Eq. (4.6) is Newton's law of cooling, a modified version of Eq. (3.3), where  $q' = Q/At$ . The surface temperature  $T_s$ , can be eliminated by combining Eqs. (4.5) and (4.6).<sup>[229]</sup> Now, due to the linear temperature profile, the flux at the mould/liquid interface can be expressed by:<sup>[229]</sup>

$$q' = \frac{T_{Z/2} - T_{MOULD}}{1/h + Z/2k} \quad (4.7)$$

The effects of the internal temperature gradient due to the heat transfer co-efficient of the BMG are depicted in **Figure 4.19** for a sample cast at  $T_l$  and a sample cast well above  $T_l$ , where the dotted red lines are representative of the cooling rate at the centre of the casting ( $Z/2$ ) given by Eq. (4.7), and the solid red line is representative of the cooling rate at the sample surface (at the mould/casting interface), given by Eq. (4.6).

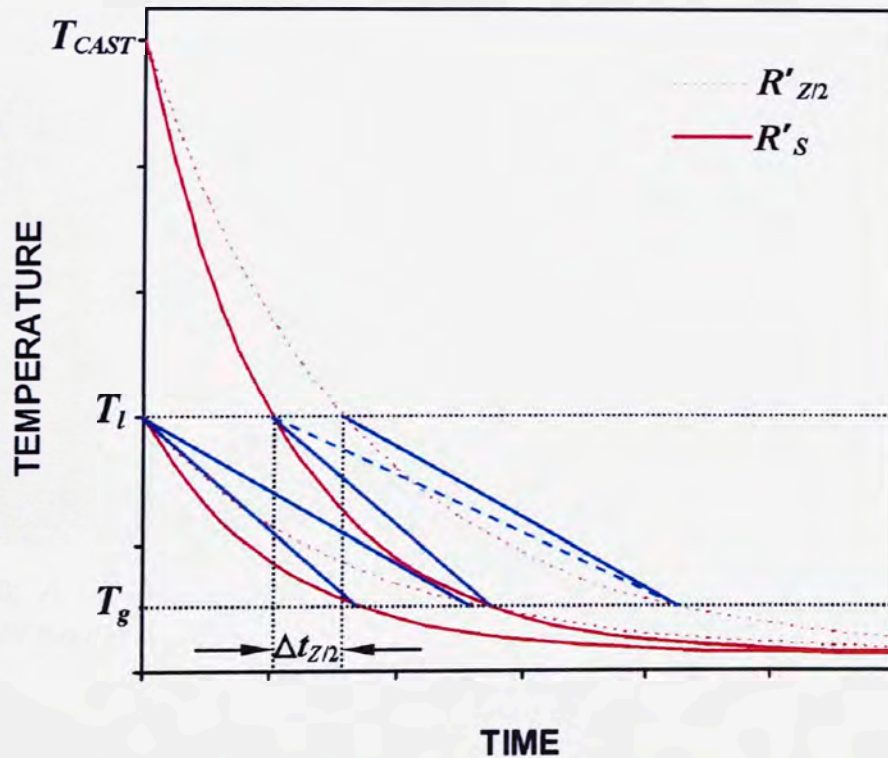


**Figure 4.19:** A representation of the effect of casting temperature on the cooling rate of a BMG casting between the mould wall and the centre of the casting.



As indicated by the solid blue lines, it can be seen that the cooling rates at the surfaces of both castings are greater than those at their interiors. However, for the sample cast at the higher temperature, the time taken for the casting to reach  $T_l$  is extended by  $\Delta t_{Z/2}$ , indicating an increase in the temperature gradient within the sample. Now, the average cooling rate of the sample cast at an elevated temperature can be represented by the dashed blue line in **Figure 4.20**, which is lower than that of the sample cast at  $T_l$ . Here it can be seen that the greater the casting temperature, the greater the value of  $\Delta t_{Z/2}$ , and the lower the sample cooling rate, as indicated by the results in **Figure 4.17**. It is also important to note that the thermal conductivity of metals (not a constant) decreases from room temperature to liquidus temperature by 10 - 20%,<sup>[290]</sup> which is expected to further hinder cooling at the centre of the casting ( $Z/2$ ).

As a molten metal flows into a mould, it cools at a rate determined by a number of processing variables and physical characteristics. As discussed in **SECTION 3.7.3**, it was found that temperature determined the viscosity of the BMG as it flowed, with viscosity in turn affecting the maximum achievable sample length. An example of this for the  $\text{Ca}_{65}\text{Mg}_{15}\text{Zn}_{20}$  alloy is shown in **Figure 4.20**. Also visible in **Figure 4.20** is a solidified reverse meniscus at the end of the sample, which indicates that immediately prior to solidification, the fluid flow front within the mould cavity was indeed uniform and stable, again highlighting the advantages of the inverted casting technique for BMG production.

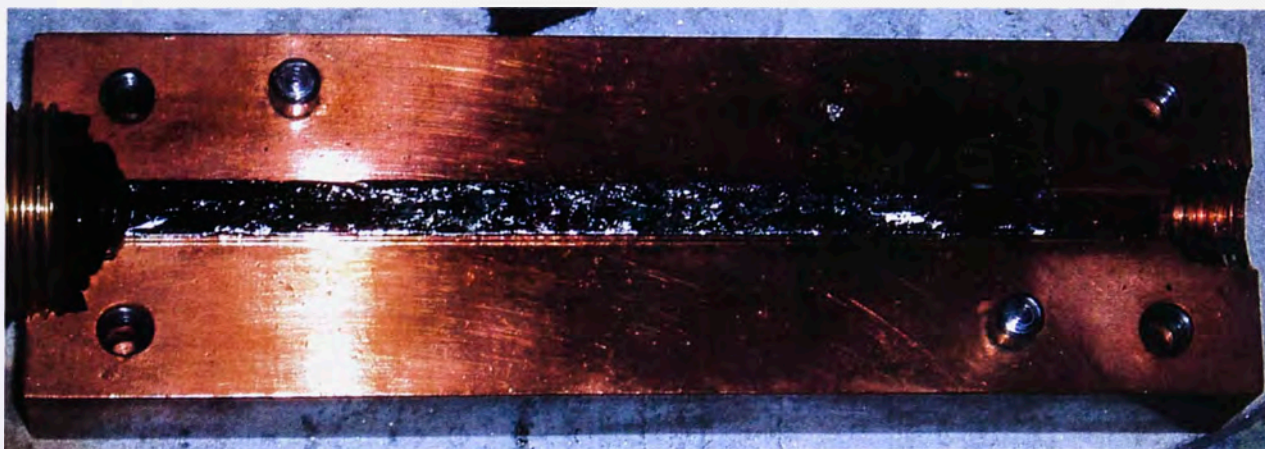


**Figure 4.20:** A  $\text{Ca}_{65}\text{Mg}_{15}\text{Zn}_{20}$  BMG sample cast at 410 °C and 2 Bar showing failure to completely fill the mould cavity.

For the  $\text{Ca}_{65}\text{Mg}_{15}\text{Zn}_{20}$  alloy, the critical casting temperatures ( $T_C$ ) for filling the entire length of the mould cavity were found to be 410 °C for an injection pressure of 2 Bar, 420 °C for a pressure of 1.8 Bar and 430 °C for an injection pressure of 1.5 Bar.



### 4.5.3 Effect of Injection Pressure/Velocity on As-Cast $\text{Ca}_{65}\text{Mg}_{15}\text{Zn}_{20}$ Samples

A majority of flow-related casting defects are caused by either trapped gases or premature solidification. In ideal circumstances, the liquid metal should displace the cavity gas ahead of the flow front as the cavity fills without creating gas pockets or sealing the vents before the gas escapes. As described in SECTION 3.7.3, the fluid velocity is prescribed at the entrance to the runner (silica tube) and the pressure boundary conditions on the free surface depend on the rate at which the excess gas escapes through the mould vent and the fluid flow behaviour can be determined by the associated Reynolds Number (Eq. (3.10)).<sup>[240]</sup>

In the case of BMGs, where cooling rates are quite high, high gate velocities must be utilised to achieve complete cavity filling, as depicted in SECTION 3.7.3. Excessive gate velocities when combined with rapid cooling rates can lead to defects such as a hollowed structure or cold shuts which reduce the structural integrity of the casting. By varying the injection pressure of this set up, the ideal fluid velocity could be determined such that a stable fluid front was achieved and a structurally sound sample produced.

Samples cast at lower temperatures and pressures tended to develop a higher number of defects such as cold shuts and voids and these samples generally had a poorer surface finish and did not replicate mould details such as sharp square corners (Figure 4.21). Here, cold shuts were generated where a section of the cast metal solidified before reaching the walls of the mould creating a surface; the advancing molten metal from another section of the casting 'back fills' over this original surface, although it does not bond to it very well. What is left is a poorly bonded skin of low structural integrity that flakes away from the main body of the casting, revealing the surface that had solidified first. Cold shuts and porosity were more common at the ends of samples cast at lower temperatures and pressures (nearest the mould vent), which would be an expected result as this is the first part of the casting to solidify and has to travel the furthest distance in the mould.



**Figure 4.21:** A sample cast at 450 °C and 1.5 Bar showing poor mould wall replication and the generation of cold shuts and porosity.



As discussed in SECTION 3.7.4, rapidly solidified alloys may form an inhomogeneous metal layer on the surface of a die casting when the alloy flows rapidly in contact with a mould wall, and that this layer generates a surface warping defect.<sup>[243]</sup> This also appears to be the case with the  $\text{Ca}_{65}\text{Mg}_{15}\text{Zn}_{20}$  alloy, as shown in Figure 4.22.

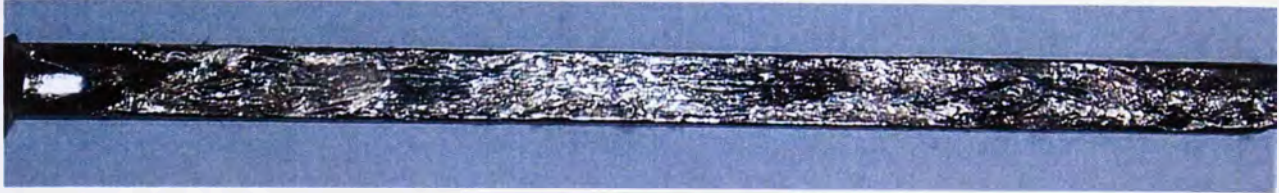


**Figure 4.22:** Rapid freezing of the metal in contact with the copper die showing the creation of striations on the surface of sample surface (casting conditions were 490 °C and 1.8 Bar).

In order to compare casting conditions of the Ca-base BMG to the Mg-base BMG in terms of fluid velocity, calculations were made using the amount a pressure  $P_R$  required to move a known mass of fluid a specified distance to the mould gate using:<sup>[291]</sup>

$$P_R = P_o + \rho gh \quad (4.8)$$

where  $P_o$  is atmospheric pressure,  $\rho$  the density of the liquid metal,  $g$  the acceleration due to gravity and  $h$  the height that the molten metal has to be raised in the silica tube. Using ideal gas theory (assuming argon behaves as an ideal gas), knowing the pressure of the gas supply (injection pressure) and using atmospheric pressure as an initial boundary pressure, the mass flow rate,  $\dot{M}$  of the argon gas (neglecting tube wall friction) into the chamber may be calculated using:<sup>[292]</sup>

$$\frac{M}{RT} \frac{P_2^2 - P_1^2}{2} + \left( \frac{\dot{M}}{A} \right)^2 \ln \frac{P_1}{P_2} = 0 \quad (4.9)$$

By knowing the amount of pressure required in the chamber to move the charge mass a required height and being able to calculate the mass flow rate for a given injection pressure, the time taken to raise the required charge can be calculated. From these times, the maximum expected velocity of the fluid front,  $v_{MAX}$ , in the silica tube at the mould gate could be calculated. Losses associated with the tube entrance, can be calculated for a given injection pressure by using a discharge coefficient,  $C_D$ , where the corrected velocity  $v_F$  can be found using:<sup>[293]</sup>

$$v_F = C_D v_{MAX} \quad (4.10)$$



where

$$C_D = \left( \frac{1}{\beta} + e_f \right)^{-1/2} \quad (4.11)$$

where  $\beta$  is the velocity distribution factor for the cross section, which is approximated as unity for turbulent flow,<sup>[293]</sup> and  $e_f$  the friction loss factor for a sudden contraction is given as:<sup>[294]</sup>

$$e_f = 0.5 \left( 1 - \frac{A_s}{A_L} \right) \quad (4.12)$$

where  $A_s$  and  $A_L$  are the cross section areas of the smaller and larger sections in the fluid circuit, respectively. This value is further corrected by a ratio associated with the type of entrance to the restriction (RESTRICTION TYPE 1 for entry into the silica tube), as shown in **Figure 4.23a**).

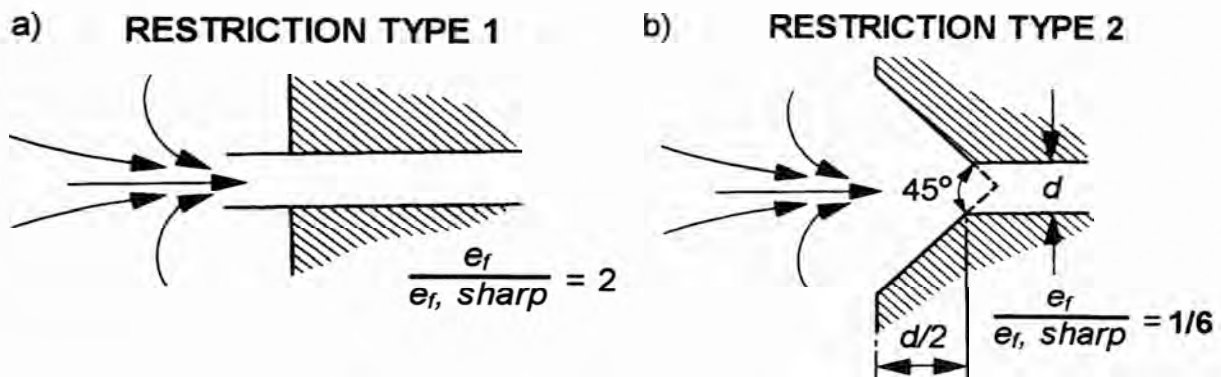


**Figure 4.23:** Entrance loss coefficients ratios for a) a protruding tube and b) a beveled edge.<sup>[295]</sup>

Finally, the approximate velocity of the flow front upon entering the mould was determined by a traditional conservation of fluid volume approach, i.e.  $A_1 v_1 = A_2 v_2$  with respect to the decrease in channel cross section area. Discharge coefficient corrections for the restriction at the mould gate were made in a similar manner to that discussed above (RESTRICTION TYPE 2, as shown in **Figure 4.23b**) to give the final velocity of the liquid entering the mould cavity. An example of these calculations is given in **APPENDIX F**.

#### 4.5.4 Effect of Relief Pressure on As-Cast $\text{Ca}_{65}\text{Mg}_{15}\text{Zn}_{20}$ Samples

An additional parameter investigated in the production of  $\text{Ca}_{65}\text{Mg}_{15}\text{Zn}_{20}$  BMG samples was relief pressure. As a safety precaution and a control measure, a pressure relief valve was fitted to the injection chamber. In the casting trials, it was found that higher injection pressures resulted in a build up of pressure in the injection chamber once the mould vent becomes sealed by the

solidifying/ progressing metal. In the case of excessive pressure build up, particularly at higher injection temperatures, the mould was found to experience either complete or partial 'blow through', whereby the entire charge is ejected through the mould vent leaving either an empty mould or a thin solidified hollow shell. By limiting the maximum chamber pressure to 1 Bar, this blow through effect was more easily managed. Experimental work was also carried out by varying the relief pressure between 0.5 and 1 Bar. It was found that a higher relief pressure generated a higher quality sample with a more desirable surface finish. Such an effect is thought to be due to a type of high temperature extrusion/compaction process. The supercooled liquid may remain a viscous fluid (governed by Eq. (2.8)) to quite low temperatures (as low as  $T_g$  is theoretically possible), so, by applying a force in the form of gas pressure to the casting whilst it is in this state, may result in further consolidation of the casting.

By integrating Eq. (4.6) with respect to time and temperature and determining the interfacial heat transfer coefficient  $h$  from SECTION 4.4.2, the expected cooling curves of the sample surface for a given injection temperature were calculated (example given in APPENDIX G). Again, by using Eq. (4.9) to determine the initial mass flow rate into the chamber for a given injection pressure, using ideal gas theory and the variation of mass flow rate with increasing chamber pressure, it is possible to calculate the increase in chamber pressure over time (example calculations are given in APPENDIX H). Figure 4.24 shows the surface cooling curves for a range of injection casting temperatures and the increase in pressure in the injection chamber (due to sealed vent) with respect to time, which is relieved once it reaches 1 Bar. By reiterating that the SCL is still capable of flowing at temperatures as low as  $T_g$ , the effect of injection pressure on the consolidation of the sample once the mould vent is sealed is depicted in Figure 4.24.

Using XRD data, it was determined that casting should be carried out at injection temperatures below 525 °C to produce fully amorphous samples. It was also determined that below 410 °C the tendency of the casting to entirely fill the mould cavity is reduced (due to viscosity effects). A small, fully dense sample of  $\text{Ca}_{65}\text{Mg}_{15}\text{Zn}_{20}$  BMG was measured for density using Archimedes method. From these results, each casting was weighed, and with respect to the expected volume (i.e. the mould cavity) was also measured for density. From this work, a contour style processing map (contours represent sample density in percent with respect to expected density) was developed (Figure 4.25), which provides information on the optimum casting conditions for generating amorphous, high density  $\text{Ca}_{65}\text{Mg}_{15}\text{Zn}_{20}$  BMG samples of dimensions 3.15 x 7 mm and a length of 125 mm.

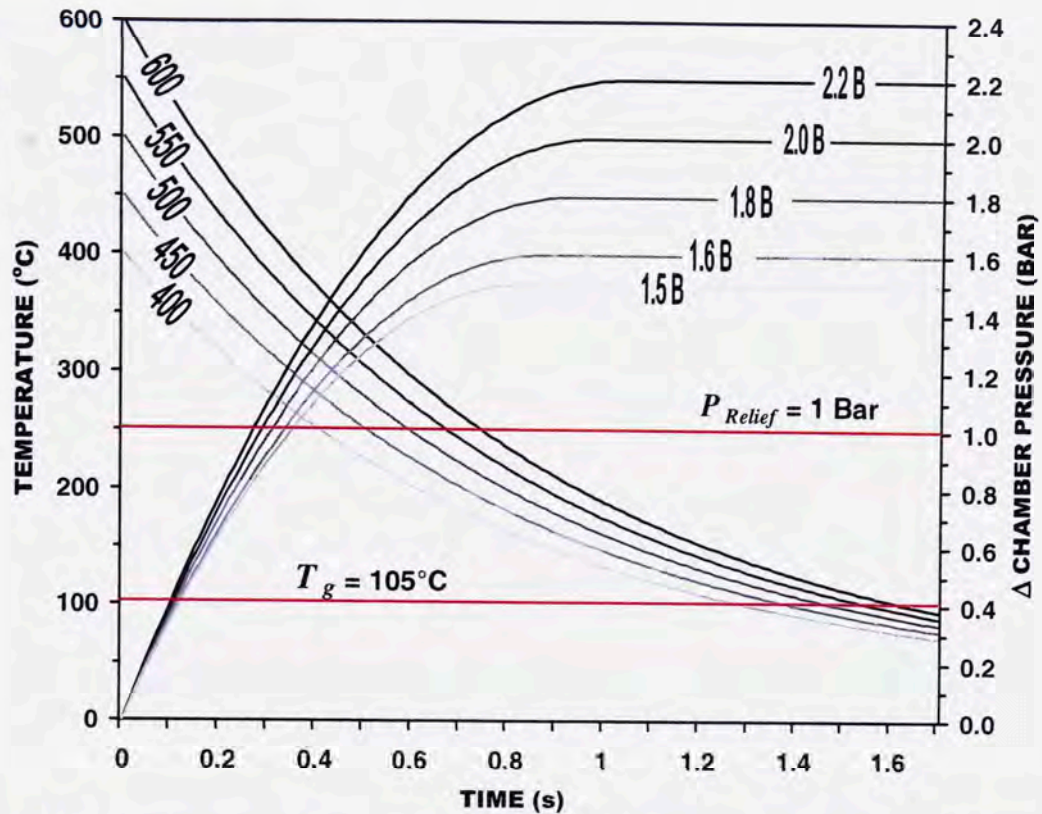


**Figure 4.24:** Calculated cooling curves for a range of injection temperatures and the increase of pressure in the injection chamber with respect to time (limited to 1 Bar by pressure relief).

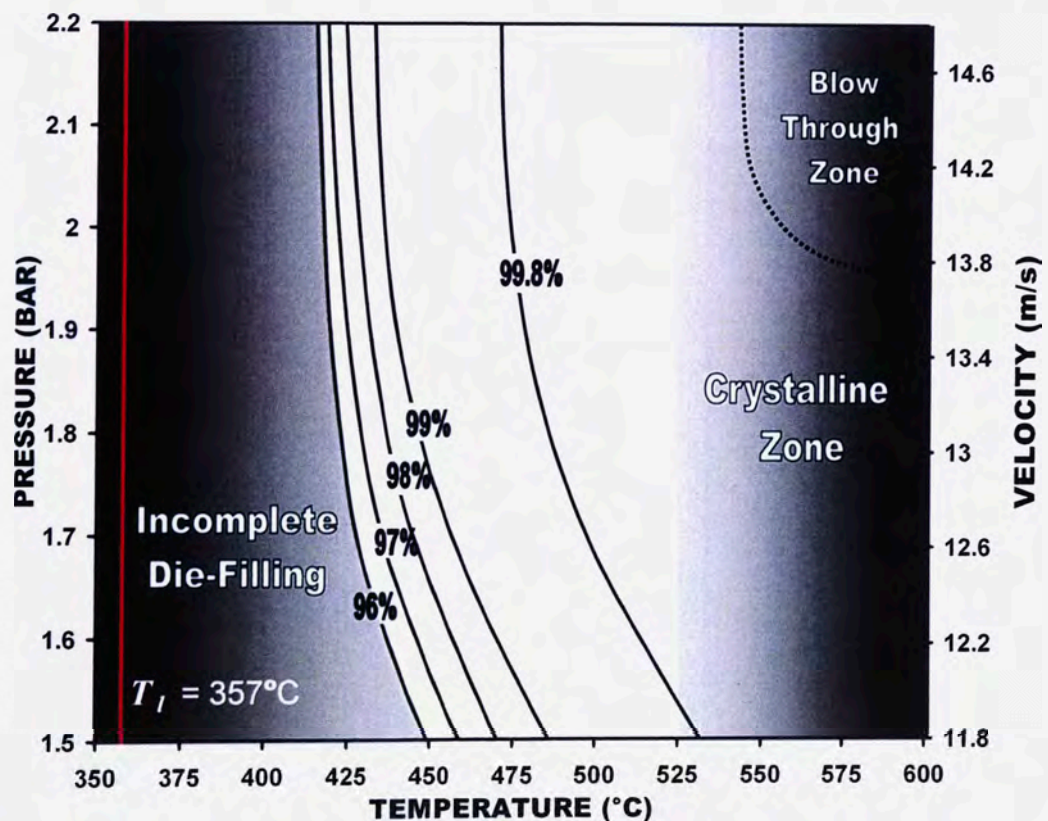


**Figure 4.25:** Contour style processing map for providing information on the optimum casting conditions for generating amorphous, high density  $\text{Ca}_{65}\text{Mg}_{15}\text{Zn}_{20}$  BMG samples of dimensions  $3.15 \times 7 \times 125$  mm.



It should be noted that the inability to achieve 100% density is likely due to surface imperfections and mould wall replication rather than sample porosity, which became evident upon further processing of the material.

It can be seen in **Figure 4.25** that the desirable processing window is reasonably large and a sound casting is expected for a range of processing parameters. The maximum density of a sample achieved was 99.84% of the theoretical density using an injection temperature of 510 °C and pressure of 2.2 Bar. Based on this diagram, the optimum combination of melt temperature and casting pressure to generate a sound casting is 485-510 °C and 1.9-2.2 Bar.

It is interesting to note that the injection velocity range is almost identical to that of the favourable casting region for  $\text{Mg}_{65}\text{Cu}_{25}\text{Y}_{10}$  (**SECTION 3.7**). It is also important to note that the variation in densities of these samples is much smaller than in the previous work, indicating a considerable improvement in the injection process (i.e. these results lie within the top 4% of sample density measurements as opposed to the top 50% in magnesium work shown in **Figure 3.32**). The processing map shown in **Figure 4.25** for casting  $\text{Ca}_{65}\text{Mg}_{15}\text{Zn}_{20}$  BMG samples of dimensions 3.15 x 7 x 125 mm was successfully utilised to consistently produce a large number of BMG samples for further testing and analysis, as shown in **Figure 4.26**.

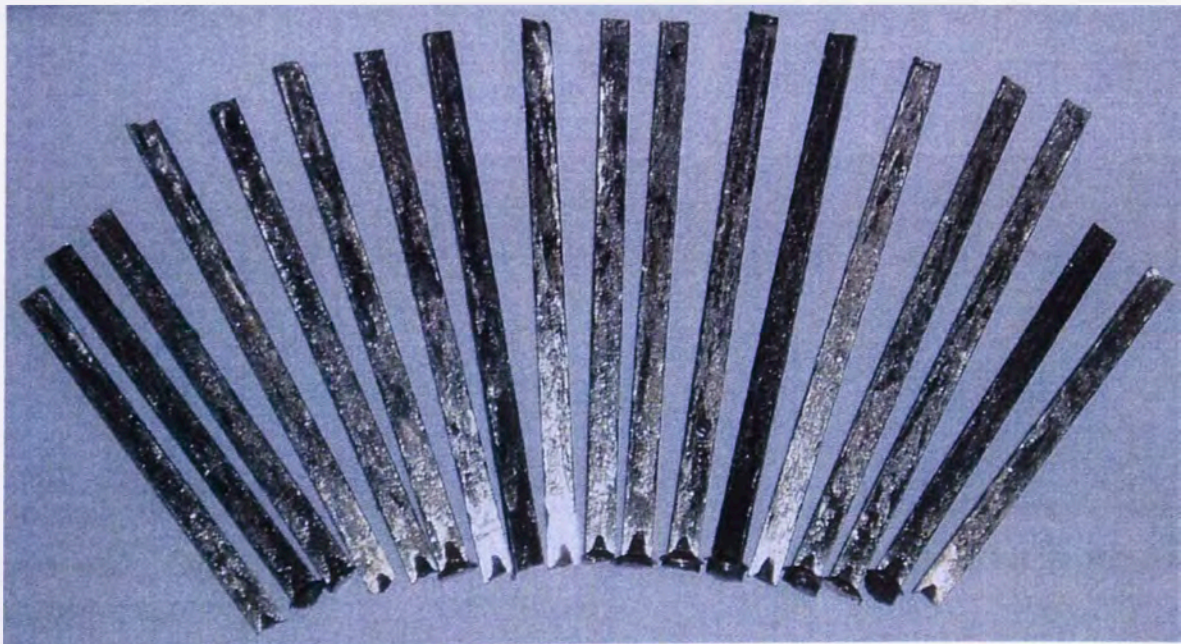


**Figure 4.26:** A number of  $\text{Ca}_{65}\text{Mg}_{15}\text{Zn}_{20}$  samples produced using **Figure 4.25** (some of these samples have been sectioned for structural analysis).



## 4.6. ELEVATED TEMPERATURE MECHANICAL BEHAVIOUR OF THE $\text{Ca}_{65}\text{Mg}_{15}\text{Zn}_{20}$ BMG

A characteristic feature of BMGs is the dramatic decrease in viscosity at temperatures above the glass transition temperature ( $T_g$ ); this behaviour is usually explained by the transformation of the glassy state into a supercooled liquid state.<sup>[180]</sup> This part of the thesis describes the elevated temperature flow behaviour of the  $\text{Ca}_{65}\text{Mg}_{15}\text{Zn}_{20}$  BMG under uniaxial tension using the standardised tensile test samples shown in **Figure 4.27**. The data generated from these tests allowed the development of deformation maps with respect to temperature and strain rate which enabled the identification of specific deformation behaviour (of particular interest, Newtonian flow behaviour) over a range of testing conditions. From an engineering viewpoint, the identification of such deformation conditions in the  $\text{Ca}_{65}\text{Mg}_{15}\text{Zn}_{20}$  BMG is beneficial for future applications of such materials since superplastic forming to generate intricate shaped components is likely to be an important method of fabrication.

### 4.6.1 Experimental Procedure

$\text{Ca}_{65}\text{Mg}_{15}\text{Zn}_{20}$  BMG samples of dimensions 3.15 x 7 x 125 mm were prepared using the repetitive die casting technique described in **SECTION 4.5**. Due to the low ductility of the alloy at ambient temperature, tensile test samples (dimensions: 12.3 mm gauge length and 3 mm diameter) in accordance with ASTM E8-04 were produced using the grinding technique described in **SECTION 3.8**. **Figure 4.27** shows a series of samples ready for tensile testing.

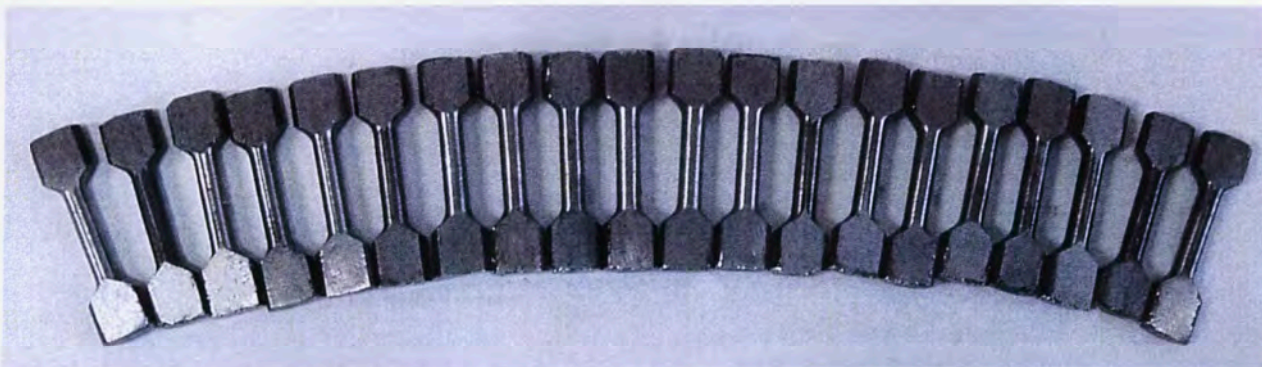


**Figure 4.27:**  $\text{Ca}_{65}\text{Mg}_{15}\text{Zn}_{20}$  BMG tensile samples produced using the grinding technique described in **SECTION 3.8**.

In conjunction with this work, the thermal properties of the BMG were determined DSC at a heating rate of 5 °C/min. Isothermal DSC measurements were also carried out at various test



temperatures for providing an indication of the maximum duration of tensile testing prior to the onset of crystallisation (**Figure 4.14**).

Due to the reactive nature of the BMG at elevated temperatures, tensile samples were subsequently deformed whilst submerged in silicon oil using an MTS 810 servo-hydraulic testing machine equipped with a 1 kN load cell. **Figure 4.28** shows a schematic representation of the experimental apparatus used for both constant strain and constant load tensile testing. A K-type thermocouple was positioned in close proximity to the specimen to monitor the temperature at the specimen surface. The chamber was preheated prior to mounting the specimens to minimise heat up time. Since  $T_g$  is not a unique physical property of the glass but rather a rate dependent kinetic quantity, the heating rate of the specimen was kept constant at  $\sim 5$  °C/min after reaching 90 °C. Tensile testing commenced at a given temperature only after the sample test temperature was stabilised for  $\sim 2$  min. Tensile testing was carried out by two methods: (i) constant strain rate ( $10^{-3}$  to  $10^{-4}$  s $^{-1}$ ) testing at constant temperature (105 to 120 °C) and (ii) constant load (20 to 50 N) testing at a heating rate of 5 °C/min. Over fifty tensile test samples were fabricated with testing repeated up to four times in some cases in order to obtain reliable and consistent data.

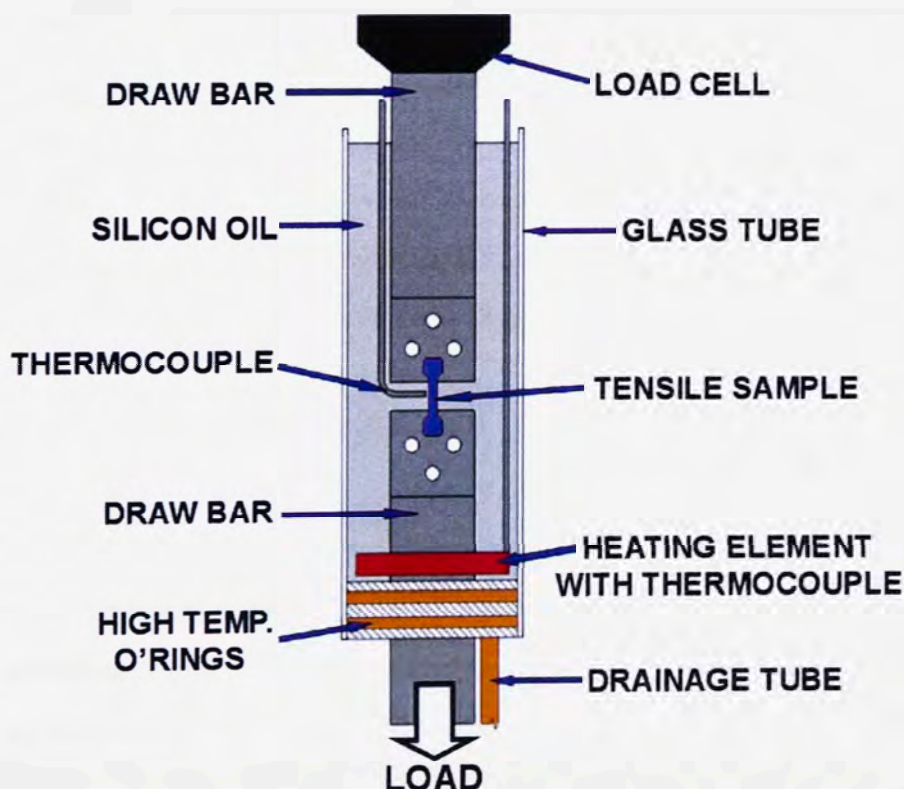


**Figure 4.28:** Schematic representation of the apparatus used for constant strain and constant load tensile testing of  $\text{Ca}_{65}\text{Mg}_{15}\text{Zn}_{20}$  BMG samples.



#### 4.6.2 Constant Strain Rate Tensile Testing

The tensile deformation behaviour of the  $\text{Ca}_{65}\text{Mg}_{15}\text{Zn}_{20}$  BMG within the supercooled liquid region (105 to 120 °C) was examined at constant strain rates ranging from  $10^{-3}$  to  $10^{-4} \text{ s}^{-1}$ . The maximum strain to failure of these samples was in excess of 590 % with most samples failing at around 200 % strain due to the onset of crystallisation.

Isothermal annealing DSC experimental results carried out at temperatures ranging from 110 to 135 °C (**Figure 4.14**) were used to determine the allowable time frame for tensile testing before the onset of crystallisation. Using this data, it had been observed that when the  $\text{Ca}_{65}\text{Mg}_{15}\text{Zn}_{20}$  BMG is held at temperatures at 125 °C or greater, the onset of crystallisation is quite short. In fact, these times were shorter than that needed to stabilise the sample temperature and commence testing. This suggests that only half of the SCL region is of practical use in low strain-rate laboratory testing or for manufacturing components if a fully amorphous structure is to be retained. Consequently, constant strain rate tensile testing was carried out at temperatures from 105 to 120 °C in increments of 5 °C.

**Table 4.3** gives various test results, including flow stress ( $\sigma_f$ ), maximum strain or elongation ( $\epsilon_{MAX}$ ) as a percentage of the original gauge length, test time to failure ( $t_{FAIL}$ ) and the time delay of the crystallisation stress response ( $\Delta t_{XD}$ ) for the samples that reached the expected crystallisation onset time. With the exception of a single sample, all samples failed in either a brittle type manner with elongations <2.3% or continued to flow plastically until failure. The failure mechanism of the sample tested at 105 °C and  $1 \times 10^{-4} \text{ s}^{-1}$  is likely to be an extreme example of non-Newtonian flow, which would be expected since the test temperature is so close to  $T_g$ . Both brittle and non-Newtonian flow regimes are marked in **Table 4.3** as dark grey and light grey, respectively, with the other values indicating Newtonian flow conditions.

For some samples that flowed in a homogeneous, plastic manner, there was a stress overshoot similar to other BMG systems.<sup>[60,247]</sup> This is typical indication of non-Newtonian flow conditions.<sup>[60,185,247]</sup> Beyond this overshoot, there was a considerable decrease in stress to a low equilibrium value. The flow stress of a given sample was determined using the methodology described in **APPENDIX C**. The strain-induced softening phenomenon after an initial peak stress is explained by an increase in free volume of the amorphous structure and the generation of shear bands.<sup>[20,25,27,248-250]</sup>

**Table 4.3:** A summary of tensile test conditions and their corresponding results for the  $\text{Ca}_{65}\text{Mg}_{15}\text{Zn}_{20}$  BMG.

		CONSTANT STRAIN RATE ( $\text{s}^{-1}$ )				
		$1 \times 10^{-3}$	$7.5 \times 10^{-4}$	$5 \times 10^{-4}$	$2.5 \times 10^{-4}$	$1 \times 10^{-4}$
T E M P E R A T U R E  (°C)	120	$\sigma_P = 14.3\text{MPa}$ $\sigma_f = 8.50\text{MPa}$ $\epsilon_{MAX} = 180\%$ $t_{FAIL} = 27\text{min}$ -	$\sigma_P = 6.55\text{MPa}$ $\sigma_f = 5.79\text{MPa}$ $\epsilon_{MAX} = 216\%$ $t_{FAIL} = 48\text{min}$ -	$\sigma_P = 5.25\text{MPa}$ $\sigma_f = 4.56\text{MPa}$ $\epsilon_{MAX} = 258\%$ $t_{FAIL} = 69\text{min}$ $\Delta t_{XD} = 10\text{min}$	$\sigma_P = 3.10\text{MPa}$ $\sigma_f = 2.42\text{MPa}$ $\epsilon_{MAX} = 132\%$ $t_{FAIL} = 79\text{min}$ $\Delta t_{XD} = 3\text{min}$	$\sigma_P = 1.01\text{MPa}$ $\sigma_f = 1.01\text{MPa}$ $\epsilon_{MAX} = 46\%$ $t_{FAIL} = 68\text{min}$ $\Delta t_{XD} < 1\text{min}$
	115	$\sigma_P = 21.0\text{MPa}$ - $\epsilon_{MAX} = 2.12\%$ - -	$\sigma_P = 20.5\text{MPa}$ - $\epsilon_{MAX} = 2.24\%$ - -	$\sigma_P = 12.3\text{MPa}$ $\sigma_f = 10.6\text{MPa}$ $\epsilon_{MAX} = 294\%$ $t_{FAIL} = 95\text{min}$ $\Delta t_{XD} = 17\text{min}$	$\sigma_P = 6.61\text{MPa}$ $\sigma_f = 5.65\text{MPa}$ $\epsilon_{MAX} = 146\%$ $t_{FAIL} = 94\text{min}$ $\Delta t_{XD} = 11\text{min}$	$\sigma_P = 3.52\text{MPa}$ $\sigma_f = 3.19\text{MPa}$ $\epsilon_{MAX} = 59\%$ $t_{FAIL} = 94\text{min}$ $\Delta t_{XD} = 5\text{min}$
	110	$\sigma_P = 21.3\text{MPa}$ - $\epsilon_{MAX} = 1.44\%$ - -	$\sigma_P = 20.5\text{MPa}$ - $\epsilon_{MAX} = 1.49\%$ - -	$\sigma_P = 26.2\text{MPa}$ $\sigma_f = 23.1\text{MPa}$ $\epsilon_{MAX} = 598\%$ $t_{FAIL} = 204\text{min}$ $\Delta t_{XD} = 102\text{min}$	$\sigma_P = 15.8\text{MPa}$ $\sigma_f = 14.1\text{MPa}$ $\epsilon_{MAX} = 346\%$ $t_{FAIL} = 231\text{min}$ $\Delta t_{XD} = 95\text{min}$	$\sigma_P = 10.6\text{MPa}$ $\sigma_f = 10.2\text{MPa}$ $\epsilon_{MAX} = 134\%$ $t_{FAIL} = 225\text{min}$ $\Delta t_{XD} = 81\text{min}$
	105	$\sigma_P = 27.3\text{MPa}$ - $\epsilon_{MAX} = 1.21\%$ - -				$\sigma_P = 24.6\text{MPa}$ $\sigma_f = \sim 24.6\text{MPa}$ $\epsilon_{MAX} = 15.8\%$ - -

**Key:**  $\sigma_P$  = peak stress  $\sigma_f$  = flow stress  $\epsilon_{MAX}$  = maximum strain ( $t_{FAIL}$ ) = time to failure

$\Delta t_{XD}$  time delay of the crystallisation stress response. Brittle failure and non-Newtonian flow regimes are marked in dark grey and light grey respectively, white cell values indicate Newtonian flow conditions.

### 4.6.3 Effect of Deformation Temperature on Flow Behaviour

As discussed in SECTION 3.9.3, plastic deformation of a metallic glass occurs by two principal modes:<sup>[251,252]</sup> (i) inhomogeneous at low temperatures, where flow is unstable due to progressive softening of the material and at higher temperatures, leading to an intrinsically brittle type failure and (ii) homogeneous deformation, whereby each volume element of the material undergoes the same strain. The latter generally generates exceedingly large elongations during tensile deformation. Typical results at a strain rate of  $5 \times 10^{-4} \text{ s}^{-1}$  for temperatures from 110 to 120 °C are shown in **Figure 4.29**. A distinct increase in initial flow stress ( $\sigma_f$ ) is evident as the test temperature is decreased for a given strain rate (see **Table 4.4**) which is analogous to the increase in viscosity of the supercooled liquid, as described by the general VFT equation (Eq. (2.8)).

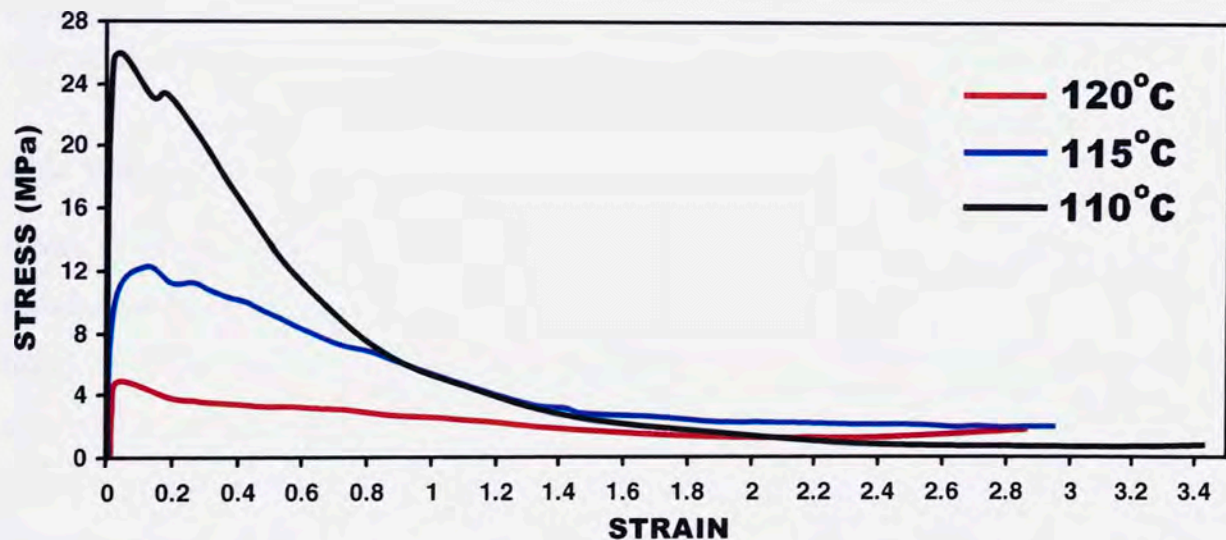


**Figure 4.29:** The effect of temperature on flow behaviour on samples strained at  $5 \times 10^{-4} \text{ s}^{-1}$  at temperatures ranging from 110 to 120 °C.

**Figure 4.30** shows the change in flow stress as a function of temperature for all strain rates: non-filled data points represent Newtonian flow conditions and filled data points represent low temperature inhomogeneous region where brittle fracture occurs. It can be seen that a distinct change in slope of each curve occurs on approaching the non-Newtonian flow regime. In the homogeneous deformation zone (both Newtonian and non-Newtonian), samples deformed to elongations greater than 200 %, which was generally limited by the onset of crystallisation.



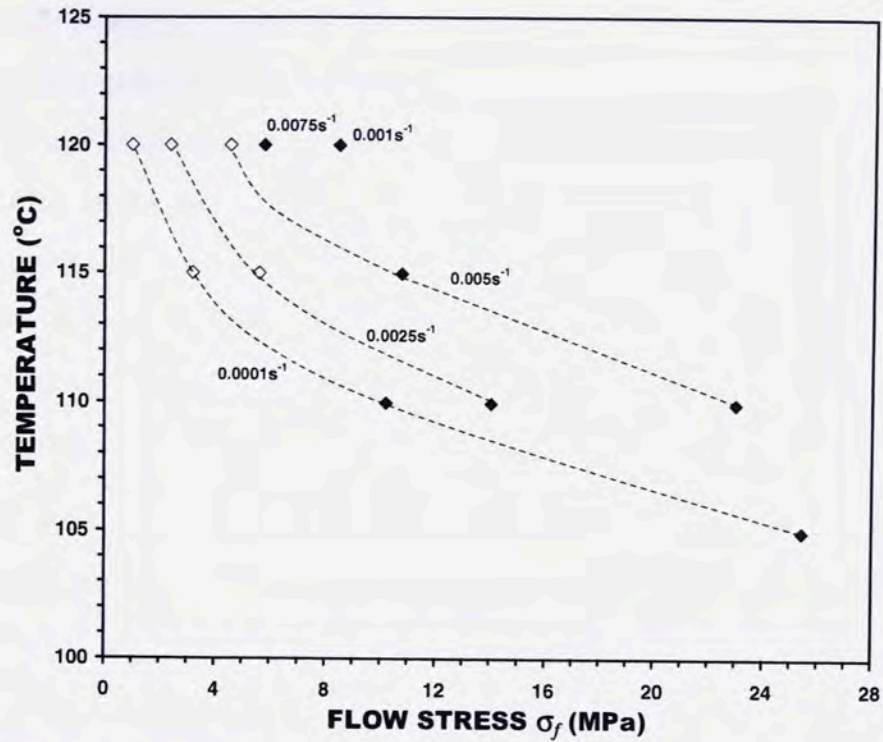


**Figure 4.30:** Effect of deformation temperature on the flow stress of the  $\text{Ca}_{65}\text{Mg}_{15}\text{Zn}_{20}$  BMG at various strain rates.

#### 4.6.4 Effect of Strain Rate on Flow Behaviour

It was observed early in the investigation that the  $\text{Ca}_{65}\text{Mg}_{15}\text{Zn}_{20}$  BMG was highly strain rate sensitive with the maximum applied strain rate achievable within the given temperature range being  $1 \times 10^{-3} \text{ s}^{-1}$ . This strain rate is quite low when compared to elevated temperature deformation other BMG systems.<sup>[20,60,244]</sup> Hence, for this work, strain rates ranging from  $1 \times 10^{-3}$  to  $1 \times 10^{-4} \text{ s}^{-1}$  were used for tensile testing. An example of the effect of strain rate on both peak stress and flow stress is given in **Figure 4.31** for samples tested at  $120^\circ\text{C}$ .

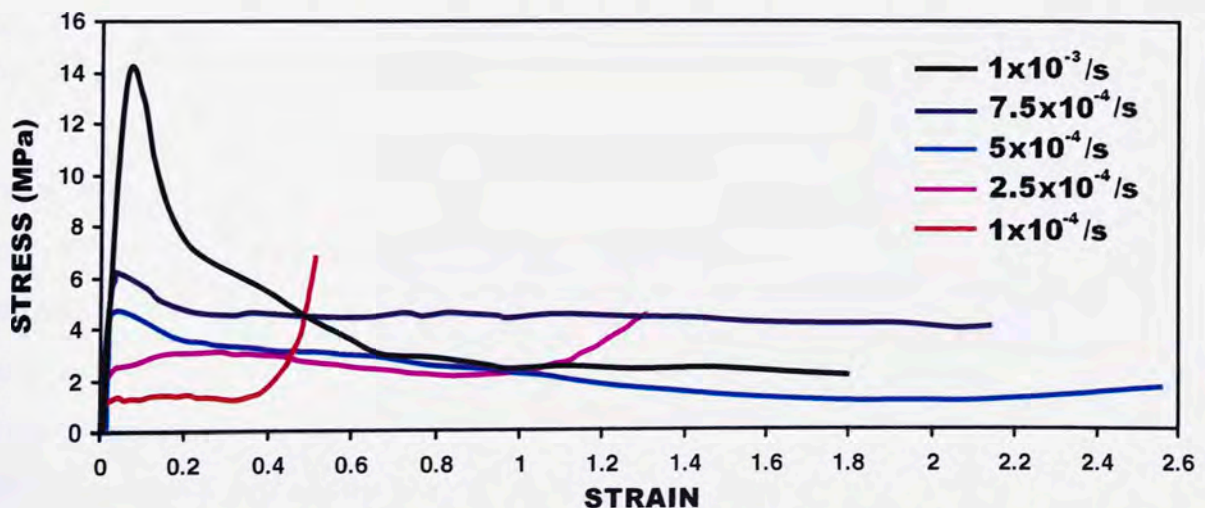


**Figure 4.31:** Effect of strain rate on flow behaviour on tensile samples held at  $120^\circ\text{C}$  strained at  $1 \times 10^{-3}$  to  $1 \times 10^{-4} \text{ s}^{-1}$ .

The flow behaviour in the SCL region was examined with respect to flow stress and strain rate. The flow stress data obtained from constant strain rate testing is plotted in log/log format in **Figure 4.32**. Similar to the Mg-base BMG, there is a distinct linear relationship between log flow stress and log strain rate at all test temperatures for part of the data range. Using Eq. (2.30), the slope of each data portion gives the strain-rate sensitivity ( $m$ ) within this test region. For the Ca-base BMG,  $m$ -values of unity were calculated for some test conditions, indicating Newtonian flow behaviour, as indicated in **Figure 4.32**, along with non-Newtonian flow and brittle fracture zones.

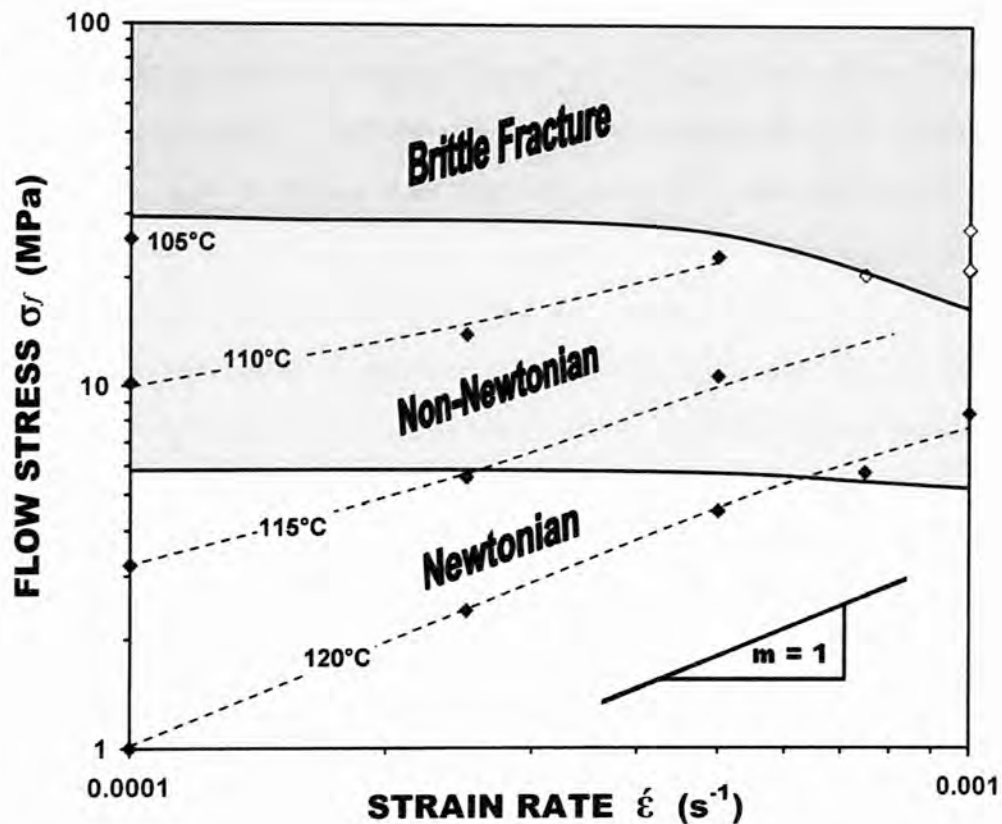


**Figure 4.32:** Flow stress for  $\text{Ca}_{65}\text{Mg}_{15}\text{Zn}_{20}$  BMG samples tested from 105 to 120 °C plotted over strain rate in log-log format, indicating the strain-rate sensitivity exponent  $m$ .

The  $m$ -value is close to unity for a large portion of the data set, suggesting that flow remains close to Newtonian conditions at these relatively low strain rates. However, a transition from Newtonian to non-Newtonian flow behaviour is seen to take place with  $m$ -values less than unity found at lower test temperatures and higher strain rates. It is also pertinent to note that the range of experimental data with respect to strain rate is quite narrow compared to the Mg-base BMG (SECTION 3.9) and BMGs investigated elsewhere,<sup>[20,60,244]</sup> further highlighting the sensitivity of the  $\text{Ca}_{65}\text{Mg}_{15}\text{Zn}_{20}$  BMG to brittle failure. **Table 4.3** shows that samples tested at 120 °C and strain rates of  $1 \times 10^{-3} \text{ s}^{-1}$  and  $7.5 \times 10^{-4} \text{ s}^{-1}$  exhibit much smaller elongations prior to failure than

might be expected, which was due to localised necking during testing. This is believed to be due to parameters pertaining to non-Newtonian flow conditions, whereby material flow is not entirely homogeneous throughout the entire sample, rather, flow is concentrated locally at a region of least resistance, resulting in premature failure.

As discussed in SECTION 2.6.4, the steady-state flow stress can be prescribed according to the transition state theory of flow stress, where the relation between  $\sigma_f$  and  $\dot{\epsilon}$  under a uniaxial loading conditions is given by Eq. (2.32).<sup>[69,173]</sup> Using this relation, the viscosity as a function of strain rate for a particular temperature is given in Figure 4.33, which exemplifies the strain-rate dependence of the viscosity at various temperatures. As discussed in detail in SECTION 2.6.4, this effect is believed to be due to either a change in the material free volume<sup>[183]</sup> or concurrent crystallisation of the material,<sup>[184]</sup> both of which alter the intrinsic plastic flow properties of the material. It can be seen in Figure 4.33 that the viscosity in the SCL region is strain-rate independent (Newtonian flow) for low strain-rates and temperatures in the range 115 to 120 °C. At both low deformation temperatures and high strain rates, viscosity becomes strain-rate dependent, indicating that the deformation mode changes from Newtonian to non-Newtonian flow. This behaviour is similar to the Mg-base BMG described in SECTION 3.9.4 and the  $\text{Zr}_{65}\text{Al}_{10}\text{Ni}_{10}\text{Cu}_{15}$  and  $\text{La}_{55}\text{Al}_{20}\text{Ni}_{25}$  BMGs studied by Kamawura et al. seen in Figure 2.33.<sup>[175,176]</sup>

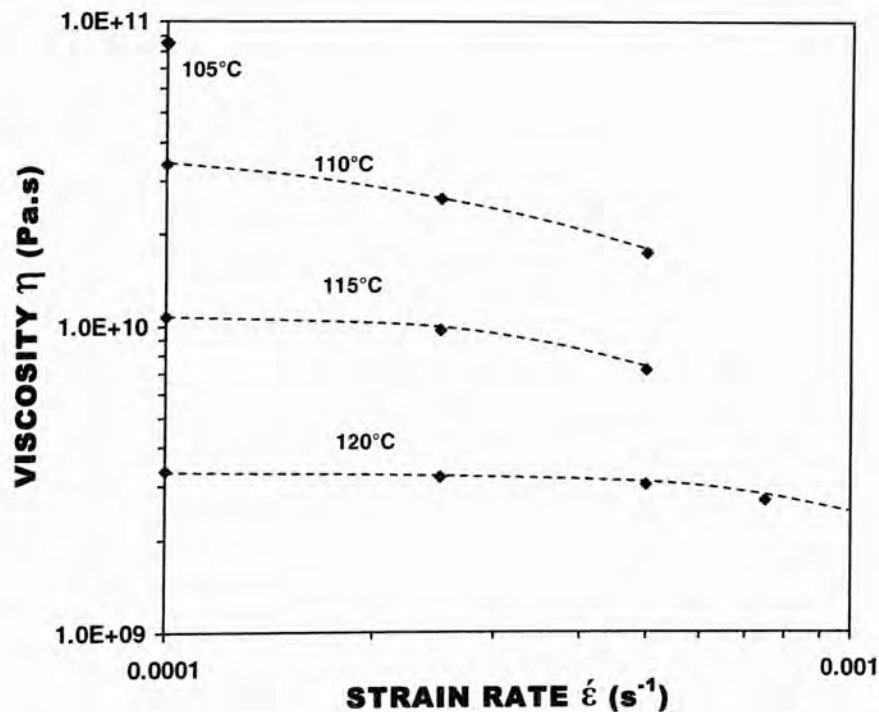


**Figure 4.33:** Calculated viscosity of the  $\text{Ca}_{65}\text{Mg}_{15}\text{Zn}_{20}$  BMG samples tested from 105 to 120 °C plotted over strain rate in log-log format.



#### 4.6.5 Flow Characterisation using the Free Volume Model<sup>[180]</sup>

Free volume is defined as excess volume owing to the disordered state of an atomic configuration (see section 2.6.4). In this model, plastic deformation is attributed to atomic jumps into neighbouring holes or flow defects that exceed a critical size, to accommodate strain. Uniaxial flow behaviour of a metallic glass may be described by Eq. (2.34).<sup>[180]</sup> Both the activation volume and frequency factor for given deformation temperature were calculated from the experimental values of flow stresses and strain rates using Eq. (2.34) and the results are given in **Table 4.4**. A typical example of the method used to calculate these values is given in **APPENDIX D**.

**Table 4.4:** Activation volume and frequency factor of the  $\text{Ca}_{65}\text{Mg}_{15}\text{Zn}_{20}$  BMG obtained from experimental data fitted to Eq. (3.15).

Temperature (°C )	$\dot{\epsilon}_o$ (/s )	$V$ ( nm <sup>3</sup> )
110	$3.31 \times 10^{-3}$	0.170
115	$1.28 \times 10^{-2}$	0.091
120	$4.92 \times 10^{-2}$	0.031

Similar to the work described in **SECTION 3.9.5**, it can be seen that an increase in temperature results in an increase in the frequency of elementary defect jumps ( $\dot{\epsilon}_o$ ), with a corresponding decrease in the activation volume involved per atomic jump ( $V$ ). However, it can be seen that the activation volumes associated with free volume generation are significantly smaller within the SCL region, which is related to the low flow stresses observed at such low strain rates, due to the strain rate sensitivity of the  $\text{Ca}_{65}\text{Mg}_{15}\text{Zn}_{20}$  BMG. These results indicate that activation volume may be a limiting factor with respect to plastic deformation, perhaps dictating the strain rate sensitivity of a material, and the brittle fracture strain rate limits.

Equation (3.17) was used to construct the viscosity master curve for the alloy whereby  $\eta/\eta_N$  is plotted as a function of  $\sigma_f V / 2\sqrt{3} k_B T$  in **Figure 4.34** for all homogeneous flow data (example shown in **APPENDIX D**). A normalised viscosity of unity indicates Newtonian flow with respect to the free volume model. The master curve shows that Newtonian flow in the supercooled state occurs at higher temperatures and lower strain rates. The decrease in normalised viscosity at higher strain rates, analogous to **Figure 4.33**, indicates a transition from Newtonian to non-Newtonian flow.

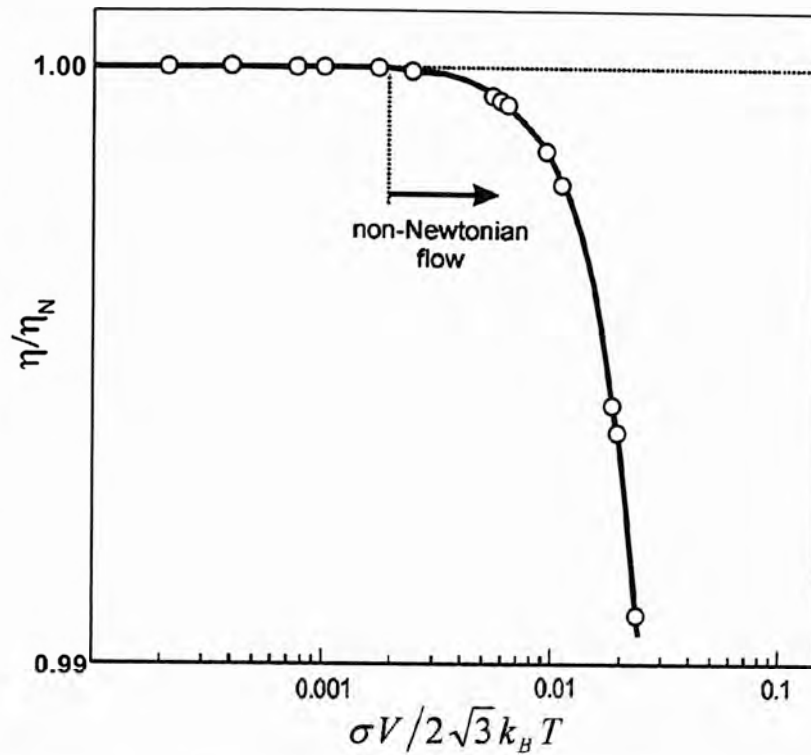


**Figure 4.34:** Master curve of normalised viscosity for the  $\text{Ca}_{65}\text{Mg}_{15}\text{Zn}_{20}$  BMG constructed using Eq. (3.17)

It is also clear that the small range of strain rates and temperatures tested results in normalised viscosity values much closer to unity than those seen in the  $\text{Mg}_{65}\text{Cu}_{25}\text{Y}_{10}$  BMG (a difference over an order of magnitude), although there is a clear transition apparent at this scale for the experimental data.

#### 4.6.6 Determination of Fragility using the VFT Equation<sup>[60,66,67]</sup>

Using the same method described in SECTION 3.9.6, viscosity data generated from the tensile test data was fitted to the VFT equation - Eq. (2.8), seen in **Figure 4.35**. Due to the small temperature range over which Newtonian flow was observed (120 - 115 °C), a single non-Newtonian viscosity point (indicated by the colour filled data point in **Figure 4.35**) from data generated at 110 °C and a strain rate of  $1 \times 10^{-4}$  was used as a reference point to better define the viscosity curve in **Figure 4.35**. Using iterative curve fitting for the constants in Eq. (2.8) it was found that  $\eta_0 = 3.6 \times 10^{-4}$  Pa.s,  $T_0 = 249$  K and  $D^* = 17.3$ . As discussed in SECTION 2.3.2, it is known that  $\eta_0 = h/v_e$ <sup>[60]</sup> which is the viscosity of the liquid in the high temperature “gas” limit. Using this relationship, it was found that  $\eta_0 = 2.6 \times 10^{-5}$  Pa.s, which is a slightly smaller value than

that found here using the VFT equation and the viscosity data obtained from experimental results, indicating a small degree of discrepancy.

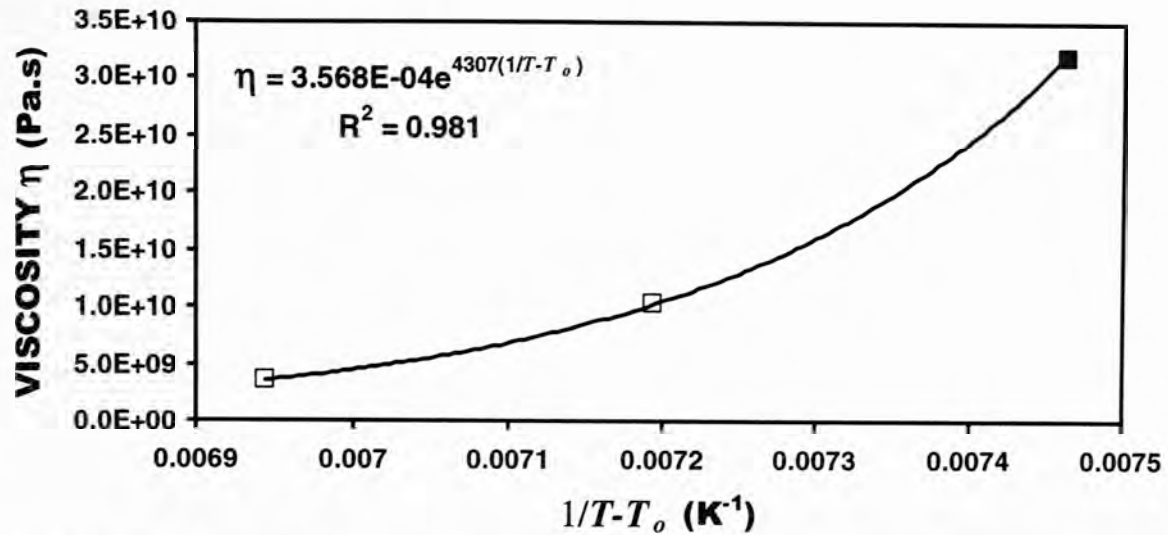


Figure 4.35: VFT curve fitted to selected viscosity data obtained using experimental results.

The alternate form of the VFT equation developed by Busch et al.<sup>[66]</sup> that combines the kinetics of glass transition to equilibrium viscosity (Eq. (2.10)). Using DSC data to determine the onset of  $T_g$  and the same mathematical methodology described in SECTION 3.9.6, Figure 4.36 was constructed and shows the best fit of Eq. (2.10). The constants were computed to be  $\tau_o = 9.8 \times 10^{-15}$  Pa.s,  $T_o = 247$  K and  $D^* = 16.8$ ; these are comparable to the values determined in Figure 4.35. This analysis shows that the  $\text{Ca}_{65}\text{Mg}_{15}\text{Zn}_{20}$  BMG has a fragility parameter  $D^*$  between 16.8 and 17.3; with respect to glass fragility, which is a useful means of comparison to other glass-forming systems such as those in Figure 2.7b).

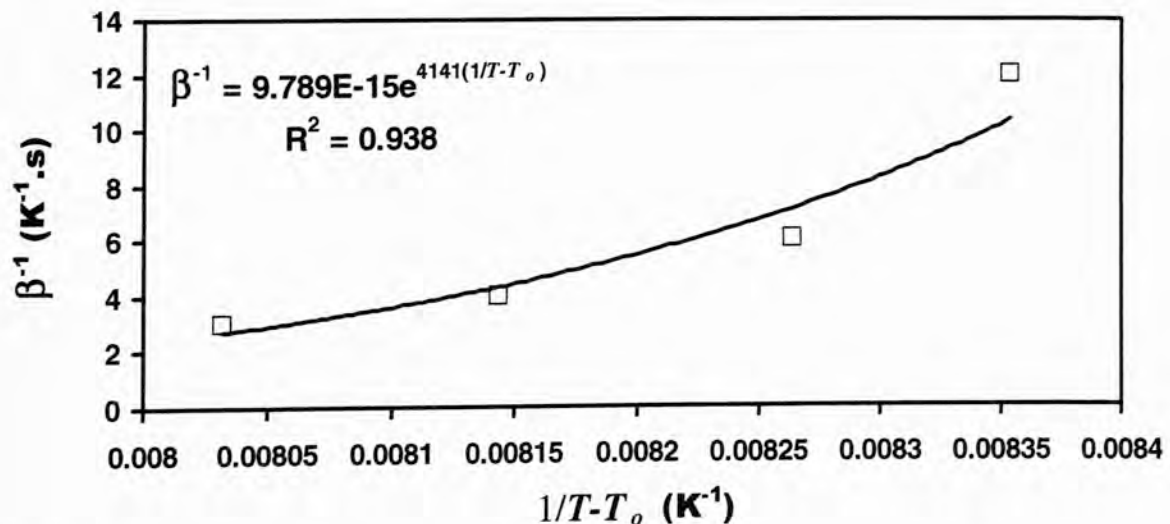
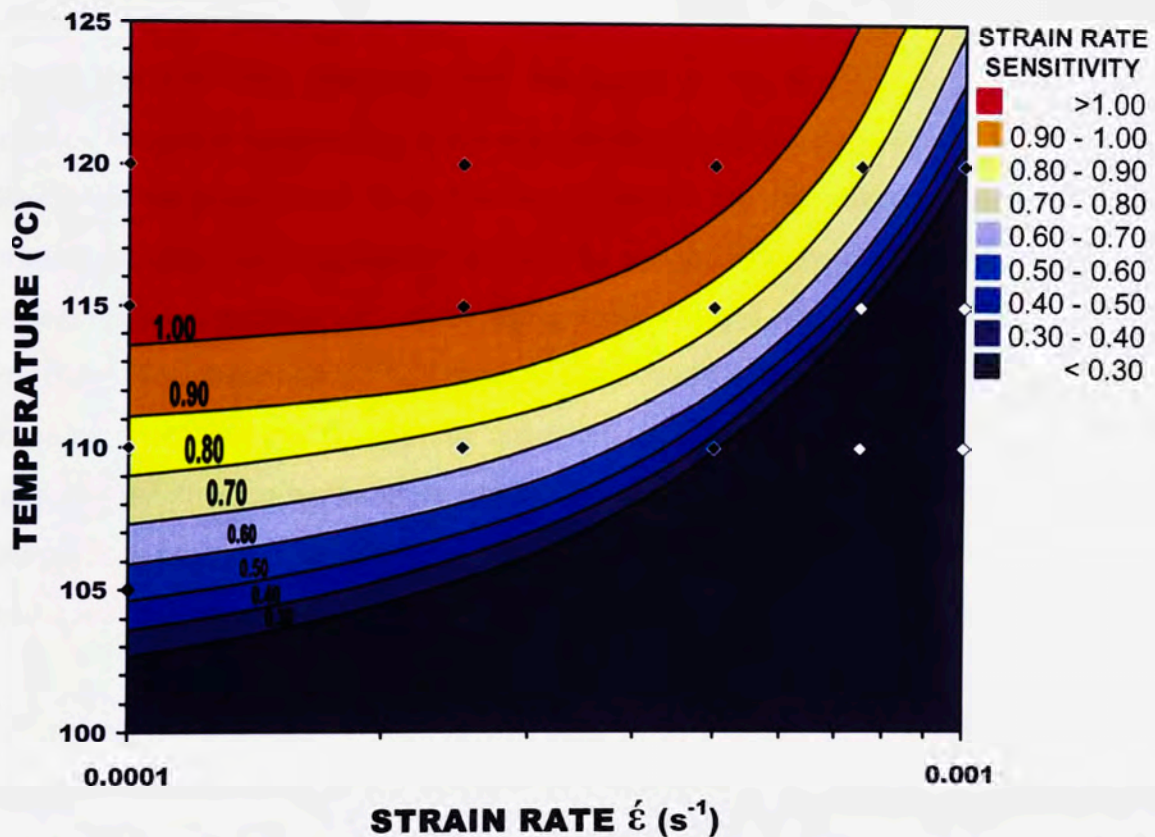


Figure 4.36: VFT curve fitted to heating rate and  $T_g$  onset data using Eq. (2.10).<sup>[60]</sup>



#### 4.6.7 Strain Rate Sensitivity and Superplastic Flow Behaviour

The negligible influence of strain rate on viscosity has an important practical consequence for forming BMGs in the SCL region. The relationship between log stress ( $\sigma_f$ ) and log strain rate ( $\dot{\epsilon}$ ) in the SCL region for the  $\text{Ca}_{65}\text{Mg}_{15}\text{Zn}_{20}$  BMG was shown in **Figure 4.32** and can be expressed by Eq. (2.30), where the slope of a tangent to the curve for any given temperature data set corresponds directly to the strain-rate sensitivity exponent, and an  $m$ -value of unity indicates ideal Newtonian flow.<sup>[175-179]</sup> The  $m$ -value also indicates the processing conditions where the material can be worked with the highest degree of efficiency.<sup>[181,182]</sup> The variation of the  $m$ -value in the SCL region with respect to temperature and strain rate is shown in **Figure 4.37**. The method used to construct this map is described in **APPENDIX E**.



**Figure 4.37:** Variation of the strain rate sensitivity exponent ' $m$ ' with respect to temperature and strain rate for the  $\text{Ca}_{65}\text{Mg}_{15}\text{Zn}_{20}$  BMG.

It can be seen in **Figure 4.37** that the strain rate sensitivity correlates closely with conditions pertaining to Newtonian flow ( $m \geq 1$ ), non-Newtonian flow ( $0.3 < m < 1$ ) and brittle failure ( $m < 0.3$ ). It can be seen that these results correspond directly with the boundaries determined using the free volume model, thereby supporting the transition state theory for BMGs described by Eq. (2.30).<sup>[69]</sup> and its relation to the free volume model<sup>[180]</sup> for the  $\text{Ca}_{65}\text{Mg}_{15}\text{Zn}_{20}$  system.



#### 4.6.8 Effect of Temperature, Strain Rate and Time on Plastic Flow

Similar to other BMG systems,<sup>[175,176,185]</sup> it was found that an increase in stress often occurs during mechanical testing in the SCL region; this behaviour is attributed to temperature-time induced crystallisation. With respect to the maximum sample strain, the governing role of the crystallisation hardening effect<sup>[185,263]</sup> becomes quite apparent. With the exception of the tests at 120 °C and strain rates of  $1 \times 10^{-3} \text{ s}^{-1}$  and  $7.5 \times 10^{-4} \text{ s}^{-1}$ , where crystallisation times are not reached before failure (indicated by DSC crystallisation curve in **Figure 4.38a**), the maximum strain achieved by sample was found to be proportional to test time.

It is pertinent to note that the stress increase due to crystallisation was delayed in comparison to the crystallisation onset times of an unstrained sample. This phenomenon has also been documented for the  $\text{Zr}_{65}\text{Al}_{10}\text{Ni}_{10}\text{Cu}_{15}$ ,<sup>[175]</sup>  $\text{La}_{55}\text{Al}_{20}\text{Ni}_{25}$ <sup>[176]</sup> and  $\text{Cu}_{54}\text{Ni}_6\text{Zr}_{22}\text{Ti}_{18}$  BMGs.<sup>[185]</sup> It is suggested that this time discrepancy in the onset of the stress increase indicates that deformation causes a degradation of the crystallisation reaction, namely, deformation-induced stabilisation of the supercooled liquid. The mechanism for this deformation-induced stabilisation is not clear, although it is suggested that it may be due to the suppression of an incipient-stage of the crystallisation reaction and, at the higher strain rates, is due to the rapid increase in flow volume during flow deformation.<sup>[20]</sup> Of greatest significance to this work, is a correlation which is yet to be reported, that this delay in the onset time ( $\Delta t_{XD}$ ) of this stress increase varies, such that a higher deformation temperature reduces  $\Delta t_{XD}$  and a higher deformation rate (strain rate) increases  $\Delta t_{XD}$ , i.e. further stabilises the amorphous phase. Values of  $\Delta t_{XD}$ , are documented in **Table 4.3** and can be seen in **Figures 4.38b** to d).

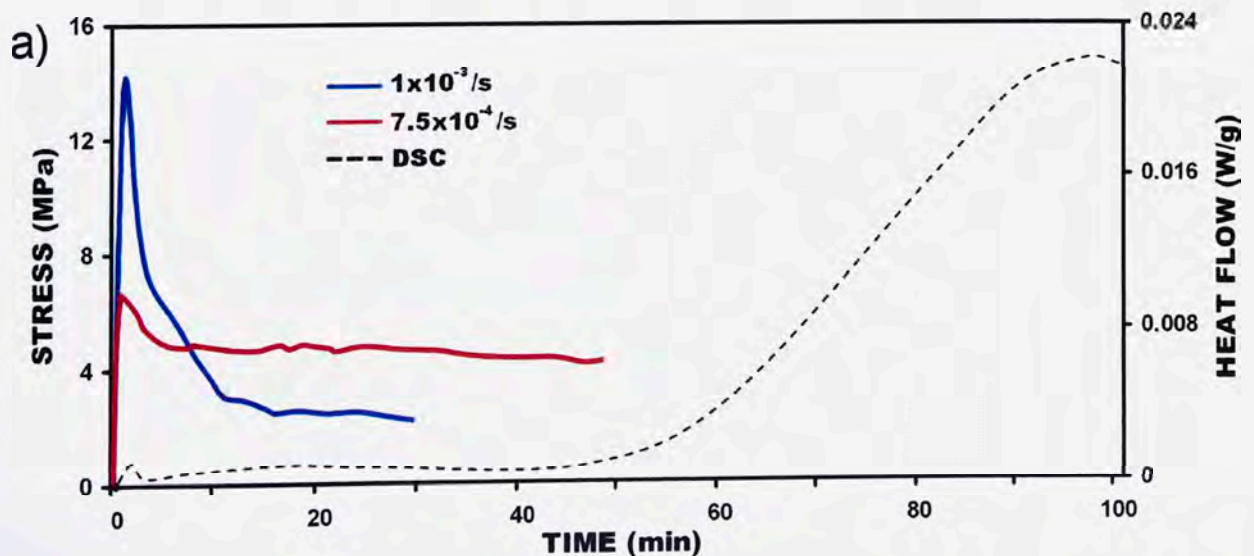


**Figure 4.38:** a) Stress - Time plot for tensile test samples held at 120 °C strained at  $1 \times 10^{-3}$  and  $7.5 \times 10^{-4} \text{ s}^{-1}$ , including static DSC crystallisation curve.



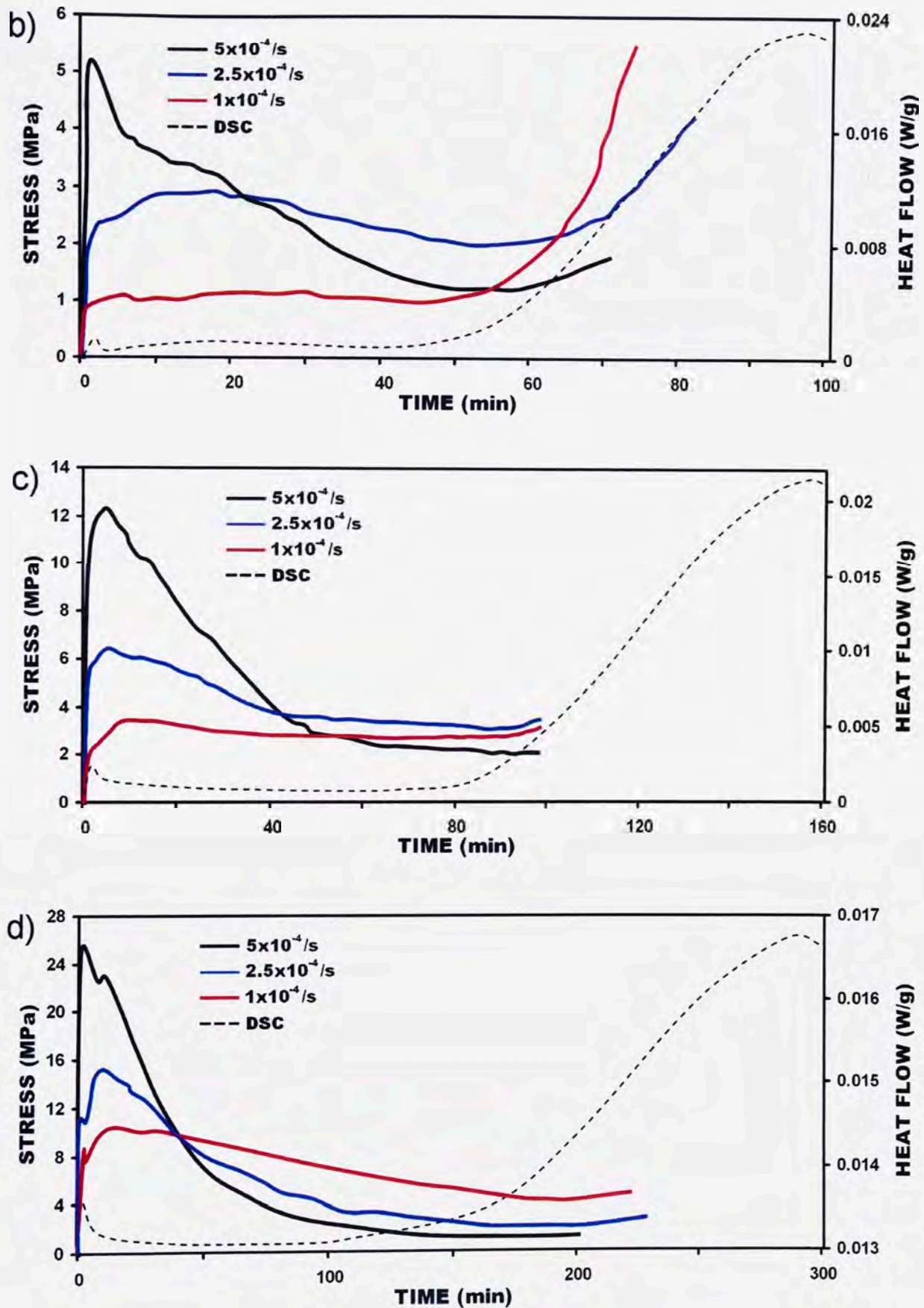


**Figure 4.38:** Stress - Time and static DSC data plots for tensile samples held at b)  $120^\circ \text{C}$  strained at  $5 \times 10^{-4} - 1 \times 10^{-4} \text{ s}^{-1}$ , c)  $115^\circ \text{C}$  strained at  $5 \times 10^{-4} - 1 \times 10^{-4} \text{ s}^{-1}$  and d)  $110^\circ \text{C}$  strained at  $5 \times 10^{-4} \text{ s}^{-1} - 1 \times 10^{-4} \text{ s}^{-1}$ .



#### 4.6.9 Constant Load Tensile Testing

In a series of experiments, samples were held under constant load conditions at loads from 20N to 50N and heated at a constant rate of 5 °C/min as to observe the variation in strain rate within the SCL region and beyond. Strain rate variation was taken with respect to the original gauge length and the increase in strain between individual data points. The maximum strain rates for all three samples were in excess of  $1 \times 10^{-1} \text{ s}^{-1}$  with respect to the original gauge length and a maximum elongation of over 850% was achieved (**Figure 4.39**). A number of results for constant load tensile testing are given in **Table 4.5**.

In order to determine the characteristic temperatures  $T_g$  (glass transition temperature) and  $T_X$  (onset crystallisation temperature), DSC scans were performed at a heating rate of 5 °C/min, as to replicate the heating rate used in constant load testing. The onset glass transition temperature,  $T_g$ , and onset crystallisation temperature,  $T_X$ , of the alloy was determined to be 103 °C and 139 °C, respectively, giving a SCL region ( $\Delta T_X = T_X - T_g$ ) of ~ 36°C which is slightly different to those values generated at a heating rate of 20 °C/min.

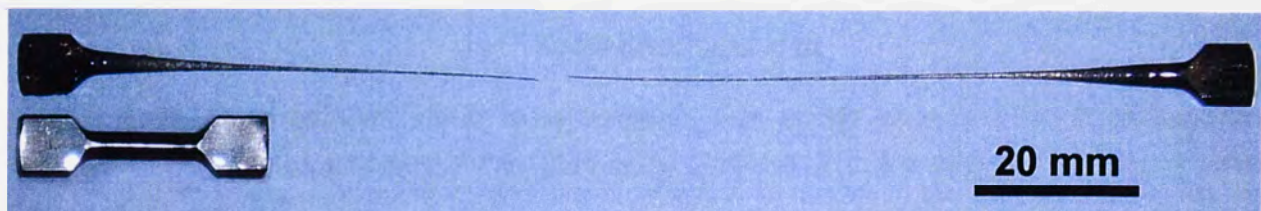


**Figure 4.39:** Sample deformed under a constant load of 50N at a heating rate of 5 °C/min. showing an elongation to failure in excess of 850%.

**Table 4.5:** A summary of constant load tensile test results including initial maximum strain % ( $\epsilon_{MAX}$ ), maximum strain rate ( $\dot{\epsilon}_{MAX}$ ), time to failure ( $t_{FAIL}$ ) and temperature at failure ( $T_{FAIL}$ ).

		$\epsilon_{MAX}$ (%)	$\dot{\epsilon}_{MAX}$ ( $\text{s}^{-1}$ )	$t_{FAIL}$ (min)	$T_{FAIL}$ (°C)
LOAD (N)	50	853	0.31	10.7	144.2
	40	517	0.27	11.9	145.2
	20	260	0.10	12.6	146.8

A plot of instantaneous strain rate between data points for constant load testing is shown in **Figure 4.40**, which also includes the DSC curve for the same temperature interval and heating rate (5 °C/min). **Figure 4.40** shows extremely low strain rates for all samples at temperatures



below  $T_g$ , followed by a steady increase through the SCL region up to  $T_X$ . Beyond  $T_X$  there is a further rapid increase in strain rate followed by failure. It is interesting to note that strain rates observed between temperatures of 105 to 120 °C are very similar to the strain rate limits for constant strain rate tensile testing in the same temperature range.

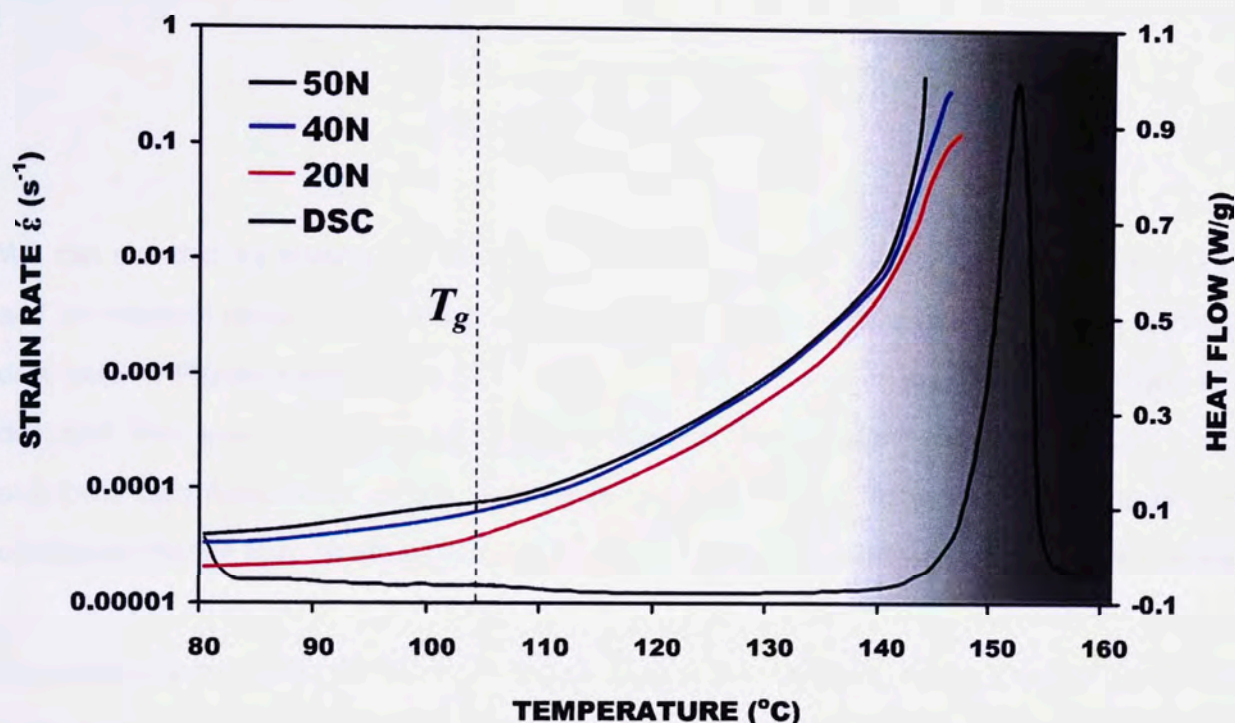


**Figure 4.40:** Instantaneous strain rates between data points as a function of temperature (constant load testing). Included in the figure is the DSC curve for the same temperature interval and heating rate (5 °C/min).

**Figure 4.40** shows a near linear trend between strain rate, applied load and temperature throughout the SCL region, with a slight departure from linearity late in the SCL region. It is reasonable to assume that this linear trend is attributed to the decrease in viscosity of the BMG as temperature is increased as will be discussed anon. Departure from linearity is most likely caused by continuous thinning of the sample, although it may also be a cumulative effect of the viscosity decreasing with the increasing strain rate under non-Newtonian flow conditions as demonstrated in **Figure 4.33**.

At low strain rates, a constant load may be approximated to a constant stress between short temperature intervals as the change in cross section of the sample is quite small. The equilibrium viscosity of a BMG with respect to temperature is often explained using the VFT relation, i.e. Eq. (2.8). It is also known that viscosity in the Newtonian regime may be described by flow stress ( $\sigma_f$ ) and strain rate by Eq. (2.30).



By combining Eqs. (2.8) and (2.32) such that:

$$\frac{\sigma_f}{3\dot{\epsilon}} = \eta_o \exp \left[ \frac{D^* T_o}{(T - T_o)} \right] \quad (4.13)$$

Rearranging Eq. (4.13) such that:

$$\ln \dot{\epsilon} = \ln \left( \frac{\sigma_f}{3\eta_o} \right) - \frac{DT_o}{T - T_o} \quad (4.14)$$

We can see that by plotting  $\ln \dot{\epsilon}$  over  $1/T - T_o$  will yield straight, parallel lines of gradient  $D^* T_o$  and an intercept related to  $\sigma_f$ , which explains the linear, parallel relationship between the three data sets in **Figure 4.40** for the SCL region. At higher strains in the SCL region there is a deviation from linearity assumed to be due to localised thinning of the samples, although it may also be a cumulative effect of the viscosity decreasing with the increasing strain rate as flow conditions change from Newtonian to non-Newtonian due to an increase in sample free volume.

An interesting phenomenon shown in **Figure 4.40** is the decrease in the apparent strain rate immediately before failure for two of the constant load samples (20 and 40 N); this behaviour coincides with the temperature range where crystallisation commences as shown by the superimposed DSC curve. It is interesting to note that the sample strained at 50 N does not show a decrease in strain rate. The decrease in strain rate is more marked in the sample held at 20 N and occurs at  $\sim 143.4^\circ\text{C}$  which was determined from the inflexion in the temperature/strain-rate curve. For the sample loaded at 40 N, such an inflexion is less pronounced and occurs at  $\sim 144.5^\circ\text{C}$ . It is clear that straining under high constant loading conditions ( $> 40\text{ N}$ ) does not result in hardening (increase in stress) needed to reduce the strain rate. This behaviour is consistent with the theory of deformation-induced stabilisation of the supercooled liquid, whereby assuming strengthening is caused by the onset of crystallisation; this transformation is delayed or completely suppressed under the higher loading conditions.

The results of constant load testing experiments shows that anisothermal, constant load deformation generates higher strains and at higher strain rates compared with samples deformed isothermally (as shown by the elongation data in **Table 4.3** and **Table 4.5**). Such anisothermal straining processes under constant load may be a useful method for drawing or forming BMGs as it results in both a higher ductility and shorter deformation/forming times.

## 4.7. CRYSTALLISATION BEHAVIOUR OF THE $\text{Ca}_{65}\text{Mg}_{15}\text{Zn}_{20}$ BMG

### 4.7.1 TTT Diagram Development

Again, by using the model developed by Takeuchi et al.<sup>[75]</sup> (SECTION 2.4.5) to predict the position of the C-curve in a BMG, a TTT diagram was constructed represented by the solid blue line in **Figure 4.41**. Included in the diagram are the liquidus (357 °C) and glass transition (105 °C) temperatures (solid red lines) and the onset (dashed black line) and completion (solid black line) of crystallisation according to isothermal annealing data (**Figure 4.14**). Also included in the diagram are the cooling curves from the graduated cylinder castings (**Figure 4.15**) of: (i) the amorphous 8 mm diameter section (dotted black line), and (ii) the partially crystalline 10 mm section (dashed black line). It can be seen that there is a reasonable correlation between the curve predicted by the Takeuchi model and the experimental data, however the model predicts that this glass to more stable than the experimental results indicate, which may be due to the presence of quenched in nuclei.<sup>[284]</sup> The sensitivity of this model may be increased,<sup>[296]</sup> shifting the C-curve to the left to better fit cooling rate data, although this makes the correlation between DSC data poorer.

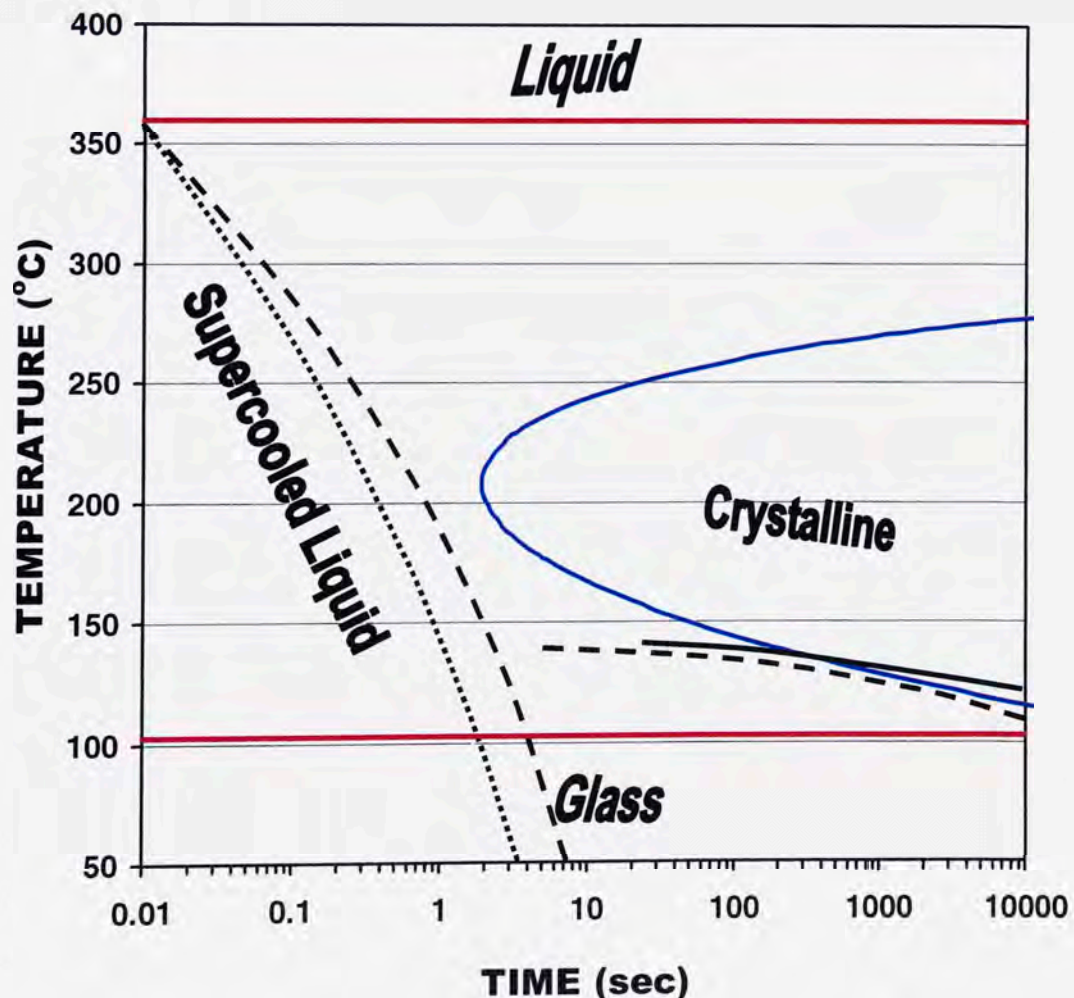


**Figure 4.41:** Time-temperature-transformation diagram for the  $\text{Ca}_{65}\text{Mg}_{15}\text{Zn}_{20}$  BMG including cooling curves from the segmented cylinder castings and isothermal annealing data.



### 4.7.2 Electron Microscopy

In order to determine the amorphous nature of the as-cast  $\text{Ca}_{65}\text{Mg}_{15}\text{Zn}_{20}$  BMG, the FIB milling technique,<sup>[297]</sup> similar to that used to produce microposts was employed to manufacture a foil suitable for TEM analysis. **Figure 4.42** shows an SEM backscattered electron image of the completed TEM foil prior to lift out. There appears to be no notable contrast eluding to nanocrystals within the foil section, however, a nanocrystalline oxide/hydroxide layer at the sample surface and (hence along the 'spine' of the foil) is evident. At this stage, it may be tentatively assumed that the amorphous structure of the sample (determined using XRD analysis in **SECTION 4.5.2**) was retained during FIB processing.

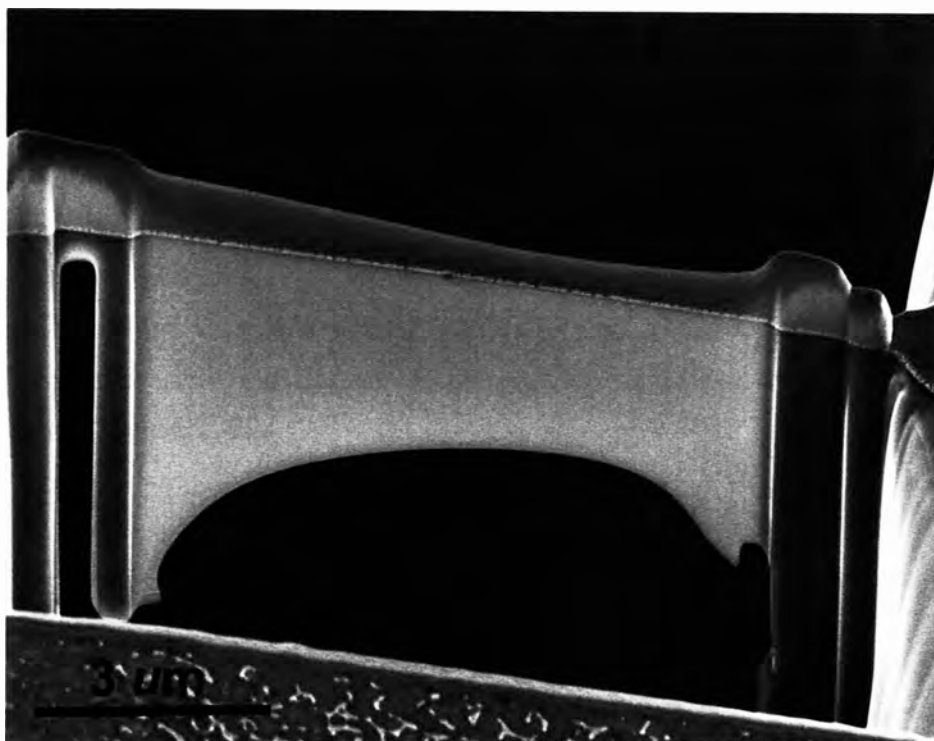


**Figure 4.42:** SEM backscattered electron image of the  $\text{Ca}_{65}\text{Mg}_{15}\text{Zn}_{20}$  BMG TEM foil produced by FIB milling.

After removing the  $\text{Ca}_{65}\text{Mg}_{15}\text{Zn}_{20}$  foil from the FIB the foil was positioned on a copper TEM grid, which was inserted into a Phillips CM200 TEM for analysis. Knowing that the sample morphology was quite fragile on a macroscopic level with respect to crystallisation, the first imaging priority was to obtain a diffraction pattern to prove the sample had an amorphous structure. A SAD pattern image was taken immediately upon exposure to the primary electron beam which can be seen in **Figure 4.43a**). The beam current here in hindsight was quite high for the sample, resulting in an extremely bright, over exposed image which has since been adjusted in order to view some of the more important characteristics of the pattern.

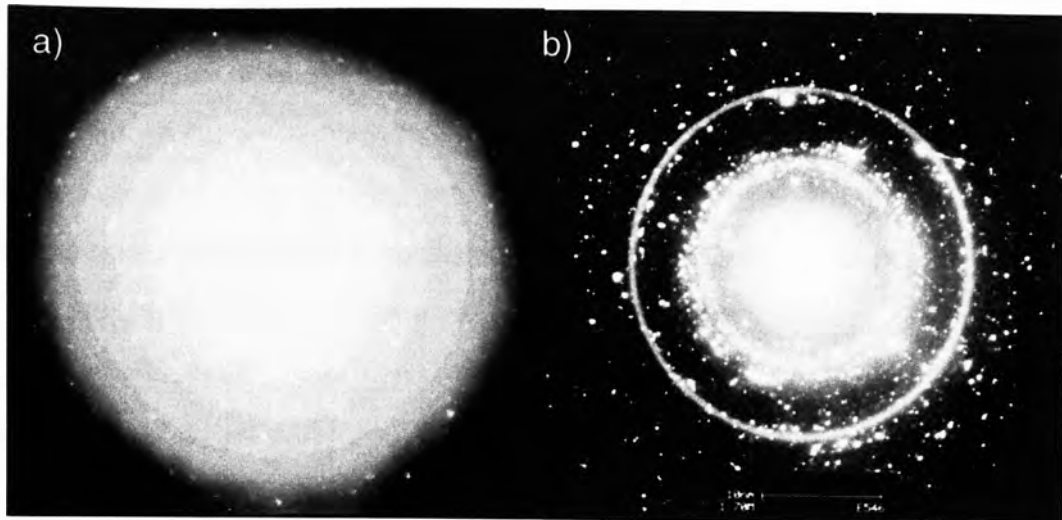


**Figure 4.43:** a) Initial TEM SAD pattern and b) SAD pattern after five minutes exposure to the electron beam of the  $\text{Ca}_{65}\text{Mg}_{15}\text{Zn}_{20}$  BMG TEM foil produced by FIB milling.

An image of the exposed foil can be seen in **Figure 4.44**, showing that crystallisation has definitely occurred. Interestingly enough, the grain size at the edge of the foil (thinnest section) is much smaller than at the base of the sample, which would indicate some type of cooling rate effect related to crystallisation. This would suggest that crystallisation has occurred after foil manufacture. This would lead to the assumption that crystallisation in this case was electron beam induced (rather than ion beam), which is also suggested by the higher number of diffraction spots in **Figure 4.43b**.

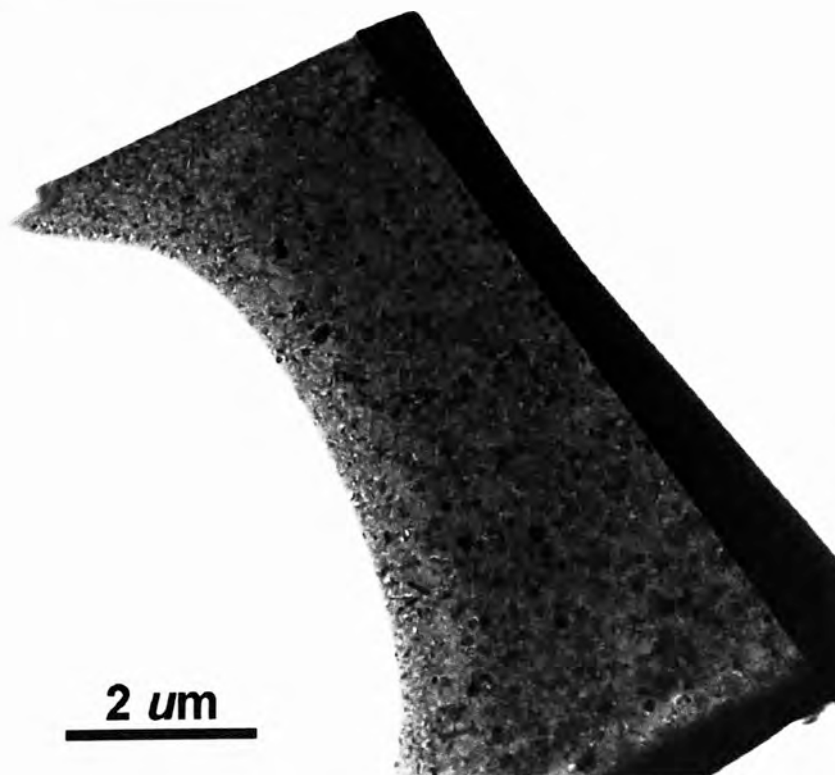


**Figure 4.44:** A bright field TEM image of the crystallised  $\text{Ca}_{65}\text{Mg}_{15}\text{Zn}_{20}$  BMG TEM foil, showing a distinct change in grain size from the edge to the base of the foil.



At high TEM magnifications, it was observed that the electron beam was melting the sample. Even at lower beam currents, the sample material had an appearance similar to boiling water at the focal point of the beam. Another interesting phenomenon observed under these crystallisation conditions was twinning, which can be seen in **Figure 4.45a**). Perhaps associated with twinning was a grain mirroring phenomenon within the structure, which is evident in **Figure 4.45b**). These observations indicate a somewhat complex crystallisation path for the  $\text{Ca}_{65}\text{Mg}_{15}\text{Zn}_{20}$  BMG under these conditions, which may reflect crystallisation mechanisms in bulk, temperature-induced static and dynamic crystallisation, however more work needs to be carried out to validate such an assumption, which would prove tedious considering the material appears to be highly unstable under a high intensity electron beam.

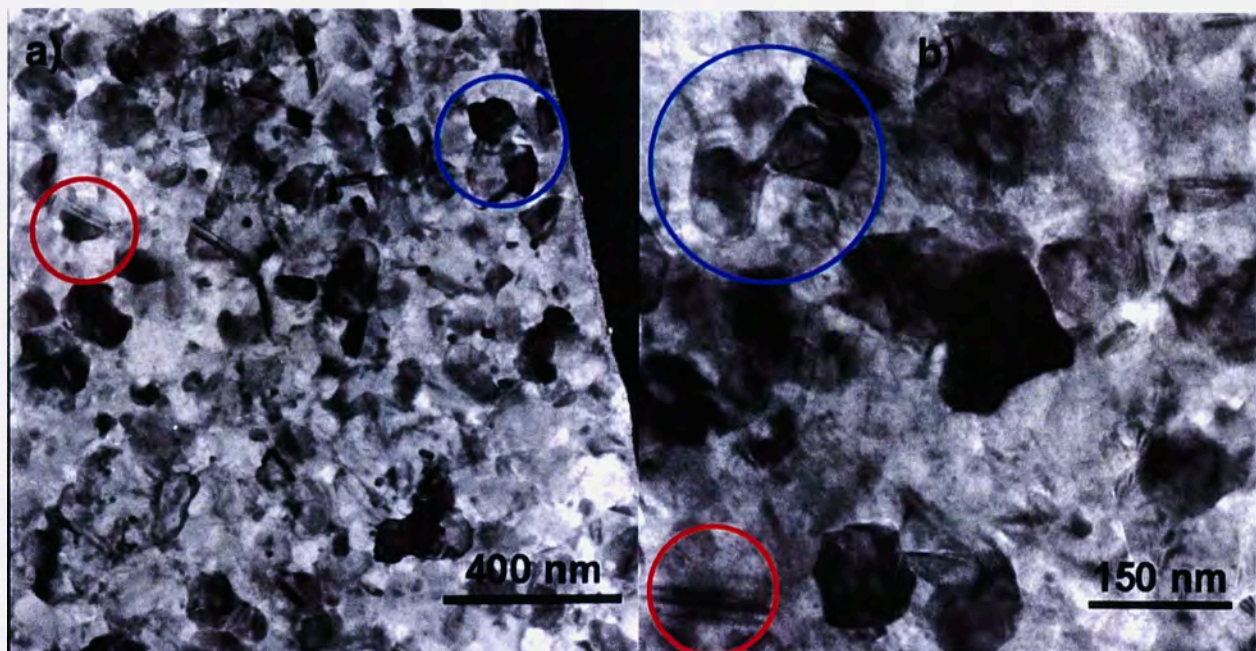


**Figure 4.45:** a) The presence of twinning (red circles) and grain mirroring (blue circles) in the microstructure of the  $\text{Ca}_{65}\text{Mg}_{15}\text{Zn}_{20}$  BMG TEM foil crystallised by the electron beam and b) Further magnification of the TEM foil highlighting the presence and size of grains/twins size (over 150 nm in this field of view).

Further enforcing the assumption that crystallisation has occurred under the electron beam of the TEM is the size of the crystals shown in Figure 4.45 (some are in excess of 150 nm), which one would assume to be resolvable in **Figure 4.42** if they were caused by FIB milling.



## SECTION 5 - GENERAL DISCUSSION

### 5.1. GLASS STABILITY

#### 5.1.1 Glass Structure

The bulk metallic glasses studied to date can be broadly categorised into two atomic size–composition classes.<sup>[45,52,87]</sup> The first BMG class, which is the least common among BMGs includes alloys with midsize atoms as the majority component (60 - 70 at.%), small atoms as the next-majority component, and large-size atoms as the minority component (~10 at.%) producing an atomic size distribution plot (ASDP) with a concave downward shape. This group of BMGs is sometimes referred to as medium atom - small atom - large atom (MSL) BMGs, to which the  $\text{Mg}_{65}\text{Cu}_{25}\text{Y}_{10}$  BMG studied in this work belongs.<sup>[87]</sup> The other BMG class includes alloys composed primarily of large-size atoms (~40 - 75 at.%) and small-size atoms (~25 - 60 at.%),<sup>[87]</sup> producing an ASDP with a concave upward shape. This group of BMGs is sometimes referred to as large atom - small atom or small atom - large atom (LS/SL) class BMGs, to which the  $\text{Ca}_{65}\text{Mg}_{15}\text{Zn}_{20}$  BMG belongs. **Figure 5.1a)** shows the ASDPs for the two alloys studied in this work. **Figure 5.1b)** illustrates the atomic radius ratios ( $R$ ), of the atomic constituents of the two alloys with respect to the solvent atom. Also included in this figure are the corresponding cluster ratios ( $R^*$ ) which predict the possible number of solvent atoms surrounding a solute atom as discussed in **SECTION 2.2.2.**<sup>[52]</sup> Here, we can see a reasonable correlation between  $R$  and  $R^*$  values for both alloys.

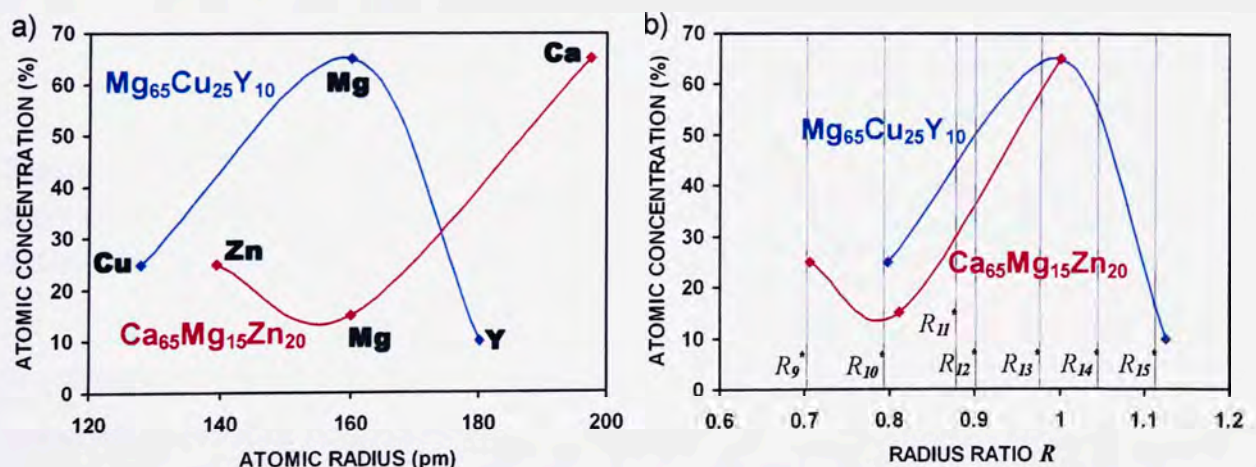


**Figure 5.1:** a) Atomic size distribution plot for the  $\text{Mg}_{65}\text{Cu}_{25}\text{Y}_{10}$  and  $\text{Ca}_{65}\text{Mg}_{15}\text{Zn}_{20}$  BMGs and b) the correlation between  $R$  and  $R^*$  values for the  $\text{Mg}_{65}\text{Cu}_{25}\text{Y}_{10}$  and  $\text{Ca}_{65}\text{Mg}_{15}\text{Zn}_{20}$  BMGs.

In MSL alloy systems, it is noted that the heats of mixing are negative and large in magnitude for the large - small atomic pairs such as Ln-B, Zr-B, Mo-(C, B, P) and Y-Cu and, in many



cases, even larger than those between elements in these pairs and their corresponding medium (solute) atom components.<sup>[45,87]</sup> The large and small atoms may therefore be seen as forming a strong L–S network or reinforced ‘backbone’ in the amorphous structure,<sup>[45,87]</sup> as illustrated in **Figure 5.2a**). Presumably, this backbone structure enhances the stability of the undercooled melt, which further suppresses crystallisation, in these glasses.<sup>[87]</sup> This network theory is somewhat similar to the structures developed in regular, covalently bonded ceramic oxide glasses,<sup>[298,299]</sup> with typical short range order atom to atom, with irregular or distorted bond angles, as given in **Figure 5.2b**) which shows a two dimensional representation of  $B_2O_3$ .<sup>[298]</sup> As described above, this ‘backbone’ network in MSL BMGs is surrounded by the solvent atom. This type of structure is similar to a fluxed silica glass (e.g. soda glass shown in **Figure 5.2c**),<sup>[299]</sup> whereby the addition of an alkaline metal, typically Na, Mg and Ca, which have an ionic type bond to oxygen in the Si–O–Si structures, partially ‘dissolving’ the covalent lattice. The  $M^{+1}$  ions break the continuous network, decreasing the viscosity of the melt at high temperatures, whereby  $M^{+2}$  ions also break the network lattice, but act as a bridge between oxygen atoms, hence are less mobile, which also influences the viscosity of the melt.<sup>[299]</sup>

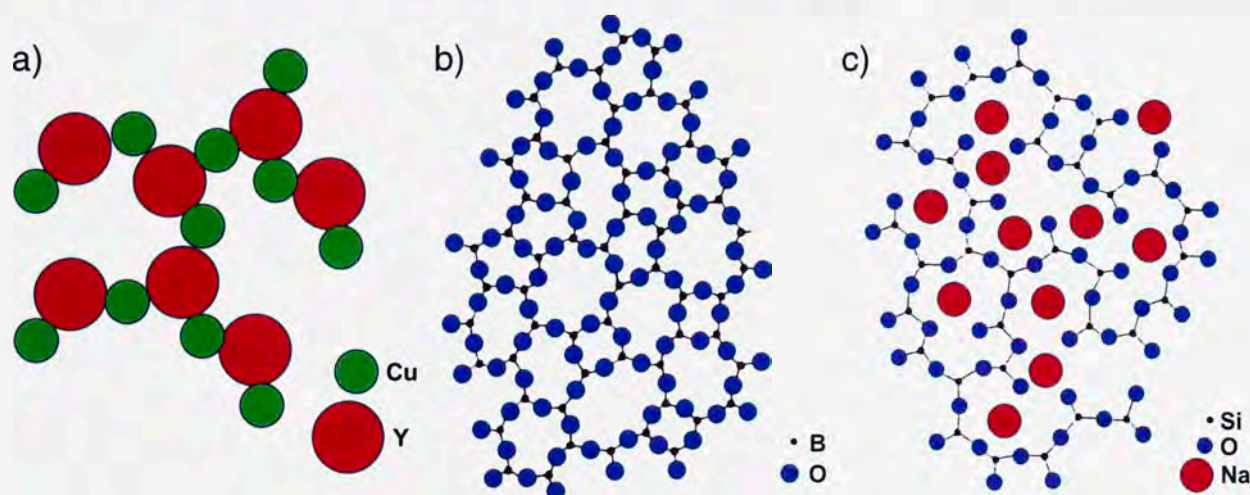


**Figure 5.2:** a) Two dimensional representation of atomistic network/backbone formed by the large atoms and small atoms in the MSL class BMGs ( $Mg_{65}Cu_{25}Y_{10}$ );<sup>[87]</sup> b) network structure in  $B_2O_3$  ceramic oxide glass<sup>[298]</sup> and c) dissolved network structure in soda glass.<sup>[299]</sup>

In comparison to LS BMGs, MSL-class BMGs contain only ~10 at.% of the large-size atoms. Based on the work of Poon et al.,<sup>[87]</sup> it is evident that the large-atom concentration of the MSL alloys cannot be extended into the LS class compositional region. It is believed that if the concentration of large atoms is significantly higher than ~10 at.%, there will be an increasing tendency for these atoms to cluster, effectively reducing the interaction between the large-small atoms.



Meanwhile, the formability of the LS/SL class of BMG to which the amorphous  $\text{Ca}_{65}\text{Mg}_{15}\text{Zn}_{20}$  alloy belongs is generally attributed to the strong bindings that exist between two different atom-size elements with the highest concentration, whereby the atomic diffusion and rearrangement into the respective crystalline phases is hindered and/or complex.<sup>[20,52,87]</sup> Here it is believed that atomic 'clusters' with a degree of short range order and stability are present in the liquidus state. These clusters have atomic structures somewhat different to the equilibrium crystalline phases of the alloy, hence upon cooling, devitrification is significantly hindered and the solid retains the structure of the liquid state.<sup>[20,52,81-87]</sup>

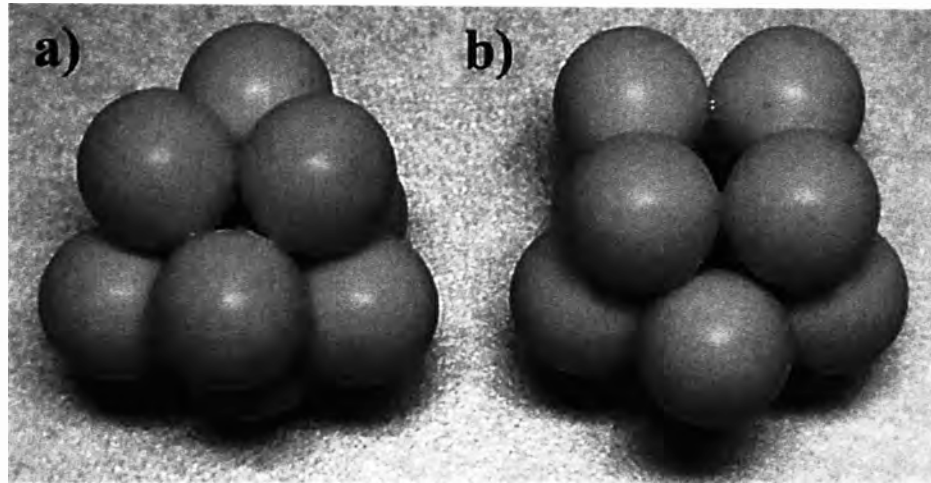


**Figure 5.3:** Possible clusters with high packing efficiency equivalent to those proposed for the  $\text{Ca}_{65}\text{Mg}_{15}\text{Zn}_{20}$  BMG: a) distorted capped trigonal prism with  $N=9$  and  $R=0.732$  and b) cluster with  $N=10$  and  $R=0.834$ .<sup>[52]</sup>

### 5.1.2 Thermal Properties of BMGs

Both the thermal properties and critical casting parameters for the  $\text{Mg}_{65}\text{Cu}_{25}\text{Y}_{10}$  and  $\text{Ca}_{65}\text{Mg}_{15}\text{Zn}_{20}$  BMGs determined in this study are given in **Table 5.1**.

**Table 5.1:** Critical casting parameters and thermal properties determined in this study for the  $\text{Mg}_{65}\text{Cu}_{25}\text{Y}_{10}$  and  $\text{Ca}_{65}\text{Mg}_{15}\text{Zn}_{20}$  BMGs.

ALLOY (at.%)	$Z_C$ (mm)	$R_C$ (°C/s)	$T_g$ (°C)	$T_X$ (°C)	$\Delta T_X$ (°C)	$T_m$ (°C)	$T_l$ (°C)	$T_{rg}$	$\gamma$	$\phi$
$\text{Mg}_{65}\text{Cu}_{25}\text{Y}_{10}$	3-3.75	49-61	148	213	65	453	480	0.559	0.413	0.429
$\text{Ca}_{65}\text{Mg}_{15}\text{Zn}_{20}$	8-9	150-170	105	138	33	336	357	0.600	0.408	0.425

Also given in this table are calculated values for the reduced glass transition temperature ( $T_{rg}$ ) using Eq. (2.18)<sup>[14]</sup> and the parameters,  $\gamma$  and  $\phi$ , which are based on thermodynamic crystallisation processes during cooling and reheating of a supercooled liquid using Eq.



(2.20)<sup>[120]</sup> and (2.23)<sup>[121]</sup> respectively. Here, higher values  $\gamma$  and  $\phi$  indicate higher glass-forming ability as described in SECTION 2.3.7. Hence, based on thermodynamic crystallisation properties of the two alloys,  $\text{Mg}_{65}\text{Cu}_{25}\text{Y}_{10}$  should be a slightly better glass former, despite the lower critical thickness values achieved.

Lu and Liu also formulated a general relationship between the  $\gamma$ -value and the critical cooling rate,  $R_C$ , regardless of the alloy system, represented by Eq. (2.21).<sup>[120]</sup> Upon substituting the foregoing values, the predicted value of  $R_C$  is 4.9 °C/s for  $\text{Mg}_{65}\text{Cu}_{25}\text{Y}_{10}$  and 8.8 °C/s for  $\text{Ca}_{65}\text{Mg}_{15}\text{Zn}_{20}$ ; this is quite a poor correlation between the data presented above and that found previously for  $\text{Mg}_{65}\text{Cu}_{25}\text{Y}_{10}$ <sup>[60,232]</sup> and  $\text{Ca}_{65}\text{Mg}_{15}\text{Zn}_{20}$ <sup>[227]</sup> BMGs. Based on more recent work by Fan et al.<sup>[121]</sup> the critical cooling rate of an alloy may be calculated using the parameter  $\phi$  in Eq. (2.24). This relationship predicts a maximum critical cooling rate of 68 °C/s, for  $\text{Mg}_{65}\text{Cu}_{25}\text{Y}_{10}$  and 77 °C/s for  $\text{Ca}_{65}\text{Mg}_{15}\text{Zn}_{20}$  which is a more reasonable estimation compared to that of Eq. (2.21).

### 5.1.3 Critical Thickness and Cooling Rate Determination for Copper Mould Casting

From the results given in Table 5.1, it can be clearly seen that with respect to copper mould casting, the critical thickness of a BMG poorly reflects the glass-forming ability of an alloy. As discussed in detail in SECTION 4.5.2 and depicted by Figure 4.21, the cooling rate of a casting is affected by the temperature at which it is cast, whereby a higher casting temperature reduces the cooling rate between  $T_l$  and  $T_g$ . Hence, it can be understood that with respect to achieving a maximum critical casting thickness  $Z_C$  of a BMG, casting temperature becomes an important parameter, whereby a lower casting temperature will achieve a greater value of  $Z_C$ . Analogous to Eq. (4.7), it can also be seen that the equilibrium temperature of the copper mould,  $T_{\text{MOULD}}$  also affects the cooling rate. Here it can be seen that, by lowering the equilibrium mould temperature, the cooling rate of the casting can be increased thereby increasing the critical casting thickness. It is clear that various casting parameters, which are rarely quoted in the literature, will affect the value of  $Z_C$ .

. Combining Eq. (4.8) with Eq. (3.4) gives the cooling rate at the centre of a casting with respect to the thermal and physical properties of the alloy:

$$\frac{dT}{dt} = \frac{2(T_{Z/2} - T_{\text{MOULD}})}{Z(1/h + Z/2k)C_p\rho} \quad (5.1)$$

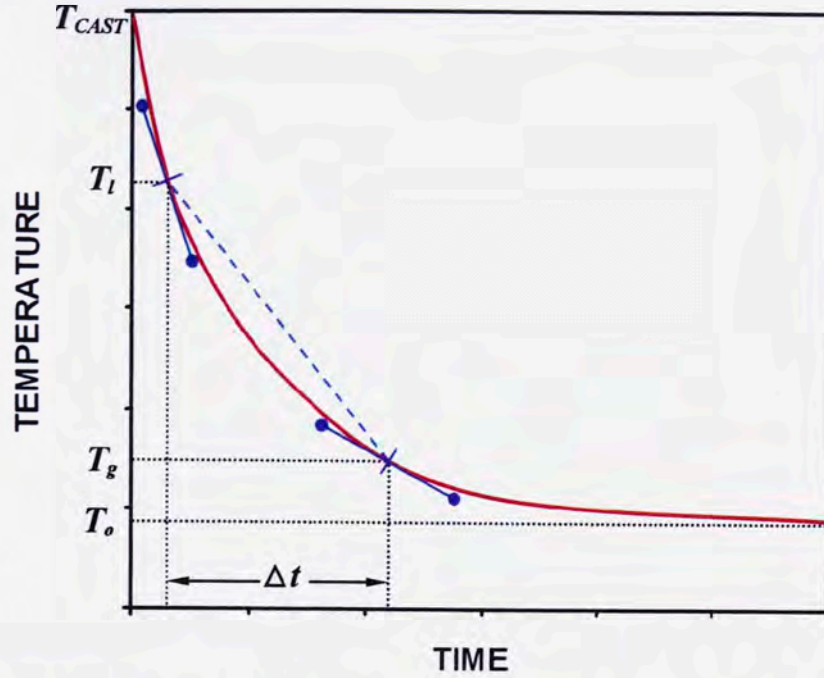


**Figure 5.4:** A representation of the cooling curve described by Eq. (5.1), indicating the cooling gradient at  $T_l$  and  $T_g$  and the average cooling rate between  $T_l$  and  $T_g$  over time  $\Delta t$ .

**Figure 5.4** shows a typical cooling relationship given by Eq. (5.1). Equation (5.1) may also be used to determine the cooling rate at any point on the cooling curve, as indicated by the solid blue tangent lines at  $T_l$  and  $T_g$  in **Figure 5.4**. Hence, the average cooling rate at the centre of the casting between  $T_l$  and  $T_g$  can be found by integrating Eq. (5.1) between  $T_l$  and  $T_g$  to give:

$$\frac{dT}{dt} = \int_{T_g}^{T_l} \frac{2(T_{Z/2} - T_{MOULD})}{Z(1/h + Z/2k)C_p\rho} = \frac{2(T_l - T_g)}{Z(1/h + Z/2k)C_p\rho} \quad (5.2)$$

Now, at the critical cooling rate for the formation of a BMG, Eq. (3.1), which describes the average cooling rate between  $T_l$  and  $T_g$  (shown by the blue dashed line in **Figure 5.4**), can be written as:

$$\left. \frac{dT}{dt} \right|_{T_g}^{T_l} = R_c = \frac{T_l - T_g}{\Delta t_c} \quad (5.3)$$

where  $\Delta t_c$  is constant for a given BMG. Combining Eq. (5.2) with Eq. (5.3) and letting  $Z = Z_c$  gives:

$$\frac{2(T_l - T_g)}{Z_c(1/h + Z_c/2k)C_p\rho} = \frac{T_l - T_g}{\Delta t_c} \quad (5.4)$$



Equation (5.4) can be rearranged and simplified to give:

$$hZ_C^2 + 2kZ_C - \frac{4kh\Delta t_C}{C_P\rho} = 0 \quad (5.5)$$

Solving Eq. (5.5) for  $Z_C$  gives:

$$Z_C = \frac{-2k + \sqrt{4k^2 + 16h^2k\Delta t_C/C_P\rho}}{2h} \quad (5.6)$$

Equation (5.6) is important as it shows that  $Z_C$  is dependent on a number of parameters, namely;  $k$ ,  $h$ ,  $C_P$  and  $\rho$ , of which  $k$ ,  $C_P$  and  $\rho$  are material properties, and can be related to the GFA of an alloy when casting. However,  $h$  is not directly related to the properties of the alloy but, rather, the experimental casting conditions. The effects of individually increasing these parameters on  $Z_C$  with respect to Eq. (5.6) are shown in **Figure 5.5**.

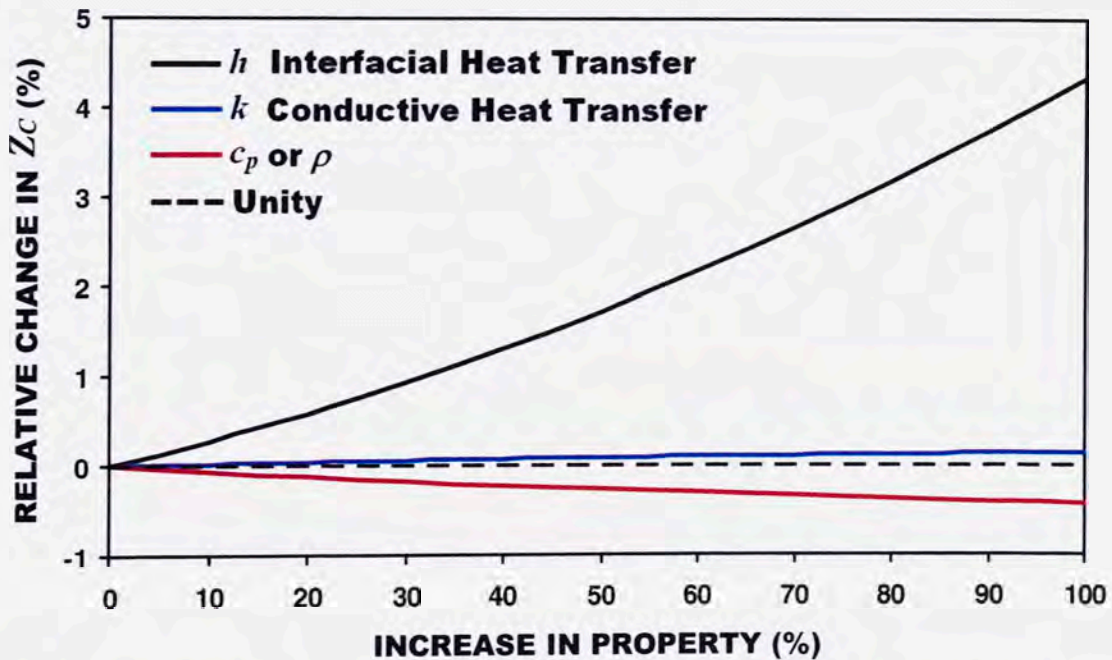


**Figure 5.5:** The effects of  $k$ ,  $h$ ,  $C_P$  and  $\rho$  on the critical casting thickness  $Z_C$  of a BMG.

It can be seen in **Figure 5.5** that the interfacial heat transfer coefficient,  $h$ , has the largest effect on  $Z_C$ . This high dependence of  $Z_C$  on  $h$  perhaps explains the difference in critical thicknesses reported for samples produced by either gravity casting or high pressure casting (injection casting) for a given composition (e.g. for  $\text{Mg}_{65}\text{Cu}_{25}\text{Y}_{10}$  BMG, Inoue et al.<sup>[214]</sup> reported  $Z_C = 4$  mm for gravity casting and  $Z_C = 7$  mm for high pressure injection casting). Naturally, an increase in pressure during casting (as discussed in **SECTION 4.5.4**), will enhance the contact between the

casting and mould wall, thereby reducing the interface resistance, and increasing interfacial heat transfer.<sup>[229]</sup> This behaviour will increase  $Z_C$ . There is evidence in other casting systems that further suggests that a higher contact pressure dramatically increases interfacial heat transfer.<sup>[300]</sup>

Based on the foregoing analysis, it can be seen that  $Z_C$  is a poor means of identifying GFA of a BMG with respect to copper mould casting. Rather, the critical cooling rate,  $R_C$ , required to generate a completely amorphous structure, (provided that  $R_C$  can be measured accurately) is a far better indicator of GFA as  $R_C$  is directly related to the alloy composition and its physical/thermal properties, i.e.  $T_L$ ,  $T_g$ ,  $k$ ,  $C_P$ ,  $\rho$  and  $\eta$ /diffusion. From this simple analysis, it can also be seen that  $Z_C$  may be substantially increased by lowering the copper mould temperature,  $T_{MOULD}$ , lowering the casting temperature  $T_{CAST}$  and increasing the interfacial heat transfer by applying a high contact pressure between the mould and casting. Based on experimental observations under constant casting conditions,<sup>[278]</sup> a relatively low liquidus temperature is desirable in reducing the amount of undercooling needed before vitrification occurs, and the GFA of BMGs is also expected to improve by a decrease in the semi-solid temperature range ( $T_m - T_l$ ).<sup>[278]</sup>

#### 5.1.4 Glass Transition and Crystallisation Behaviour

A major concern with BMGs is their restricted use at elevated temperature due to their inherent thermodynamic instability, leading to a drastic change in properties due to crystallisation.<sup>[251]</sup> Upon heating, various reactions are known to occur, the first being the change from glassy behaviour to that of a supercooled liquid at  $T_g$ . This is followed by one or more consecutive crystallisation reactions. The extent of the SCL region ( $\Delta T_X = T_X - T_g$ ) is determined by the alloy type, composition and heating rate and is associated with glass stability.<sup>[20,60,267]</sup> With respect to isochronal heating (constant heating rate), this behaviour is described in **SECTION 2.3.2** by Eq. (2.10); this is a variant of the VFT equation that combines the kinetics of glass transition with the equilibrium viscosity.<sup>[60]</sup> **Figure 5.6** shows that, with respect to heating rate, the characteristics of the onset of  $T_g$  and  $T_X$  for  $Mg_{65}Cu_{25}Y_{10}$  and  $Ca_{65}Mg_{15}Zn_{20}$  BMGs are very different. Here, it can be seen that onset behaviour for the  $Mg_{65}Cu_{25}Y_{10}$  is highly heating rate dependant whereas, in the case of the  $Ca_{65}Mg_{15}Zn_{20}$  BMG, there is very little variation of the thermal characteristics of the glass over a range of heating rate. The variation of  $T_g$  and  $T_X$  with respect to heating rate is related to glass stability/fragility, whereby a lower heating rate dependence indicates a more fragile glass.<sup>[60]</sup> As seen in **Figure 5.6**, a higher heating rate



generates higher values of  $T_g$  and  $T_X$  and a larger SCL region, which has industrial significance, as this effect yields a larger temperature window for superplastic deformation in the SCL region.

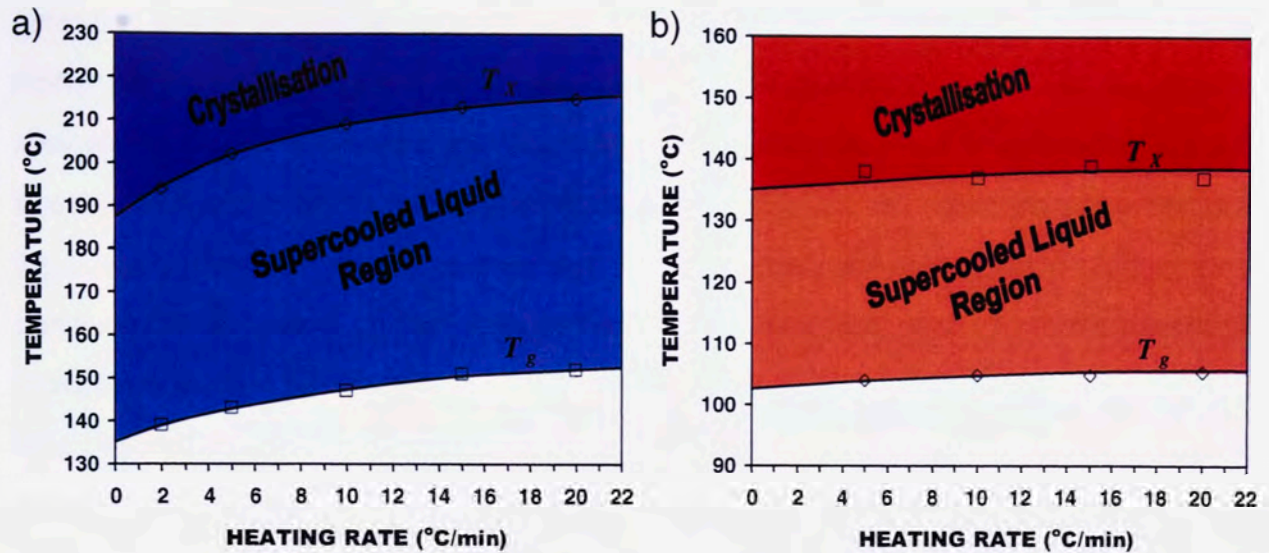


**Figure 5.6:** Effect of heating rate on  $T_g$  and  $T_X$ , as determined by DSC: a)  $Mg_{65}Cu_{25}Y_{10}$  BMG and b)  $Ca_{65}Mg_{15}Zn_{20}$  BMG.

**Figure 5.7** shows a comparison of the isochronal DSC crystallisation curves (both taken at 20 °C/min), for the  $Mg_{65}Cu_{25}Y_{10}$  and  $Ca_{65}Mg_{15}Zn_{20}$  BMGs studied in this thesis. It can be seen in **Figure 5.7** that these curves have dissimilar shapes i.e. the DSC curve of the Mg-based alloy is clearly skewed to higher temperatures, whereas the Ca-based alloy has a more symmetrical DSC curve.

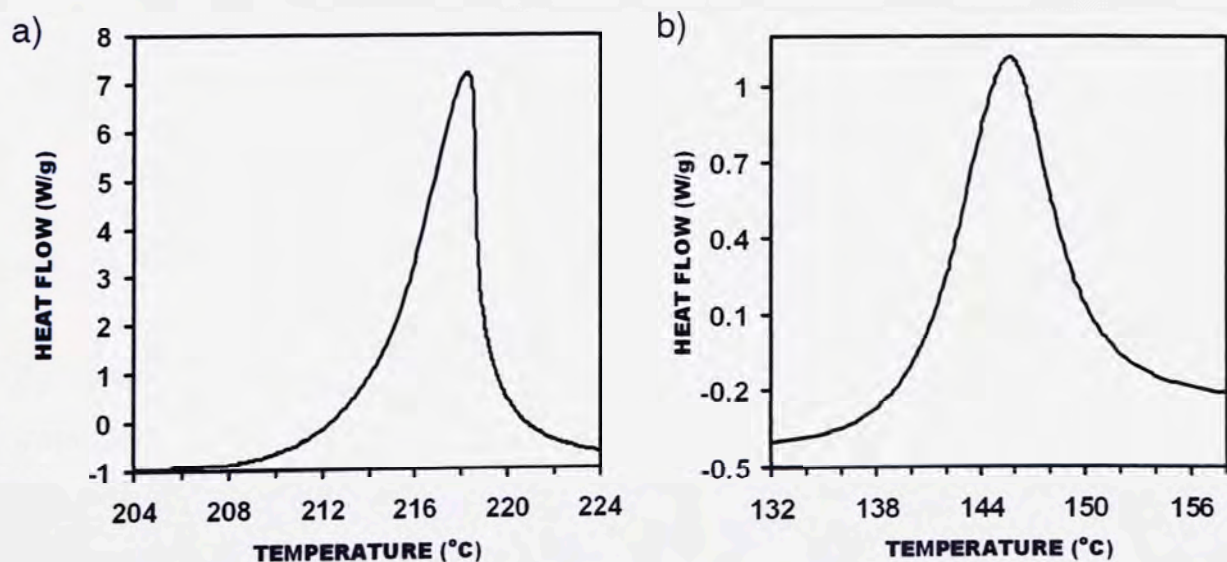


**Figure 5.7:** The difference in shape of the DSC crystallisation curves for: a)  $Mg_{65}Cu_{25}Y_{10}$  BMG and b)  $Ca_{65}Mg_{15}Zn_{20}$  BMG (heating rate = 20 °C/min).



Based on the Kissinger method<sup>[116]</sup> described in SECTION 2.3.4, the local activation energies required for a given crystallised fraction of the two DSC curves are shown in **Figure 5.7**. **Figure 5.8** shows local activation energy as a function of crystallised fraction for both BMGs. The initial activation energy required for crystallisation of the Mg-based BMG is obviously higher due to its higher crystallisation temperature (related to the atomic species present). The  $\text{Ca}_{65}\text{Mg}_{15}\text{Zn}_{20}$  alloy shows a steeper decent in activation energy in the initial stages of crystallisation, indicating that the initial stages of this particular crystallisation reaction occurs more readily than that of the  $\text{Mg}_{65}\text{Cu}_{25}\text{Y}_{10}$  alloy. It can also be seen that the decrease in activation energy required for the complete crystallisation of the Mg-based alloy is greater than that of the Ca-based alloy indicating that once the reaction has started it continues more rapidly. Hence, there is a shorter time required to complete the crystallisation reaction of the former alloy. It may therefore be assumed that the final stages of crystallisation are more complex for the Ca-based alloy.

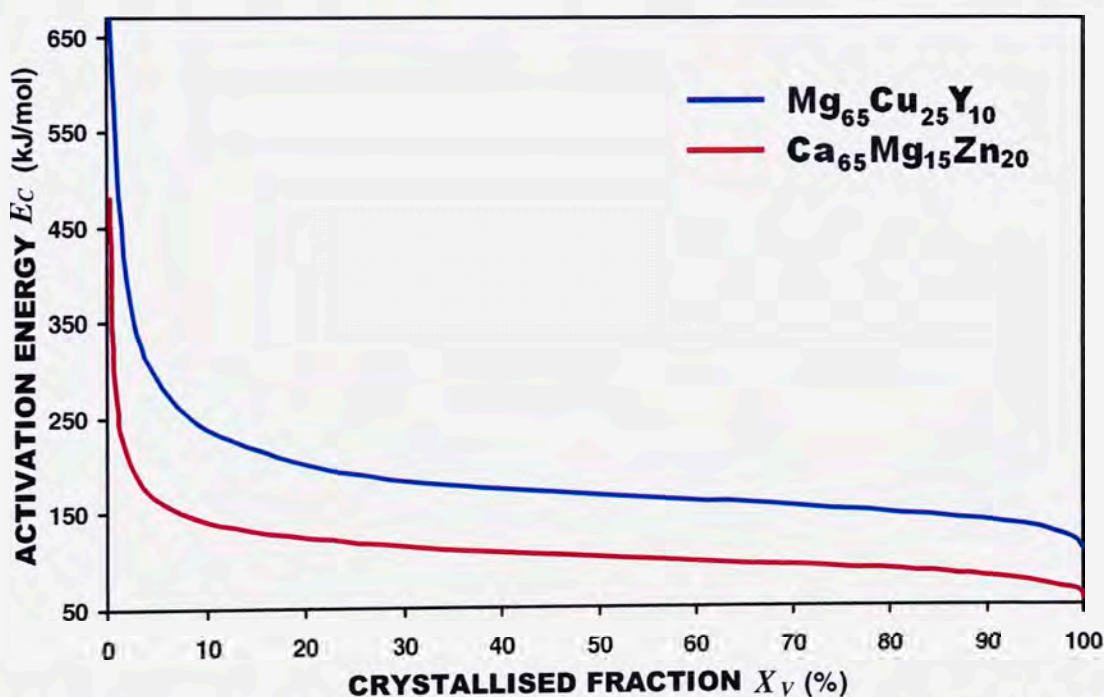


**Figure 5.8:** Comparison of the change in activation energy during crystallisation for the  $\text{Mg}_{65}\text{Cu}_{25}\text{Y}_{10}$  and  $\text{Ca}_{65}\text{Mg}_{15}\text{Zn}_{20}$  BMGs (heating rate = 20 °C/min).

By combining the Kissinger relation<sup>[116]</sup> with the method devised by Ozawa et al.<sup>[117]</sup> the instantaneous value of the Avrami<sup>[110-112]</sup> exponent,  $n$  may be calculated using constant heating rate data, which can be seen in APPENDIX I. However, this method tends to give higher values of  $n$  compared to the isothermal analysis due to the variation of the diffusivity of the atoms and short relaxation/stabilisation times. A plot of the instantaneous Avrami exponent during crystallisation for both alloys, as calculated from the DSC traces of **Figure 5.7**, is given in **Figure 5.9**.



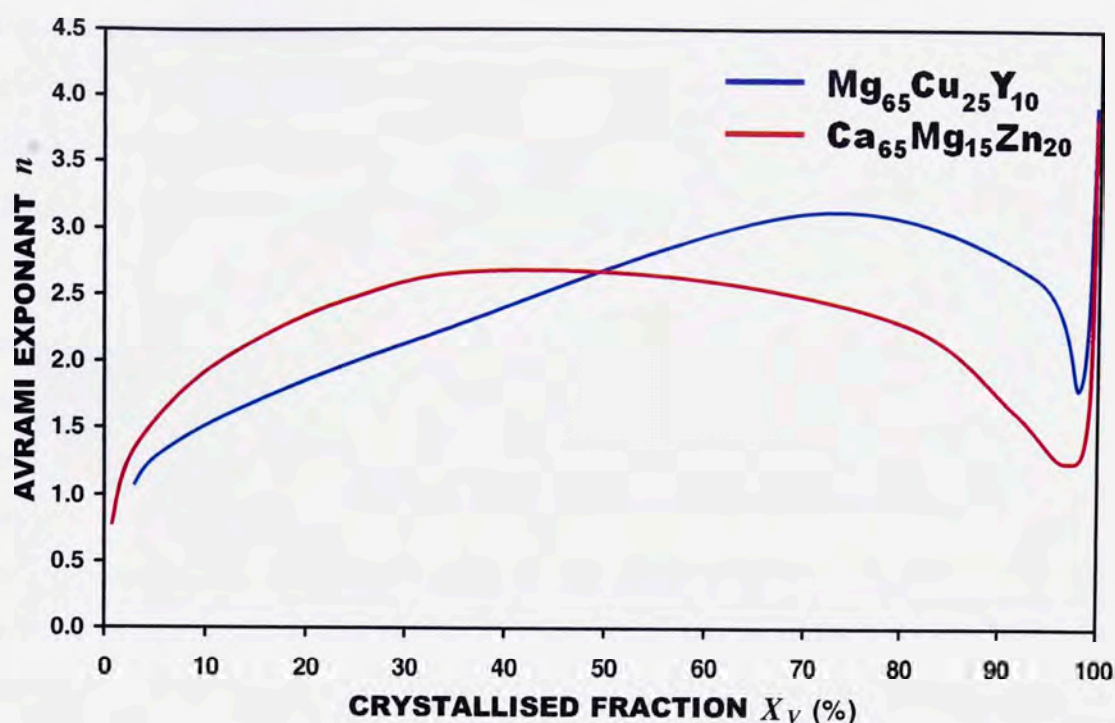


**Figure 5.9:** Comparison of the instantaneous Avrami exponent with respect to crystallised fraction for  $\text{Mg}_{65}\text{Cu}_{25}\text{Y}_{10}$  and  $\text{Ca}_{65}\text{Mg}_{15}\text{Zn}_{20}$  BMGs (heating rate = 20 °C/min).

The instantaneous Avrami exponent curve provides insight into the rate of diffusion-controlled nucleation and growth of crystalline particles during heating. A value of  $1 < n < 1.5$  indicates particles with appreciable initial volume and a zero nucleation rate, whereas the range  $1.5 < n < 2.5$  indicates particle growth at a decreasing nucleation rate. Values of  $n > 2$  are indicative of a crystallisation process governed by three-dimensional growth (spherical particles) where  $n > 2.5$  sees a transition from a decreasing nucleation rate to that of an increasing nucleation rate. In the latter stages of crystallisation, the local Avrami exponent tends to decrease to a value lower than 2.5, indicating a decreasing nucleation rate. This is attributed to nucleation saturation and three-dimensional growth of crystalline nuclei, leading to subsequent crystal impingement<sup>[301]</sup> and the mutual contact of crystals.<sup>[302]</sup> **Figure 5.9** shows that the  $\text{Mg}_{65}\text{Cu}_{25}\text{Y}_{10}$  BMG exhibits much slower nucleation and growth kinetics for the first 50% of the crystallisation transformation reaction at a constant heating rate of 20 °C/min than that of the  $\text{Ca}_{65}\text{Mg}_{15}\text{Zn}_{20}$  BMG. This initially sluggish crystallisation behaviour suggests that the structure of the Mg-based BMG is that of a somewhat stronger liquid compared to the Ca-Based BMG. Also evident from this plot is the earlier and deeper decrease of the Avrami exponent in the  $\text{Ca}_{65}\text{Mg}_{15}\text{Zn}_{20}$  alloy in the final 50% of crystallisation. Again, this behaviour is likely to be associated with nucleation saturation or, as suggested by the activation energy, a complex, high energy crystallisation mechanism, perhaps related to the twinning seen in **SECTION 4.7.2**.



**Figure 5.10** shows the isothermal DSC time-temperature-transformation data for both alloys. Similar to the behaviour shown in **Figure 5.7**, the two alloys display quite different crystallisation characteristics. For the Mg-based BMG, the transformation follows the expected Arrhenius-type crystallisation reaction, whereas the Ca-based alloy deviates somewhat from expected crystallisation behaviour, as shown by the non linearity of the plots.

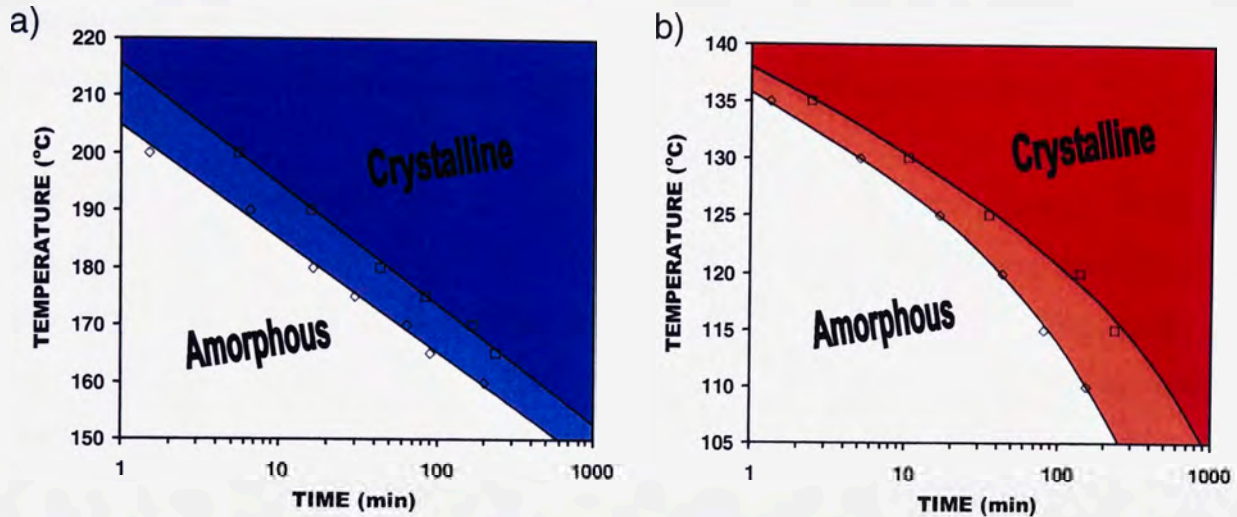


**Figure 5.10:** Time-Temperature-Transformation diagrams showing the transition from the non-equilibrium amorphous phase to the equilibrium crystalline structure for: a)  $\text{Mg}_{65}\text{Cu}_{25}\text{Y}_{10}$  BMG and b)  $\text{Ca}_{65}\text{Mg}_{15}\text{Zn}_{20}$  BMG.

The behaviour shown in **Figure 5.10b**), which appears to be a type of acceleration of the crystallisation reaction at higher temperatures, may be explained in two ways:

- (i) Using the VFT relation (**Eq. 2.8**),<sup>[66,67]</sup> which describes the change in viscosity as a function of temperature and liquid fragility, it can be seen that a more fragile liquid will deviate further from Arrhenius-type viscosity behaviour. Viscosity, which is proportional to the inverse diffusivity, (**SECTION 2.3.2**), is regarded as a kinetic factor controlling the jumping and rotation rates of atoms or molecules across a nucleus-liquid interface.<sup>[15,22,60-63]</sup> This transportation rate of atoms across this interface is a determining factor in both the nucleation rate (**Eq. (2.3)**) and growth (**Eq. (2.11)**) of crystalline phases.
- (ii) The possible presence of quenched-in nuclei may contribute to the deviation. In a recent study, the average value of the Avrami exponent was given as 3.0 for  $\text{Mg}_{65}\text{Cu}_{15}\text{Ag}_{10}\text{Y}_{10}$  alloy.<sup>[283]</sup> In this case, it was found that the addition of Ag altered the crystallisation behaviour substantially and it was proposed that crystallisation was governed by diffusional growth of quenched-in nuclei.<sup>[283]</sup>



### 5.1.5 Chemical Reactivity

It is known that the chemical reactivity of metallic calcium far exceeds that of magnesium. It was observed in this work that the charge preparation of the Ca-based BMG was far more difficult than that of the Mg-based BMG due to the rapid formation of oxide film on the calcium balance material. It was also found that attempting to prepare the  $\text{Ca}_{65}\text{Mg}_{15}\text{Zn}_{20}$  alloy in a resistance furnace in a crucible with a non-sealed pouring spout under a circulating argon atmosphere was inadequate, with the majority of metal being oxidised due to the long heating times. Here, it became necessary to develop the induction-heated, inverted injection-casting unit.

Once quality BMG samples were produced, it became apparent that the corrosion resistance of the Mg-based BMG far exceeded that of the Ca-based BMG; the latter was found to corrode into a black powder within two months, whereas the former retained a metallic lustre for years under indoor/laboratory conditions. This reactivity posed some problems with the storage of samples both pre- and post-testing. In order to maintain the samples close to their as-cast nature, they were stored in silicon oil in sealed specimen containers. Nevertheless, the Ca-based BMG continued to tarnish in this environment, at a rate much faster than that of the Mg-based BMG which remains relatively unchanged. **Figure 5.11** shows the two alloys exposed to different conditions for different periods of time. **Table 5.2** shows the available electrochemical data for the corresponding BMG alloys and some reference crystalline metals in different electrolyte solutions.

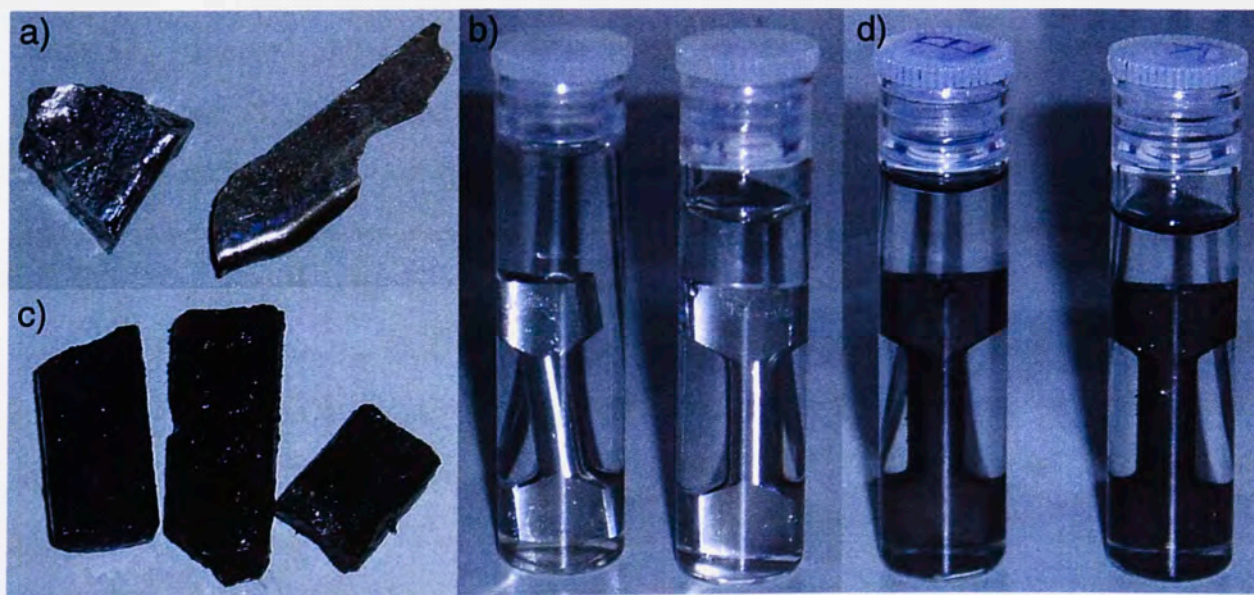


**Figure 5.11:** The condition of: a)  $\text{Mg}_{65}\text{Cu}_{25}\text{Y}_{10}$  BMG exposed to air for two years and b) sealed in silicon oil for two years; c)  $\text{Ca}_{65}\text{Mg}_{15}\text{Zn}_{20}$  BMG exposed to air for 2 months and d) sealed in silicon oil for 9 months.

**Table 5.2:** Electrochemical data for Ca- and Mg-based BMGs and similar crystalline metals.

ALLOY (at.%)	ELECTROLYTE	CORROSION POTENTIAL (mv)	CURRENT DENSITY (mA)	MEAN CPR (mm/year)	REF
<b>Ca<sub>65</sub>Mg<sub>15</sub>Zn<sub>20</sub></b>	0.05 M Na <sub>2</sub> SO <sub>4</sub>	-1535	0.17	5.691	[303]
<b>Ca<sub>55</sub>Mg<sub>18</sub>Zn<sub>11</sub>Cu<sub>16</sub></b>	0.05 M Na <sub>2</sub> SO <sub>4</sub>	-479	0.011	0.311	[303]
<b>Ca<sub>50</sub>Mg<sub>20</sub>Cu<sub>30</sub></b>	0.05 M Na <sub>2</sub> SO <sub>4</sub>	-1165	0.053	1.503	[303]
<b>Mg<sub>97.6</sub>Zn<sub>2.2</sub>Zr<sub>0.2</sub></b> <sup>(C)</sup>	0.05 M Na <sub>2</sub> SO <sub>4</sub>	-1501	0.019	0.425	[303]
<b>PURE Mg</b> <sup>(C)</sup>	0.01 M Na <sub>2</sub> SO <sub>4</sub>			>1	[304]
<b>Mg<sub>65</sub>Cu<sub>25</sub>Y<sub>10</sub></b>	0.01 M NaCl	-346	0.002	41	[305]
<b>Mg<sub>65</sub>Ni<sub>20</sub>Nd<sub>15</sub></b>	0.01 M NaCl	-634	0.003	75	[305]
<b>PURE Mg</b> <sup>(C)</sup>	0.01 M NaCl	-1525	0.004	88	[305]
<b>Mg<sub>65</sub>Cu<sub>25</sub>Y<sub>10</sub></b>	0.1 M NaOH	-575	0.5		[189]
<b>PURE Mg</b> <sup>(C)</sup>	0.1 M NaOH	-1241	1.1		[189]

<sup>(C)</sup> denotes a crystalline material

## 5.2. CASTABILITY OF BMGS

### 5.2.1 Composition Characteristics

Of the two alloy compositions examined in this thesis, the Mg<sub>65</sub>Cu<sub>25</sub>Y<sub>10</sub> BMG proved far more time consuming to prepare due to the intermediate step of master alloy preparation, which involved the tedious task of arc melting. However, this preparation step may now be eliminated using the induction-heated inverted die-casting unit described in **SECTION 4.2** by using a preparation method similar to that of the Ca<sub>65</sub>Mg<sub>15</sub>Zn<sub>20</sub> alloy (described in **SECTION 4.3**). However, the Mg<sub>65</sub>Cu<sub>25</sub>Y<sub>10</sub> BMG proved significantly easier to cast and handle in the molten state opposed to the Ca<sub>65</sub>Mg<sub>15</sub>Zn<sub>20</sub> BMG. This was generally due to the reactivity of elemental calcium in the Ca-based BMG as opposed to the reactivity of Mg-based BMG and the noble/passivating effects of using copper as an alloying element in the latter.

Due to the relative differences in liquidus temperatures, casting of the Ca-based alloy was possible at much lower temperatures. **Figure 5.12** shows a comparison of the casting temperatures (normalised to  $T_g$ , the theoretical temperature at which viscous flow is physically



no longer possible), and gate velocities for both alloys at which the charge material did not completely fill the entire length of the copper mould.

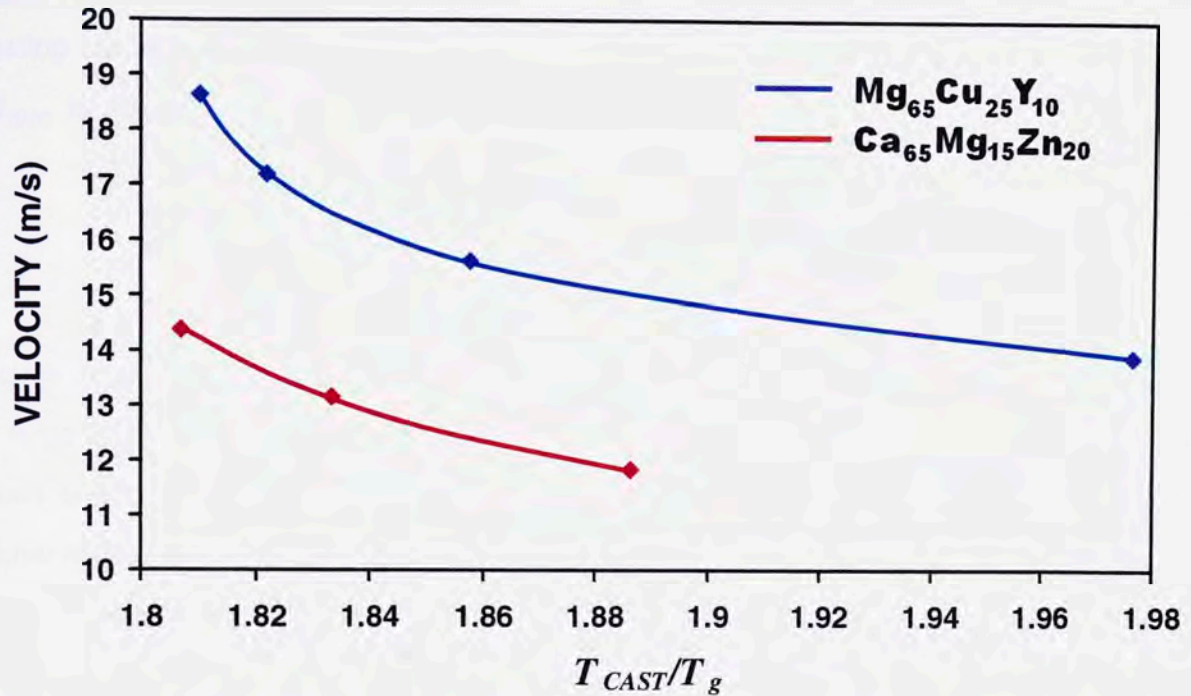


**Figure 5.12:** Comparison of incomplete mould filling with respect to normalised casting temperature and molten metal velocity at the mould gate for  $Mg_{65}Cu_{25}Y_{10}$  and  $Ca_{65}Mg_{15}Zn_{20}$ .

It can be seen that the  $Mg_{65}Cu_{25}Y_{10}$  BMG requires higher casting temperatures and gate velocities to achieve complete mould filling than the  $Ca_{65}Mg_{15}Zn_{20}$  BMG. This suggests that the viscosity of the molten Mg-based alloy is greater than that of the Ca-based alloy. As was discussed in SECTION 2.3.3 a lower melt viscosity is associated with a lower packing efficiency and short range order bond strength that, in turn, is related to poorer glass-forming ability.<sup>[60]</sup> These results indicate that, based on melt viscosity, the  $Mg_{65}Cu_{25}Y_{10}$  BMG would have a higher glass forming ability than the  $Ca_{65}Mg_{15}Zn_{20}$  BMG, which, according to previous discussion appears to be the case.

In terms of permanent copper mould casting of BMG parts with large aspect ratios (e.g. long bars, large sheets, plates or thin component housings), a metal with a lower molten viscosity would prove more advantageous with respect to cavity filling. As was observed in this thesis, a higher injection temperature promoted more extensive cavity filling due to a decrease in metal viscosity and an increase in stagnation time,  $t_r$ , (described in Eq. (3.13)). However, as depicted in Figure 4.21, a higher injection temperature results in a lower rate of cooling that, at some point, will become critical in forming an amorphous structure upon cooling.

Ideally, BMGs amenable to copper mould casting should exhibit a low critical cooling rate for glass-forming ability, a low liquidus temperature and melt viscosity to promote complete mould cavity filling and a high material heat capacity and density for enabling the molten metal to retain heat. A BMG castability parameter,  $\Omega_{BMG}$ , is used here to identify superior copper mould casting characteristics between alloys. Based on the aforementioned properties of an alloy,  $\Omega_{BMG}$  is defined as:

$$\Omega_{BMG} = \frac{C_P \rho}{R_C T_l \eta_m} \quad (5.7)$$

A large value of  $\Omega_{BMG}$  indicates an alloy that is highly suitable for copper mould casting. In terms of large-scale production by permanent mould casting, in theory lightweight BMG components could become more competitive with commercial crystalline alloys. Although BMGs exhibit higher melt viscosities than those of pure metals (lightweight BMG viscosities 2 - 5 Pa.s compared to  $10^{-3}$  Pa.s of pure metals),<sup>[25]</sup> they exhibit much lower melting temperatures due to deep eutectic reactions and no heat of fusion upon cooling compared to Mg-based commercial alloys.

With respect to cooling a metal casting to a temperature at which it may be removed from a mould (i.e.  $T_{MOULD}$ ) the amount of heat to be removed from a crystalline metal casting can be given by the general equation:

$$Q = \rho_l V C_{P,l} \Delta T_s + \rho_s V H_f + \rho_s V C_{P,s} (T_m - T_{MOULD}) \quad (5.8)$$

where  $\rho_s$  and  $\rho_l$  is the density of the solid and the liquid, respectively,  $C_{P,s}$  and  $C_{P,l}$  is the solid and liquid heat capacities, respectively,  $V$  the volume of material,  $H_f$  the heat of fusion,  $\Delta T_s$  the degree of superheat and  $T_m$  the melting temperature. Comparing Eq. (5.8) with the heat of a molten BMG-forming alloy (Eq. (3.4) - no heat of fusion) it may be appreciated that, provided similar mould filling properties are reached, the production time of a BMG cast component will be less than that of a commercial crystalline alloy, leading to greater production efficiency. If high-pressure consolidation methods similar to those seen in SECTION 4.5.4 of this work are utilised, there is also the possibility of generating a surface finish of higher quality than that achievable in a crystalline material due to: (i) the homogeneous structure of the material (no grain etching effects), and (ii) the high formability of the material in the SCL region whilst cooling, which exhibits enhanced mould feature replication on a micro scale.<sup>[172]</sup>



### 5.2.2 Sample Density and Injection Velocity Range

Figures 3.32 and 4.25 show the processing maps developed for casting of 3.15x7x125 mm  $\text{Mg}_{65}\text{Cu}_{25}\text{Y}_{10}$  and  $\text{Ca}_{65}\text{Mg}_{15}\text{Zn}_{20}$  BMG samples. It is interesting to note that, throughout the evolution of the inverted injection casting process, sample density and, hence, integrity was improved from a control window within 50% to ~100% fully dense range for the Mg-based alloy to 96% to > 98.8% fully dense for the Ca-based alloy (the inability to achieve 100% density was due to surface imperfections rather than porosity). This substantial improvement in processing is thought to be due to an early stabilisation of the fluid flow front, bought about by the change in acceleration due to the increase in melt chamber volume, as discussed in SECTION 4.2. It is also interesting to note that the injection velocity range for achieving high quality castings in the  $\text{Ca}_{65}\text{Mg}_{15}\text{Zn}_{20}$  BMG is similar to that of the favourable casting region for the  $\text{Mg}_{65}\text{Cu}_{25}\text{Y}_{10}$  BMG. Figure 5.13 shows a comparison of the two casting zones with respect to the injection velocity at the gate and temperature normalised to  $T_g$ . This indicates that, provided the material viscosity remains low enough to entirely fill the mould cavity (higher in the casting temperature region), the ideal gate velocity of the material is a physical characteristic of the casting system, namely the mould cavity/gate geometry. Here, an excessive gate velocity will destabilise the progressing fluid front, introducing structural defects such as cold shuts and hollow sections, thereby decreasing the structural integrity of the casting.

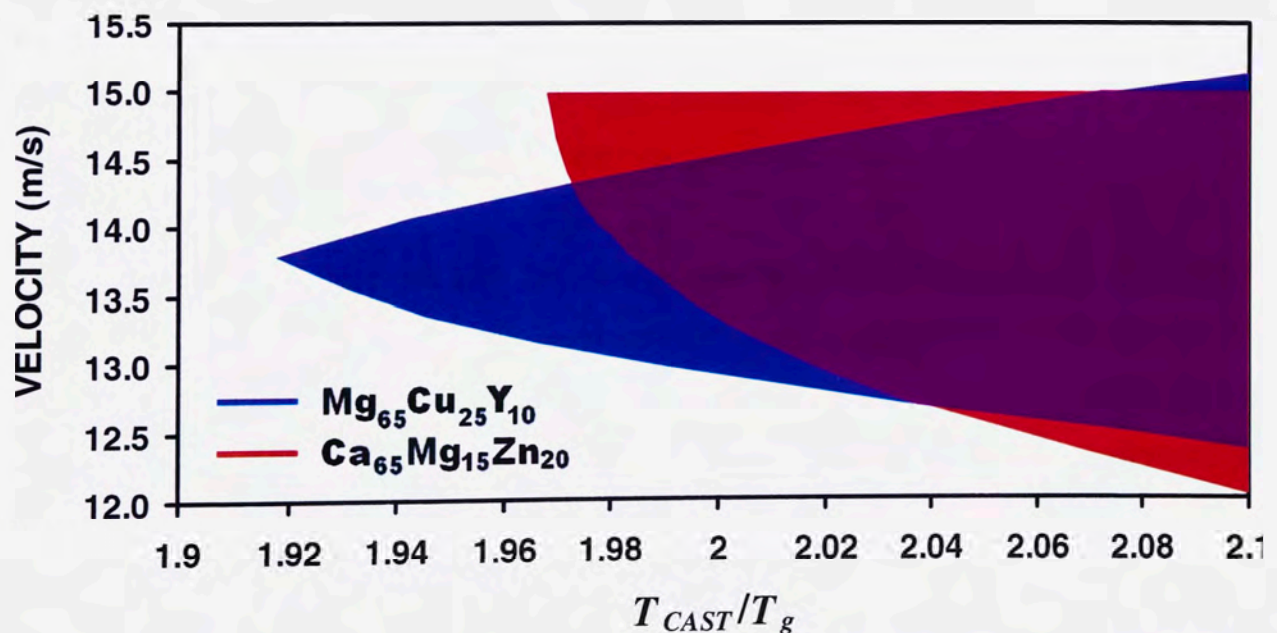


**Figure 5.13:** A comparison of the favourable casting zones for  $\text{Mg}_{65}\text{Cu}_{25}\text{Y}_{10}$  and  $\text{Ca}_{65}\text{Mg}_{15}\text{Zn}_{20}$  BMGs with respect to injection velocity and normalised casting temperature  $T_{\text{CAST}}/T_g$ .

### 5.3. ELEVATED TEMPERATURE MECHANICAL PROPERTIES

As discussed by Ashby and Greer,<sup>[148]</sup> who compared the elastic limit of BMGs to other commercial alloys (**Figure 2.24**), BMGs approach the theoretical strength limit ( $\sigma_y = E/20$ ) more closely than any other bulk metallic materials. This ideal strength limit is essentially based on interatomic potentials,<sup>[306]</sup> that is, the rupture strength of individual atomic bonds within a material. This result is somewhat expected in a BMG as there are no grain boundary interactions and no dislocations to accommodate strain, resulting in material properties close to that of the interatomic bond strength and stiffness.

#### 5.3.1 Effects of Temperature and Strain Rate on BMG Flow Stress and Viscosity

Both BMGs investigated in this thesis displayed stress strain curves typical of other bulk metallic glasses<sup>[174,185,244]</sup> whereby a high peak stress is reached and, quite often, a stress overshoot is observed, followed by a much lower flow stress. (See e.g. **Figures 3.41** and **4.31**). A stress overshoot is usually associated with non-Newtonian behaviour<sup>[60,247]</sup> at high strain rates or low temperatures and generally attributed to the change in atomic-mobility at a yield point due to a rapid, deformation-induced, change in free volume<sup>[60,185,247]</sup> and its gradual return to an equilibrium state during stress relaxation. The strain-induced softening is generally explained by an increase in the free volume and generation of shear bands.<sup>[20,25,27,248-250]</sup>

As discussed throughout this thesis, temperature, strain rate, flow stress and viscosity are interrelated. These relationships are generally expressed using equations **(2.8)** and **(2.32)**, which are referred to in **SECTION 2.3.2** and **SECTION 2.6.4**, respectively.

It was observed throughout this work that, at temperatures within the SCL region accessible to tensile testing, the  $\text{Ca}_{65}\text{Mg}_{15}\text{Zn}_{20}$  BMG would only flow in a homogeneous manner at strain rates one to two orders of magnitude lower than those achieved by the  $\text{Mg}_{65}\text{Cu}_{25}\text{Y}_{10}$  BMG. **Figure 5.14** shows, for a given temperature, viscosity as a function of strain rate for the two alloys, which were calculated using Eq. **(2.32)**. Also included (inset) in **Figure 5.14** as a means of comparison is a table of temperatures normalised to the glass transition temperature of each alloy. Normalised viscosity in the Newtonian flow region is discussed in **SECTION 5.3.2 (Figure 5.16)**.



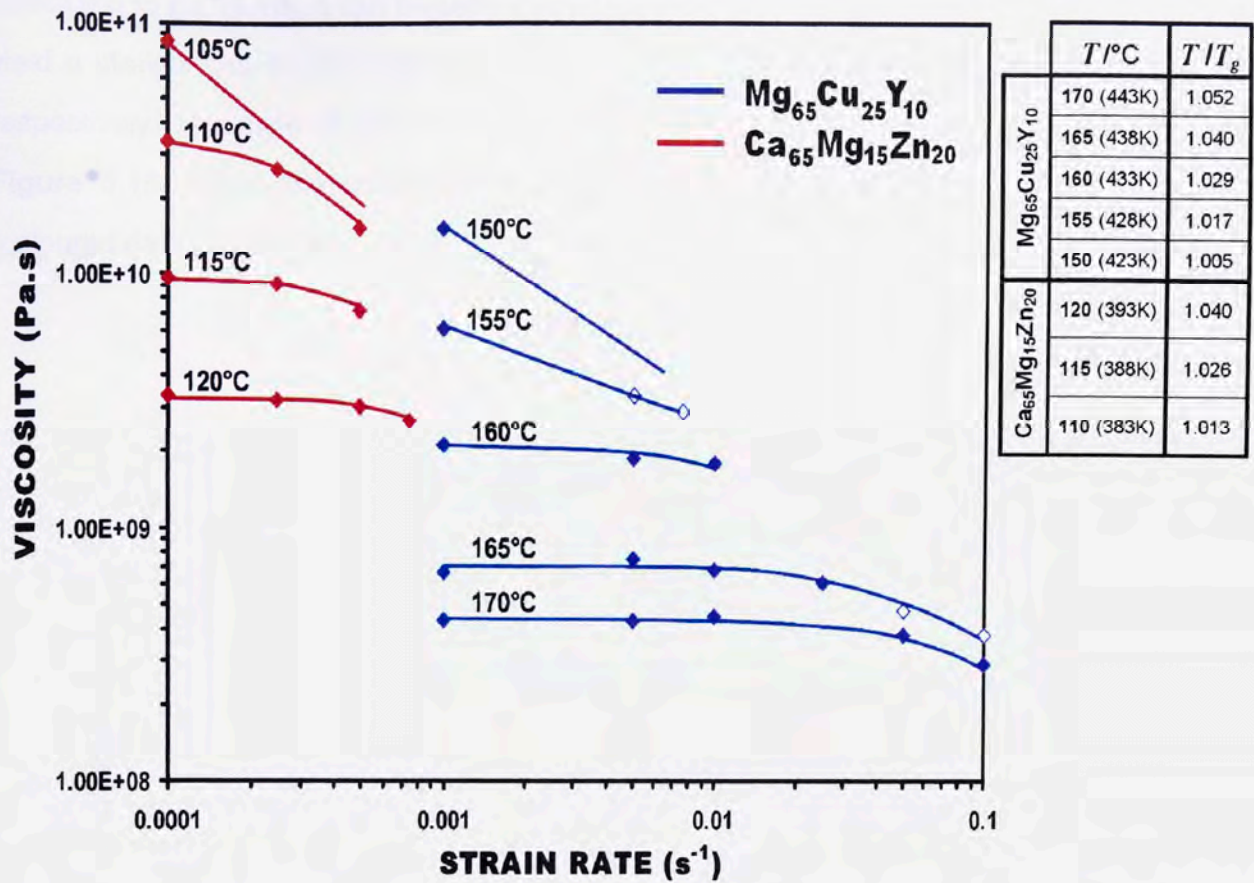


**Figure 5.14:** Effect of strain rate on viscosity of the  $\text{Mg}_{65}\text{Cu}_{25}\text{Y}_{10}$  and  $\text{Ca}_{65}\text{Mg}_{15}\text{Zn}_{20}$  BMGs at a given temperature (Inset Table: Temperatures normalised to  $T_g$ ).

As discussed in SECTION 4.6.9, the combined relationship between flow stress, strain rate and temperature can be described by Eq. (4.13). Rearranging this equation to better represent the experimental data and variables used during constant strain rate tensile testing gives:

$$\sigma_f = 3\dot{\epsilon}\eta_o \exp\left[\frac{D^*T_o}{(T - T_o)}\right] \quad (5.9)$$

Using the VFT relation (Eq. (2.8)), values of  $\eta_o$ ,  $D^*$  and  $T_o$  were determined in SECTIONS 3.9.6 and 4.6.6 for the  $\text{Mg}_{65}\text{Cu}_{25}\text{Y}_{10}$  and  $\text{Ca}_{65}\text{Mg}_{15}\text{Zn}_{20}$  BMGs, respectively.

Equation (5.9) may be rearranged to give:

$$\ln \sigma_f = \ln(3\dot{\epsilon}\eta_o) + \left[\frac{D^*T_o}{(T - T_o)}\right] \quad (5.10)$$

According to Eq. (5.10), it can be seen that a plot of  $\ln \sigma_f$  as a function of  $1/T-T_o$  is expected to yield a straight line for the data with  $D^*T_o$  and  $\ln(3\dot{\epsilon}\eta_o)$  being the gradient and y-intercept, respectively. This type of plot for both the  $\text{Mg}_{65}\text{Cu}_{25}\text{Y}_{10}$  and  $\text{Ca}_{65}\text{Mg}_{15}\text{Zn}_{20}$  BMG is given in **Figure 5.15**, where the dashed lines represent the expected fit for Newtonian flow data (coloured data points) using Eq. (5.10) and previously calculated values of  $D^*$  and  $T_o$ .

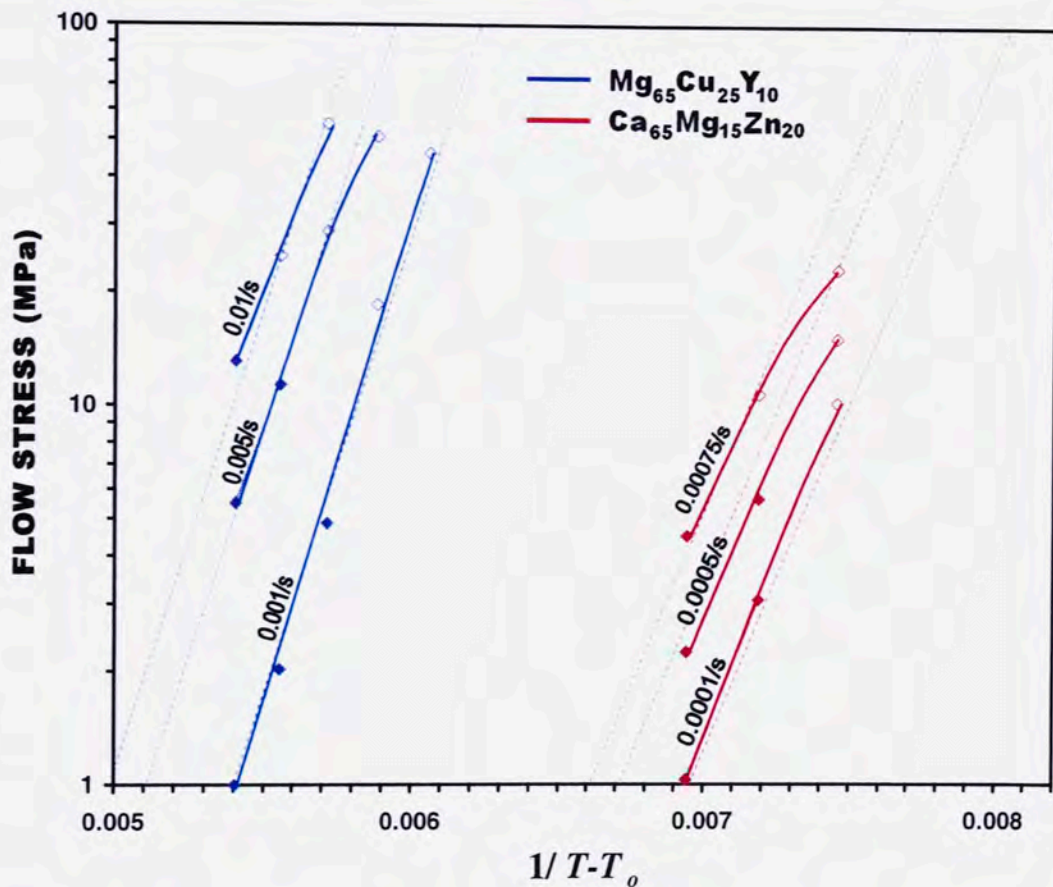


**Figure 5.15:** Comparison of the relationship between temperature, flow stress and strain rate highlighting the correlation between data and Eq. (5.10).

It is clear from **Figure 5.15** that the Newtonian data points (confirmed using the free volume model) correlate quite well with the expected fit whereas the non-Newtonian data (unfilled points) deviate from linearity, as indicated by the solid lines. This information shows that the free volume model and the VFT relation correspond quite well with one another and the data generated in this thesis.



### 5.3.2 Fragility

The concept of fragility was introduced by Angell<sup>[66-68]</sup> to characterise the increase in liquid viscosity during cooling; it is considered to be a measure of the degree of co-operativity of atomic motion. Fragility of liquids is defined as the apparent activation energy of shear viscosity,  $\eta$ , or structural relaxation time at the glass transition temperature,  $T_g$ , normalised to  $T_g^*$ .<sup>[66-68]</sup> On the basis of the experimental results there is a positive correlation between GFA and the strong nature of liquids with BMGs showing behaviour similar to strong glasses.<sup>[60,70,71]</sup> The parameter,  $D^*$ , derived from the VFT equation (Eq. (2.8)) is often used as a measure of liquid fragility with values ranging from 3 to 5 for fragile liquids such as organic glasses, and up to 100 for a strong liquid, such as  $\text{SiO}_2$  glass. Typically,  $D^*$ -values range from 15 - 25 for BMGs.<sup>[60,63-65]</sup> By normalising Newtonian viscosity data points generated during tensile testing in the SCL region of  $\text{Mg}_{65}\text{Cu}_{25}\text{Y}_{10}$  ( $D^* = 21.6$ ) and  $\text{Ca}_{65}\text{Mg}_{15}\text{Zn}_{20}$  ( $D^* = 17.3$ ), an 'Angell plot'<sup>[66]</sup> was constructed to show the distinct differences that temperature has on the Newtonian viscosity of the two BMGs (Figure 5.16). A detailed description of the methods used to construct this plot is given in APPENDIX J. With respect to the viscosity data, Figure 5.16 indicates that  $\text{Mg}_{65}\text{Cu}_{25}\text{Y}_{10}$  is a stronger liquid than  $\text{Ca}_{65}\text{Mg}_{15}\text{Zn}_{20}$ , although both alloys display relatively strong liquid behaviour.

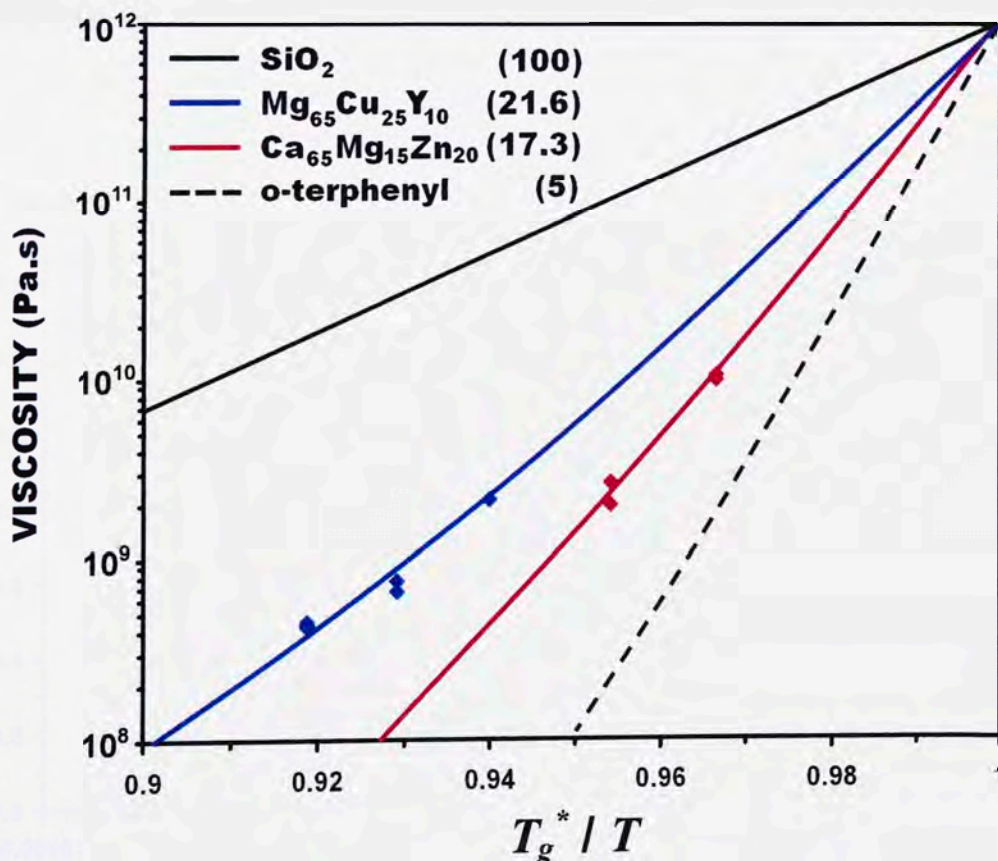


**Figure 5.16:** An 'Angell plot' consisting of Newtonian viscosity data for the  $\text{Mg}_{65}\text{Cu}_{25}\text{Y}_{10}$  and  $\text{Ca}_{65}\text{Mg}_{15}\text{Zn}_{20}$  BMGs normalised to  $T_g^*$  (also included are curves for  $\text{SiO}_2$  and o-terphenyl).



### 5.3.3 Workability of Bulk Metallic Glasses

Fabrication of light-weight BMG components is limited by a number of factors: (i) Their machinability is generally limited to fine surface grinding (as used in the fabrication of tensile samples in SECTION 3.8) due to the brittle nature of the alloys at room temperature; and (ii) Industrial type welding processes are also not possible due to crystallisation of the BMGs associated with remelting and crystallisation of the heat affected zone/s. A promising method of component fabrication for lightweight BMGs is near-net-shape fabrication. This can be achieved by: (i) direct casting although complex components are difficult to produce due to the high cooling rates required (see e.g. **Figure 3.23**) or (ii) plastic forming in the SCL region, as discussed in SECTION 2.6.4. The hot workability of amorphous materials by industrial-type processes is expected to be higher for a fragile liquid, since they would reach the viscosity of a stronger liquid at a lower working temperature (**Figure 5.16**). Based on fragility data alone, the  $\text{Ca}_{65}\text{Mg}_{15}\text{Zn}_{20}$  BMG is expected to show better workability. However, fragility does not take into account strain rate sensitivity, nor do the two parameters appear to be related. Superplasticity is characterised by the strain rate sensitivity,  $m$ : this parameter, is considered to be a material property, related to the stoichiometry of the individual BMG.<sup>[20]</sup> **Figure 5.17** shows strain rate sensitivity as a function of both strain rate and temperature for the two BMGs. Also included in this figure is a table of test temperatures normalised to  $T_g$  for comparison.

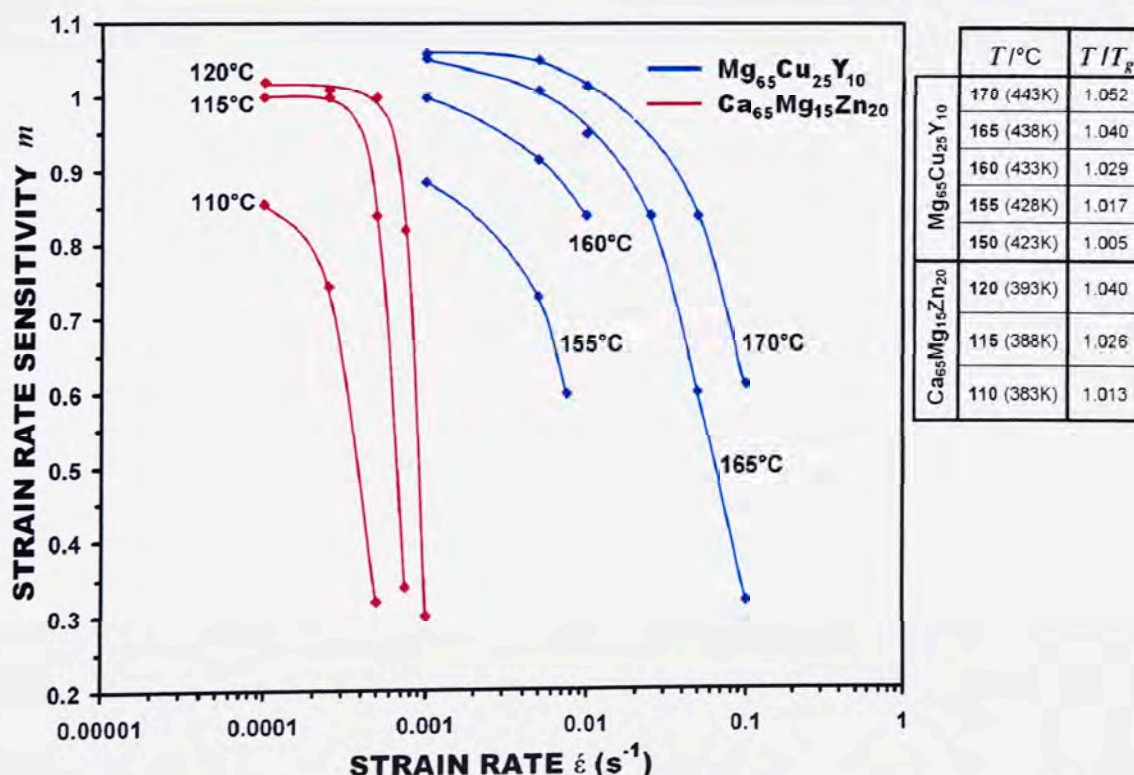


**Figure 5.17:** Effect of strain rate on strain rate sensitivity of the  $\text{Mg}_{65}\text{Cu}_{25}\text{Y}_{10}$  and  $\text{Ca}_{65}\text{Mg}_{15}\text{Zn}_{20}$  BMGs for a range of test temperatures. (Inset Table: Temperatures normalised to  $T_g$ ).



With respect to constant strain rate deformation within the SCL region, the Mg-based BMG appears to be far more suitable, due to its higher superplasticity, implying that it may be worked at a much faster rate without brittle failure. The data also indicate that ideal flow conditions (Newtonian) were achieved in more cases and at much higher strain rates for the  $\text{Mg}_{65}\text{Cu}_{25}\text{Y}_{10}$  BMG. In a more practical sense, the larger SCL region of the  $\text{Mg}_{65}\text{Cu}_{25}\text{Y}_{10}$  BMG (**Table 5.1**) is expected to allow easier access to more favourable deformation parameters including the avoidance of the onset of crystallisation.

Constant load tensile testing of the Ca-based BMG was carried out at a heating rate of 5 °C/min for various loads to observe the variation in strain rate within the SCL region and beyond (**SECTION 4.6.9**). The strain rates generated by constant load testing were in excess of  $1 \times 10^{-1} \text{ s}^{-1}$  with respect to the original gauge length and maximum elongations of over 850% were achieved. These elongations were larger than that achieved by constant strain rate tensile testing. It is pertinent to note that this mode of deformation may be advantageous for an industrial type forming process as initial deformation at low temperatures and lower strain rates tends to overcome the initial activation energy and stress overshoot effects involved in flow initiation, thereby resulting in smooth flow characteristics at an increasing strain rate. It can also be appreciated that, by using this deformation method at a constant load just below the fracture strength of a glassy material, deformation/forming times can be kept to a minimum. For the  $\text{Ca}_{65}\text{Mg}_{15}\text{Zn}_{20}$  BMG, where crystallisation (time) tended to be the predetermining factor with respect to sample elongation, this mode of deformation may be useful for generating greater elongations before failure associated with crystallisation hardening.

### 5.3.4 Influence of Dynamic Crystallisation on Flow Behaviour

Both types of BMG studied in this thesis showed a crystallisation-related increase in flow stress during the latter stages of tensile testing which was followed by fracture. A rise in flow stress is generally attributed to the strengthening effect associated with nano-crystallisation of the supercooled liquid, where the strength/viscosity of the partially nanocrystalline solid is higher than that of an amorphous phase at elevated temperatures.<sup>[175,176,264]</sup> It is possible to explain such flow behaviour if the material is assumed to behave like a semi-crystalline composite.<sup>[264]</sup> During constant strain rate deformation in the SCL region, flow stress can be explained in terms of viscosity. As discussed in **SECTION 3.9.7**, an increase in flow stress of a crystallising BMG can be considered to be the result of interactions between crystalline agglomerates in the amorphous matrix, whereby when these agglomerates collide, stress increases due to the increase in viscosity.<sup>[264]</sup> As the number of crystallites increases with time (and strain), the

crystallised volume fraction of the sample increases, resulting in an increase in the number of agglomerate interactions in the amorphous matrix. The result is an increase in the material viscosity and, hence, an increase in flow stress.<sup>[263,264]</sup> Constant strain rate deformation studies on Zr-based BMG systems have reported the formation of nanocrystalline precipitates in the amorphous matrix but an increase in flow stress occurred only when the fraction of crystallites reached a certain value (~20% by volume).<sup>[266,307]</sup>

### 5.3.5 Dynamic Stabilisation and Deterioration of the Amorphous Structure

During tensile deformation in the SCL region, both BMGs studied in this thesis exhibited vastly different onset times for crystallisation compared with statically crystallised samples. It can be seen in **Figure 3.48** for the  $\text{Mg}_{65}\text{Cu}_{25}\text{Y}_{10}$  BMG that tensile deformation reduces the time for the onset of crystallisation (denoted as  $\Delta t_{XR}$ ) compared to static crystallisation (DSC data); this behaviour is consistent with other studies on various BMG systems.<sup>[69,183,244]</sup> It can also be seen in **Figure 3.48** that this stress increase appears to be related to deformation time and temperature whereby a higher deformation temperature yields a smaller  $\Delta t_{XR}$  rather than the amount of plastic strain.

There are two major mechanisms proposed for the reduction of crystallisation time during BMG deformation in the SCL region:<sup>[265]</sup> (i) Deformation-induced disordering, whereby the extent atomic diffusion necessary for nucleation is enhanced due to the increase in free volume caused by plastic flow;<sup>[265]</sup> and (ii) Non-equilibrium phase separation caused by plastic deformation which is argued to generate local compositional changes resulting in regions exhibiting a reduced viscosity compared that of the nominal composition. Such behaviour is expected to induce flow localisation in these low-viscosity regions causing further decomposition. Due to the thermodynamic instability of BMGs in the SCL region, phase separation into two or more slightly different supercooled liquids may occur and trigger primary crystallisation.<sup>[266-269]</sup> There is evidence of phase separation prior to crystallisation in the  $\text{Mg}_{65}\text{Cu}_{25}\text{Y}_{10}$  BMG, as shown by the APT analysis in **SECTION 3.10.5**.

On the other hand, **Figure 4.38** distinctly shows that tensile deformation of the  $\text{Ca}_{65}\text{Mg}_{15}\text{Zn}_{20}$  BMG delays the onset time (denoted by  $\Delta t_{XD}$ ) of the stress increase due to crystallisation. Here, it can be clearly seen that a higher deformation temperature reduces  $\Delta t_{XD}$ . It can also be seen that a higher deformation rate (strain rate) increases  $\Delta t_{XD}$ , i.e. there is a stabilisation of the amorphous phase, as observed in other BMG systems. This phenomenon has also been



documented by Inoue et al. for the  $\text{Zr}_{65}\text{Al}_{10}\text{Ni}_{10}\text{Cu}_{15}$ <sup>[175]</sup> and  $\text{La}_{55}\text{Al}_{20}\text{Ni}_{25}$ <sup>[176]</sup> amorphous alloys and can be seen in the data given by Kim for the  $\text{Cu}_{54}\text{Ni}_6\text{Zr}_{22}\text{Ti}_{18}$  BMG.<sup>[185]</sup> It is suggested that this time discrepancy in the onset of the stress increase indicates that deformation under appropriate conditions causes a degradation of the crystallisation reaction, namely, deformation-induced stabilisation of the supercooled liquid. The mechanism for this deformation-induced stabilisation is not clear, although it is possible that it may be due to the suppression of the of an incipient-stage reaction for crystallisation and, at higher strain rates, due to a rapid increase in flow volume generated during deformation.<sup>[20]</sup>

This difference in dynamic crystallisation characteristics for the BMGs studied in this thesis may be explained by the difference in their amorphous structures. With respect to atomic sizes, the MSL-type  $\text{Mg}_{65}\text{Cu}_{25}\text{Y}_{10}$  BMG is believed to have a 'backbone' network amorphous structure,<sup>[45,87]</sup> whereas the LS-type  $\text{Ca}_{65}\text{Mg}_{15}\text{Zn}_{20}$  BMG has an efficiently packed cluster structure.<sup>[52,87]</sup> Hence, deformation may result in break up of the network structure in MSL-type BMGs, leading to premature crystallisation. Although temperature affects the thermodynamics and kinetics of crystallisation for both types of BMGs, temperature may allow greater flexibility of the network structure, which would account for the decrease in  $\Delta t_{XR}$  with increasing temperature.

In the case of an LS-type BMG, deformation may increase the amount of free volume in the structure,<sup>[180]</sup> thereby increasing the average distance between the tightly bound atomic clusters. This is expected to make it more difficult for atomic rearrangement needed for crystallisation. This theory would support the observed increase in  $\Delta t_{XD}$  with increasing strain rate for the Ca-based BMG, since free volume is also believed to increase with increasing strain rate.<sup>[180]</sup> Naturally,  $\Delta t_{XD}$  decreases with increasing temperature due to thermodynamic and kinetic factors, where the atomic binding within these clusters becomes weaker due to atomic vibrations. Hence, the atomic spacing increases during deformation which increases the ease of atomic rearrangement and hence, crystallisation is promoted.

# CONCLUSIONS

An extensive analysis has been carried out on the production techniques, castability, stability, elevated temperature mechanical properties and microstructural evolution of lightweight bulk metallic glasses. The major findings of this work are summarised below.

## Light-Weight Bulk Metallic Glass Production

- It was found that the inverted injection die casting method provided superior results to that of conventional gravity casting into a copper mould.
- High quality lightweight bulk metallic glasses were consistently produced using the inverted injection die casting method in lengths of at least 125 mm, by choosing injection parameters that stabilise the molten metal flow front within the mould cavity. It was also determined that favourable injection parameters are closely related to the casting system geometry and melt viscosity.
- The use of higher holding pressures when casting was found to increase the sample surface quality due to a post-casting consolidation process during sample cooling.
- It was also determined that the critical casting thickness  $Z_C$ , at which a completely amorphous structure is obtained, is affected more so by interfacial heat transfer than material properties, and is related to casting/mould interface contact pressure.

## Glass Stability

- Light-weight bulk metallic glasses that indefinitely retain an amorphous structure at room temperature may be produced from the  $\text{Mg}_{65}\text{Cu}_{25}\text{Y}_{10}$  and  $\text{Ca}_{65}\text{Mg}_{15}\text{Zn}_{20}$  alloys.
- The  $\text{Mg}_{65}\text{Cu}_{25}\text{Y}_{10}$  BMG was found to have a critical cooling rate between 49 and 61 °C/s, and may be gravity cast in a copper mould to achieve a completely amorphous structure with thicknesses up to 3 mm, or readily cast using the inverted injection method successfully to obtain a thickness of 3.15 mm.
- The  $\text{Ca}_{65}\text{Mg}_{15}\text{Zn}_{20}$  BMG was found to have a critical cooling rate between 150 and 170 °C/s, and may be cast using the inverted injection method to achieve a completely amorphous structure of diameter of 8 mm.
- The  $\text{Mg}_{65}\text{Cu}_{25}\text{Y}_{10}$  BMG was found to have a glass transition temperature ( $T_g$ ) and crystallisation temperature ( $T_X$ ) that varied with heating rate.  $T_g$  varied from 138 °C for a heating rate of 2 °C/min to 148 °C for a heating rate of 20 °C/min.  $T_X$  varied from 195 °C for



a heating rate of 2 °C/min to 213 °C for a heating rate of 20 °C/min. This indicates a supercooled liquid interval of 57 to 65 °C.

- The  $\text{Ca}_{65}\text{Mg}_{15}\text{Zn}_{20}$  BMG was found to have a  $T_g$  that varied little with heating rate.  $T_g$  varied from 102 °C for a heating rate of 5 °C/min to 105 °C for a heating rate of 20 °C/min.  $T_X$  remained relatively unchanged with heating rate at 137 °C. This indicates a supercooled liquid interval of ~32°C.
- Isothermal annealing results show that the onset of crystallisation occurs much more quickly in the  $\text{Ca}_{65}\text{Mg}_{15}\text{Zn}_{20}$  BMG and follows a non-Arrhenius type relationship as opposed to the  $\text{Mg}_{65}\text{Cu}_{25}\text{Y}_{10}$  BMG.
- Crystallisation kinetics were found to vary between the  $\text{Mg}_{65}\text{Cu}_{25}\text{Y}_{10}$  and  $\text{Ca}_{65}\text{Mg}_{15}\text{Zn}_{20}$  BMGs, the former showing a steady increase in the local Avrami exponent from 1.0 to 3.0 between 5 to 85% crystallised volume fraction, whereas the Ca-based alloy displayed a rapid increase in the local Avrami exponent from 1.0 to 2.6 between 5 to 40% crystallised volume fraction, then decreased from 2.6 to 2 between 40 to 85% crystallised volume fraction.
- From observations made over time, it was discovered that the Mg-based BMG was far more corrosion resistant than the Ca-based BMG.
- Overall, the Mg-based BMG was found to be less prone to crystallisation when compared with the Ca-based BMG and hence was considered to be the more stable glass.

### Castability

- Lightweight BMGs based on magnesium and calcium, although reactive by nature, were successfully prepared and produced under a circulating argon atmosphere using inverted injection die casting and a naturally cooled copper mould.
- The  $\text{Mg}_{65}\text{Cu}_{25}\text{Y}_{10}$  BMG was found to be more time consuming to prepare due to the intermediate master alloying step for the high temperature Cu and Y constituents. However the  $\text{Ca}_{65}\text{Mg}_{15}\text{Zn}_{20}$  alloy melt was found to be more difficult to handle due to the reactivity of elemental calcium.
- The  $\text{Ca}_{65}\text{Mg}_{15}\text{Zn}_{20}$  BMG was found to be more susceptible to core crystallisation when casting was carried out at higher superheats due to a lower thermal conductivity than the  $\text{Mg}_{65}\text{Cu}_{25}\text{Y}_{10}$  BMG.
- The casting parameter range for achieving highest quality castings for the Mg- and Ca-based BMGs was almost identical and related to the casting system geometry.

## Elevated Temperature Mechanical properties

- For lightweight BMGs when deformed at an elevated temperature under constant strain rate conditions, it was found that an increase in test temperature resulted in a decrease in flow stress.
- It was also found that an increase in strain rate resulted in an increase in flow stress for these materials.
- It was established that Newtonian flow occurred at temperatures higher in the SCL region and lower strain rates.
- The  $\text{Ca}_{65}\text{Mg}_{15}\text{Zn}_{20}$  BMG was found to be far more strain rate sensitive with respect to brittle fracture, exhibiting a maximum achieved strain rate for homogeneous flow of  $10^{-3} \text{ s}^{-1}$  compared to  $10^{-1} \text{ s}^{-1}$  for the  $\text{Mg}_{65}\text{Cu}_{25}\text{Y}_{10}$  BMG.
- Elongations achieved for the  $\text{Mg}_{65}\text{Cu}_{25}\text{Y}_{10}$  BMG were in excess of 1300% compared to a maximum elongation of 598% for the  $\text{Ca}_{65}\text{Mg}_{15}\text{Zn}_{20}$  BMG under constant temperature/constant strain rate conditions, with elongation usually limited by the onset of crystallisation.
- Based on elevated temperature deformation results, the  $\text{Ca}_{65}\text{Mg}_{15}\text{Zn}_{20}$  BMG was determined to be the more fragile glass with a fragility parameter ( $D^*$ ) of 17.3 as opposed to the  $\text{Mg}_{65}\text{Cu}_{25}\text{Y}_{10}$  BMG with a  $D^*$  value of 21.6.
- Both BMGs experienced crystallisation under certain deformation conditions where it was found that the partially crystalline state exhibited a higher viscosity/flow stress than the fully amorphous phase.
- Under deformation conditions where crystallisation did occur, the Mg-based BMG was found to display a stress increase due to crystallisation prior to the times determined by static crystallisation experiments. Accelerated crystallisation in the  $\text{Mg}_{65}\text{Cu}_{25}\text{Y}_{10}$  alloy under dynamic conditions was determined to be due to dynamic segregation of the amorphous phase into Cu rich and Y rich regions, which destabilises the amorphous structure, leading to crystallisation at a time premature to that seen in static crystallisation.
- In contrast, the Ca-based BMG was found to display a delayed stress increase due to crystallisation in comparison to the times determined by static crystallisation experiments. I.e. dynamic stabilisation of the amorphous phase. The dynamic stabilisation of the amorphous phase in the  $\text{Ca}_{65}\text{Mg}_{15}\text{Zn}_{20}$  alloy was found to increase with increasing strain rate and decreasing with increasing test temperature.
- Constant load straining during heating in the SCL region was found to be a useful means of deforming/working the Ca-based BMG, as the stress overshoot behaviour was avoided and larger strains were achieved prior to crystallisation hardening.



- In general the Mg-based BMG was found to be the more promising material with respect to elevated temperature superplastic forming due to its ability to be strained at high rates to large elongations without crystallisation. This material also exhibits superior elevated temperature corrosion resistance and is a more viable alloy for use as fabricated components.

# REFERENCES

- [1] W. Buckel and R. Hilsch, *Zeitschrift fuer Physik (Journal of Physics)* Vol.138, p.109 & 136 (1954)
- [2] W. Klement, R.H. Willens and P. Duwez, *Nature*, Vol.187, p.869 (1960)
- [3] P. Duwez and R.H. Willens, *Transactions of the Metallurgical Society, AIME* Vol.227, p.362 (1963)
- [4] S. Kavesh, **Metallic Glasses** (Eds.) J.J. Gilman and J.H. Leamy, American Society for Metals (ASM), Metals Park, Ohio, USA. (1978) Ch.2, p.921
- [5] D.E. Polk and B.C. Giessen, **Metallic Glasses** (Eds.) J.J. Gilman and J.H. Leamy, American Society for Metals (ASM), Metals Park, Ohio, USA. (1978) Ch.1, p.1
- [6] D. E. Polk, B. C. Giessen and F. S. Gardner, *Materials Science and Engineering*, Vol.23, No.2-3, p.309-316 (1976)
- [7] A. Kerns, D.E. Polk, R. Ray, and B.C. Giessen, *Materials Science and Engineering* Vol.38, p.49 (1979)
- [8] F. Spaepen and D. Turnbull, Proceedings of the: 2nd International Conference on Rapidly Quenched Metals, (Eds.) N.J. Grant and B.C. Giessen, M.I.T. Press, Cambridge, MA, USA. (1976) Sec.1, p.205
- [9] A. Calka, M. Madhava, D.E. Polk, B.C. Giessen, H. Matyja and J. Vander Sande, *Scripta Metallurgica* Vol.11, No.1, p.65 (1977)
- [10] R. St.Amand and B.C. Giessen, *Scripta Metallurgica* Vol.12, p.1021 (1978)
- [11] D. Turnbull, *Transactions of the Metallurgical Society, AIME* Vol.221, p.422 (1961)
- [12] H.S. Chen and D. Turnbull, *Journal of Chemical Physics* Vol.48, p.2560 (1968)
- [13] H.S. Chen and D. Turnbull, *Acta Metallurgica* Vol.17, p.1021 (1969)
- [14] D. Turnbull and J.C. Fisher, *Journal of Chemical Physics* Vol.17, p.71 (1969)
- [15] D. Turnbull, *Contemporary Physics* Vol.10, p.437 (1969)
- [16] H.S. Chen, *Acta Metallurgica*. Vol.22, p.1505 (1974)
- [17] A.L. Drehman, A.L. Greer and D. Turnbull, *Applied Physics Letters* Vol.41, p.716 (1982)
- [18] W.H. Kui, A.L. Greer and D. Turnbull, *Applied Physics Letters* Vol.45, p.615 (1984)
- [19] A. Inoue, T. Zhang and T. Masumoto, *Materials Transactions, JIM* Vol. 30, p.965 (1989)
- [20] A. Inoue, *Acta Materialia* Vol.48, p.279 (2000)
- [21] A. Inoue, T. Nakamura, N. Nishiyama and T. Masumoto, *Materials Transactions, JIM* Vol.33, p.937 (1992)
- [22] A. Inoue, *Materials Transactions, JIM* Vol.36, p.866. (1995)
- [23] A. Inoue, T. Zhang, N. Nishiyama, K. Ohba and T. Masumoto, *Materials Transactions JIM* Vol.34, p.1234 (1993)
- [24] A. Inoue and N. Nishiyama, *Materials Science and Engineering A* Vol.401, p.226 (1997)
- [25] W.L. Johnson, *MRS Bulletin* Vol.24, No.10, p.42 (1999)
- [26] A. Peker and W.L. Johnson, *Applied Physics Letters* Vol.63, p.2342 (1993)
- [27] W.H. Wang, C. Dong and C.H. Shek, *Materials Science and Engineering R* Vol.44 p.45 (2004)
- [28] <http://www.liquidmetaltechnologies.com> Liquidmetal® Technologies 30452 Esperanza Rancho Santa Margarita, CA 92688
- [29] H.S. Chen, J.T. Krause and E. Coleman, *Journal of Non-Crystalline Solids* Vol.18, p.157 (1975)
- [30] Y. He, C.E. Price and S.J. Poon, *Philosophical Magazine Letters* Vol.70, p.371 (1994)
- [31] X.H. Lin and W.L. Johnson, *Journal of Applied Physics* Vol.78, p.6514 (1995)
- [32] H. Tan, Z.P. Lu, H.B. Yao, B. Yao, Y.P. Feng and Y. Li, *Materials Transactions, JIM* Vol.42, p.551 (2001)
- [33] M. Leonhardt, W. Lo"ser and H.G. Lindenkreuz, *Acta Materialia* Vol.47, p.2961 (1999)
- [34] Y. Zhang, D.Q. Zhao, B.C. Wei, P. Wen, M.X. Pan and W.H. Wang, *Journal of Materials Research, MRS* Vol.16, p.1675 (2001)



- [35] S.J. Poon, G.J. Shiflet, V. Ponnambalam, V.M. Keppens, R. Taylor and G. Petculescu, Proceedings of the: Materials Research Society (MRS) Symposium, (Eds.) T. Egami, A.L. Greer, A. Inoue and S. Ranganathan, Materials Research Society 506 Keystone Drive, Warrendale, PA, 15086-7573, USA (2002) Vol.754, CC1.2, p.1
- [36] K. Amiya, A. Inoue, *Materials Transactions, JIM* Vol.43, p.81 (2002)
- [37] K. Amiya, A. Inoue, *Materials Transactions, JIM* Vol.43, p.2578 (2002)
- [38] H. Choi-Yim, D. Xu and W.L. Johnson, *Applied Physics Letters* Vol.82, p.1030 (2003)
- [39] Z.F. Zhao, Z. Zhang, P. Wen, M.X. Pan, D.Q. Zhao, W.H. Wang and W.L. Wang, *Applied Physics Letters* Vol.82, p.4699 (2003)
- [40] O.N. Senkov and J.M. Scott *Scripta Materialia* Vol.50, p.449 (2004)
- [41] A. Inoue, B.L. Shen, H. Koshiba, H. Kato and A.R. Yavari, *Acta Materialia* Vol.52, p.1631 (2004)
- [42] X. Gu, G.J. Shiflet, F.Q. Guo and S.J. Poon, *Journal of Materials Research, MRS* Vol.20, No.8, p.1935 (2005)
- [43] S. Li, X.K. Xi, Y.X. Wei, Q. Luo, Y.T. Wang, M.B. Tang, B. Zhang, Z.F. Zhao, R.J. Wang, M.X. Pan, D.Q. Zhao, and W.H. Wang, *Science and Technology of Advanced Materials* Vol.6, p.823 (2005)
- [44] A.L. Greer, *Nature* Vol.366, p.303 (1993)
- [45] D.B. Miracle and O.N. Senkov, *Journal of Non-Crystalline Solids* Vol.319, p.174 (2003)
- [46] O.N. Senkov and D.B. Miracle, *Materials Research Bulletin* Vol.36, p.2183 (2001)
- [47] O.N. Senkov and D.B. Miracle, *Journal of Non-Crystalline Solids* Vol.317, p.34 (2003)
- [48] O.N. Senkov, D.B. Miracle and S. Rao. MRS Proceedings; **Supercooled Liquids, Glass Transition, and Bulk Metallic Glasses** (Eds.) T. Egami, A.L. Greer, A. Inoue, S. Ranganathan, Warrendale, PA (2003) Vol.754, p.59
- [49] H.A. Davies, **Amorphous Metallic Alloys** (Eds.) F.E. Luborsky, London: Butterworths; (1983) p.8.
- [50] T. Egami and Y. Waseda, *Journal of Non-Crystalline Solids* Vol.64, p.113 (1984)
- [51] D.B. Miracle and O.N. Senkov, *Materials Science and Engineering A* Vol.347, p.50 (2003)
- [52] D.B. Miracle, O.N. Senkov, W.S. Sanders and K.L. Kendig, *Materials Science and Engineering A* Vol.375-377 p.150 (2004)
- [53] P.H. Gaskell, **Models for the Structure of Amorphous Metals** (Eds.) H. Beck and H.-J. Guntherodt, Springer-Verlag, Berlin, Germany. (1983) p.5-49.
- [54] F.C. Frank and J.S. Kasper, *Acta Crystallographica* Vol.11, p.184 (1958)
- [55] F.C. Frank and J.S. Kasper, *Acta Crystallographica* Vol.12, p.483 (1959)
- [56] D.B. Miracle, W.S. Sanders and O.N. Senkov, *Philosophical Magazine A* Vol.83, p.2409 (2003)
- [57] J.W. Christian, **The Theory of Transformations in Metals and Alloys** 3<sup>rd</sup> edition, Pergamon, Oxford, UK. (2002) Parts I and II
- [58] M. C. Flemmings, **Solidification Processing**, McGraw-Hill, USA. (1974) p.292
- [59] J.H. Holloman and D. Turnbull, *Progress in Metal Physics* (Continued as *Progress in Materials Science*), Vol.4, p.333 (1953)
- [60] R. Busch, W. Liu and W.L. Johnson, *Journal of Applied Physics* Vol.83, p.4134 (1998)
- [61] R. Busch, Y.J. Kim, and W.L. Johnson, *Journal of Applied Physics* Vol.77, p.4039 (1995)
- [62] P.G. Debenedetti, "Metastable Liquids", (Thesis) Princeton University, Princeton, USA. (1997)
- [63] H. Tanaka, *Journal of Non-Crystalline Solids* Vol.351, p.678 (2005)
- [64] R. Busch, E. Bakke and W.L. Johnson, *Acta Materialia* Vol.46, p.4725 (1998)
- [65] E. Bakke, R. Busch and W.L. Johnson, *Applied Physics Letters* Vol.67, p.3260 (1995)
- [66] Angell, C. A. *Journal of Non-Crystalline Solids* Vol.73, p.1 (1985)
- [67] C.A. Angell, *Journal of Non-Crystalline Solids* Vol.131-133, p.13 (1991)
- [68] C.A. Angell, *Science* Vol.267, p.1924 (1995)
- [69] W. L. Johnson, J. Lu and M. D. Demetriou, *Intermetallics* Vol.10, p.1039 (2002)
- [70] D.N. Perera, *Journal of Physics: Condensed Matter* Vol.11, p.3807 (1999)
- [71] Z.P. Lu, Y. Li and C.T. Liu, *Journal of Applied Physics* Vol.93, p.286 (2003)

- [72] A. Meyer, J. Wuttke and W. Petry, *Physical Review Letters* Vol.80, p.4454 (1998)
- [73] A. Meyer, R. Busch and H. Schober, *Physical Review Letters* Vol.83, p.5027 (1999)
- [74] A. Inoue and A. Takeuchi, *Materials Transactions, JIM* Vol.43, p.1992 (2002)
- [75] A. Takeuchi and A. Inoue, *Materials Science and Engineering A* Vol.375-377 p.449 (2004)
- [76] A. Inoue, T. Negishi, H.M. Kimura, T. Zhang and A.R. Yavari, *Materials Transactions, JIM* Vol.39, p.318 (1998)
- [77] W.H. Wang, R.J. Wang, D.Q. Zhao, M.X. Pan and Y.S. Yao, *Physical Review B* Vol.62, p.11292 (2000)
- [78] W.H. Wang, Q. Wei, S. Friedrich, M.P. Macht, N. Wanderka and H. Wollenberger, *Applied Physics Letters* Vol.71, p.1053 (1997)
- [79] W.H. Wang, Q. Wei and S. Friedrich, *Physical Review B* Vol.57, p.8211 (1998)
- [80] A. Inoue, *Bulk Amorphous Alloys-Preparation and Fundamental Characteristics*, Trans Tech Publications inc., Zurich, Switzerland. (1998) Vol.4, p.2
- [81] J. Eckert, N. Mattern, M. Zinkevitch and M. Seidel, *Materials Transactions, JIM* Vol.39 p.623 (1998)
- [82] W.H. Wang, E. Wu, R.J. Wang, S.J. Kennedy and A.J. Studer, *Physical Review B* Vol.66, p.104205 (2002)
- [83] J. Saida, M. Matsushita and A. Inoue, *Applied Physics Letters* Vol.79, p.412 (2001)
- [84] T.A. Waniuk, J. Schroers and W.L. Johnson, *Physical Review B* Vol.67, p.184203 (2003)
- [85] R. Wang, *Nature* Vol.278, p.700 (1979)
- [86] A. Inoue, T. Negishi, H.M. Kimura, T. Zhang and A.R. Yavari, *Materials Transactions, JIM* Vol.39, p.318 (1998)
- [87] S. J. Poon, G. J. Shiflet, F.Q. Guo and V. Ponnambalam *Journal of Non-Crystalline Solids* Vol.317, p.1 (2003)
- [88] A. Gebert, J. Ekert and L. Schultz, *Acta Materialia* Vol.46, p.5475 (1998)
- [89] A. Inoue, *Nanostructured Materials* Vol.6, p.53 (1995)
- [90] A. Inoue, T. Zhang and Y.H. Kim, *Materials Transactions, JIM* Vol.38, p.749 (1997)
- [91] A. Inoue, C. Fan, and A. Takeuchi, *Advanced Materials*, Vol.4, p.373 (1998)
- [92] C. Fan and A. Inoue, *Materials Transactions, JIM* Vol.38, p.1040 (1997)
- [93] C. Fan and A. Inoue, *Materials Transactions JIM* Vol.40, p.42 (1999)
- [94] J. J. Kim, Y. Choi, S. Suresh and A.S. Argon, *Science* Vol.295, p.654 (2002)
- [95] J. Schroers, W.L. Johnson and R. Busch, *Applied Physics Letters* Vol.76, p.2343 (2000)
- [96] J. Schroers and W.L. Johnson, *Journal of Applied Physics* Vol.88, p.44 (2000)
- [97] J. Schroers, A. Masuhr, W.L. Johnson and R. Busch, *Physical Review B* Vol.60, p.11855 (1999)
- [98] J. Schroers, R. Busch, A. Masuhr and W.L. Johnson, *Applied Physics Letters* Vol.74, p.2806 (1999)
- [99] J. Schroers, Y. Wu, R. Busch and W.L. Johnson, *Acta Materialia* Vol.49, p.2773 (2001)
- [100] J. Zhang, K.Q. Qiu, A.M. Wang, H.F. Zhang, M.X. Quan and Z.Q. Hu, *Journal of Materials Research* Vol.17, p.2935 (2002)
- [101] M. Yousuf and K.G. Rajan, *Journal of Materials Science Letters* Vol.3, p.149 (1984)
- [102] T.A. Waniuk, J. Schroers and W.L. Johnson, *Applied Physics Letters* Vol.78, p.1213 (2001)
- [103] W.H. Wang, *Journal of Metastable Nanocrystalline Materials* Vol.15/16, p.73 (2003)
- [104] W.H. Wang, D.W. He, D.Q. Zhao, Y.S. Yao and M. He, *Applied Physics Letters* Vol.75, p.2770 (1999)
- [105] W.H. Wang, Y.X. Zhuang, M.X. Pan and Y.S. Yao, *Journal of Applied Physics* Vol.88, p.3914 (2000)
- [106] Z. Zhang, L. Xia, R.J. Wang, B.C. Wei, M.X. Pan and W.H. Wang, *Applied Physics Letters* Vol.81, p.4371 (2002)
- [107] Q. Chen, L. Liu and K.C. Chan, *Journal of Alloys and Compounds* Vol.419, No.1-2, p.71 (2006)
- [108] L. Liu, Z.F. Wu and J. Zhang, *Journal of Alloys and Compounds* Vol.339, p.90 (2002)
- [109] Z.J. Yan, S.R. He, J.R. Li and Y.H. Zhou, *Journal of Alloys and Compounds* Vol.368, p.175 (2004)
- [110] M. Avrami, *Journal of Chemical Physics* Vol.7, p.1103 (1939)



- [111] M. Avrami *Journal of Chemical Physics* Vol.8, p.212 (1940)
- [112] M. Avrami *Journal of Chemical Physics* Vol.9, p.177 (1941)
- [113] W.A. Johnson and R.F. Mehl, *Transactions of the American Institute of Mining Metallurgy and Petroleum Engineering, (AIME)* Vol.135, p.416(1939)
- [114] A. Calka and A.P. Radinski, *Journal of Materials Research* Vol.3, p.59 (1985)
- [115] S. Ranganathan and M.V. Heimendahl, *Journal of Materials Science* Vol.16, p.2401 (1981)
- [116] H.E. Kissinger, *Analytical Chemistry* Vol.29, p.1702 (1957)
- [117] T. Ozawa, *Polymer* Vol.12, p.150 (1971)
- [118] D.R. Uhlmann and H. Yinnon, *The Formation of Glasses: Glass Science and Technology* (Eds.) D. R. Uhlman and N. J. Kreidl, Academic Press, New York. (1983) Vol.1, p.1
- [119] Y. Li, S.C. Ng'p, C.K. Ong, H.H. Hng' and T.T. Gob *Scripta Materialia*. Vol.36, No.1, p.783 (1991)
- [120] Z.P. Lu and C.T. Liu *Acta Materialia* Vol.50 p.3501 (2002)
- [121] G.J. Fan, H. Choo and P.K. Liaw, *Journal of Non-Crystalline Solids* Vol.353, p.102 (2007)
- [122] O.N. Senkov and J.M. Scott *Materials Letters* Vol.58, p.1375 (2004)
- [123] [http://mmp.iphy.ac.cn/EX4/results\\_Eng.htm](http://mmp.iphy.ac.cn/EX4/results_Eng.htm) **Amorphous Materials and Physics Group**, Institute of Physics (IOP), Chinese Academy of Sciences (CAS), Beijing, China.
- [124] A. Inoue and T. Zhang, *Metals*, No.3, p.47 (1994)
- [125] A. Inoue, Y. Yokoyama, Y. Shinohara and T. Masumoto, *Materials Transactions, JIM*, Vol.35, p.923 (1994)
- [126] N.H. Pryds, M. Eldrup, M. Ohnuma, A.S. Pedersen, J. Hattel and S. Linderroth, *Materials Transactions, JIM* Vol.41, No.11, p.1435 (2000)
- [127] E.S. Park, J.Y. Lee, and D.H. Kim, *Journal of Materials Research, MRS* Vol.20, No.9, p.2379 (2005)
- [128] N.H. Pryds, *Materials Science and Engineering A* Vol. 375-377 p.186 (2004)
- [129] A. Inoue, T. Zhang, N. Nishiyama, K. Ohba and T. Masumoto, *Materials Transactions, JIM*, Vol.34, p.1234 (1993)
- [130] A. Inoue, **Bulk Amorphous Alloys-Preparation and Fundamental Characteristics**, Trans Tech Publications inc., Zurich, Switzerland. (1998) Vol.4, p.94
- [131] K. Amiya and A. Inoue, *Materials Transactions, JIM* Vol.42, p.543 (2001)
- [132] X.Z. Wang, Y. Li, J. Ding, L. Si and H.Z. Kong, *Journal of Alloys and Compounds* Vol.290, p.209 (1999)
- [133] A.T.W. Kempen, F. Sommer and E.J. Mittemeijer, *Acta Materialia* Vol.50, p.1319 (2002)
- [134] Q. Li, *Materials Letters*, Vol.60, No.25-26, p.3113 (2006)
- [135] K.Q. Qiu and Y.L. Ren, *Materials Letters* Vol.60, p.1851 (2006)
- [136] A. Inoue and T. Zhang, *Materials Transactions, JIM*, Vol.36, p.1184 (1995)
- [137] D. Xing, J. Sun, J. Shen, G. Wang and M. Yan, *Journal of Alloys and Compounds* Vol.375, p.239 (2004)
- [138] S. Wu, B. Shen and A. Inoue *Intermetallics* Vol.12, p.1261 (2004)
- [139] J. G. Lee, H. Lee, Y.S. Oh, S. Lee and N. J. Kim, *Intermetallics* Vol.14, p.987 (2006)
- [140] K.A. Lee, Y.C. Kim, J.H. Kim, C.S. Lee, J. Namkung and M.C. Kim, *Materials Science and Engineering A* Vol.449-451, p.181 (2007)
- [141] Y.S. Oh, J.G. Lee and N.J. Kim, Proceedings of the: 4<sup>th</sup> International Symposium on Bulk Metallic Glasses. (Eds.) P.K. Liaw and R.A. Buchanan, TMS Publications CD-ROM, (2006) p.119
- [142] E.S. Park, H.K. Lim, W.T. Kim and D.H. Kim, *Journal of Non-Crystalline Solids* Vol.15, p.298 (2002)
- [143] S.S. Park, D.H. Kang, G.T. Bae and N.J. Kim, *Materials Science Forum* Vol.431, p.488 (2005)
- [144] S.S. Park, J.G. Lee, Y.S. Park and N.J. Kim, *Materials Science Forum* Vol.599, p.419 (2003)
- [145] S.S. Park, Y.S. Park and N.J. Kim, *Metals and Materials International* Vol.6, p.551 (2002)
- [146] S.S. Park, Y.M. Kim, D.H. Kang and N.J. Kim, *Materials Science Forum* Vol.457, p.475 (2005)
- [147] Y.S. Park, S.B. Lee and N.J. Kim. *Materials Transactions, JIM* Vol.44, p.2617 (2003)
- [148] M.F. Ashby and A.L. Greer, *Scripta Materialia* Vol.54, p.321 (2006)

- [149] M.F. Ashby, **Materials Selection in Mechanical Design**, 3<sup>rd</sup> ed. Oxford: Butterworth-Heinemann; (2005)
- [150] C.A. Schuh, T.G. Nieh and Y. Kawamura, *Journal of Materials Research* Vol.17, p.1651 (2002)
- [151] C.A. Schuh and T.G. Nieh, *Acta Materialia* Vol.51, p.87 (2003)
- [152] H. Kakiuchi, A. Inoue, M. Onuki, Y. Takano, and T. Yamaguchi, *Materials Transactions, JIM*, Vol.42, No.4, p.678 (2001)
- [153] A. Inoue, **Bulk Amorphous Alloys - Practical Characteristics and Applications**, Trans Tech Publications inc., Zurich, Switzerland, (1999) Vol.6, p.1
- [154] A. Inoue, T. Zhang and A. Takeuchi, *Applied Physics Letters* Vol.71, p.464 (1997)
- [155] W.H. Wang, R.J. Wang, F.Y. Li, D.Q. Zhao and M.X. Pan, *Applied Physics Letters* Vol.74, p.1803 (1999)
- [156] Y. Yokoyama, K. Fukaura and A. Inoue, *Materials Science and Engineering A* Vol.375-377 p.427 (2004)
- [157] E.S. Park and D.H. Kim, *Acta Materialia* Vol.54, p.2597 (2006)
- [158] T. Zhang and A. Inoue, *Materials Transactions, JIM* Vol.39, p.857 (1998)
- [159] K.M. Flores and R.H. Dauskardt, *Acta Materialia* Vol.49, p.2527 (2001)
- [160] C.J. Gilbert, R.O. Ritchie and W.L. Johnson, *Applied Physics Letters* Vol.71, p.464 (1997)
- [161] D.R. Askeland, **Science and Engineering of Materials**, PWS Publishing, Boston (1994) p.152
- [162] C.J. Gilbert, V. Schroeder and R.O. Ritchie, *Metallurgical and Materials Transactions* Vol.30A, p.1739. (1999)
- [163] Y. Yokoyama, K. Yamano, H. Fukaura, H. Sunada and A. Inoue, *Materials Transactions JIM* Vol.40, p.1382 (1999)
- [164] K.M. Flores and R.H. Dauskardt, *Scripta Materialia* Vol.41, p.937 (1999)
- [165] K.M. Flores and R.H. Dauskardt, *Journal of Materials Research* Vol.14, p.638 (1999)
- [166] R. Raghavan, P. Murali and U. Ramamurty, *Intermetallics* Vol.14, p.1051 (2006)
- [167] Y. Yokoyama, N. Nishiyama, K. Fukaura, H. Sunada and A. Inoue, *Materials Transactions, JIM* Vol.40, p.696 (1999)
- [168] T. Ogura, T. Masumoto and K. Fukushima, *Scripta Metallurgica* Vol.9, p.979 (1975)
- [169] H. Izumi, H. Sunada and Y. Hayashi, *Journal of the Japanese Institute of Metals*, Vol.48, p.371 (1984)
- [170] Y. Saotome, T. Zhang and A. Inoue, Proceedings of: Materials Research Society Symposium, Materials Research Society, (1999) Vol.554, p.385
- [171] T.G. Nieh, J. Wadsworth, *Scripta Materialia* Vol.54, No.3, p.387(2006)
- [172] J. Schroers, Q. Pham, A. Peker, N. Paton and R.V. Curtis, *Scripta Materialia* Vol.57, p.341 (2007)
- [173] F.A. McClintock and S.A. Argon, **Mechanical Behavior of Materials**: Addison-Wesley; (1966) p.273
- [174] Y. Kawamura, T. Nakamura, A. Inoue, T. Masumoto, *Materials Transactions, JIM* Vol.40, p.794 (1999)
- [175] Y. Kawamura, H. Kato, A. Inoue and T. Masumoto, *International Journal of Powder Metallurgy* Vol.33, No.2, p.50 (1997)
- [176] A. Inoue, Y. Kawamura and Y. Saotome, *Materials Science Forum* Vol.233-234, p.147 (1997)
- [177] A.R. Bhatti and B. Cantor, *Materials Science and Engineering* Vol.97, p.479 (1988)
- [178] A. Inoue and Y. Saotome, *Metals* Vol.3, p.51 (1993)
- [179] T. Zhang, A.P. Tsai, A. Inoue and T. Masumoto, *Boundary* Vol.7, No.9, p.39. (1991)
- [180] F. Spaepen, *Acta Metallurgica* Vol.25, p.407 (1977)
- [181] Y.V.R.K. Prasad, H.L. Gegel, S.M. Doraivelu, J.C. Malas, J.T. Morgan, L.A. Lark and D.R. Barker, *Metallurgical Transactions* Vol.15A, p.1883 (1984)
- [182] K.S. Lee, H.J. Jun and Y.W. Chang, *Materials Science and Engineering A* Vol.449-451 p.941 (2007)
- [183] M. Bletry, P. Guyot, Y. Brechet, J.J. Blandin and J.L. Soubeyroux, *Materials Science and Engineering A* Vol.387-389, p.1005 (2004)



- 
- [184] T.G. Nieh, T. Mukai, C.T. Liu and J. Wadsworth, *Scripta Materialia* Vol.40, p.1021 (1999)
- [185] W.J. Kim, *Intermetallics* Vol.15, p.282 (2007)
- [186] M.H. Cohen and D. Turnbull, *Journal of Chemical Physics* Vol.31, p.1164 (1959)
- [187] M.H. Cohen and D. Turnbull, *Journal of Chemical Physics* Vol.34, p.120 (1961)
- [188] M. Bletry, P. Guyot, J.J. Blandin and J.L. Soubeyroux, *Acta Materialia* Vol.54, p.1257 (2006)
- [189] A. Gebert, U. Wolff, A. John, and J. Eckert, *Scripta Materialia* Vol.43, p.279 (2000)
- [190] K. Hashimoto, K. Osada, T. Masumoto and S. Shimodaira, *Corrosion Science* Vol.16, p.71 (1976)
- [191] K. Hashimoto, *Passivity of Metals and Semiconductors* (Eds.) M. Froment, Elsevier Science Publishers, Amsterdam, The Netherlands. (1984) p.235
- [192] S. Virtanen and H. Bohni, *Corrosion Science* Vol.31, p.333 (1990)
- [193] X.J. Gu, S. Joseph Poon, G.J. Shiflet, *Journal of Materials Research* Vol.22, No.2, p.344
- [194] A. Inoue, K. Ohtera and T. Masumoto, *School Report: Materials Research Institute, Tohoku University* Vol.A35, p.115 (1990)
- [195] A. Inoue and T. Masumoto, Proceedings of the: 3rd International Conference on Aluminum Alloys, (Eds.) L. Arnberg, SINTEF, Trondheim, Norway, (1992) Vol.3, p.45.
- [196] K. Hashimoto, P.Y. Park, J.H. Kim, H. Yoshioka, H. Mitsui, E. Akiyama, H. Habazaki, A. Kawashima, K. Asami, Z. Grzesik and S. Mrowec, *Materials Science and Engineering A* Vol.198, p.1 (1995)
- [197] A. Kato, H. Horikiri, A. Inoue and T. Masumoto, *Materials Science and Engineering A* Vol.179-180, p.114 (1993)
- [198] Aroule P, *Magnesium Demand and Supply*, IMA-55, A Global Vision for Magnesium, International Magnesium Association, Coronado, CA, USA. (1998) p.36
- [199] X. Hui, W. Dong, G.L. Chen and K.F. Yao, *Acta Materialia* Vol.55, p.907 (2007)
- [200] P. Predel and K. Hulse, *Journal of Less Common Metals* Vol.63, No.1, p.45 (1979)
- [201] F. Sommer, G. Bucher and B. Predel, *Journal de Physique* Vol.C8, No.8, p.563 (1980)
- [202] A. Inoue, K. Ohtera, K. Kita and T. Masumoto, *Japanese Journal of Applied Physics* Vol.27, p.2248 (1988)
- [203] A. Inoue, M. Kohinata and A. Tasi, *Materials Transactions, JIM* Vol.30, p.378 (1989)
- [204] K.S. Gyoo, A. Inoue and T. Masumoto, *Materials Transactions, JIM* Vol.31, No.11, p.929 (1990)
- [205] A. Inoue, M. Kohinata A.P.Tsai and T. Masumoto, *Materials Transactions, JIM* Vol.30, p.378 (1989)
- [206] Z.P. Lu, Y. Li and S.C. Ng, *Journal of Non-crystalline Solids* Vol.270, p.103 (2000)
- [207] M. Ohnuma, N.H. Pryds, S. Linderroth, M. Eldrup, A.S. Pedersen and J.S. Pedersen, *Scripta Materialia* Vol.41, p.889 (1999)
- [208] X.K. Xi, D.Q. Zhao, M.X. Pan and W.H. Wang, *Journal of Non-Crystalline Solids* Vol.344, p.189 (2004)
- [209] X.K. Xi, R.J. Wang, D.Q. Zhao, M.X. Pan and W.H. Wang, *Journal of Non-crystalline Solids* Vol.344, p.105 (2004)
- [210] H. Men, Z.Q. Hu and J. Xu, *Scripta Materialia* Vol.46, p.699 (2002)
- [211] E.S. Park, H.G. Kang, W.T. Kim and D.H. Kim, *Journal of Non-crystalline Solids* Vol.279, p.154 (2001)
- [212] H. Ma, L.L. Shi, J. Xu, Y. Li and E. Ma, *Applied Physics Letters* Vol.87, p.181915 (2005)
- [213] H. Ma, E. Ma and J. Xu, *Journal of Materials Research* Vol.18, p.2288 (2003)
- [214] A. Inoue and T. Masumoto, *Materials Science and Engineering A* Vol.173, p.1 (1993)
- [215] K. Amiya and A. Inoue *Materials Transactions, JIM* Vol.41, No.11, p.1460 (2000)
- [216] E.S. Park and D.H. Kim *Journal of Materials Research, MRS* Vol.20, No.6, p.1465 (2005)
- [217] Y.T. Cheng, T.H. Hung, J.C. Huang, J.S.C. Jang, C.Y.A. Tsao and P.Y. Lee, *Intermetallics* Vol.14, p.866 (2006)
- [218] G. Yuana and A. Inoue, *Journal of Alloys and Compounds* Vol.387, p.134 (2005)
- [219] G. Yuan, K. Amiya and A. Inoue, *Journal of Non-Crystalline Solids* Vol.351, p.729 (2005)
-

- [220] Y. Liu, H.F. Zhang, Z.Q. Hua and H. Wang, *Journal of Alloys and Compounds* Vol.397, p.202 (2005)
- [221] Q. Zheng, H. Ma, E. Mab and J. Xua, *Scripta Materialia* Vol.55, p.541 (2006)
- [222] Y. Li, H.Y. Liu and H. Jones, *Journal of Materials Science* Vol.31, p.1957 (1996)
- [223] D.J. Chakrabarti and D.E. Laughlin *Binary Alloy Phase Diagrams* (Eds.) T.B. Massalski, J.L. Murray, L.H. Bennett and H. Baker, American Society for Metals, Metals Park, Ohio, USA. (1986) p.1505
- [224] A. Inoue, Y. Shinohara, Y. Yokoyama and T. Masumoto, *Materials Transactions, JIM*, Vol.36, p.1276 (1995)
- [225] Y.S. Oh, Conference Presentation; "Solidification Behaviour of Fe-Base Amorphous Alloys during Twin-Roll strip Casting" TMS 2006 135<sup>th</sup> Annual Meeting & Exhibition March 12-16, 2006, San Antonio, Texas, USA (SESSION: Bulk Metallic Glasses: Physical Properties)
- [226] G.W. Scherer, *Glass and Amorphous Materials* (Eds.) R.W. Cahn, P. Haasen, D.R. Uhlmann and N.J. Kreidl, VCH Publications, New York, USA. (1991) Vol.9, Ch.3
- [227] E.S. Park and D.H. Kim, *Journal of Materials Research, MRS* Vol.19, p.685 (2004)
- [228] M.C. Flemings, *Solidification Processing*, McGraw-Hill, USA. (1974) p.12-13
- [229] G. H. Gieger and D.R. Poirier, *Transport Phenomena in Metallurgy*, Adison-Wesley USA. (1980) p.344-347
- [230] G. H. Gieger and D.R. Poirier, *Transport Phenomena in Metallurgy*, Adison-Wesley USA. (1980) p.335
- [231] G. H. Gieger and D.R. Poirier, *Transport Phenomena in Metallurgy*, Adison-Wesley USA. (1980) p.291
- [232] A. Inoue, A. Kato, T. Zhang, S.G. Kim and T. Masumoto, *Materials Transactions, JIM*, Vol.32, p.609 (1991)
- [233] N. El-Mahallaw, M.A. Taha, E. Pokora and F. Klein, *Journal of Materials Processing Technology* Vol.73, p.125 (1998)
- [234] B.H. Hu, K.K. Tong, X.P. Niu and I. Pinwill, *Journal of Materials Processing Technology* Vol.105, p.128 (2000)
- [235] M. Regev, E. Aghion and A. Rosen, *Materials Science and Engineering A* Vol.234, p.123 (1997)
- [236] S. Mahaney and C.W. Kim, *Die Casting Engineer* 96-034 (1996)
- [237] M.R. Barone, D.A. Caulk, *International Journal of Engineering Science* Vol.38, p.1279 (2000)
- [238] W.R. McKenzie, "Characterisation of the Processing of Silicon-on-Sapphire Devices for Integrated Circuit Applications" (Thesis) University of New South Wales, Sydney, Australia (2007)
- [239] D.R. Gaskell, *An Introduction to Transport Phenomena in Materials Engineering*, Macmillan, New York, USA. (1992) p.186
- [240] D.R. Gaskell, *An Introduction to Transport Phenomena in Materials Engineering*, Macmillan, New York, USA. (1992) p.31
- [241] S.E. Booth and D.F. Allsop, Transactions of the 12th SDCE International Die Casting Congress and Exposition, MN, USA, (1983), p.1.
- [242] M.C. Flemings, *Solidification Processing*, McGraw-Hill, USA. (1974) p.217-218.
- [243] D.H. Wu and M.S. Chang, *Materials Science and Engineering A* Vol.379, p.366 (2004)
- [244] G. Wang, J. Shen, J.F. Sun, Y.J. Huang, J. Zou, Z.P. Lu, Z.H. Stachurski and B.D. Zhou, *Journal of Non-Crystalline Solids* Vol.351, p.209 (2005)
- [245] J.A. Wert, N. Pryds and E. Zhang, Proceedings of the: 22nd Riso International Symposium on *Materials Science: Science of Metastable and Nanocrystalline Alloys-Structure, Properties and Modelling* (Eds.) A.R. Dinesen, M. E., D. Juul Jensen, S. Linderroth, T.B. Pedersen, N.H. Pryds, A.S. Pedersen, J.A. Wert, Riso National Laboratory, Roskilde, Denmark. (2001) p.423-428.
- [246] U. Wolff, N. Pryds, E. Johnson and J.A. Wert, *Acta Materialia* Vol.52, p.1989 (2004)
- [247] Y. Kawamura, T. Shibata and A. Inoue, *Materials Transactions, JIM* Vol.40, p.335 (1990)



- [248] W.L. Johnson, Conference Presentation; "Plastic yielding, Flow and Configurational Entropy in Metallic Glasses" TMS 2006 135<sup>th</sup> Annual Meeting & Exhibition March 12-16, 2006, San Antonio, Texas, USA (SESSION: Bulk Metallic Glasses: Elastic, Plastic Behavior, and Computation)
- [249] O.N. Senkov, TMS 2006 135<sup>th</sup> Annual Meeting & Exhibition March 12-16, 2006, San Antonio, Texas, USA, *Personal Communication* (2006)
- [250] M. Kusy, U. Kühn, A. Concustell, A. Gebert, J. Das, J. Eckert, L. Schultz and M.D. Baro, *Intermetallics* Vol.14, p.982 (2006)
- [251] R. Busch, *Journal of Metals* Vol.52, p.39 (2000)
- [252] J.F. Löffler, *Intermetallics* Vol.11, P.529 (2003)
- [253] C. Donati, J.F. Douglas, W. Kob, S.J. Plimpton, P.H. Poole and S.C. Glotzer, *Physical Review Letters* Vol.80, p.2338 (1998)
- [254] B.T. Schröder and J.C. Dyre, *Journal of Non-Crystalline Solids* Vol.235-237, p.331 (1988)
- [255] D. Deng, F. Zheng, Y. Xu, G. Qi and A.S. Argon, *Acta Metallurgica et Materialia* Vol.41, p.1089 (1993)
- [256] M. Heilmaier, J. Eckert, *Journal of Advanced Engineering Materials* Vol.7, p.835 (2005)
- [257] P.A. Duine, J. Sietsma, A. Beukel, Van Den, *Acta Metall et Materialia*. Vol.40, p.268743 (1992)
- [258] B. Maxwell and M. Nguyen, *Polymer Engineering Science* Vol.19, p.1140 (1979)
- [259] P. de Hey, J. Sietsma, A. Van den Beukel, *Acta Materialia* Vol.46, p.5873 (1998)
- [260] D.H. Bae, J.M. Park, J.H. Na, D.H. Kim, Y.C. Kim and J.K. Lee, *Journal of Materials Research, MRS* Vol.19, p.937 (2004)
- [261] J.P. Chu, C.L. Chiang, T.G. Nieh and Y. Kawamura, *Intermetallics* Vol.10, p.1191 (2002)
- [262] S.L. Hwang and I.W. Chen, *Journal of the American Ceramic Society* Vol.77, No.10, p.2575 (1994)
- [263] T.G. Nieh and J. Wadsworth, *Scripta Materialia*, Vol.54, p.387 (2006)
- [264] W.J. Kim, D.S. Ma and H.G. Jeong, *Scripta Materialia*, Vol.49, p.1067 (2003)
- [265] M.D. Demetriou and W.L. Johnson, *Acta Materialia*, Vol.52, p.3403 (2004)
- [266] A.V. Sergueeva, N. Mara and A.K. Mukherjee, *Journal of Non-Crystalline Solids*, Vol.317, p.169 (2003)
- [267] T.A. Waniuk, R. Busch, A. Masuhr and W.L. Johnson, *Acta Materialia* Vol.46, p.5229 (1998)
- [268] M.K. Miller, T.D. Shen and R.B. Schwarz, *Journal of Non-Crystalline Solids* Vol.317, p.10 (2003)
- [269] J.M. Pelletier and B. Van de Moortele, *Journal of Non-Crystalline Solids* Vol.325, p.133 (2003)
- [270] S. Linderoth, N. Pryds, M. Eldred, A.S. Pedersen, M. Inhuman, T.-J. Zhou, L. Gerward, J.Z. Jiang and C. Lathe, Proceedings of the: Supercooled Liquid, Bulk Glassy and Nanocrystalline States of Alloys Symposium (MRS), (Eds.) A. Inoue Materials Research Society 506 Keystone Drive, Warrendale, PA, 15086-7573, USA. (2001), Vol.644, L4.1 p.1
- [271] W.R. McKenzie, P.R. Munroe, D. McGrouther, D. Saxey D and E. Marquis, "FIB Fabrication of Site Specific Atom Probe Tips" *Microscopy Research and Techniques* (Submitted) (2007),
- [272] D-C. Kawauchi "Composite calcium clads for treating molten iron" U.S. Patent No. **4698095**, May 29, 1986
- [273] S. Ainsworth, Australian Refined Alloys Pty. Ltd. *Personal Communication* (2006)
- [274] F. Q. Guo, S. J. Poon and G. J. Shiflet, *Applied Physics Letters* Vol.84, p.37 (2004)
- [275] O.N. Senkov and J.M. Scott, *Journal of Non-Crystalline Solids* Vol.351, p.3087 (2005)
- [276] E.S. Park and D.H. Kim, *Applied Physics Letters* Vol.86, p.201912 (2005)
- [277] O.N. Senkov, J.M. Scott and D.B. Miracle *Journal of Alloys and Compounds* Vol.424, No.1-2, p.394 (2006)
- [278] O.N. Senkov, D.B. Miracle and J.M. Scott, *Intermetallics* Vol.14, p.1055 (2006)
- [279] V.P. Itkin and C.B. Alcock *Binary Alloy Phase Diagrams* (Eds.) T.B. Massalski, J.L. Murray, L.H. Bennett and H. Baker, American Society for Metals, Metals Park, Ohio, USA. (1986) p.968-969
- [280] A.A. Nayeab-Hasemi and J.B. Clarke *Binary Alloy Phase Diagrams* (Eds.) T.B. Massalski, J.L. Murray, L.H. Bennett and H. Baker, American Society for Metals, Metals Park, Ohio, USA. (1986) p.925-927

- [281] J.B. Clarke, L. Zabdyr and Z. Moser **Binary Alloy Phase Diagrams** (Eds.) T.B. Massalski, J.L. Murray, L.H. Bennett and H. Baker, American Society for Metals, Metals Park, Ohio, USA. (1986) p.2571-2572
- [282] W.Y. Liu, H.F. Zhang, A.M. Wang, H. Li and Z.Q. Hu, **Materials Science & Engineering A** Vol.459, No.1-2, p.196 (2007)
- [283] S.V. Madge and A.L. Greer, **Materials Science and Engineering A**, Vol.375-377, p.759 (2004)
- [284] D.B. Miracle, TMS 2006 135<sup>th</sup> Annual Meeting & Exhibition March 12-16, 2006, San Antonio, Texas, USA, *Personal Communication* (2006)
- [285] H. Choi-Yim, R. Busch and W.L. Johnson, **Journal of Applied Physics** Vol.83, p.7993 (1998)
- [286] C.T. Liu and Z.P. Lu, **Intermetallics** Vol.13, p.415 (2005)
- [287] L. Brewer, "molybdenum: Physico-Chemical Properties of its compounds and alloys", (Eds.) O. Kubaschewski, *Atomic Energy Review Special Issue No 7*, International Atomic Energy Agency, Vienna (1980).
- [288] A.A. Nayeb-Hashemi and J.B. Clarke, **Binary Alloy Phase Diagrams** (Eds.) T.B. Massalski, J.L. Murray, L.H. Bennett and H. Baker, American Society for Metals, Metals Park, Ohio, USA. (1986) p.2520-2522
- [289] A. E. Martin, J.B. Knighton, H.M. Feder, **Journal of Chemical Engineering Data** Vol.6, p.598 (1961).
- [290] D.R. Gaskell, **An Introduction to Transport Phenomena in Materials Engineering**, Macmillan, New York, USA. (1992) p.306
- [291] D.R. Gaskell, **An Introduction to Transport Phenomena in Materials Engineering**, Macmillan, New York, USA. (1992) p.15
- [292] D.R. Gaskell, **An Introduction to Transport Phenomena in Materials Engineering**, Macmillan, New York, USA. (1992) p.219-220
- [293] G. H. Gieger, D.R. Poirier, **Transport Phenomena in Metallurgy**, Adison-Wesley USA. (1980) p.134-135
- [294] D.R. Gaskell, **An Introduction to Transport Phenomena in Materials Engineering**, Macmillan, New York, USA. (1992) p.191
- [295] G. H. Gieger, D.R. Poirier, **Transport Phenomena in Metallurgy**, Adison-Wesley USA, (1980) p.119
- [296] D. R. Uhlmann, **Journal of Non-Crystalline Solids** Vol.7, p.337 (1972)
- [297] J. Li, T. Malis and S. Dionne, **Materials Characterization** Vol.57, p.64 (2006)
- [298] A.K. Varshneya, **Fundamentals of Inorganic Glasses** (1994) p.27-32
- [299] W. Baumgart, A.C. Durham and G.C. Amstutz, (Eds.) **Process Mineralogy of Ceramic Materials** (1984) p. 28-29
- [300] G-X. Wang and E.F. Matthys, Proceedings of the: International Symposium on Melt Spinning, Strip Casting and Slab Casting, (Eds.) E.F. Matthys and W.G. Truckner, TMS, USA (1996) 205-236.
- [301] L.C. Zhang, J. Xu and J. Eckert, **Journal of Applied Physics** Vol.100, p.1 (2006)
- [302] N. Prasad and K.B.R Varma, **Journal of the American Ceramic Society**, Vol.88, p.357 (2005)
- [303] M.L. Morrison, R.A. Buchanan, O.N. Senkov, D.B Miracle and P.K. Liaw, **Metallurgical and Materials Transactions A** Vol.37A, p.1239 (2006)
- [304] G. Baril and N. Pebere, **Corrosion Science** Vol.43, p.471 (2001)
- [305] H.B. Yao, Y. Li and A.T.S. Wee, **Electrochimica Acta** Vol.48, p.2641 (2003)
- [306] M.F. Ashby and D.R.H. Jones **Engineering Materials 1**, 2<sup>nd</sup> Ed. Butterworth-Heinemann, Oxford, UK. (1998) p.93-94
- [307] J. Eckert, U. Kuhn, N. Mattern, A. Reger-Leonhard, A. and M. Heilmaier, **Scripta Materialia** Vol.44, p.1587 (2001)
- [308] J.A. Augis and J.A. Bennett, **Journal of Thermal Analysis** Vol.13, p.283 (1978)



## APPENDIX A - CALCULATION OF COOLING RATE

The cooling rate for the interval between the liquidus temperature,  $T_l$  and the glass transition temperature,  $T_g$  is found using the relation:

$$\frac{dT}{dt} = \frac{T_l - T_g}{\Delta t}$$

where  $\Delta t$  is the time interval between  $T_l$  and  $T_g$ . This time interval was determined using cooling curve data. An example using the data gathered for the  $Mg_{65}Cu_{25}Y_{10}$  wedge casting can be seen below in **Figure A**, with the results shown in **Table A**. The same method was used for the analysis of the  $Ca_{65}Mg_{15}Zn_{20}$  segmented cylinder casting.

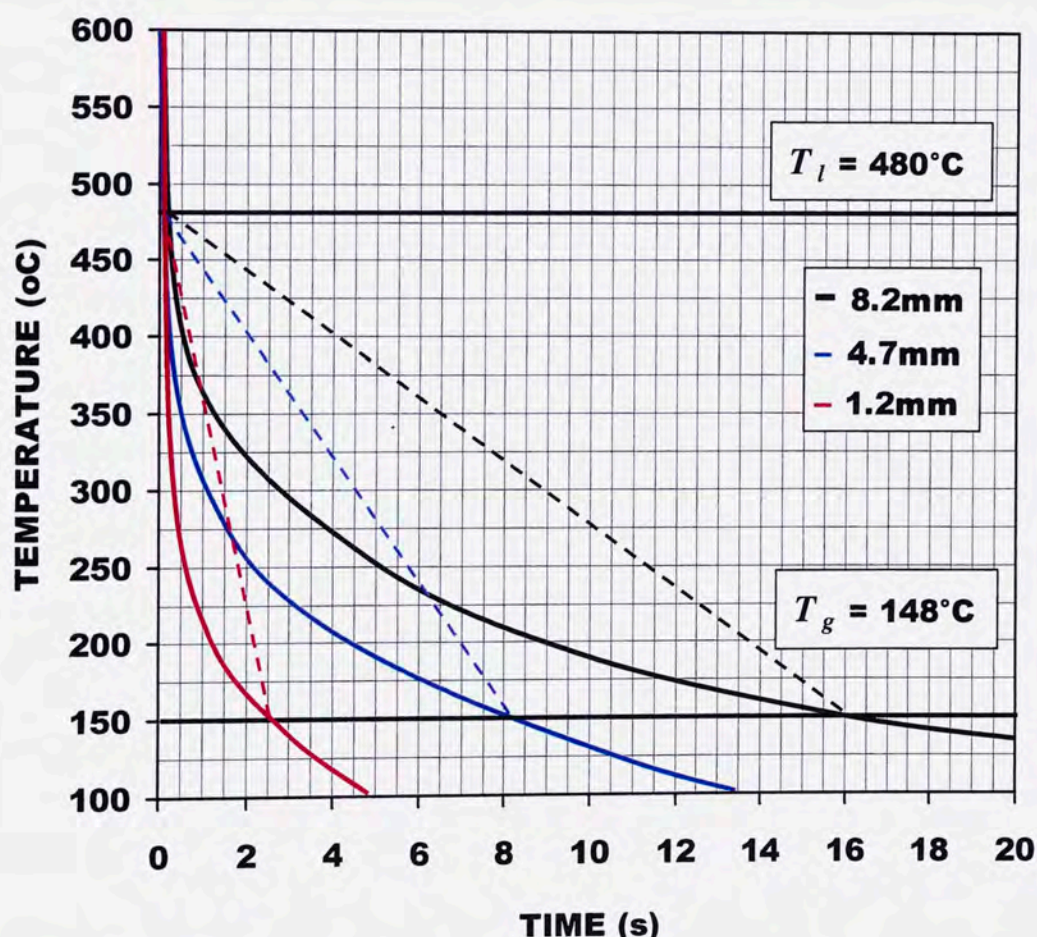


**Figure A:** Cooling curves for the  $Mg_{65}Cu_{25}Y_{10}$  wedge casting showing average cooling rates.

**Table A:**  $Mg_{65}Cu_{25}Y_{10}$  wedge casting cooling rate data and calculations.

THERMOCOUPLE POSITION (mm)	CORRESPONDING TIMES (s)			CALCULATED COOLING RATE (°C/s)
	$\sim T_l$	$\sim T_g$	$\Delta t$	
8.2	0.18	16	15.8	22
4.7	0.10	8.3	8.2	43
1.2	0.10	2.5	2.4	145

## APPENDIX B - CALCULATION OF INJECTION VELOCITY (I)

Pressure was a major experimental variable in this work. However, much of the work in the field of die casting is explained in terms of fluid velocity. For the Mg-based material velocity calculations were made using the Bernoulli integral of the momentum equation for various casting pressures so that a comparison may be made for different casting systems.

$$P_1 + \frac{1}{2}\rho v_1^2 = P_2 + \frac{1}{2}\rho v_2^2 + \rho gh$$

Assuming that the applied pressure was instantaneous and constant, the movement of the flow front was determined by a traditional volume of fluid approach i.e.  $A_1 v_1 = A_2 v_2$  to give an approximate melt flow velocity ( $v_F = v_2$ ) at the end of the silica tube for a particular injection pressure that is:

$$v_F = \sqrt{\frac{2(P_1 - P_2 - \rho gh)}{\rho[1 - (A_2/A_1)^2]}}$$

where:

- $P_1$  is the total injection pressure, which is the reading of the injection pressure gauge (relative to atmospheric pressure) plus atmospheric pressure:

E.g. an injection pressure of 1 Bar =  $1 \times 10^5$  Pa +  $1.013 \times 10^5$  Pa =  $2.013 \times 10^5$  Pa

- $P_2 = P_o = 1.013 \times 10^5$  Pa (atmospheric pressure)
- $\rho$  is the density of the liquid metal, which was approximated to that of the solid  
=  $3260 \text{ kg/m}^3$  - determined using Archimedes method
- $A_1$  the cross-sectional area of the crucible melt surface to which  $P_1$  is applied:  
E.g. crucible inner surface area minus the outer cross sectional area of the silica tube  
=  $1.78 \times 10^{-3} \text{ m}^2$
- $A_2$  the inner cross-sectional area of the silica draw tube  
=  $6.09 \times 10^{-5} \text{ m}^2$  and
- $h$  the silica draw tube height  
=  $0.06 \text{ m}$  – assuming the change in depth of the crucible change is negligible upon injection, that is  $A_1 \gg A_2$ ),



Using these values the melt flow velocity in the silica tube was calculated for the injection pressures used, given in the **VELOCITY 2** column in **Table B**. Again, using the volume of fluid approach i.e.  $A_1 v_1 = A_2 v_2$ , the velocity of the charge drop in the crucible was calculated (**VELOCITY 1**). The cross sectional area of the rectangular mould cavity is  $2.1 \times 10^{-5} \text{ m}^2$ , which was then used to determine the final velocity of the melt entering the mould (gate velocity, given as - **VELOCITY 3** in **Table B**).

**Table B:** Calculated velocities for given cross-sections of the casting apparatus.

RELATIVE INJECTION PRESSURE (BAR)	$P_1 \times 10^5 \text{ Pa}$	VELOCITY 1	VELOCITY 2	VELOCITY 3
1.0	2.013	0.264	7.71	22.34
0.8	1.813	0.235	6.88	19.93
0.7	1.713	0.220	6.43	18.61
0.6	1.613	0.203	5.94	17.19
0.5	1.513	0.185	5.40	15.64
0.4	1.413	0.164	4.81	13.92
0.3	1.313	0.141	4.13	11.95

This method of calculation gives a maximum possible velocity entering the mould channel, neglecting friction effects of the wall of the silica tube and energy losses associated with flow system restrictions.

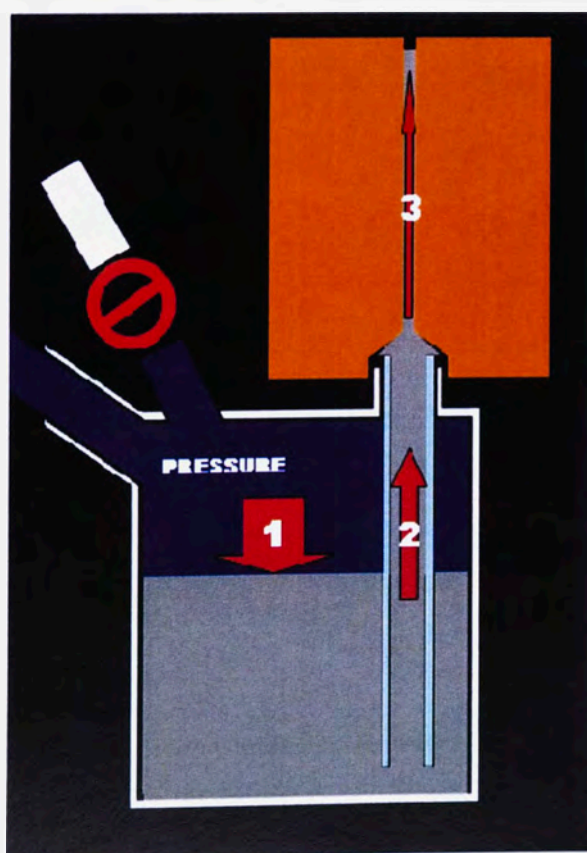


**Figure B:** The designated velocity cross-sections for the apparatus from **Table B**.



## APPENDIX C - DETERMINATION OF FLOW STRESS

The method used to determine flow stress as opposed to peak stress when a stress overshoot occurs involves extrapolating the flow stress curve from beyond the stress overshoot back to the initial elastic region of the curve is indicated in **Figure C(i)** for the  $\text{Ca}_{65}\text{Mg}_{15}\text{Zn}_{20}$  BMG (from **Figure 4.31**). This method has been used by numerous research groups like in **Figure C(ii)** which is from the work of Kim et al. for the  $\text{Cu}_{54}\text{Ni}_6\text{Zr}_{22}\text{Ti}_{18}$  BMG.<sup>[185]</sup>

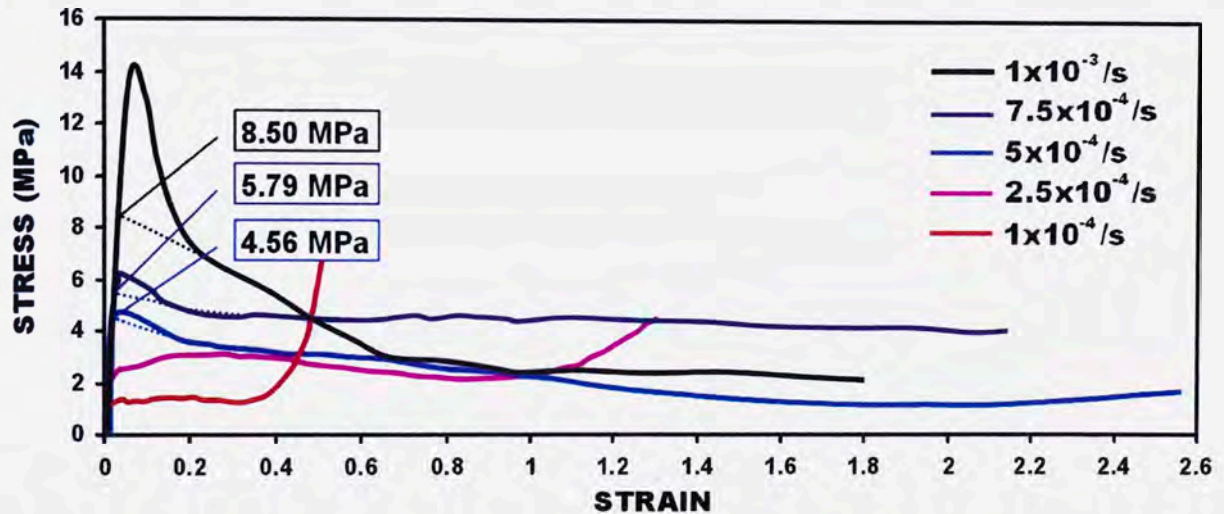


**Figure C(i):** Flow stress determination for  $\text{Ca}_{65}\text{Mg}_{15}\text{Zn}_{20}$  BMG tensile samples tested at 120 °C.

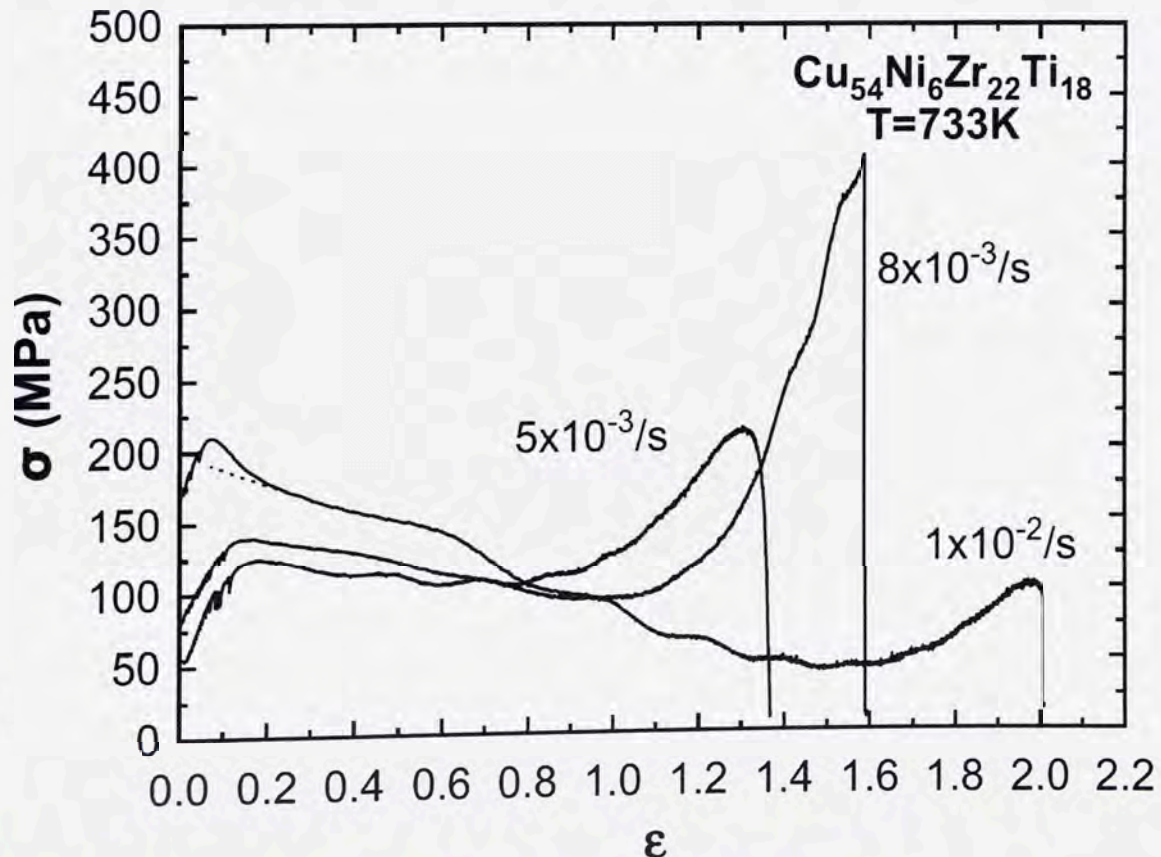


**Figure C(ii):** Flow stress determination for the  $\text{Cu}_{54}\text{Ni}_6\text{Zr}_{22}\text{Ti}_{18}$  BMG.<sup>[185]</sup>



## APPENDIX D - CALCULATION OF NORMALISED VISCOSITY

The steady-state flow stress can be prescribed according to the transition state theory of flow stress originally suggested by Spaepen<sup>[180]</sup>, for uniaxial flow. I.e.:

$$\dot{\epsilon} = \dot{\epsilon}_0 \sinh \frac{\sigma_f V}{2\sqrt{3}k_B T}$$

where  $\dot{\epsilon}_0$  denotes a frequency factor, defined as a measure of the effective number of attempts per unit time to overcome a particular energy barrier, and expected to be constant for a given deformation temperature,<sup>[188]</sup>  $\dot{\epsilon}$  is the uniaxial strain rate and  $\sigma_f$  the uniaxial flow stress. To determine the activation volume,  $V$  and the frequency factor,  $\dot{\epsilon}_0$  of a given glass at a particular temperature, flow stress and strain rate data at that temperature are plotted against one another as shown in **Figure D** for flow stress data generated for the  $\text{Ca}_{65}\text{Mg}_{15}\text{Zn}_{20}$  BMG under uniaxial tension at 120 °C. Essentially, a curve is fitted to the data (using ORIGIN 6.0 Software) corresponding to the above formula (Eq. (2.34)), resulting in values of the activation volume,  $V$  and the frequency factor,  $\dot{\epsilon}_0$  of a given glass at a particular temperature. For the example below,  $m1 = \dot{\epsilon}_0 = 0.049229$  and  $m2 = V = 3.0581 \times 10^{-20} \text{ mm}^3$ .

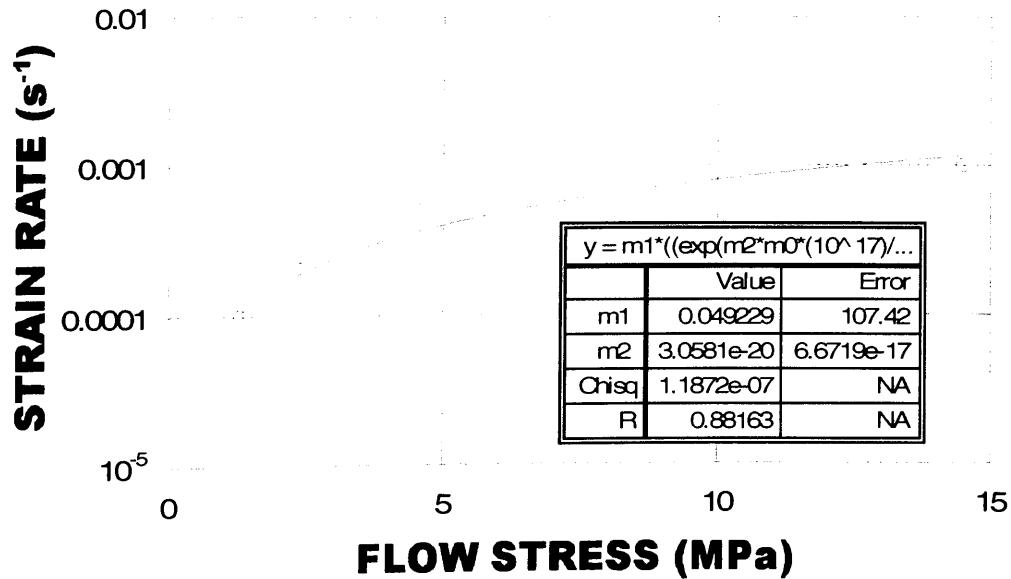


**Figure D:** Curve fitted to the tensile flow stress and strain rate data for the  $\text{Ca}_{65}\text{Mg}_{15}\text{Zn}_{20}$  BMG for samples tested at 120 °C and corresponding  $V$  - and  $\dot{\epsilon}_0$  - values.

Viscosity can also be defined in terms of the free-volume model by combining Eq. (2.32) with Eq. (2.34) to give:

$$\eta = \frac{\sigma_f}{3\dot{\epsilon}_o \sinh(\sigma_f V / 2\sqrt{3} k_B T)}$$

Newtonian viscosity ( $\eta_N$ ) is expected at high temperatures and low stresses, so Eq. (3.15) can be rewritten as:<sup>[183,188]</sup>

$$\eta_N = \frac{2\sqrt{3}k_B T}{3\dot{\epsilon}_o V}$$

Based on the work of Bletry et al.,<sup>[183,188]</sup> normalised viscosity ( $\eta/\eta_N$ ) can be determined by:

$$\frac{\eta}{\eta_N} = \frac{\sigma_f V / 2\sqrt{3}k_B T}{\sinh(\sigma_f V / 2\sqrt{3}k_B T)}$$

Equation (3.17) was used to construct the viscosity master curves shown in **Figure 3.44** and **Figure 4.34** in terms of  $\eta/\eta_N$  as a function of  $\sigma_f V / 2\sqrt{3}k_B T$  for all homogeneous flow data. The master curve successfully demonstrates Newtonian flow in the supercooled state at higher temperatures and lower strain rates where normalised viscosity is unity. **Table D** shows the results for the  $\text{Ca}_{65}\text{Mg}_{15}\text{Zn}_{20}$  BMG under uniaxial tension from 110°C to 120 °C.

**Table D:** Normalised viscosity calculations for the  $\text{Ca}_{65}\text{Mg}_{15}\text{Zn}_{20}$  BMG under uniaxial tension from 110°C to 120 °C.

$T$ (°C)	$T$ (K)	$\sigma$ (MPa)	$\dot{\epsilon}$ (s <sup>-1</sup> )	$\eta$ (Pa.s)	$\sigma V / 2\sqrt{3}k_B T$	$\sinh(\sigma V / 2\sqrt{3}k_B T)$	$\frac{\sigma V / 2\sqrt{3}k_B T}{\sinh(\sigma V / 2\sqrt{3}k_B T)}$
120	393	14.5	1.0E-03	4.83E+09	0.0236	0.02361	0.99991
120	393	6.03	7.5E-04	2.68E+09	0.00982	0.00982	0.99998
120	393	4.56	5.0E-04	3.04E+09	0.00742	0.00742	0.99999
120	393	2.42	2.5E-04	3.23E+09	0.00394	0.00394	1.00000
120	393	1.31	1.0E-04	4.37E+09	0.00213	0.00213	1.00000
115	388	12.5	1.0E-03	4.17E+09	0.06137	0.0614	0.99937
115	388	11.9	7.5E-04	5.29E+09	0.05842	0.05845	0.99943
115	388	10.8	5.0E-04	7.20E+09	0.05302	0.05305	0.99953
115	388	4.85	2.5E-04	6.47E+09	0.02381	0.02381	0.99991
115	388	3.49	1.0E-04	1.16E+10	0.01713	0.01713	0.99995
110	383	20.5	1.0E-03	6.83E+09	0.18476	0.18581	0.99433
110	383	21.3	7.5E-04	9.47E+09	0.19197	0.19315	0.99388
110	383	26.1	5.0E-04	1.74E+10	0.23523	0.23741	0.99084
110	383	12.1	2.5E-04	1.61E+10	0.10905	0.10927	0.99802
110	383	10.2	1.0E-04	3.40E+10	0.09193	0.09206	0.99859



## APPENDIX E - CALCULATION OF STRAIN RATE SENSITIVITY

The relationship between log stress ( $\sigma_f$ ) and log strain rate ( $\dot{\epsilon}$ ) in the SCL region for a BMG can be expressed by Eq. (2.30),  $\sigma_f = K\dot{\epsilon}^m$ , The average strain rate sensitivity exponent (used to construct Figures **Figure 3.47** and **4.37** was calculated for a particular strain rate interval using:

$$\bar{m} = \frac{\partial \log \sigma_f}{\partial \log \dot{\epsilon}}$$

for that particular interval.

E.g. for the first strain rate interval shown in **Table E**:

$$\partial \log \sigma_f = \log(87400000) - \log(57600000) = 0.181$$

$$\partial \log \dot{\epsilon} = \log(0.1) - \log(0.05) = 0.301$$

Now,

$$\bar{m} = \frac{\partial \log \sigma_f}{\partial \log \dot{\epsilon}} = 0.602$$

Calculated values for the average the average strain rate sensitivity of a given interval for the  $\text{Mg}_{65}\text{Cu}_{25}\text{Y}_{10}$  BMG flow stress data at 170 °C can be seen in **Table E**. These data values, together with those for all other intervals were plotted on a Temperature/log Strain Rate plot and an average contour map was developed in terms of  $\bar{m}$  from these data points.

**Table E:** Calculated  $\bar{m}$  -values and associated data for given strain rate intervals at 170 °C for the  $\text{Mg}_{65}\text{Cu}_{25}\text{Y}_{10}$  BMG.

TEMP (°C)	$\sigma_f$ (MPa)	$\dot{\epsilon}$ (/s)	$\partial \log \sigma_f$	$\partial \log \dot{\epsilon}$	$\bar{m}$ for interval
170	87.4	0.1	0.181	0.301	0.602
	57.6	0.05			
170	57.6	0.05	0.581	0.698	0.832
	15.1	0.01			
170	15.1	0.01	0.365	0.301	1.21
	6.52	0.005			
170	6.52	0.005	0.814	0.698	1.16
	1	0.001			

## APPENDIX F - CALCULATION OF INJECTION VELOCITY (II)

For the production of the  $\text{Ca}_{65}\text{Mg}_{15}\text{Zn}_{20}$  BMG bars the induction-heated die caster was constructed with a much larger casting chamber than that of the apparatus used to manufacture the  $\text{Mg}_{65}\text{Cu}_{25}\text{Y}_{10}$  BMG bars. Hence the assumptions made with respect to velocity calculation were no longer valid and it became necessary to develop a more accurate method of velocity calculation than the simple Bernoulli approach. Firstly, calculations were made to determine the amount of pressure  $P_R$  required to move a known mass of fluid a specified distance to the mould gate using:<sup>[291]</sup>

$$P_R = P_o + \rho gh$$

where:

- $P_o = 1.013 \times 10^5$  Pa (atmospheric pressure)
- $\rho$  is the density of the liquid metal, which was approximated to that of the solid  
 $= 2120 \text{ kg/m}^3$  - determined using Archimedes method
- $h$  the silica draw tube height  
 $= 0.08 \text{ m}$  – assuming the change in depth of the crucible change is negligible upon injection, that is  $A_1 \gg A_2$ ),
- $g$  the acceleration due to gravity  
 $= 9.8 \text{ m/s}^2$  - determined using Archimedes method

Calculating using these values:

$$P_R = 1.013 \times 10^5 + (2120 \times 9.8 \times 0.08) = 1.030 \times 10^5 \text{ Pa}$$

Now, pressure in this case is supplied by the argon gas. Pressure of a fluid is considered to be generated by a certain number of atoms or molecules (argon in this case) colliding with the walls of the vessel in which they are contained. It is reasonable to assume argon behaves as an ideal gas, with the number of moles of gas required to generate the above required pressure determined using:

$$P_R V = nRT$$

- $V$  is the volume of the injection system calculated to be  $6.17 \times 10^{-3} \text{ m}^3$
- $R$  the universal gas constant  $= 8.31451 \text{ J/Kmol}$
- $T$  is the gas temperature  $= 300 \text{ K}$



Now, the chamber is already at atmospheric pressure, so there are already a certain number of moles of gas present. Calculating the increase in the number of moles of gas required to raise the pressure to  $P_R$ :

$$n = \frac{(P_R - P_o)V}{RT} = \frac{(1.030 \times 10^5 - 1.013 \times 10^5) \times 6.17 \times 10^{-3}}{8.315 \times 300} = 4.205 \times 10^{-3} \text{ moles}$$

Knowing the pressure (number of moles of argon in a specific volume) required to raise the charge material to the mould gate, the time required to achieve this pressure in the casting chamber may be calculated by a knowledge of the mass flow rate,  $\dot{M}$  of the gas flowing into the chamber for a given injection pressure, which, neglecting gas injection tube wall friction may be calculated using:

$$\frac{M}{RT} \frac{P_2^2 - P_1^2}{2} + \left( \frac{\dot{M}}{A} \right)^2 \ln \frac{P_1}{P_2} = 0$$

where:

- $M$  is the molecular mass of the gas (argon = 0.039948 kg/kgmol)
- $P_2$  is the total injection pressure, which is the reading of the injection pressure gauge (relative to atmospheric pressure) plus atmospheric pressure:  
e.g. an injection pressure of 2.2 Bar =  $2.2 \times 10^5$  Pa +  $1.013 \times 10^5$  Pa =  $3.213 \times 10^5$  Pa
- $P_1 = P_o = 1.013 \times 10^5$  Pa (atmospheric pressure)
- $A$  is the inner cross-sectional area of the gas injection tube =  $1.964 \times 10^{-5} \text{ m}^2$

Rearranging and calculating for an injection pressure of 2.2 Bar gives:

$$\dot{M} = A \sqrt{\frac{-M(P_2^2 - P_1^2)}{2RT \ln(P_1/P_2)}} = 1.964 \times 10^{-5} \sqrt{\frac{-0.03995 \times ((3.213 \times 10^5)^2 - (1.013 \times 10^5)^2)}{2 \times 8.315 \times 300 \times \ln(1.013 \times 10^5 / 3.213 \times 10^5)}}$$

$$= 0.0157 \text{ kg/s}$$

Using this value of mass flow rate, the volume flow rate may now be determined simply using the following density relationship (density of argon gas is  $1.623 \text{ kg/m}^3$  at 300K):

$$\dot{V} = \frac{\dot{M}}{\rho} = \frac{0.0157}{1.623} = 9.673 \times 10^{-3} \text{ m}^3/\text{s} = 9.673 \text{ L/s}$$

Since a value of the molar flow rate is required (to raise the chamber pressure to a molar equivalent of 1.030 moles), the previous result can be converted, again assuming one mole of an ideal gas occupies 24.465 L the molar flow rate is determined to be:

$$\text{Molar Flow Rate} = \frac{9.673}{24.465} = 0.395 \text{ mol/s}$$

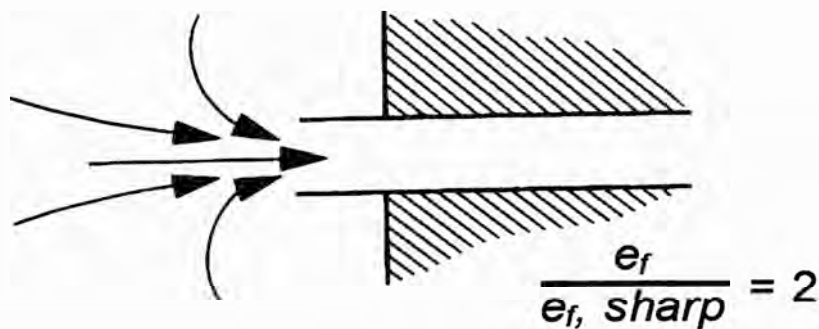
Now, the time required for the charge to reach the mould gate can be calculated by:

$$\text{TIME} = \frac{4.205 \times 10^{-3}}{0.395} = 0.0106 \text{ s}$$

Since the mass flow rate is constant, it must be assumed that the velocity in the silica tube is constant, which can be calculated by dividing the displacement of the molten metal in the silica tube by the time it takes to travel that distance. i.e.:

$$\text{VELOCITY} = \frac{0.08}{0.0106} = 7.556 \text{ m/s}$$

This value of velocity is the maximum possible value for velocity,  $v_{MAX}$ , (neglecting wall friction and flow path restrictions) and should be corrected due to the presence of a flow restriction upon entering the silica tube, depicted below:



Losses associated with the tube entrance, could be calculated for a given injection pressure by using a discharge coefficient,  $C_D$ , where the corrected velocity  $v_F$  can be found using:<sup>[293]</sup>

$$v_F = C_D v_{MAX}$$

where

$$C_D = \left( \frac{1}{\beta} + e_f \right)^{-1/2}$$

where  $\beta$  is the velocity distribution factor for the cross section, which is approximated as unity for turbulent flow,<sup>[293]</sup> and  $e_f$ , the friction loss factor for a sudden contraction is given as:<sup>[294]</sup>

$$e_f = 0.5 \left( 1 - \frac{A_s}{A_L} \right)$$

where  $A_s$  and  $A_L$  are the cross section areas of the smaller and larger sections in the fluid circuit, respectively. This value is further corrected by a ratio associated with the type of entrance to the restriction. Hence:

$$v_F = \left( \frac{1}{\beta} + \left[ 0.5 \left( 1 - \frac{A_s}{A_L} \right) \times \frac{e_f}{e_{f \text{ sharp}}} \right] \right)^{-1/2} \times v_{MAX}$$

$$v_F = \left( 1 + \left[ 0.5 \left( 1 - \frac{6.08212 \times 10^{-5}}{5.20719 \times 10^{-4}} \right) \times 2 \right] \right)^{-1/2} \times 7.556 = 5.5057 \text{ m/s}$$

The maximum velocity of the flow front upon entering the mould gate,  $v_{GATE}$ , was determined by a traditional conservation of fluid volume approach, i.e.  $A_1 v_1 = A_2 v_2$  with respect to the decrease in channel cross section area. Discharge coefficient corrections for the type of restriction at the mould gate shown below were made in a similar manner to that described above.

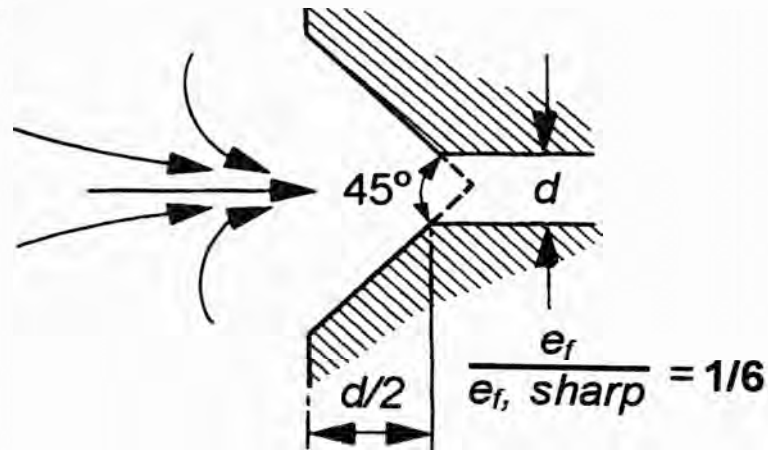
Given:

- $A_1$  the inner cross-sectional area of the silica draw tube  $= 6.08212 \times 10^{-5} \text{ m}^2$
- $A_2$  the cross sectional area of the rectangular mould cavity is  $= 2.1 \times 10^{-5} \text{ m}^2$

Calculating:

$$v_{MAXGATE} = \frac{A_1 v_F}{A_2} = \frac{6.08212 \times 10^{-5} \times 5.5057}{2.1 \times 10^{-5}} = 15.786 \text{ m/s}$$





Making corrections for the restriction entry into the mould pattern as shown above:

$$v_{GATE} = \left( \frac{1}{\beta} + \left[ 0.5 \left( 1 - \frac{A_s}{A_L} \right) \times \frac{e_f}{e_{f, \text{sharp}}} \right]^{-1/2} \right) \times v_{MAXGATE}$$

Calculating:

$$v_{GATE} = \left( 1 + \left[ 0.5 \left( 1 - \frac{2.1 \times 10^{-5}}{6.08212 \times 10^{-5}} \right) \times \frac{1}{6} \right]^{-1/2} \right) \times 15.786$$

=14.799 m/s

= The calculated velocity of the molten metal flow front upon entry to the mould pattern for an injection pressure of 2.2 Bar.

This calculation was carried out for all injection pressures used, as represented by the velocity scale in **Figure 4.25**.

## APPENDIX G - CALCULATION OF SAMPLE COOLING RATE

To estimate the cooling rate curves for  $\text{Ca}_{65}\text{Mg}_{15}\text{Zn}_{20}$  BMG bars given in **Figure 4.24**, firstly the interfacial heat transfer coefficient for copper mould casting  $h$  must be estimated. This was achieved using critical cooling rate data gathered for a sample of diameter 6 mm as the cross section area and surface area of this sample is comparable to that of the as-cast bars. From this data, the average cooling rate from the casting temperature was determined to be  $357\text{ }^{\circ}\text{C/s}$ . Since the cavity in the mould has a circular cross section of various diameters, by assuming that the heat flux is interface-controlled (neglecting frictional effects between the casting and mould wall), the heat leaving the volume element (casting) is equal to heat entering the mould which may be described by:<sup>[242]</sup>

$$\frac{dT}{dt} = - \frac{h(T_{\text{CAST}} - T_o)(A)}{VC_p\rho}$$

where:

- $T_{\text{CAST}}$  is the initial injection/casting temperature, e.g.  $420\text{ }^{\circ}\text{C} = 693\text{ K}$ .
- $V$  is the volume of metal present in the mould
- $A$  is the surface area through which the heat is being transferred (i.e. between the casting and the mould wall).
- $\rho$  is the density of the metal, determined to be  $2120\text{ kg/m}^3$  using Archimedes principle (assumed to be constant for calculations).
- $C_p$  is the heat capacity of the alloy, which was estimated using the rule of mixtures and the individual heat capacities of the alloy constituents. i.e.:

$$\text{Ca} = 650\text{ J/K.kg}$$

$$\text{Mg} = 1020\text{ J/K.kg}$$

$$\text{Zn} = 390\text{ J/K.kg}$$

Calculating:

$$C_p = (0.65 \times 650) + (0.15 \times 1020) + (0.20 \times 390) = 653.5\text{ J/K.kg}$$

Rearranging and calculating for a sample of length  $L$ :

$$h = \frac{dT}{dt} \left[ \frac{(\pi^2 L) C_p \rho}{(T_{CAST} - T_o) 2\pi L} \right] = 357 \times \left[ \frac{(\pi \times (3 \times 10^{-3})^2) \times 653.5 \times 2120}{(693 - 300) \times (2 \times \pi \times 3 \times 10^{-3})} \right] = 1888 \text{ W/m}^2\text{K}$$

Now, the cooling rate of the sample is given by:<sup>[231]</sup>

$$\frac{dT}{dt} V C_p \rho = -hA(T - T_o)$$

Here  $A$  is the surface area through which the heat is being transferred (i.e. between the casting and the mould wall). This equation can be used to determine the change (drop) in temperature for small increments in time for a given temperature interval. Rearranging this expression, and dividing by the sample length, in the volume and surface area terms in order to get a cooling rate at any point on the surface (this is a dynamic casting system where the metal is flowing in a channel) i.e.:

$$dT = -\frac{hA(T - T_o)}{V C_p \rho} dt = \frac{h(2 \times (Z + W) \times L)(T - T_o)}{(Z \times W \times L) C_p \rho} dt$$

where  $Z$ ,  $W$  and  $L$  are the thickness, width and length of the casting respectively. As an example, the temperature drop for a point on the casting surface for the first 0.01 seconds of cooling at a casting temperature of 600 °C (873 K) with an equilibrium mould temperature ( $T_o$ ) of 27 °C (300 K) may be found to be:

$$\Delta T = \frac{1888 \times (2 \times (0.00315 + 0.007)) \times (873 - 300)}{(0.00315 \times 0.007) \times 653.5 \times 2120} \times 0.01 = 7.22 \text{ °C}$$

Now, by subtracting the above answer from the initial temperature of 600 °C (873 K), the temperature drop for the next 0.01 second interval may be calculated i.e.:

$$\Delta T = \frac{1888 \times (2 \times (0.00315 + 0.007)) \times ((873 - 7.134) - 300)}{(0.00315 \times 0.007) \times 653.5 \times 2120} \times 0.01 = 7.13 \text{ °C}$$



As an example, **TABLE G** shows the calculated temperature drop for the first 0.2 s in 0.01 s intervals for a casting temperature of 600 °C. The calculated cooling curves are given in **Figure 4.24**.

**TABLE G:** Calculated temperature decrease for a  $\text{Ca}_{65}\text{Mg}_{15}\text{Zn}_{20}$  BMG bar sample cast at 600 °C for the first 0.2 s of cooling.

TIME (s)	TEMP DROP	TEMP (°C)	TIME (s)	TEMP DROP	TEMP (°C)
0	0	600.000			
0.01	7.219	592.781	0.11	6.355	525.430
0.02	7.128	585.653	0.12	6.275	519.155
0.03	7.038	578.615	0.13	6.195	512.959
0.04	6.949	571.667	0.14	6.117	506.842
0.05	6.861	564.806	0.15	6.039	500.803
0.06	6.774	558.032	0.16	5.963	494.840
0.07	6.688	551.345	0.17	5.887	488.952
0.08	6.603	544.741	0.18	5.813	483.140
0.09	6.519	538.222	0.19	5.739	477.400
0.10	6.437	531.785	0.20	5.667	471.734

## APPENDIX H - CALCULATION OF CHAMBER PRESSURE INCREASE

To estimate the pressure increase curves given in **Figure 4.24**, a model was developed. The model simplifies the increase of pressure in the chamber by considering the injection gas as a flow front in a long tube of nominal diameter (pressure being non-geometry specific). The increase in pressure is then considered as the fraction of the progression of this flow front.

Assuming argon behaves as an ideal gas, the number of moles of gas required to generate a given pressure can be determined using:

$$PV = nRT$$

- $P$  is the pressure applied to the vessel wall by the gas
- $V$  is the volume of the closed injection chamber, calculated to be  $2.32 \times 10^{-3} \text{ m}^3$
- $n$  is the number of moles present
- $R$  the universal gas constant =  $8.31451 \text{ J/Kmol}$
- $T$  is the gas temperature =  $300 \text{ K}$

In this case,  $V$ ,  $R$  and  $T$  are considered constant so to calculate the number of moles required to raise the pressure inside a sealed vessel from  $P_1$  to  $P_2$  we can use:

$$\frac{P_1}{n_1} = \frac{P_2}{n_2}$$

Here, the example of an injection pressure of 2.2 Bar ( $2.2 \times 10^5 \text{ Pa}$ ) will be used such that:

- $P_1 = P_o = 1.013 \times 10^5 \text{ Pa}$  (initial chamber pressure equals the atmospheric pressure)
- $P_2$  is the total injection pressure, which is the reading of the injection pressure gauge (relative to atmospheric pressure) plus atmospheric pressure:  
 e.g. an injection pressure of 2.2 Bar =  $2.2 \times 10^5 \text{ Pa} + 1.013 \times 10^5 \text{ Pa} = 3.213 \times 10^5 \text{ Pa}$   
 (This is the pressure that the chamber approaches when the mould vent is sealed).
- $n_1$  is the number of moles initially in the chamber when held at atmospheric pressure.
- $n_2$  is the number of moles in the chamber when held at a pressure of  $3.213 \times 10^5 \text{ Pa}$

Calculating  $n_1$ :

$$n_1 = \frac{PV}{RT} = \frac{1.013 \times 10^5 \times 2.32 \times 10^{-3}}{8.31451 \times 300} = 0.0942 \text{ moles}$$

Calculating  $n_2$ :

$$n_2 = \frac{P_2 n_1}{P_1} = \frac{3.213 \times 10^5 \times 0.0942}{1.013 \times 10^5} = 0.2988 \text{ moles}$$

Now the number of moles required to raise the chamber pressure to  $P_2$  is the difference between  $n_1$  and  $n_2$ , which is equal to 0.2045 moles for this example. Converting the number of moles required to the volume of gas required, again assuming one mole of an ideal gas occupies 24.465 L the required volume is determined to be:

$$\text{Required Volume} = \frac{0.2045 \times 24.465}{1000} = 5.003 \times 10^{-3} \text{ m}^3$$

As pressure builds within the chamber, the flow rate of the injected gas decreases (to zero) until the chamber pressure is equal to the injection pressure. Using the aforementioned model, a volume of  $5 \times 10^{-3} \text{ m}^3$  is the equivalent of a tube of diameter 5 mm (identical to the inner diameter of the injection outlet) and a length,  $L$ , of 254.85 m. Using the methodology to determine the volume flow rate determined in **APPENDIX F**, the initial velocity of the flow front in the tube can be calculated. Calculating for an injection pressure of 2.2 Bar gives:

$$\begin{aligned} \dot{M} &= A \sqrt{\frac{-M(P_2^2 - P_1^2)}{2RT \ln(P_1/P_2)}} = 1.964 \times 10^{-5} \sqrt{\frac{-0.03995 \times ((3.213 \times 10^5)^2 - (1.013 \times 10^5)^2)}{2 \times 8.315 \times 300 \times \ln(1.013 \times 10^5 / 3.213 \times 10^5)}} \\ &= 0.01577 \text{ kg/s} \end{aligned}$$

Using this value of mass flow rate, the volume flow rate may now be determined simply by using the density relationship (density of argon gas at atmospheric pressure is  $1.623 \text{ kg/m}^3$  at 300K):

$$\dot{V} = \frac{\dot{M}}{\rho} = \frac{0.01577}{1.623} = 9.7165 \times 10^{-3} \text{ m}^3/\text{s}$$



By dividing this value by the cross sectional area of the tube model, the initial velocity of the flow front may be calculated:

$$v_i = \frac{9.7165 \times 10^{-3}}{1.9635 \times 10^{-5}} = 493.47 \text{ m/s}$$

Using boundary conditions i.e. the final velocity of the flow front is zero, the basic motion equation may be used to calculate the 'deceleration' of the volume flow rate as pressure in the chamber increases:

$$v^2 = u^2 + 2aL$$

where:

- $v$  is the final velocity, which is zero once the chamber pressure has reached the injection pressure.
- $u = v_i$  is the initial velocity, which for the tube model was calculated to be 493.47 for an injection pressure of 2.2 Bar.
- $L$  is the distance of the tube in the model, which for 2.2 Bar was calculated to be 254.85 m.
- $a$  is the 'deceleration' value.

For an injection pressure of 2.2 Bar,  $a$  can be calculated as:

$$a = -\frac{v_i^2}{2x} = -\frac{493.47^2}{2 \times 254.85} = -477.757 \text{ m/s}^2$$

Now, using the tube model, the displacement  $x$  of the gas front in the tube may also be calculated using the basic motion equation:

$$x = v_i t + at^2/2$$

Calculating for an injection pressure of 2.2 Bar and a time increment of 0.01 s:

$$x = 493.47 \times 0.01 - 477.757 \times 0.01^2 = 4.887 \text{ metres}$$

From this calculation, the fraction of the total volume in the tube (model) that has been injected into the system can be calculated, using the total length of the tube,  $L$  in the model i.e.

$$\text{FRACTION OF GAS INJECTED} = \frac{x}{L} = \frac{4.887}{254.85} = 0.1917$$

Since this tube model volume is based on the number of moles required to fill a volume, this is equivalent to the fraction of the total moles required to generate a final chamber pressure of  $3.213 \times 10^5$  Pa (or a change in pressure  $\Delta P$  of 2.2 Bar). For the current example:

$$\Delta P = \left( P_1 + \left[ \frac{x}{L} \times P_2 \right] \right) - P_1 = \left( 1.013 \times 10^5 + \left[ 0.1917 \times 2.2 \times 10^5 \right] \right) - 1.013 \times 10^5 = 4239 \text{ Pa}$$

An example of calculations for an injection pressure of 2.2 Bar for the first 0.2 s of injection casting is given in **Table H**. The calculated pressure increase curves are given in **Figure 4.24**.

**Table H:** Calculated pressure increase for the injection chamber for the first 0.2 s of injection casting.

TIME (s)	FRACTION	$\Delta P$ (Pa)	TIME (s)	FRACTION	$\Delta P$ (Pa)
0.00	0.000	0.00E+00			
0.01	0.019	4.24E+03	0.11	0.202	4.44E+04
0.02	0.038	8.44E+03	0.12	0.219	4.81E+04
0.03	0.057	1.26E+04	0.13	0.236	5.19E+04
0.04	0.076	1.67E+04	0.14	0.253	5.56E+04
0.05	0.094	2.08E+04	0.15	0.269	5.93E+04
0.06	0.113	2.48E+04	0.16	0.286	6.29E+04
0.07	0.131	2.88E+04	0.17	0.302	6.65E+04
0.08	0.149	3.28E+04	0.18	0.318	7.00E+04
0.09	0.167	3.67E+04	0.19	0.334	7.35E+04
0.10	0.184	4.05E+04	0.20	0.350	7.70E+04

## APPENDIX I - DETERMINATION OF LOCAL; ACTIVATION ENERGY, AND AVRAMI EXPONENT

Considering an isochronal transformation is basically a continuous successions of infinitesimal isotherms (as done by Augis and Bennett)<sup>[308]</sup> The calculation of the local activation energy associated with a single heating rate (20 °C/min or 0.33 °C/s), was determined by plotting  $\ln(\beta/T - T_o)$  as a function of  $1/RT$ , (similar to the work of Augis and Bennett)<sup>[308]</sup> From this plot, the slope of the individual data intervals (which equals the local activation energy) was calculated, the results of which can be seen in **Figure 5.8** for both the  $\text{Mg}_{65}\text{Cu}_{25}\text{Y}_{10}$  and  $\text{Ca}_{65}\text{Mg}_{15}\text{Zn}_{20}$  alloys.

An example of this calculation for the temperature interval between 144 °C (417 K) and 146 °C (419 K) for the  $\text{Ca}_{65}\text{Mg}_{15}\text{Zn}_{20}$  BMG is given using the following data:

- The onset ( $T_{START}$ ) and completion ( $T_{COMP}$ ) temperatures of crystallisation were determined to be:  $T_o = 132\text{ °C} = 405\text{ K}$  and  $T_{COMP} = 158\text{ °C} = 431\text{ K}$ .
- The heating rate for this test was 20 °C/min or in SI units, 0.33 °C/s

Calculating  $\delta \ln(\beta/(T - T_{START}))$ :

$$\delta \ln(\beta/(T - T_{START})) = [\ln(0.333/(417 - 405))] - [\ln(0.333/(419 - 405))] = 0.154$$

Calculating  $\delta 1/RT$ :

$$\delta 1/RT = [1/(8.315 \times 417)] - [1/(8.315 \times 419)] = 1.377 \times 10^{-6}$$

Now, calculating to determine the local activation energy,  $E_C$  for the given temperature interval:

$$E_C = \frac{\delta \ln(\beta/(T - T_{START}))}{\delta 1/RT} = \frac{0.154}{1.377 \times 10^{-6}} = 111970 = 111.97\text{ kJ/mol}$$



The well known Kissinger equation<sup>[116]</sup> may be used to analyse the crystallisation kinetics and determine the activation energy of the crystallisation reaction (and the glass transition) for characteristic temperatures at a given heating rate (non-isothermal event), given by:

$$\ln\left(\frac{\beta}{T_p^2}\right) = -\frac{E_c}{RT_p} + \text{constant}$$

where  $\beta$  is the heating rate,  $E_c$  is the activation energy for crystallisation,  $T_p$  is the characteristic or peak crystallisation temperature and  $R$  is the universal gas constant. It is also known that  $k = k_o \exp(-E_c/RT)$ . The Avrami exponents ( $n$ ) for isochronal heating (constant heating rate conditions) may be calculated using the Ozawa method,<sup>[117]</sup> where the crystallised volume fraction ( $X_v$ ) can be expressed by:

$$X_v = 1 - \exp\left[-\left(k \frac{T - T_o}{\beta}\right)^n\right]$$

where again,  $k$  is a reaction rate constant and  $T_o$  an initial temperature. The value of  $n$  can be obtained from the plot of  $\log[-\ln(1 - x)]$  against  $\log \beta$ . Now, this relationship may be combined with the Kissinger equation to obtain the local Avrami exponent for data gathered from a single isochronal DSC trace by relating  $\log \beta$  to  $\log(T_p)^2 = 2\log(T_p)$  through  $k$ . Here  $T_p$ , the characteristic temperature is represented by  $T - T_o$ . Hence the local Avrami exponent can be calculated for a given temperature and crystallised fraction interval by:

$$n = \frac{\delta \log(-\ln(1 - X_v))}{\delta \log(T - T_o) \times 2}$$

An example of this calculation for the temperature interval between 144 °C and 146 °C for the  $\text{Ca}_{65}\text{Mg}_{15}\text{Zn}_{20}$  BMG is given using the following data:

- The onset ( $T_o$ ) and completion ( $T_{COMP}$ ) temperatures of crystallisation were determined to be:  $T_o = 132 \text{ °C} = 405 \text{ K}$  and  $T_{COMP} = 158 \text{ °C} = 431 \text{ K}$ .
- At 144 °C (417 K) the volume fraction ( $X_v$ ) of crystalline phase was determined to be:  
 $X_v = 0.3345$  (determined using Thermal Advantage Version 1.1a) Software, which uses the fraction of the area under the DSC curve between  $T_{x1}$  (onset) and  $T_{x2}$  (finish).

▪146 °C (419 K) the volume fraction ( $X_v$ ) of crystalline phase was determined to be:

$$X_v = 0.5943$$

Calculating  $\delta \log(-\ln(1 - X_v))$ :

$$\delta \log(-\ln(1 - X_v)) = [\log(-\ln(1 - 0.5943))] - [\log(-\ln(1 - 0.3345))] = 0.3453$$

Calculating  $\delta(\log(T - T_o)) \times 2$ :

$$\delta(\log(T - T_o) \times 2) = [(\log(419 - 405)) \times 2] - [(\log(417 - 405)) \times 2] = 0.1339$$

Now, calculating to determine the local Avrami exponent  $n$  for the given temperature and transformation interval:

$$n = \frac{\delta \log(-\ln(1 - X_v))}{\delta \log(T - T_o) \times 2} = \frac{0.3453}{0.1339} = 2.58$$

The local Avrami exponents for both the  $\text{Mg}_{65}\text{Cu}_{25}\text{Y}_{10}$  and  $\text{Ca}_{65}\text{Mg}_{15}\text{Zn}_{20}$  alloys upon isochronal heating/crystallisation are shown in **Figure 5.9**.

## APPENDIX J - ANGEL PLOT CONSTRUCTION

The concept of fragility was introduced by Angell<sup>[66-68]</sup> to characterise the increase in liquid viscosity during cooling; it is considered to be a measure of the degree of co-operativity of atomic motion. Fragility of liquids is defined as the apparent activation energy of shear viscosity,  $\eta$ , or structural relaxation time at the glass transition temperature,  $T_g$ , normalised to  $T_g^*$ .<sup>[66-68]</sup> Generally, to compare the fragility of different glassy materials, a plot, known as an 'angel plot' was developed to normalise the viscosity of the glass to a value of  $10^{12}$  Pa.s. This was done by plotting Newtonian flow data in the form of viscosity over inverse temperature as shown below. Curves were fitted to this data and extrapolated to  $10^{12}$  Pa.s. From the intersection at  $10^{12}$  Pa.s, the value of  $T_g^*$  was determined. This value was then used to normalise viscosity/temperature for a direct comparison of the two glasses and others as seen in **Figure 5.16**.

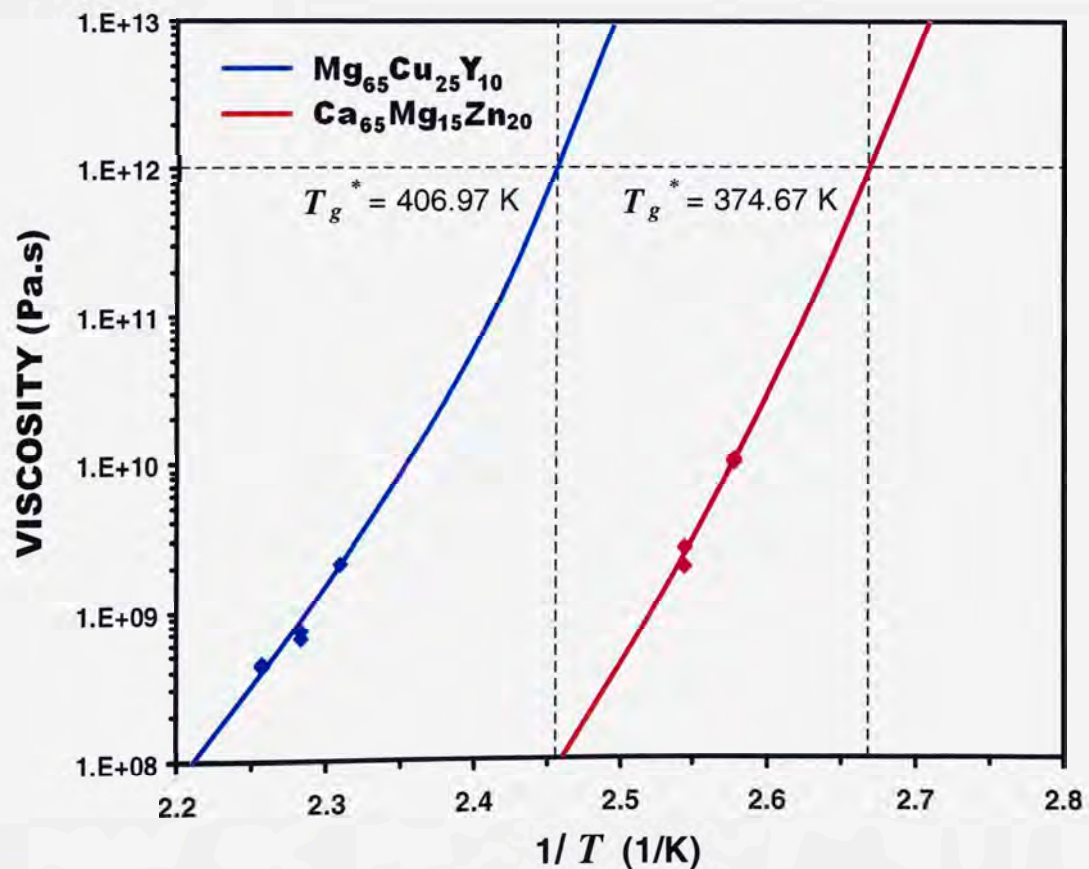


**Figure J:** Curve fitted to the Newtonian viscosity data and extrapolated to  $10^{12}$  Pa.s to determine  $T_g^*$ .



Fin lib.

**ALLBOOK  
BINDERY**

91 RYEDALE ROAD  
WEST RYDE 2114  
PHONE: 9807 6026



